Compressed Baryonic Matter Experiment

Technical Design Report for the CBM

Transition Radiation Detector (TRD)

The CBM Collaboration

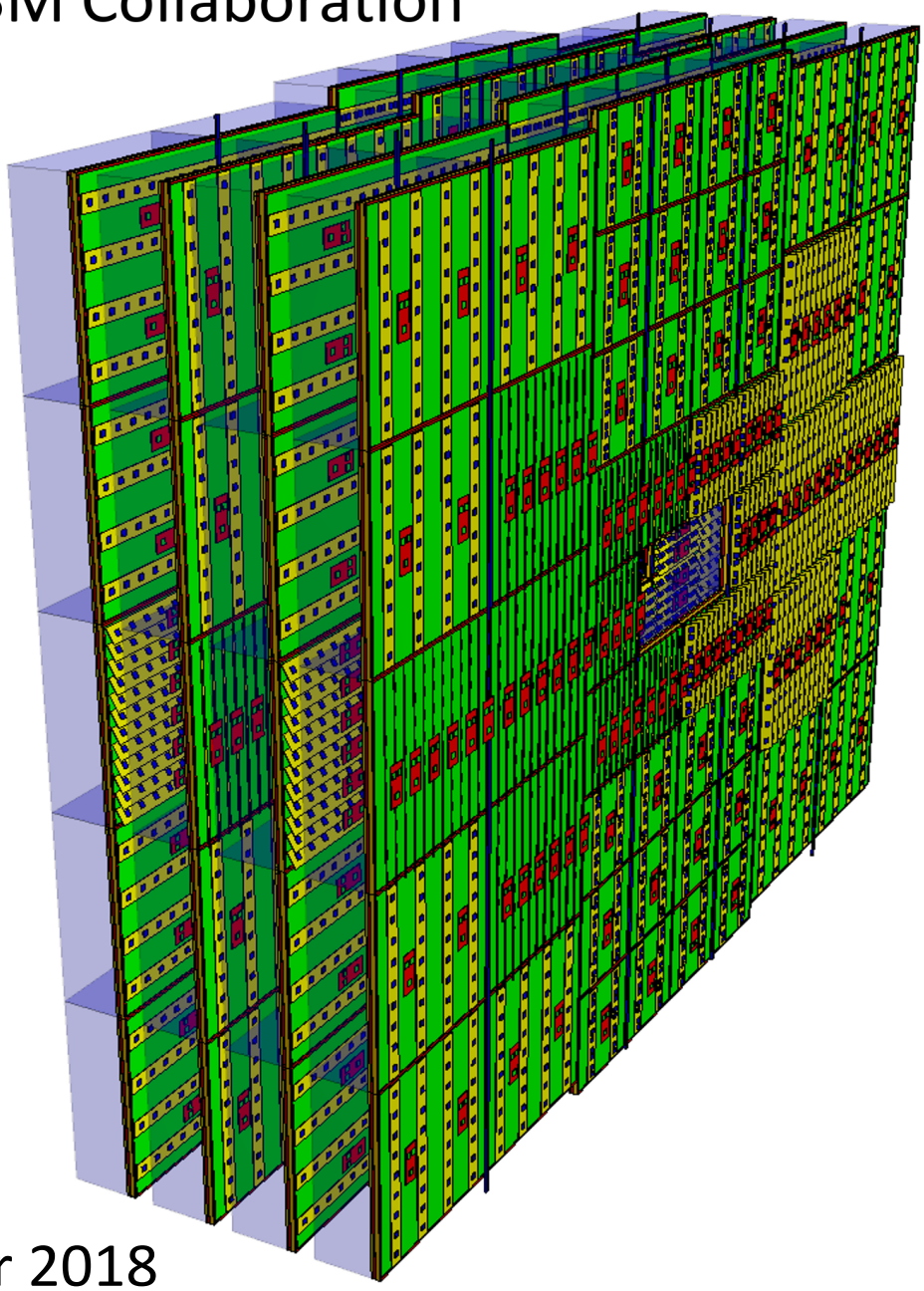

October 2018

The Transition Radiation Detector of the CBM Experiment at FAIR

The CBM Collaboration[1]

Editors: C. Blume[2], C. Bergmann and D. Emschermann

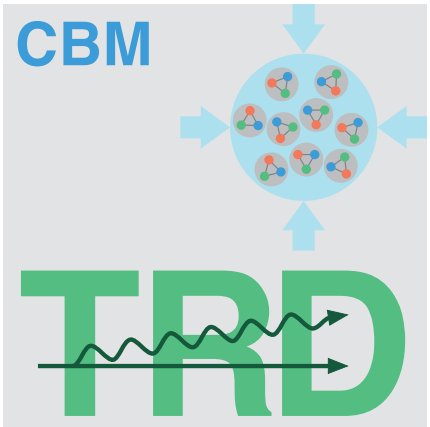

Approved by FAIR-ECE on October 9, 2018

DOI:10.15120/GSI-2018-01091

[1]The full list of CBM members is provided in Appendix A
[2]Corresponding author

The CBM-TRD Working Group

The TRD working group comprises participants from the CBM Collaboration and cooperating institutes:

Horia Hulubei National Institute of Physics and Nuclear Engineering (IFIN-HH), Bucharest, Romania
V. Aprodu, A. Bercuci, D. Bartoş, G. Caragheorgheopol, V. Cătănescu, F. Constantin, M. Petriş, M. Petrovici, L. Prodan, A. Radu, L. Rădulescu, C. Şchiaua, M.G. Târzilă.

GSI Helmholtz Center for Heavy-Ion Research GmbH (GSI), Darmstadt, Germany
D. Emschermann, W. Niebur, A. Lebedev.

Institut für Kernphysik Frankfurt (IKF), Goethe-Universität Frankfurt, Frankfurt am Main, Germany
W. Amend, H. Appelshäuser, E. Bechtel, C. Blume, J. Book, P. Dillenseger, M. Esen, D. Giang, S. Gläßel, F. Roether, S. Schreiber, H. Schuldes, D. Spicker, M. Tanha.

Institut für Infrastruktur und Rechnersysteme in der Informationsverarbeitung (IRI), Goethe-Universität Frankfurt, Frankfurt am Main, Germany
J. Gebelein, U. Kebschull, J.A. Lucio Martínez, D. Schmidt.

Institut für technische Informatik (ZITI), Ruprecht-Karls-Universität Heidelberg, Germany
P. Fischer, M. Krieger.

Institut für Kernphysik (IKP), Westfälische Wilhelms-Universität Münster, Münster, Germany
A. Andronic, J. Beckhoff, R. Berendes, C. Bergmann, D. Bonaventura, F. Fidorra, N. Heine, C. de Jésus García Chávez, P. Kähler, C. Klein-Bösing, M. Kohn, A. Meyer-Ahrens, P. Munkes, R. Weber, J.P. Wessels.

Acknowledgements

The Technical Design Report for the CBM-TRD was written and edited by the following persons:
A. Bercuci, C. Bergmann[3], C. Blume[3], J. Book, V. Cătănescu, D. Emschermann[3], P. Fischer, C. de Jésus García Chávez, P. Kähler, C. Klein-Bösing, M. Krieger, A. Lebedev, S. Lebedev, M. Petriş, M. Petrovici and F. Roether.

We gratefully acknowledge the contributions by the following persons and institutions to the work presented in this Technical Design Report:
A. Andronic, W. Amend, H. Appelshäuser, V. Aprodu, A. Arend, T. Armbruster, A. Bercuci, T. Ballé, D. Bartoş, C. Baumann, E. Bechtel, J. Beckhoff, I. Berceanu, R. Berendes, C. Bergmann, T. Bel, C. Blume, D. Bonaventura, J. Book, G. Caragheorgheopol, V. Cătănescu, J. de Cuveland, F. Constantin, P. Dillenseger, D. Emschermann, N. Feuerborn, F. Fidorra, P. Fischer, T. Galatyuk, S. Gläßel, M. Hartig, N. Heine, E. Hellbär, C. Höhne, D. Hutter, C. de Jésus García Chávez, P. Kähler, U. Kebschull, J. Kochanowski, C. Klein-Bösing, M. Klein-Bösing, M. Kohn, M. Krieger, A. Lebedev, S. Lebedev, E. Lebedeva, S. Linev, J.A. Lucio Martínez, A. Maevskaya, A. Meyer-Ahrens, P. Munkes, W.F.J. Müller, W. Niebur, G. Ososkov, M. Petcu, M. Petriş, M. Petrovici, L. Prodan, A. Radu, L. Rădulescu, P. Reichelt, K. Reuß, F. Roether, A. Senger, P. Senger, A. Schell, C. Şchiaua, S. Schreiber, H. Schuldes, M. Seidl, V. Simion, M. Tanha, M.G. Târzilă, F. Uhlig, Y. Vassiliev, W. Verhoeven and J.P. Wessels.

We also would like to express our gratitude to CERN and DESY for providing their test beam facilities to our group. In particular, we would like to thank M. Stanitzki (DESY) and M. Jäckel (CERN-GIF) for their very helpful support during our test measurements.
The help provided by the ALICE collaboration is greatly appreciated. Special thanks go to C. Garabatos for his expert advice on designing the gas system and Y. Pachmayer for sharing valuable experiences with operating the ALICE-TRD.

Funding agencies and supporting institutions:
This work was supported in part by the GSI Helmholtzzentrum für Schwerionenforschung, Darmstadt, its F&E-cooperation contracts with Frankfurt and Münster, the Facility for Antiproton and Ion Research (FAIR), the German BMBF-Verbundforschung (05P15RFFC1 and 05P16PMFC1), the EU FP6 and FP7 projects HadronPhysics2 (WP18 “FutureGas”) and HadronPhysics3 (WP19 “FuturePID”), the Romanian ANCSI/CAPACITATI Modul III Contract F02, the NUCLEU Project Contract PN 09370103, the Hessian LOEWE initiative HICforFAIR and the ExtreMe Matter Institute EMMI at GSI.

[3]Editors

Summary

This document describes the technical design and the performance of the Transition Radiation Detector (TRD) of the Compressed Baryonic Matter (CBM) experiment at FAIR. The main task of the TRD is to identify electrons above momenta of 1 GeV/c and thus to extend the electron identification capabilities of the Ring Image CHerenkov (RICH) detector above momenta of $p \sim 5\,\mathrm{GeV}/c$. This identification has to be achieved with a pion suppression factor of about 20 at 90 % electron efficiency, in order to allow for a measurement of dielectrons in the mass range from below the ρ and ω masses to beyond the J/ψ mass with a good signal-to-background ratio. Due to its capability of identifying charged particles via their specific energy loss, the TRD in addition will provide valuable information for the measurement of nuclear fragments. This is in particular important for the separation of, e.g, deuterons and ^{4}He, which cannot be achieved using a time-of-flight measurement alone.

These requirements can be fulfilled with Xe/CO_2 filled Multi-Wire Proportional Chambers (MWPC) in combination with an adequate radiator. The default MWPC for the CBM-TRD is composed of a symmetric amplification area of $3.5 + 3.5$ mm thickness, followed by a 5 mm drift region to enhance the TR-photon absorption probability in the active gas volume. This geometry provides also efficient and fast signal creation as well as readout, with timescales below 200 ns per charged particle track. The performance of the detector is optimized by reducing the material budget between radiator and gas volume to a minimum.

The baseline design of the TRD foresees one station composed of four detector layers. It will be positioned between the RICH and the Time-Of-Flight (TOF) detector and thus allows to reduce the background in the TOF resulting from track mismatches by providing additional position information for high precision tracking between Silicon Tracking System (STS) and TOF. In the muon configuration of CBM the TRD will also be used as tracking station behind the last absorber of the MUCH detector.

In this technical design report the design and performance of the TRD, as planned for the SIS100 accelerator, is described in detail. The TRD project is currently being realized in cooperation of institutes from Germany and Romania. The detector system is foreseen to be constructed and installed into the CBM experiment for the Modularized Start Version (MSV) of FAIR.

Contents

Chapter 1

The Compressed Baryonic Matter Experiment

1.1 Exploring the phase diagram of nuclear matter

Substantial experimental and theoretical efforts worldwide are devoted to the exploration of the phase diagram of nuclear matter. Figure 1.1 illustrates the possible phases of nuclear matter and their boundaries in a diagram of temperature versus the baryon chemical potential. Cold nuclear matter - as found in normal nuclei with a net-baryon density equal to one - consists of protons and neutrons (i.e. nucleons) only. At moderate temperatures and densities, nucleons are excited to short-lived states (baryonic resonances) which decay by the emission of mesons. At higher temperatures, also baryon-antibaryon pairs are created. This mixture of baryons, anti-baryons and mesons, all strongly interacting particles, is generally called hadronic matter, or baryonic matter if baryons prevail. At very high temperatures or densities the hadrons melt, and the constituents, the quarks and gluons, form a new phase: the Quark-Gluon-Plasma (QGP). For very low net-baryon densities where the numbers of particles and anti-particles are approximately equal, Quantum Chromo-Dynamics (QCD) on the lattice predicts that hadrons dissolve into quarks and gluons above a temperature of about 160 MeV [1, 2]. The inverse process happened in the universe during the first few microseconds after the big bang: the quarks and gluons were confined into hadrons. In this region of the phase diagram the transition is expected to be a smooth crossover from partonic to hadronic matter [3]. Calculations suggest a critical endpoint at relatively large values of the baryon chemical potential [4]. Beyond this critical endpoint, for larger values of net-baryon densities (and for lower temperatures), one expects a phase transition from hadronic to partonic matter with a phase coexistence region in between. A new phase of so called quarkyonic matter has been proposed to exist beyond the first order phase transition at large baryon chemical potentials and moderate temperatures [5]. High-density but cold nuclear matter is expected to exist in the core of neutron stars, and at very high densities correlated quark-quark pairs are predicted to form a color superconductor.

As illustrated in Fig. 1.1, it is expected that the QCD phase diagram exhibits a rich structure at finite values of baryon chemical potentials, such as the critical point, the predicted first order phase transition between hadronic and partonic or quarkyonic matter, and the chiral phase transition. The experimental discovery of these prominent landmarks of the QCD phase diagram would be a major breakthrough in our understanding of the properties of nuclear matter. Equally important is quantitative experimental information on the properties of hadrons in dense matter which may shed light on chiral symmetry restoration and the origin of hadron masses.

In the laboratory hot and dense nuclear matter is generated in a wide range of temperatures and densities by colliding atomic nuclei at high energies. The goal of the experiments at RHIC

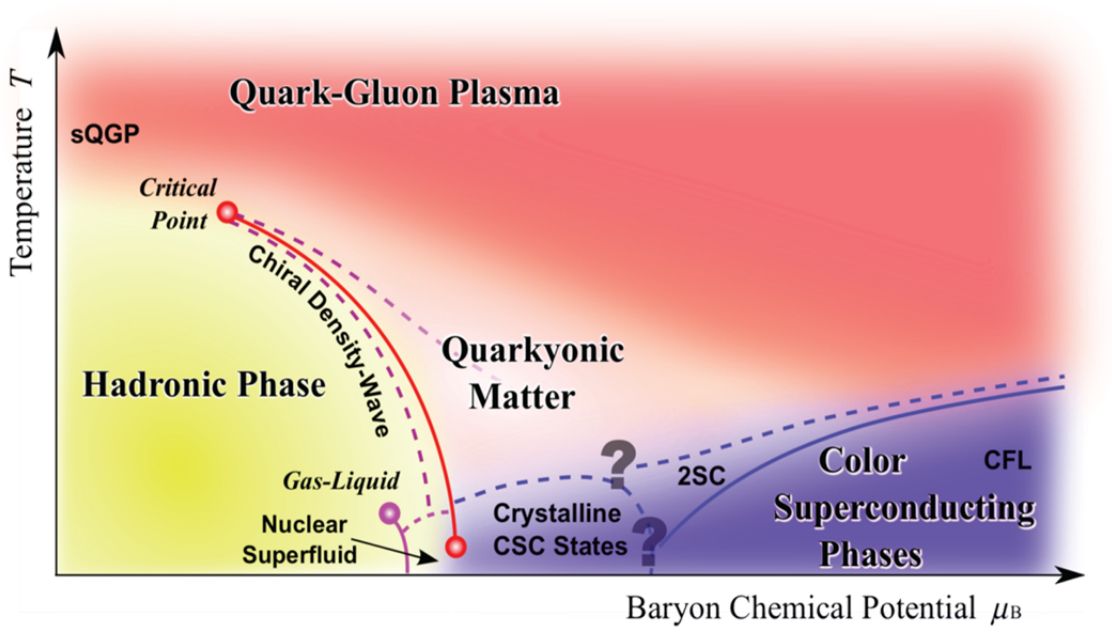

Figure 1.1: Sketch of the phase diagram for strongly-interacting matter (taken from [6]).

and LHC is to investigate the properties of deconfined QCD matter at very high temperatures and almost zero net-baryon densities. Several experimental programs are devoted to the exploration of the QCD phase diagram at high net-baryon densities. The STAR collaboration at RHIC scanned the beam energies in order to search for the QCD critical endpoint [7]. For the same reason, measurements are performed at the CERN-SPS with the upgraded NA49 detector (NA61) using light and medium size ion beams [8]. At the Joint Institute for Nuclear Research (JINR) in Dubna, a heavy-ion collider project (NICA) is planned with the goal to search for the coexistence phase of nuclear matter [9]. However, due to luminosity or detector limitations these experiments are constrained to the investigation of particles which are abundantly produced. In contrast, the Compressed Baryonic Matter (CBM) experiment at the Facility for Antiproton and Ion Research (FAIR) in Darmstadt is designed for precision measurements of multidimensional observables including particles with very low production cross sections using the high-intensity heavy-ion beams provided by the FAIR accelerators.

The SIS100/300 accelerators at FAIR are very well suited to create high net-baryon densities. This is illustrated in Fig. 1.2 which depicts results of transport code calculations for central Au + Au collisions. According to these calculations, densities of up to seven times saturation density can be produced already at beam energies of 10 AGeV. Under these conditions the nucleons overlap, and theory predicts a transition to a mixed phase of baryons and quarks.

1.2 Diagnostic probes of the high-density fireball

Figure 1.3 depicts three snapshots of the evolution of a heavy-ion collision at FAIR energies as calculated with the UrQMD transport code [11], and illustrates the time of production and eventual emission of various particle species. Particles containing charm quarks are expected to be created in the very first stage of the reaction. Then, D mesons and J/ψ mesons may serve as probes for the dense fireball and its degrees of freedom. Vector mesons like ω, ρ and ϕ mesons are produced continuously via $\pi\pi$ annihilation during the course of the reaction, and decay either

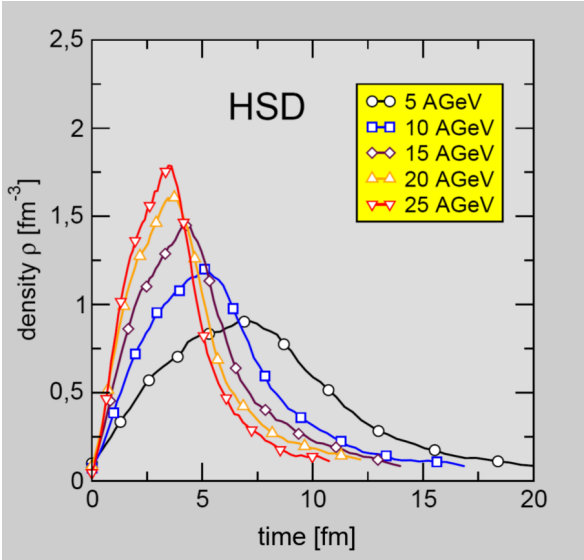

Figure 1.2: Baryon density as function of elapsed time for central Au + Au collisions at different energies as calculated with the HSD transport code [10].

again into mesons or into a pair of leptons. However, as leptons are not affected by final-state interactions, the dileptonic decay offers the possibility to look into the fireball. In particular, the short-lived ρ meson is a promising diagnostic probe of hot and dense nuclear matter. Due to their small hadronic cross sections, also multi-strange hyperons and ϕ mesons carry information on the dense phase of the collision, in particular via their collective flow. Finally, the bulk of the particles freezes out at densities below saturation density. Up to date, essentially only these bulk particles have been measured in heavy-ion collisions at beam energies between 2 and 40 AGeV (on stationary target). Diagnostic probes of the dense stage of the fireball such as multi-strange baryons, dilepton pairs and charmed particles will be measured for the first time by the CBM experiment in this beam energy range. Therefore, the CBM experiment has a unique discovery potential both at SIS100 and SIS300 energies.

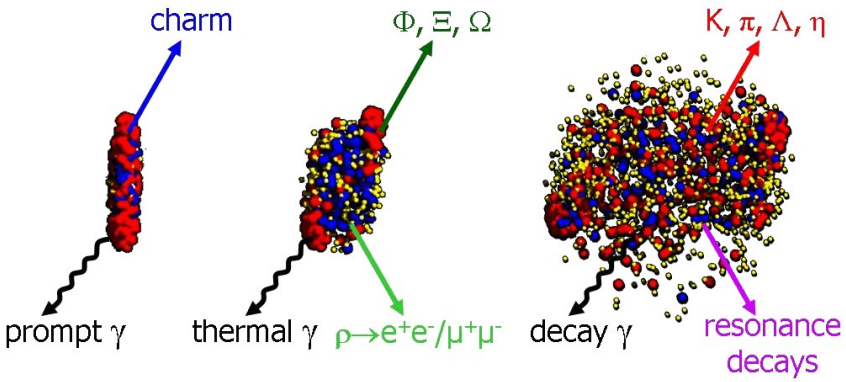

Figure 1.3: Three stages of a U+U collision at a laboratory beam energy of 23 AGeV as calculated with the UrQMD model [11]: The initial stage where the two Lorentz-contracted nuclei overlap (left), the high density phase (middle), and the final stage ("freeze-out") when all hadrons have been formed (right). Different particles are created in different stages of the collisions or escape from the interaction region at different times (see text). Almost 1000 charged particles are created in such a collision, most of them are pions.

The experimental challenge is to measure multi-differential observables and particles with very low production cross sections such as multi-strange (anti-)hyperons, particles with charm and lepton pairs with unprecedented precision. The situation is illustrated in the left panel of Fig. 1.4 which depicts the multiplicities for various particle species produced in central Au + Au collisions at 4 AGeV. The data points are calculated using the thermal model based on the corresponding temperature and baryon-chemical potential [12]. The dilepton decay of vector mesons, here illustrated for the ϕ meson, is suppressed by the square of the electromagnetic coupling constant $(1/137)^2$, resulting in a dilepton yield which is about six orders of magnitude below the pion yield, similar to the multiplicity of multi-strange anti-hyperons.

In order to produce high-statistics data even for the particles with the lowest production cross sections, the CBM experiment is designed to run at reaction rates of 100 kHz up to 1 MHz. For charmonium measurements - where a trigger on high-energy lepton pairs can be generated - reaction rates up to 10 MHz are envisaged. This exceeds the rate capabilities of other existing and planned heavy-ion experiments by orders of magnitude, as illustrated in the right panel of Fig. 1.4.

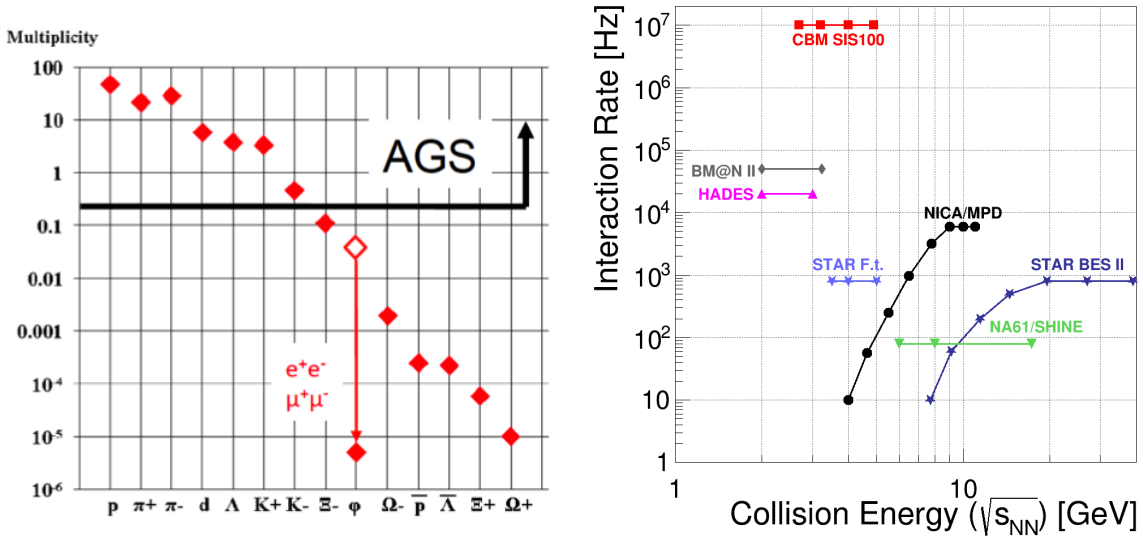

Figure 1.4: Left: Particle multiplicities for central Au + Au collisions at 4 AGeV as calculated with a statistical model [12]. For the ϕ meson also the branching fraction for the decay into lepton pairs is included (open symbol). The black line roughly indicates the multiplicities that were available to the AGS heavy-ion program at BNL at this energy. Right: Interaction rates achieved by existing anf planned heavy-ion experiments as a function of center-of-mass energy [13]. "STAR F.t." denotes the fixed-target operation of STAR.

1.3 CBM physics cases and observables

The CBM research program is focused on the following physics cases:

The equation-of-state of baryonic matter at neutron star densities.
The relevant measurements are:

- The excitation function of the collective flow of hadrons which is driven by the pressure created in the early fireball (SIS100).

- The excitation functions of multi-strange hyperon yields in Au + Au and C + C collisions at energies from 2 to 11 AGeV (SIS100). At sub-threshold energies, Ξ and Ω hyperons are produced in sequential collisions involving kaons and Λ, and are therefore sensitive to the density in the fireball.

In-medium properties of hadrons.
The restoration of chiral symmetry in dense baryonic matter will modify the properties of hadrons. The relevant measurements are:

- The in-medium mass distribution of vector mesons decaying in lepton pairs in heavy-ion collisions at different energies ($2 - 45\,A$GeV), and for different collision systems. Leptons are penetrating probes carrying the information out of the dense fireball (SIS100/300).
- Yields and transverse mass distributions of charmed mesons in heavy-ion collision as a function of collision energy (SIS100/300).

Phase transitions from hadronic matter to quarkyonic or partonic matter at high net-baryon densities.
Already at SIS100 energies densities of up to seven times of the normal nuclear density are reached in central collisions between heavy-ions. A discontinuity or sudden variation in the excitation functions of sensitive observables would be indicative of a transition. The relevant measurements are:

- The excitation function of yields, spectra and collective flow of strange particles in heavy-ion collisions from $6 - 45\,A$GeV (SIS100/300).
- The excitation function of yields, spectra and collective flow of charmed particles in heavy-ion collisions from $6 - 45\,A$GeV (SIS100/300).
- The excitation function of yields and spectra of lepton pairs in the intermediate mass region in heavy-ion collisions from $6 - 45\,A$GeV (SIS100/300).
- Event-by-event fluctuations of conserved quantities like baryons, strangeness, net-charge etc. in heavy-ion collisions with high precision as function of beam energy from $6 - 45\,A$GeV (SIS100/300).

Hypernuclei, strange dibaryons and massive strange objects.
Theoretical models predict that single and double hypernuclei, strange dibaryons and heavy multi-strange short-lived objects are produced via coalescence in heavy-ion collisions with the maximum yield in the region of SIS100 energies. The planned measurements include:

- The decay chains of single and double hypernuclei in heavy-ion collisions at SIS100 energies.
- Search for strange matter in the form of strange dibaryons and heavy multi-strange short-lived objects. If these multi-strange particles decay into charged hadrons including hyperons they can be identified via their decay products.

Charm production mechanisms, charm propagation and in-medium properties of charmed particles in (dense) nuclear matter.
The relevant measurements are:

- Cross sections and momentum spectra of open charm (D-mesons) in proton-nucleus collisions at SIS100/300 energies. In-medium properties of D-mesons can be derived from the transparency ratio $T_A = (\sigma_{pA} \rightarrow DX)/(A \times \sigma_{pN} \rightarrow DX)$ measured for different size target nuclei.

- Cross sections, momentum spectra and collective flow of open charm (D-mesons) in nucleus-nucleus collisions at SIS300 energies.

- Cross sections, momentum spectra and collective flow of charmonium (J/ψ) in proton-nucleus and nucleus-nucleus collisions at SIS100/300 energies.

As discussed above, a substantial part of the CBM physics cases can be addressed already with beams from the SIS100 synchrotron [13]. The intended measurements at SIS100 including the results of simulations and count rate estimates are described in [14]. A general review of the physics of compressed baryonic matter, the theoretical concepts, the available experimental results and predictions for relevant observables in future heavy-ion collision experiments can be found in the CBM Physics Book [15].

1.4 The Facility for Antiproton and Ion Research (FAIR)

The international Facility for Antiproton and Ion Research (FAIR) in Darmstadt will provide unique research opportunities in the fields of nuclear, hadron, atomic and plasma physics [16]. The research program devoted to the exploration of compressed baryonic matter will start with primary beams from the SIS100 synchrotron (protons up to 29 GeV, Au up to 11 AGeV, nuclei with $Z/A = 0.5$ up to 14 AGeV), and will be continued with beams from the SIS300 synchrotron (protons up to 90 GeV, Au up to 35 AGeV, nuclei with $Z/A = 0.5$ up to 45 AGeV). The layout of FAIR is presented in Fig. 1.5. The beam extracted to the CBM cave reaches intensities up to 10^9 Au ions per second.

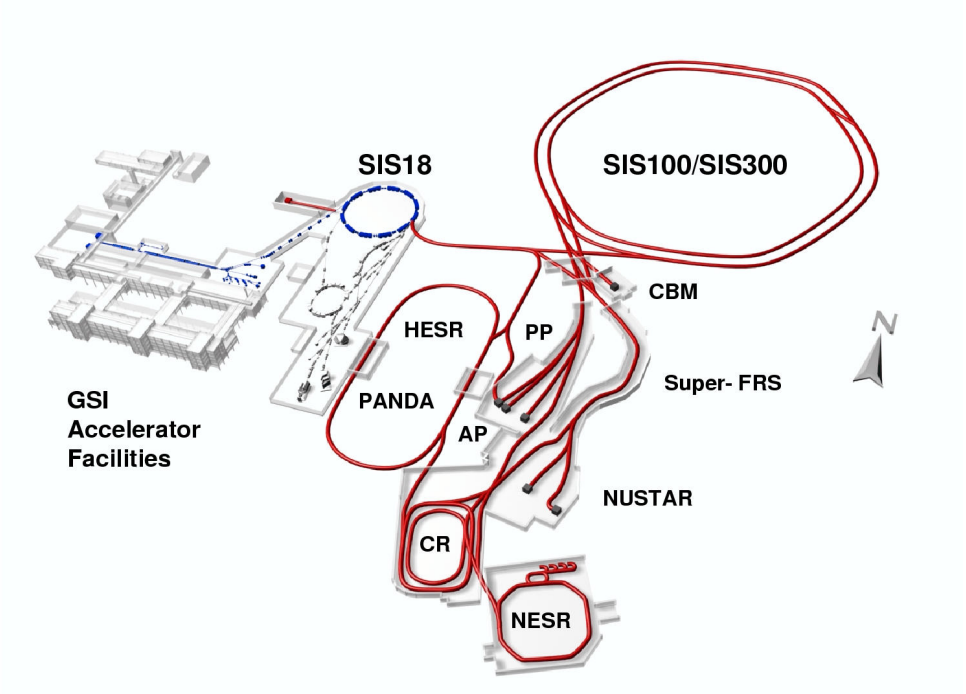

Figure 1.5: Layout of the Facility for Antiproton and Ion Research (FAIR) [16].

1.5 The Compressed Baryonic Matter (CBM) experiment

The CBM experimental strategy is to perform systematic both integral and differential measurements of almost all the particles produced in nuclear collisions (i.e. yields, phase-space distributions, correlations and fluctuations) with unprecedented precision and statistics. These measurements will be performed in nucleus-nucleus, proton-nucleus, and - for baseline determination - proton-proton collisions at different beam energies. The identification of multi-strange hyperons, hypernuclei, particles with charm quarks and vector mesons decaying into lepton pairs requires efficient background suppression and very high interaction rates. In order to select events containing those rare observables, the tracks of each collision have to be reconstructed and filtered online with respect to physical signatures. This concept represents a paradigm shift for data taking in high-energy physics experiments: CBM will run without hierarchical trigger system. Self-triggered readout electronics, a high-speed data processing and acquisition system, fast algorithms, and, last but not least, radiation hard detectors are indispensable prerequisites for a successful operation of the experiment. Figure 1.6 and depict the CBM experimental setup for SIS100. The CBM experiment comprises the following components:

Dipole magnet
The dipole magnet will be superconducting in order to reduce the operation costs. It has a large aperture of $\pm 25^{\circ}$ polar angle, and provides a magnetic field integral of 1 Tm.

Micro-Vertex Detector (MVD)
The MVD will provide excellent position resolution and low material budget as required for the identification of open charm particles by the measurement of their displaced decay vertex. It consist of four layers of Monolithic Active Pixel Sensor (MAPS) detectors located from 5 cm to 20 cm downstream of the target in vacuum. The detector arrangement provides a resolution of secondary vertices of about $50 - 100\,\mu$m along the beam axis.

Silicon Tracking System (STS)
The task of the STS is to provide track reconstruction and momentum determination of charged particles. The system consists of eight tracking layers of silicon strip detectors, located downstream of the target at distances between 30 cm and 100 cm inside the magnetic dipole field, and provides a momentum resolution of about $\Delta p/p = 1.5\,\%$.

Ring Imaging Cherenkov Detector (RICH)
The RICH detector will provide the identification of electrons via the measurement of their Cherenkov radiation. This will be achieved using a gaseous RICH detector build in a standard projective geometry with focusing mirror elements and a photon detector. The detector will be positioned behind the dipole magnet about 1.6 m downstream of the target. It will consist of a 1.7 m long gas radiator (overall length approximately 2 m) and two arrays of mirrors and photon detector planes. The design of the photon detector plane is based on MAPMTs in order to provide high granularity, high geometrical acceptance, high detection efficiency of photons also in the near UV region and a reliable operation.

Muon Chamber System (MUCH)
The concept of the muon detection system is to track the particles through a hadron absorber and thus perform a momentum dependent muon identification. The absorber/detector system is placed downstream of the STS, which determines the particle momentum. In order to reduce meson decays into muons the absorber/detector system is designed as compact as possible. It consists of six hadron absorber layers made of iron plates and 18 gaseous tracking chambers

located in triplets behind each iron slab (SIS300 setup). The trigger concept is based on the measurement of short track segments in the last tracking station triplet, and extrapolation of these tracks to the target. For J/ψ measurements at SIS100 a MUCH start version with three chamber triplets is sufficient.

Transition Radiation Detector (TRD)
The Transition Radiation Detector, consisting of four detector layers grouped into one station in the SIS100 configuration (ten layers in three stations for SIS300), will serve for particle tracking and for the identification of electrons and positrons with $p > 1.0\,\mathrm{GeV}/c$ ($\gamma \geq 1000$). The detector layers are located at approximately 4.1 m to 5.9 m downstream of the target, the total active detector area amounts to about $114\,\mathrm{m}^2$ (SIS100). The TRD readout will be realized in rectangular pads giving a resolution of $\sim 300\,\mu\mathrm{m}$ across and $3 - 30\,\mathrm{mm}$ along the pad. Every second TRD layer is rotated by 90°.

Time-Of-Flight System (TOF)
An array of Multi-gap Resistive Plate Chambers (MRPC) will be used for hadron identification via TOF measurements. The TOF wall covers an active area of about $120\,\mathrm{m}^2$ and is located about 6 m downstream of the target for measurements at SIS100, and at 10 m at SIS300. The required time resolution is on the order of 80 ps. At small deflection angles the pad size is about $5\,\mathrm{cm}^2$ corresponding to an occupancy of below 5 % for central Au + Au collisions at 25 AGeV.

Electromagnetic Calorimeter (ECAL)
A "shashlik" type calorimeter as installed in the HERA-B, PHENIX and LHCb experiments will be used to measure direct photons and neutral mesons (π^0, η) decaying into photons. The ECAL will be composed of modules which consist of 140 layers of lead and scintillator sheets. The shashlik modules can be arranged either as a wall or in a tower geometry with variable distance from the target.

Projectile Spectator Detector (PSD)
The PSD will be used to determine the collision centrality and the orientation of the reaction plane. The detector is designed to measure the number of non-interacting nucleons from a projectile nucleus in nucleus-nucleus collisions. The PSD is a fully compensating modular lead-scintillator calorimeter which provides very good and uniform energy resolution. The calorimeter comprises 44 individual modules, each consisting of 60 lead/scintillator layers.

Online event selection and data acquisition
High-statistics measurements of particles with very small production cross sections require high reaction rates. The CBM detectors, the online event selection systems and the data acquisition will be designed for event rates of 10 MHz, corresponding to a beam intensity of 10^9 ions/s and a 1 % interaction target, for example. Assuming an archiving rate of 1 GByte/s and an event volume of about 10 kByte for minimum bias Au + Au collisions, an event rate of 100 kHz can be accepted by the data acquisition. Therefore, measurements with event rates of 10 MHz require online event selection algorithms (and hardware) which reject the background events (which contain no signal) by a factor of 100 or more. The event selection system will be based on a fast online event reconstruction running on a high-performance computer farm equipped with many-core CPUs and graphics cards (GSI GreenIT cube). Track reconstruction, which is the most time consuming combinatorial stage of the event reconstruction, will be based on parallel track finding and fitting algorithms, implementing the Cellular Automaton and Kalman Filter methods. For open charm production the trigger will be based on an online search for secondary vertices, which requires high speed tracking and event reconstruction in the STS and MVD. The

highest suppression factor has to be achieved for J/ψ mesons where a high-energetic pair of electrons or muons is required in the TRD or in the MUCH. For low-mass electron pairs no online selection is possible due to the large number of rings/event in the RICH caused by the material budget of the STS. In the case of low-mass muon pairs some background rejection might be feasible.

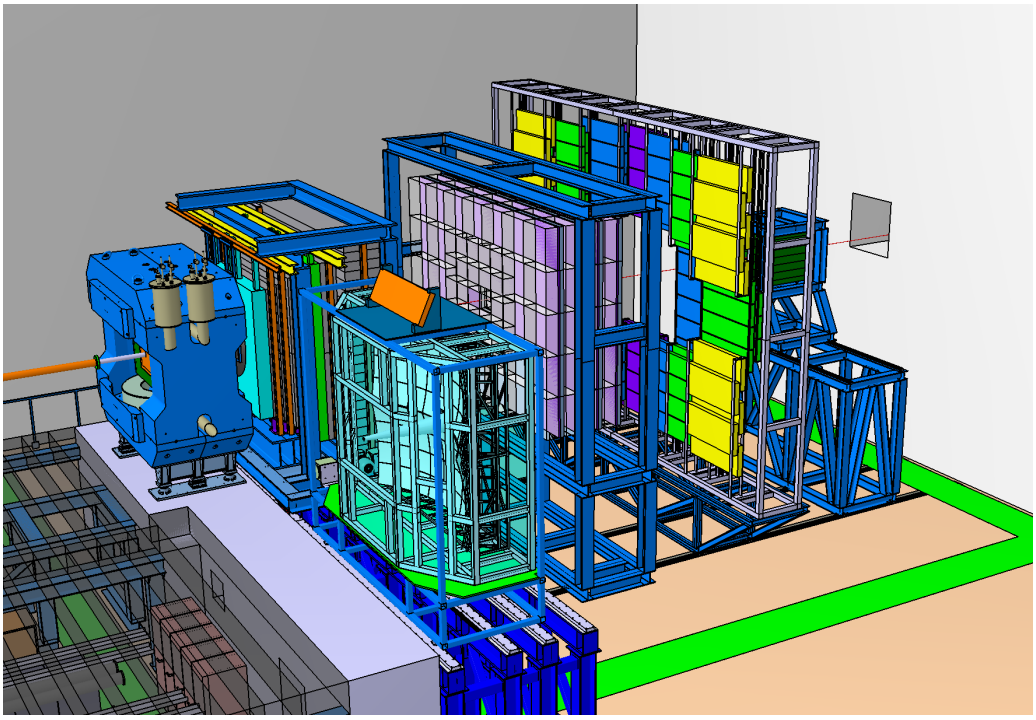

Figure 1.6: Drawing of the experimental setup of CBM for the SIS100.

Chapter 2

Physics Objectives and Design Parameters

Here we give a brief overview on the physics observables which mainly define the requirements on the CBM-TRD. Based on these considerations the design parameters of the TRD have been defined and are also summarized here.

2.1 Physics objectives

The capability to measure dielectrons with high precision and low background is of essential relevance for the CBM physics program at the SIS100 accelerator, since crucial observables in heavy-ion physics, such as low mass vector mesons and quarkonia, are addressed via this decay channel.

Within CBM electron identification is the task of two detector systems, the RICH detector and the TRD, which in conjunction will provide the necessary hadron suppression. Since the electron identification capabilities of the RICH are limited to the lower momentum region ($p < 6\,\mathrm{GeV}/c$), the TRD will be mandatory as an additional device to supplement and extend the electron PID towards higher momenta. The TRD configuration envisaged for the CBM setup at the SIS100 will therefore be able to identify electrons above a momentum threshold of $p > 1\,\mathrm{GeV}/c$ with a 90 % efficiency, while simultaneously suppressing the hadronic background by a factor of 10 – 20. This additional pion rejection capabilities will on one side augment the measurement of low mass vector mesons ($m_{ee} < m(\phi)$), but on the other side will be essential for the study of dielectrons in the intermediate mass region ($m(\phi) < m_{ee} < m(\mathrm{J}/\psi)$). This mass region is of particular interest, since it allows to access thermal radiation from the hot and dense medium created in heavy-ion collisions. A systematic study of the thermal dilepton component as a function of centre-of-mass energy will thus provide very important information relevant for the characterization of the strongly interacting medium, especially since this observable covers the whole time evolution of the system. Without the addition of a TRD to the CBM setup this physics will not be accessible and therefore this observable defines the main physics case for the TRD. Due to its capability to identify electrons at high momenta, the TRD will also allow for a clean measurement of the J/ψ in proton-nucleus, and potentially also in nucleus-nucleus collisions at the SIS100. Finally, photons can be detected via their conversion into $\mathrm{e}^+\mathrm{e}^-$-pairs in the material of the tracking detectors (MVD and STS). This measurement will also significantly benefit from the additional electron identification provided by the TRD.

Another important contribution of the TRD to the CBM physics program arises from the possibility to support the identification of nuclear fragments via the measurement of the their specific energy loss inside the TRD detector gas. This provides essential information in addition

to what is accessible with the TOF detector system and will be important for the detection of hyper- and anti-nuclei. In particular, the TRD will allow to differentiate between $Z = 1$ and $Z = 2$ fragments (e.g. d and ^{4}He), which cannot be separated via a time-of-flight measurement alone.

In summary, the TRD is therefore being designed for the following main physics observables:

- **Intermediate mass dileptons:** dileptons in the mass range between the ϕ and the J/ψ meson can provide access to thermal radiation from the hot and dense fireball and thus convey unique information on its properties and time evolution.
- **Fragments:** the measurement of nuclear fragments is essential for the study of hyper- and anti-nuclei.
- **Quarkonia:** quarkonia states, such as the J/ψ meson, are probes for the presence of deconfined matter, since free color charges can screen the c$\bar{\text{c}}$-potential and thus reduce the production rates of these particles ("J/ψ-suppression").
- **Low mass vector mesons:** the measurement of these mesons provides informations on medium induced modification of the hadron spectral functions and is thus essential for understanding of the chiral phase transition and the origin of hadron masses.
- **Photons:** direct photons can provide information on the temperatures of the early stages in a heavy-ion collision. They can be measured via their conversion into dielectron pairs, either in the target and first MVD and STS layers or in a dedicated converter.

A detailed discussion of the performance of CBM with a TRD for the first three physics observables (intermediate mass dileptons, fragments and quarkonia) and collisions systems at the SIS100 can be found in the Chap. 3.

2.2 Design considerations

To fulfil the above listed physics objectives the design of the TRD for an operation at the SIS100 has to take the following considerations into account:

- **Pion rejection capability:** the required pion rejection dictates the number of detector layers needed in the TRD setup, as well as the thickness of the gas volume of the readout chambers and the choice of the radiator. For the physics program envisaged with the TRD, a pion suppression factor of about 20 at an electron efficiency of 90 % will be necessary.
- **Charged particle identification:** in order to be able to separate fragments with masses higher than the proton mass, a resolution in the energy loss measurement in the $1/\beta^2$ region of better than 30 % will be needed.
- **Tracking capabilities:** the TRD is supposed to ensure an efficient track matching between the STS and the TOF, since track mismatches would significantly deteriorate the particle identification capabilities, both of TRD and TOF. Also, the charge measurement by the TRD will be essential for a correct momentum determination of heavier fragments. In order to achieve a sufficient spatial space point resolution (around 300 µm), a correspondingly high pad granularity is required. This also minimizes the occupancy in the TRD. Furthermore, the material budget of the TRD should be kept minimal to keep the number of secondary particles produced in the TRD on an acceptable level.

- **Interaction rates:** in order to be able to cope with the high interaction rates and particle multiplicities, the signal collection in the TRD readout chambers should be sufficiently fast (signal collection times below 0.3 µs). Therefore, the thickness of the gas volume is kept as low as possible without compromising the pion rejection capabilities. Also, the pad granularity has to be adjusted such that the corresponding hit rates stay on average below 100 kHz in order to keep the occupancy on a level that allows for a clean separation of hits. The current design should be able to handle interaction rates up to 10 MHz, as might be necessary for rare observables such as the J/ψ.
- **Tracking of muons:** it is foreseen to use the TRD as a tracking device together with the MUCH detector. In this setup no electron-pion separation is needed. However, it needs to be ensured that the TRD acceptance matches the one of the MUCH in an optimal way.

To guarantee the required performance for the bulk of the measured tracks, we foresee for the SIS100 a baseline detector layout of four TRD layers. In combination with the RICH pion suppression factors of more than $5 \cdot 10^3$ can be achieved, which is mandatory for the measurement of dileptons in the intermediate mass region and will in addition allow for an observation of J/ψ mesons in proton-nucleus reactions at SIS100 beam energies. The TRD will be composed of modules with only two different sizes (small: $57 \times 57\,\mathrm{cm}^2$, large: $99 \times 99\,\mathrm{cm}^2$), which facilitates the readout chamber production. Also, the number of pad planes with different granularities has been optimized in a way that limits on one side the construction complexity, while on the other side it keeps the recorded hit rates per pad on a tolerable level. Simulations with a realistic overall material budget indicate that this can be achieved with four different pad plane configurations. The corresponding pad areas range between $1.2\,\mathrm{cm}^2$ and $8\,\mathrm{cm}^2$. The readout chain will provide, in addition to the data transfer, an efficient online data reduction and feature extraction (e.g. digital filtering and online clustering). The TRD setup will also be movable along the beam direction so that its position can be adjusted to the MUCH detector, when the TRD is used as tracking station for the muon measurements.

It is foreseen that this TRD setup can easily be extended for an operation at the SIS300. This will be possible, since the mean occupancy is expected to rise only moderately when going from 10 to 30 AGeV and the chosen pad granularities and readout bandwidth should still be sufficient. However, as higher pion suppression factors will be required at higher energies the final configuration of the TRD is planned to consist of maximally ten layers, grouped into three stations (station 1: layers 1 – 4 as in the SIS100 setup, station 2: layers 5 – 8, station 3: layers 9 – 10). Therefore, the upgrade to the full setup will imply the addition of the stations 2 and 3 without modifications on the already available station 1.

2.3 Summary of TRD design parameters

The following table summarizes its main parameters for the TRD setup at the SIS100:

Table 2.1: Synopsis of TRD design parameters (SIS100 setup)

Maximal pseudo-rapidity coverage	$1.15 < \eta < 3.65$
Azimuthal coverage	2π
z position	$4.1\,\mathrm{m} < z < 5.9\,\mathrm{m}$
Maximal height	5.15 m
Maximal width	6.25 m
Gas volume	$1.36\,\mathrm{m}^3$
Total thickness of one layer	0.45 m
Number of stations	1
Number of layers	4
Total number of modules	216
Number of readout channels	329728
Dimension of large module	$99 \times 99\,\mathrm{cm}^2$
Dimension of small module	$57 \times 57\,\mathrm{cm}^2$
Average pad size	$3.44\,\mathrm{cm}^2$
Detector active area	$113.4\,\mathrm{m}^2$
Radiator thickness	30 cm per layer
Detector radiation length (active area)	$< 5\,\%\,X_0$ per layer
Detector gas (electron setup)	Xe (85 %), CO_2 (15 %)
Detector gas (hadron setup)	Ar (80 %), CO_2 (20 %)
Depth of amplification region	7 mm
Depth of drift region	5 mm
Drift field	100 V/mm
Maximal signal collection time	0.3 µs
Maximal hit rate (minimum bias Au + Au at 10 AGeV)	$\lesssim 100$ kHz
Maximal cell occupancy (central Au + Au at 10 AGeV)	$\lesssim 10\,\%$
Radiation level TID	40 Gy (2 months)
Radiation level NIEL	$5{\times}10^{11}\,\mathrm{cm}^{-2}$ (2 months)
Typical space point resolution at $p = 1\,\mathrm{GeV}/c$	$\sim 300\,\mu\mathrm{m}$
Pion suppression at 90 % electron efficiency and $p \geq 1.5\,\mathrm{GeV}/c$	20
dE/dx resolution above $p = 1\,\mathrm{GeV}/c$	$\leq 30\,\%$

Chapter 3

Physics Performance at SIS100

In the following we discuss the performance of CBM at the SIS100 for several physics observables which require the addition of the TRD to the experimental setup. The main focus of these studies lies on the measurement of dielectrons in the intermediate mass range (IMR) in Au + Au collisions, which can only be accessed with the electron identification capabilities of the TRD. Also, the performance for measuring J/ψ mesons in proton-nucleus collisions is presented. Finally, the contribution of the TRD to the identification of fragments by exploiting their measured energy loss is discussed.

3.1 Physics cases for the TRD

3.1.1 Dielectron measurements with CBM

It is foreseen to follow two complementary approaches within CBM to perform dilepton measurements. One is based on muon detection with the MUCH in a dedicated setup (see Fig. 4.5). The advantages of di-muon measurements are that muon identification is relatively simple and that it is easy to provide a corresponding trigger which allows to quickly accumulate statistics. This has e.g. been demonstrated by the NA60 collaboration that was able to measure dilepton spectra in In+In collisions at 158 AGeV with unprecedented precision. However, dimuon measurements alone would not be sufficient to complete the CBM physics program and should be complemented by dielectron measurements (the corresponding setup is shown in Fig. 4.4). On one side they will provide an independent cross check of all dilepton physics results and are subject to completely different systematic effects. On the other side, dimuon measurements will become more and more difficult to perform the lower the beam energy will be. Since the average velocity of the particles will be reduced, thinner absorber will have to be used at lower energies, thus introducing different systematic effects at different energies. Also, a larger fraction of the pions will decay weakly before the absorber and result in a higher amount of background muons, which will make the triggering less efficient. The dielectron performance on the other side is essentially independent of the centre-of-mass energy. Also, it is easier to cover acceptance regions towards low transverse momenta, in particular near mid-rapidity, due to the absence of an absorber. Furthermore, it is in the CBM electron setup no problem to correlate hadronic observables obtained with full particle identification with dielectron results within the same event. This will possibly provide new insights that are not obtainable with dimuon measurements alone. Therefore, it is essential to equip CBM also with detectors that allow to an electron identification over a large acceptance region. This task will be fulfilled by the combination of the RICH and the TRD.

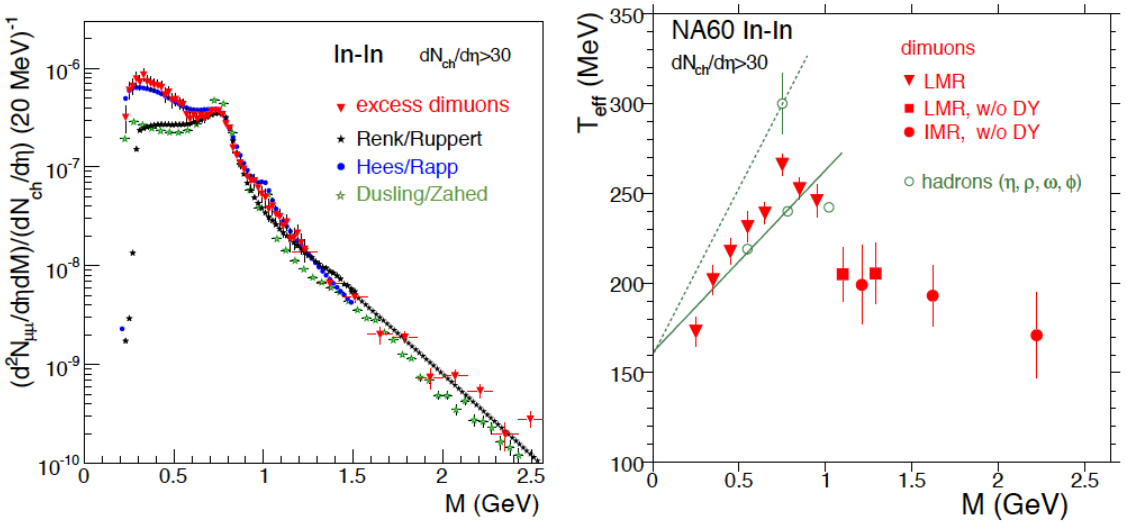

Figure 3.1: Left panel: p_t integrated invariant mass spectrum of excess dimuons as measured by NA60 for In+In collisions at 158 AGeV. The data are compared to several thermal model calculations. Right panel: The inverse slope parameter $T_{\rm eff}$ of the dimuon m_t spectra as a function of their invariant mass. The figures are taken from [17].

3.1.2 Intermediate mass dileptons

The intermediate mass range between the masses of the ϕ and the J/ψ meson is of particular interest in heavy-ion physics. At lower centre-of-mass energies, where charm and Drell-Yan production is not dominant, this range provides a direct access to dileptons originating from thermal sources. At SPS energies this kind of measurement has been performed already by the NA60 collaboration, as shown in Fig. 3.1. On one side they extracted an inverse slope parameter $T_{\rm eff}$ from the m_t spectra as a function of their invariant mass M in In+In collisions at 158 AGeV [20] (see right panel of Fig. 3.1). A rise of $T_{\rm eff}$ up to $M \sim 0.8\,{\rm GeV}/c^2$ was observed here, similar to what is seen for hadrons, followed by a drop and an approximately constant behaviour above $M \sim 1\,{\rm GeV}/c^2$, indicating a non-hadronic origin, since other components in this mass range, such as Drell-Yan and semi-leptonic decays of open charm mesons, are negligible at these energies. On the other side, NA60 has extracted the inverse slope parameter $\langle T_{\rm s} \rangle$ directly from the invariant mass distribution of dimuon pairs in the mass range above $1.2\,{\rm GeV}/c^2$ which was found to be (205 ± 12) MeV. The corresponding invariant mass distribution of excess dimuons is shown in the left panel of Fig. 3.1, together with several thermal model calculations [17].

This kind of measurement is unique, since it allows to study the thermal properties of the early stages of the produced medium and is also sensitive to the thermal radiation from a QGP phase. A systematic study of the energy dependence of $\langle T_{\rm s} \rangle$ in the IMR towards lower energies can therefore provide information on the onset of partonic thermal radiation and might allow to locate the phase boundary. This is illustrated in the left panel of Fig. 3.2, which shows the energy dependence of the inverse slope parameter of IMR dileptons as calculated by [18] for $\sqrt{s_{NN}} > 6\,{\rm GeV}$. While at these higher energies a clear signature of thermal QGP radiation is expected, with temperatures above the pseudo-critical ($T_{\rm pc}$) and relatively close to initial temperature ($T_{\rm i}$), at lower energies the situation is still quite open. As pointed out in [13, 21, 18] this energy range is therefore of particular interest, since it allows to map out the transition regime between partonic and hadronic matter. The presence of a first order phase transition might reveal itself as a flattening in the energy dependence of $T_{\rm s}$ extracted from IMR dileptons as a consequence of a latent heat at the phase boundary. This is illustrated in the right panel of

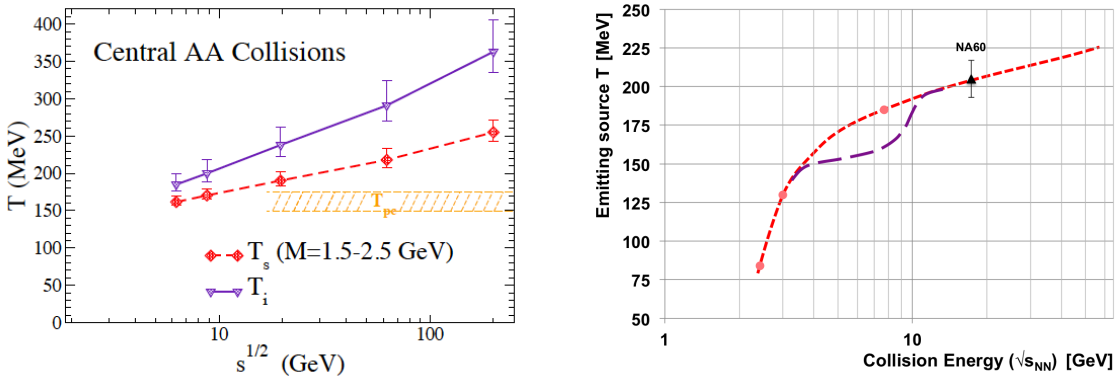

Figure 3.2: Left panel: excitation function of the inverse slope parameter for IMR dileptons (here denoted as T_s) in the mass range $1.5 < m_{ee} < 2.5\,\mathrm{GeV}/c^2$ (diamond symbols) as calculated by [18]. This is compared to the initial temperature T_i of the system (triangles) and the pseudo-critical temperature T_{pc} (hatched band). Right panel: excitation function of T_{eff} as calculated with a coarse-graining approach (dotted red curve) [19]. The dashed violet line corresponds to a hypothetical energy dependence in the presence of a first order phase transition. Also shown is the value by NA60 [17]. The figure is taken from [13].

Fig. 3.2, where the dashed violet curve depicts the possible energy dependence in the presence of a first order phase transition.

3.1.3 J/ψ mesons in proton-nucleus collisions

The measurement of J/ψ mesons is of prime importance in the field of heavy-ion physics, since their production rate is supposed to be modified by the presence of a deconfined state of matter [22]. While at high centre-of-mass energies (SPS, RHIC, and LHC) a significant suppression of J/ψ in nucleus-nucleus collisions has been observed relative to the corresponding yield in pp-collisions, scaled by the number of binary nucleon-nucleon collisions [23, 24, 25], with a stronger suppression at SPS and RHIC than at the LHC, the evolution of this modification towards even lower energies is still unclear. Especially, how the high net-baryon densities present at FAIR energies will modify the J/ψ production is generally unknown and might reveal new effects. In order to extend these measurements into these unexplored energy range via the dielectron channel with a sufficiently high signal-to-background ratio a good electron identification is required. Due to its high mass the J/ψ mesons decay into dielectrons of predominantly high momenta, so that the TRD will be necessary to suppress hadronic background in this region of phase space sufficiently well, where the RICH is no longer efficient.

The p+A collision system will provide an indispensable baseline for the interpretation of the heavy-ion data. It allows the investigation of cold nuclear matter effects whose measurement is needed to quantify any non-trivial J/ψ suppression. It is therefore important to also be able to measure the J/ψ production in these more elementary reactions at all the relevant centre-of-mass energies. This is especially true for very low energies just above threshold, where currently no precision data are existing. The SIS100 will make available proton beams up to 30 GeV beam energy, which can be exploited to perform these measurements.

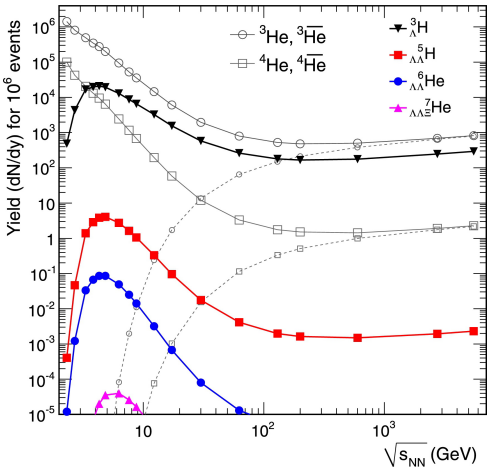

Figure 3.3: Energy dependence of predicted hypernuclei yields at mid-rapidity for 10^6 central Pb+Pb collisions at [26].

3.1.4 Hypernuclei

In addition to its electron identification capabilities, the TRD will also be able to separate hadrons on the basis of a measurement of their specific energy loss dE/dx. This will extend the possibilities of the CBM experiment beyond what is accessible with a time-of-flight measurement alone. A general disadvantage of a hadron identification with the TOF detector is that it is not able to distinguish different charge states. E.g. the TOF detector will not be able to separate $Z = 1$ and $Z = 2$ fragments. Since the dE/dx measured in the TRD depends on Z^2, this additional information will allow for a separation of these states.

This is in particular crucial for the identification of double-Λ hypernuclei, such as ${}^{6}_{\Lambda\Lambda}\mathrm{He}$ which decays as ${}^{6}_{\Lambda\Lambda}\mathrm{He} \rightarrow {}^{5}_{\Lambda}\mathrm{He} + \mathrm{p} + \pi^-$ and subsequently as ${}^{5}_{\Lambda}\mathrm{He} \rightarrow {}^{4}\mathrm{He} + \mathrm{p} + \pi^-$. However, the latter decay would be indistinguishable from the decay ${}^{3}_{\Lambda}\mathrm{H} \rightarrow \mathrm{d} + \mathrm{p} + \pi^-$ without the additional TRD information that allows the separation of ${}^{4}\mathrm{He}$ and deuterons. Therefore, the TRD will help to significantly extend the number of hypernuclei states accessible within the CBM physics program. As discussed in [13], a high statistics measurement of double-Λ hypernuclei would represent a breakthrough in this field of physics, since up to now only very few double-Λ hypernuclei events have been identified. With CBM one could expect to record, e.g., around 160 ${}^{6}_{\Lambda\Lambda}\mathrm{He}$ per week of data taking in central Au + Au collisions at 10 AGeV, assuming a multiplicity of $2.5 \cdot 10^{-8}$ according to a statistical model prediction [26] (see Fig. 3.3), a branching ratio of 0.08 for the decay into ${}^{5}_{\Lambda}\mathrm{He}\,\mathrm{p}\,\pi^-$, an interaction rate of 10 MHz and a detection efficiency of 1.3 % [27]. This capability of identifying a substantial number of these exotic nuclei will open up new possibilities in studying the hyperon-nucleon and hyperon-hyperon interaction with unprecedented precision and thus will provide essential ingredients for the understanding of the structure of neutron stars.

3.2 Simulation setup

3.2.1 Simulation setup and geometries

The simulations presented in the following were performed within the CBMROOT framework, which is based on the object-oriented `C++` ROOT software environment [28]. CBMROOT supports several external particle generators and transport algorithms, such as GEANT3 [29], GEANT4 [30] or FLUKA [31], without the need for a change in the user code. It features detailed descriptions of the geometries and responses of the CBM sub-detectors and therefore allows for a realistic study of the CBM performance for different physics observables. The overall CBM

detector setup used here includes, apart from the TRD, also STS, RICH, and TOF, as well as the beam pipe and the magnet. In the following studies the particles are propagated through the CBM detector model using the transport code GEANT3.

For the TRD the four layer SIS100 geometry, arranged in one detector station, is used as default option, as described in Chap. 4 and as implemented in the simulation software (see e.g. Fig. 4.2). In addition, also setups consisting of three and five layers have been studied. The details of the simulation of the TRD response are given in Chap. 9. For the following studies the full simulation chain, including digitization and clustering, was used (see Sect. 9.2). Electron identification was performed with the likelihood approach (see Sect. 9.3.2).

The STS detector is composed of eight tracking stations equidistantly positioned between 30 cm and 100 cm downstream of the target. Each station comprises double-sided silicon strip sensors of 300 µm thickness with a 58 µm pitch of the strips. The detector simulation includes the complete chain of physical processes caused by a charged particle traversing the detector, from charge creation in the silicon to the digital output signals. Signal sharing between strips together with charge collection inefficiency, Lorentz shift due to the presence of the magnetic field, channel dead time, and single-channel inefficiency are taken into account.

For the RICH detector a setup is used which includes a mirror with a tilt of 10°, mounted on a carbon support structure combined with a grid of aluminum tubes. The multi-anode photomultipliers (MAPT) are mounted inside two steel boxes that shield them from the magnetic stray field. The simulated detector response describes MAPT photon detectors of the type Hamamatsu H8500-03 with a UV window. Their quantum efficiency, the effect of cross talk between neighboring pixels and noise pixels are taken into account here. A realistic description of the mirror reflectivity and inhomogeneity is implemented as detailed in [32].

The TOF geometry used in these simulations is describing the setup intended for dielectron measurements at SIS100, which is positioned at a distance to the target of $z = 10$ m. The simulations include a detailed modelling of the detector response.

An Au-target with a thickness of 25 µm was chosen for these studies in order to keep the amount of conversions inside the target minimal. This target thickness corresponds to an interaction probability of 0.1 %, i.e. for a beam intensity of 10^9 ions/s it will provide an interaction rate of 1 MHz.

3.2.2 Input to the simulations

Source	$BR_{e^+e^-}$	Total multiplicities	
		p + Au	Au + Au
ω	$7.28 \cdot 10^{-4}$	$5.7 \cdot 10^{-3}$	19.0
ϕ	$2.97 \cdot 10^{-4}$	$1.7 \cdot 10^{-4}$	0.12
J/ψ(1S)	$5.97 \cdot 10^{-2}$	$5.1 \cdot 10^{-8}$	—
ψ(2S)	$7.89 \cdot 10^{-3}$	$1.3 \cdot 10^{-9}$	—
In-medium SF radiation	—	—	$2.2 \cdot 10^{-2}$
QGP radiation	—	—	$5.8 \cdot 10^{-3}$

Table 3.1: Input multiplicities (4π) and the corresponding branching ratios for the dielectron decay as used in the p + Au and Au + Au simulations (see text for details).

As input to the simulation studies Au + Au events (10 % most central, i.e. impact parameter $b < 4.65$ fm) at a beam energy of 8 AGeV or minimum bias p + Au events at 30 GeV, both generated with the UrQMD model [11], were used. These UrQMD events provide the hadronic

background events with a realistic multiplicity of particles into which the considered signals are embedded.

To study the CBM performance with respect to intermediate mass dileptons, a corresponding signal has been added to the UrQMD background events described above. This signal is composed of a cocktail of low mass vector mesons (ω, ω-Dalitz, and ϕ), the J/ψ and thermal radiation from the hadronic (in-medium Spectra Functions (SF)) and partonic medium (QGP) and is generated with the PLUTO event generator [33]. The decay of the low mass vector mesons was also performed by PLUTO, while for the J/ψ the EVTGEN package [34], using the PHOTOS model [35], was employed to include the effect of final state radiation. This introduces, together with bremsstrahlung in the detector material, a tail towards lower masses in the reconstructed J/ψ signal distribution.

In order to accumulate sufficient statistics the dielectron signals were generated with a yield of one pair per event for each dielectron source. After reconstruction the dielectron pairs were rescaled according to the yields expected from their corresponding source (see Tab. 3.1). In case of the low mass vector mesons and of the J/ψ the yields were adjusted following the predictions of the HSD model [36]. The yields of the thermal components (in-medium SF and QGP radiation) are chosen as predicted by the MC approach described in [37, 19]. This model, which also calculates the mass dependence of the thermal dielectron components, is based on a coarse grained transport model calculation to extract the space-time evolution of the local temperatures and chemical potentials and uses the parametrized SF for vector and axial-vector mesons, e.g. the ρ meson, provided by [38]. Since a complete set of predictions by this model was available for a beam energy of 8 AGeV, we used it for the performance studies presented in the following.

The simulations performed to investigate the TRD performance in terms of fragment identification are also based on the 10 % most central Au + Au events at 8 AGeV generated with UrQMD. To this background events fragments of the type d, t, ^{3}He, and ^{4}He have been added. These were generated with a flat p_t distribution between $0 < p_t < 3\,\mathrm{GeV}/c$ and a rate of one particle per event to obtain sufficient statistics.

3.2.3 Track reconstruction and electron identification

The simulated events were reconstructed with the standard reconstruction algorithms as described in detail in Sect. 9.3.

In the analysis of the simulated events the following selection criteria were applied to the reconstructed tracks: they should be inside the geometrical acceptance of the RICH and TRD detector and have a transverse momentum of $p_t > 200\,\mathrm{MeV}/c$ (this cut can be adjusted according to the observed signal-to-background ratio). To guarantee a sufficient reconstruction quality the track was in addition required to have more than six reconstructed hits in the STS and a primary vertex fit with $\chi^2/ndf < 3$.

Electron identification with the RICH is performed by applying a momentum dependent cut on the corresponding ANN output, which results in a momentum independent electron efficiency of 90 %, and an additional cut on the number of reconstructed hits in the RICH of $N_{\mathrm{hit}}^{\mathrm{RICH}} \geq 6$. In the case of the TRD the requirement for the minimum number of reconstructed hits is $N_{\mathrm{hit}}^{\mathrm{TRD}} \geq 3$. Here, the likelihood method is used to select electron candidates and the cuts are tuned such that a momentum independent electron efficiency of 80 % is achieved (see also Fig. 9.15 and Tab. 9.1). In addition, TOF information is used to further improve the electron selection by applying a cut on the reconstructed velocity of $|\Delta\beta_{\mathrm{electron}}| < 1.65 \cdot 10^{-3}$.

3.3 Reconstruction of IMR dielectrons with the TRD

3.3.1 Pion suppression in the IMR

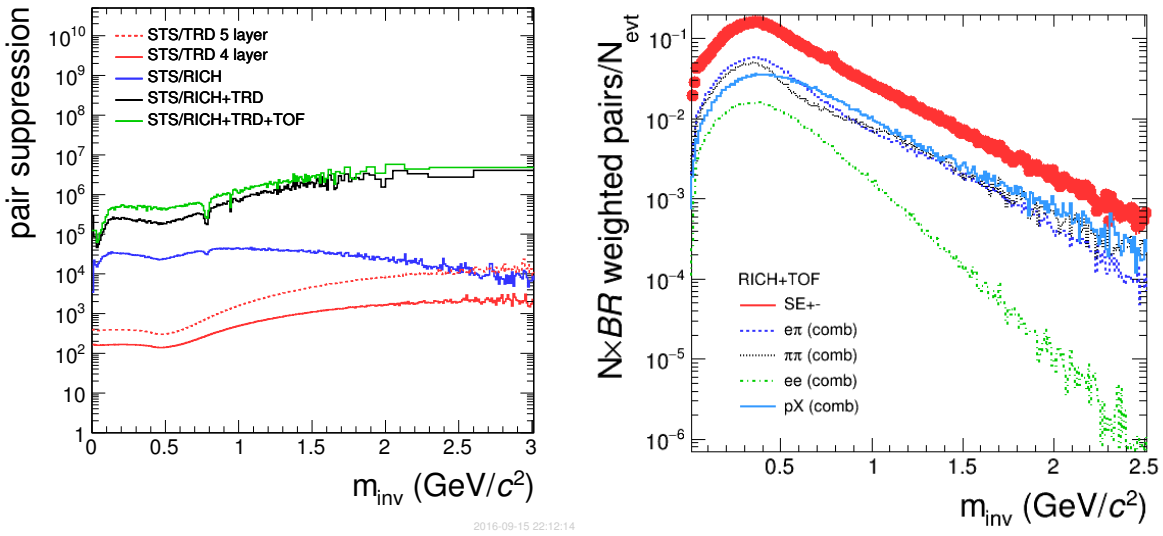

Figure 3.4: Left: The suppression factor obtained for opposite-sign track pairs as a function of their invariant mass measured with different detector combinations (red: TRD alone, blue: RICH alone, black: RICH and TRD, green: RICH, TRD and TOF). In addition, also the values for a TRD configuration with an additional fifth layer is shown (dashed red line). All curves are obtained for the dielectron cocktail (see text for details) in the 10 % most central Au + Au collisions at 8 AGeV. Right: The total reconstructed invariant mass distribution of unlike-sign electron pairs as identified by the combination of RICH and TOF for 5×10^6 most central (10 %) Au + Au collisions at 8 AGeV (red symbols). Also shown are the different contributions to the combinatorial background: eπ, $\pi\pi$, ee and pX combinations.

As discussed above, it is essential for the CBM physics program to be able to address dilepton measurements in the IMR. The dielectron channel will be important in this context, since it allows to measure also the low p_t region at mid-rapidity with high accuracy. However, for a dielectron study in the IMR it will be mandatory to achieve a sufficient pion suppression also at electron momenta higher than those accessible with the RICH alone. As illustrated in the right panel of Fig. 9.15, the RICH is effective for momenta only up to 5 – 6 GeV/c. To identify electrons at higher momenta the TRD will have to supply additional information. In fact, the electron identification for $p \geq 7$ GeV/c is effectively only provided by the TRD. As demonstrated in the left panel of Fig. 3.4, this additional pion suppression is particularly important for pair combinations in the higher mass region above $m_{\mathrm{inv}} > 2\,\mathrm{GeV}/c^2$, where the contribution of the TRD reaches the same level than the one obtainable with the RICH detector. The TRD will of course also enhance the electron identification capabilities of CBM in the low mass region as well and will thus augment the RICH measurement of low mass vector mesons by providing an important safety margin in the case of detector inefficiencies. The right panel of Fig. 3.4, illustrates that the a combination of RICH and TOF alone is not able to sufficiently reduce the combinatorial background, in particular in the higher mass regions above 1 GeV/c. The background obtained with the input cocktail described above is dominated by pair combinations including misidentified hadrons, i.e. combinations of real electrons with misidentified pions (eπ), of two misidentified pions ($\pi\pi$) and of misidentified protons with all electron candidates (pX), by several orders of magnitude. Thus, it is obvious that additional electron identification is

mandatory if one wants to address dielectron physics in the IMR.

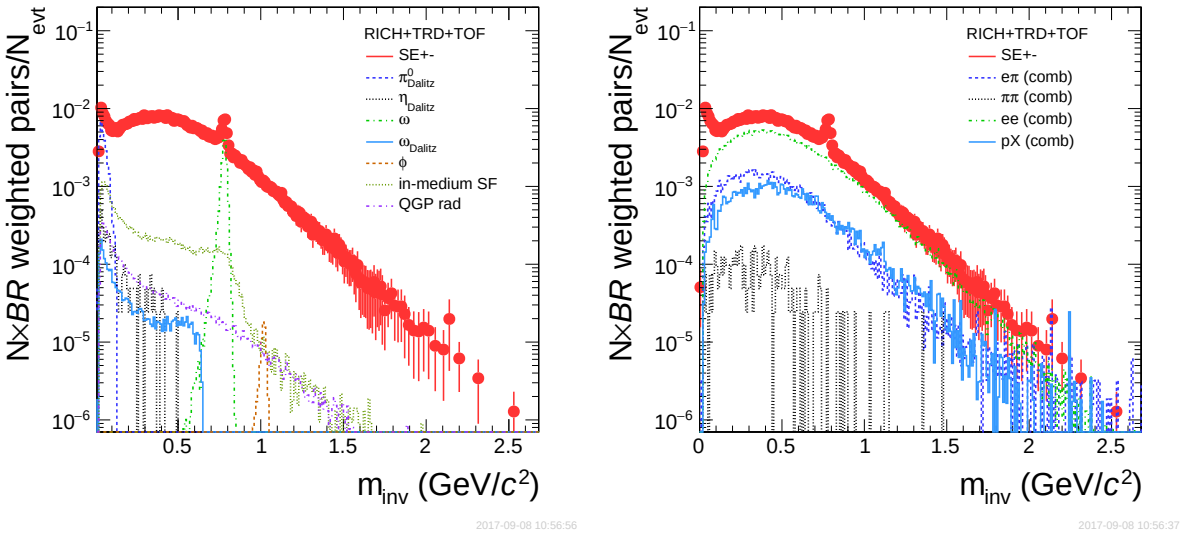

Figure 3.5: The total reconstructed invariant mass distribution of unlike-sign electron pairs as identified by the combination of RICH, TRD (standard configuration with four layers) and TOF for 5×10^6 most central (10 %) Au + Au collisions at 8 AGeV. Please note that a track cut of $p_t > 0.2\,\mathrm{GeV}/c$ was applied, which effectively reduces the low mass region. The different direct dielectron sources (π^0-Dalitz, η-Dalitz, ω, ω-Dalitz, ϕ, and thermal radiation) are shown on the left panel together with the total invariant mass spectrum including the combinatorial background (red dots). The right panel shows different components of the combinatorial background (eπ, $\pi\pi$, ee and pX combinations), together with the same total invariant mass spectrum (red dots) as presented in the left panel. All contributions are weighted according to their expected yield and the corresponding branching ratios (see Tab. 3.1).

For the TRD three alternative scenarios have been evaluated. In addition to the standard configuration, which is composed of four detector layers, geometries have been studied that are either composed of only three layers or include an additional fifth layer, identical to the others. A five layer TRD naturally provides a higher pion suppression factor (see Fig. 9.15 and Tab. 9.1) and would in case of the simulation cocktail analyzed here even exceed the suppression achieved by the RICH detector alone for masses above $2.5\,\mathrm{GeV}/c^2$ (see Fig. 3.4). However, since the addition of a further detector layer would substantially increase the overall cost of the project (roughly by 25 %), it is important to assess whether it is really mandatory to achieve the main physics goals (i.e. the measurement of dielectrons in the IMR and the extraction of their inverse slope parameter). On the other side, it needs to be investigated whether a TRD with only three layers would suffice for the planned physics program, even though the achievable pion suppression factors will be considerably lower (see Tab. 9.1).

3.3.2 Dielectron reconstruction in the IMR

The reconstruction of dielectrons proceeds by combining unlike-sign pairs of electron candidates, as identified with the TRD, RICH and TOF. Since a large fraction of electrons and positrons originate from π^0-Dalitz decays and the conversion of photons inside the target and the following material, algorithms aiming at a suppression of this contribution need to be applied. For this purpose all electron candidates were combined into unlike-sign pairs and rejected, if any of these pairs resulted in an invariant mass below $25\,\mathrm{MeV}/c^2$. In order to inspect as many pairs

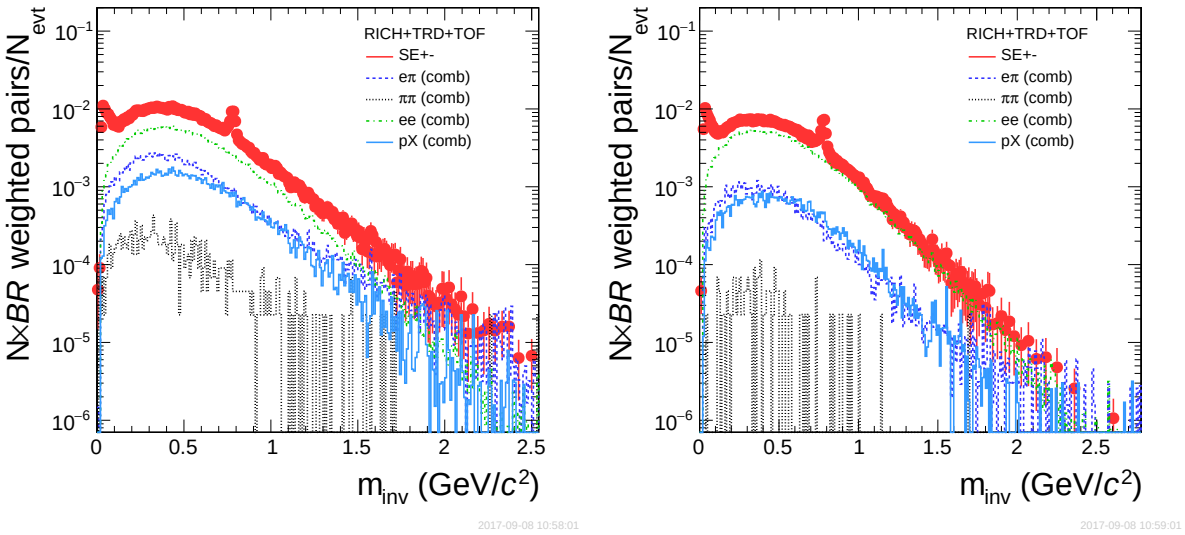

Figure 3.6: The total reconstructed invariant mass distribution of unlike-sign electron pairs as identified by the combination of RICH, TRD and TOF for 5.0×10^6 most central (10 %) Au + Au collisions at 8 AGeV, together with the different components of the combinatorial background (eπ, $\pi\pi$, ee and pX combinations). Shown are the results for a modified TRD setup with three (left panel) and five (right panel) layers.

as possible in this procedure, the identification of the electron candidates is using in this case more relaxed criteria than the ones applied to the electron candidates for the final invariant mass spectra. Here, the identification is performed with the RICH only (no TOF), while the TRD identification is applied in addition only for those tracks with $N_{\text{hits}}^{\text{TRD}} \geq 3$, i.e. tracks with $N_{\text{hits}}^{\text{TRD}} < 3$ are accepted without TRD identification.

The reconstructed final invariant mass distributions of the various components of unlike-sign electron pairs are shown in Fig. 3.5. They are weighted according to the expected yields as described above (see Tab. 3.1) and multiplied by the corresponding branching ratios. Apart from the direct contributions (π^0-Dalitz, η-Dalitz, ω, ω-Dalitz, ϕ and thermal radiation, left panel) also the background resulting from combinations between real electrons and misidentified pions (eπ, $\pi\pi$, ee and pX, right panel) is shown.

	S/B-Ratio		
Mass region	3 layers	4 layers	5 layers
$0.65 - 0.80\,\text{GeV}/c^2$	$(2.56 \pm 0.04) \cdot 10^{-1}$	$(2.95 \pm 0.06) \cdot 10^{-1}$	$(3.13 \pm 0.06) \cdot 10^{-1}$
$0.95 - 1.05\,\text{GeV}/c^2$	$(1.03 \pm 0.16) \cdot 10^{-2}$	$(1.69 \pm 0.29) \cdot 10^{-2}$	$(1.77 \pm 0.30) \cdot 10^{-2}$
$1.10 - 2.10\,\text{GeV}/c^2$	$(1.05 \pm 0.05) \cdot 10^{-2}$	$(1.47 \pm 0.08) \cdot 10^{-2}$	$(1.61 \pm 0.08) \cdot 10^{-2}$

Table 3.2: The total signal-to-background (S/B) ratios for a dielectron measurement in the IMR in central Au + Au collisions at 8 AGeV for a three, four and five layer TRD configuration.

The default TRD setup (i.e. four detector layers) results in a pion suppression that is sufficient to reduce the $\pi\pi$-component (i.e. remaining pions misidentified as electrons) in the combinatorial background below the level of the thermal signal above $m_{\text{inv}} = 1\,\text{GeV}/c^2$ (compare left and right panel of Fig. 3.5). The dominant background component results from uncorrelated e^+e^--pairs, which cannot further be reduced by additional electron identification, followed by combinations of electrons and misidentified pions. The overall signal-to-background (S/B) ratios

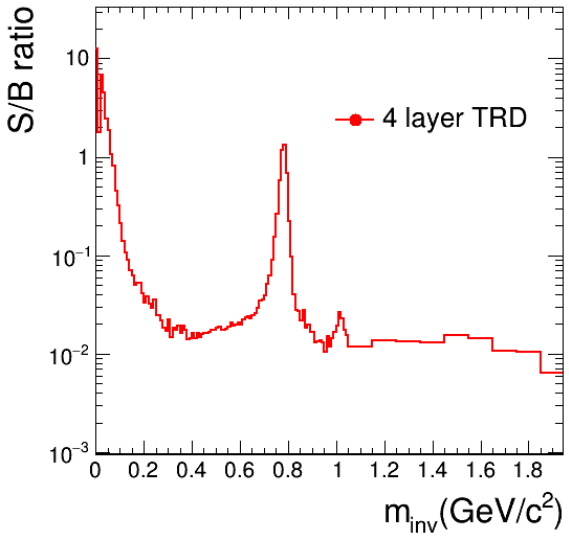

Figure 3.7: The total signal-to-background ratio (S/B) as a function of the invariant mass of the electron pairs.

for 5×10^6 central Au + Au events at 8 AGeV are shown in Figs. 3.7 and 3.8 and summarized in Tab. 3.2 for the three different TRD configurations (three, four and five layers). The standard TRD setup with four detector layers will result in a total S/B-ratio in the mass region of the thermal component which is significantly higher than the one obtained with the three layer setup, but on the same level than the one for five layers. The reason for this lies in the fact that with four layers the eπ-background-component is already strongly suppressed in relation to the ee-component, so that additional pion suppression does not improve the situation any further. As is visible in the right panel of Fig. 3.8, the ee-background is independent of the number of layers as expected, while the eπ-component changes significantly between three and four layers, but only slightly between four and five layers. Therefore we conclude that a setup with four TRD layers will be sufficient to address a measurement of IMR dielectrons at these energies, while three layers will result in a clear performance loss and five layers do not offer a significant advantage. Consequently, this configuration is chosen as the baseline design for the TRD at SIS100. Figure 3.8 and Tab. 3.2 also show the S/B-ratios in the regions around the ω and ϕ-mass. In both cases five layers do not perform better than four as far as the total S/B-ratio is concerned. In the case of the ω five layers do still improve the $S/(\pi\pi)$ and $S/(\mathrm{e}\pi)$ ratios (see left panel of Fig. 3.8). However, since the background is in any case dominated by the ee-component in this mass region, this will not provide any advantage.

Before extracting the signal in the mass range of the thermal component, the combinatorial background has to be carefully determined with a mixed event technique and subtracted. In the case of a small signal-to-background ratio this procedure will introduce a systematic uncertainty. This uncertainty on the combinatorial background will be the dominant systematic effect and propagates into the systematic uncertainty of the extracted signal as $\delta_{\mathrm{sys}}(S)/S = \delta_{\mathrm{sys}}(B)/B/(S/B)$. A conservative assumption on the background assumption is $\delta_{\mathrm{sys}}(B)/B \approx 0.25\,\%$ [39], however, it was demonstrated that a description of the combinatorial background in dielectron distributions on the level of $\sim 0.1\,\%$ is achievable without problems [40]. In the latter case a S/B-ratio of 10^{-2} ($2 \cdot 10^{-2}$) would correspond to a systematic error of 10 % (5 %). It should therefore be possible to extract the thermal dielectron component with good significance.

The huge number of events, which would be required to perform a full analysis of the thermal dielectron spectrum at the expected S/B-ratio, and the corresponding requirements in terms of CPU time and storage space make such a study on MC events in the full simulation framework

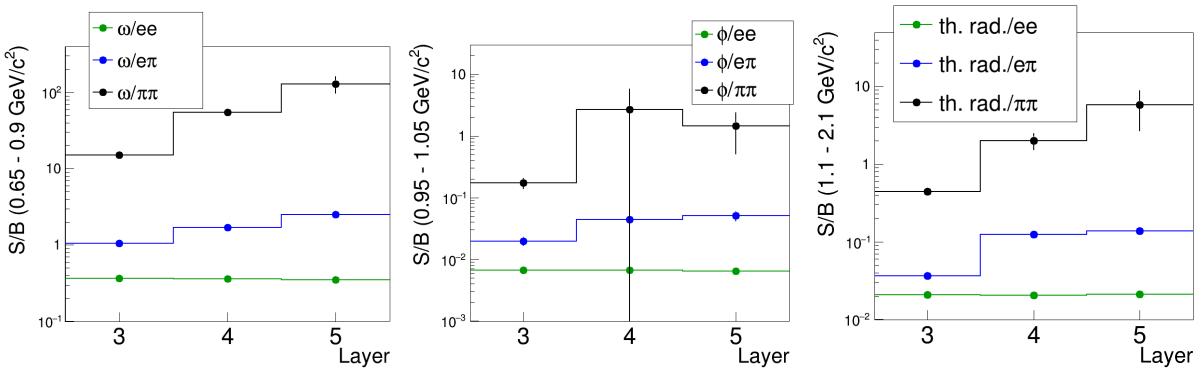

Figure 3.8: Signal-to-background ratios in different invariant mass regions. Shown are the range around the ω-mass ($0.65 - 0.80\,\mathrm{GeV}/c^2$, left panel), the ϕ-mass ($0.95 - 1.05\,\mathrm{GeV}/c^2$, middle panel) and where the thermal (QGP + in-medium) component is expected to be the dominant signal ($1.1 - 2.1\,\mathrm{GeV}/c^2$, right panel). The different main background components (ee, eπ and $\pi\pi$) are presented separately here.

impossible. In order to determine the needed significance of the the signal component, and thus be able to estimate the required event statistics, a simulation with an artificially enhanced S/B-ratio was performed, see Fig. 3.9. In this case minimum bias Au + Au events at 8 AGeV from UrQMD were used as background, while the yield of the dielectron signal components was increased such that a S/B ratio of ~ 0.2 for $m_{\mathrm{inv}} > 1\,\mathrm{GeV}/c^2$ results, i.e. higher by a factor of ~ 10 compared to the realistic values given in Tab. 3.2. A data set of $2.5 \cdot 10^6$ events in this scenario corresponds to a significance of $S/\sqrt{S+B} \approx 3.5$. The left panel of Fig. 3.9 shows the resulting invariant mass distribution of all unlike-sign electron pairs. Due to the different weighting of the signal contributions and the different centrality selection, the data points shown here are naturally very different to the ones shown in the realistic simulation in Fig. 3.5. Figure 3.9 also displays the corresponding combinatorial background (shown as a solid line), as estimated with the mixed event technique. Here, uncorrelated $\mathrm{e}^+\mathrm{e}^-$ pairs are formed by combining tracks from different events. In order to achieve a most realistic description of the combinatorial background only electron candidates from those events are combined that have similar total multiplicities and main vertex positions. The mixed event technique allows to construct an estimate of the background with arbitrarily small statistical uncertainty by combining many different events of the same characteristics (10 in this case). By subtracting the constructed background from all $\mathrm{e}^+\mathrm{e}^-$ combinations the signal distribution displayed in the right panel of Fig. 3.9 is obtained. This reconstructed signal distribution agrees very well with the distribution of thermal dielectrons that was used as input to the simulation procedure. The signal is fitted with an exponential function $\propto \exp(-m_{\mathrm{inv}}/\langle T \rangle)$ in the IMR $0.9 < m_{\mathrm{inv}} < 1.5\,\mathrm{GeV}/c^2$ in order to extract the inverse slope parameter $\langle T \rangle$. It is found to be $\langle T \rangle = 216 \pm 64(\mathrm{stat.})\,\mathrm{MeV}$, which agrees well with the inverse slope parameter of the MC input distribution of $T^{\mathrm{MC}} = 230\,\mathrm{MeV}$ (please note the corresponding source temperature $\langle T_{\mathrm{s}} \rangle$ is lower since an additional weighting by $1/m_{\mathrm{inv}}^{3/2}$ has to be included in this case). This demonstrates that the proposed analysis is feasible, if a corresponding significance in the region of ≥ 10 is achieved.

In the case of a realistic scenario, corresponding to the numbers given in Tab. 3.1 and as shown in Figs. 3.5 and 3.8, i.e. a S/B ratio of around 10^{-2} and a signal per event of $S/\mathrm{evt.} \approx 6 \cdot 10^{-6}$, about 10^{10} central (10 %) Au + Au events at 8 AGeV will be needed to reach a significance of ≥ 10, respectively 10^{11} minimum bias events. Assuming an interaction rate of 1 MHz and a spill duty cycle of 50 %, this would translate into a measurement time of ~ 60 h for one specific configuration (i.e. system size or beam energy). Therefore, systematic studies should be feasible

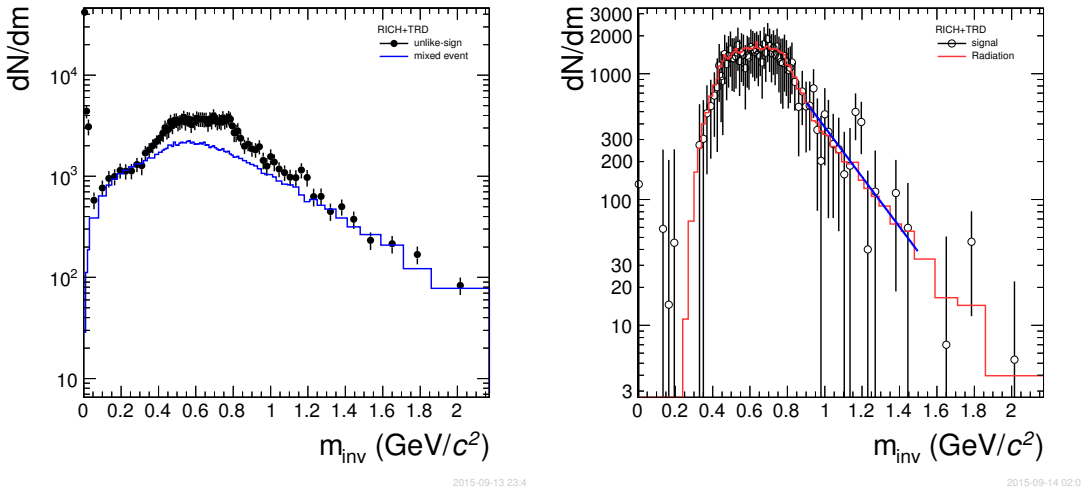

Figure 3.9: Left panel: The invariant mass distribution of unlike-sign electron pairs (symbols) as identified by the combination of RICH and TRD (four layers) for minimum bias Au + Au collisions at 8 AGeV, together with the combinatorial background evaluated with the mixed event technique (solid line). In this simulation the S/B ratio has been increased to values around ~ 0.2. Right panel: The remaining signal distribution after subtraction of the combinatorial background (symbols). The simulated thermal component is shown in comparison (red solid line). The result of an exponential fit to the IMR ($0.9 < m_{\mathrm{inv}} < 1.5\,\mathrm{GeV}/c^2$) is displayed as the blue solid line.

within a reasonable time scale.

3.4 Reconstruction of J/ψ with the TRD

3.4.1 p+A Collisions

Figure 3.10 shows in the left panel a simulated invariant mass distribution of electron-positron pairs for p + Au collisions at 30 GeV beam energy. As a generator for the signal distribution of J/ψ the HSD model has been used [41], providing an input multiplicity per event of $1.0 \cdot 10^{-8}$. In this analysis all tracks were required to have at least five hits in the STS and three in the TRD and a minimum momentum of $p_t > 1\,\mathrm{GeV}/c$. Electrons were identified using RICH and TRD information. The resulting distribution corresponds to $2.5 \cdot 10^{13}$ collected events, equivalent to about 40 days of data taking at an interaction rate of 10 MHz and assuming a spill duty factor of 80 % for p+A. A clean J/ψ signal over a moderate background can be observed with a S/B ratio around 1.25. Around 600 J/ψ are reconstructed after background subtraction according to the HSD prediction. Given the fact that the charged particle multiplicities in p + Au collisions are lower by more than one order of magnitude than in Au + Au collisions at the same energy, much higher interaction rates could easily be accommodated by the same detector and readout configuration if all possibilities of the 4D-reconstruction scheme are exploited. Thus, the here described scenario can be considered as rather conservative.

The right panel of Fig. 3.10 shows the acceptance and reconstruction efficiency for J/ψ mesons as a function of p_t at 30 GeV. The red symbols represent the pure acceptance and is found to be around 35 %. The introduction of the p_t cut on the electron tracks at $1\,\mathrm{GeV}/c$ lowers it to ~ 20 % above a J/ψ p_t of $1.5\,\mathrm{GeV}/c$ (blue symbols). The inefficiencies of the reconstruction procedure cause a further reduction towards a value for the product of acceptance and efficiency of about 15 % (green symbols), independent on the J/ψ transverse momentum.

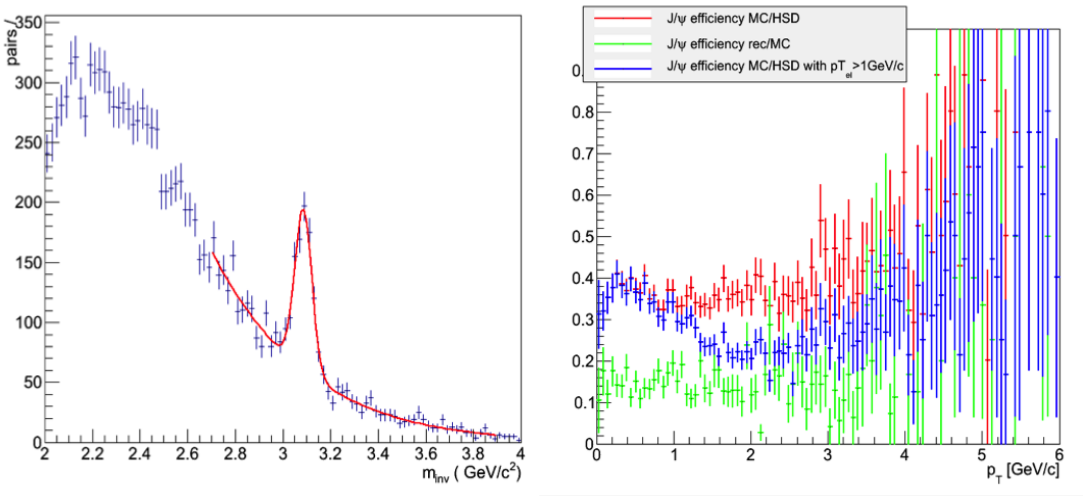

Figure 3.10: The invariant mass distribution of e^+e^- pairs in the J/ψ mass region in p + Au collisions at 30 GeV beam energy (left panel) measured with a four layer TRD. The right panel shows the corresponding total efficiency and acceptance as a function of the J/ψ transverse momentum.

3.5 Reconstruction of fragments with the TRD

3.5.1 Fragment identification via TRD-dE/dx

The TRD is able to provide up to four independent measurements of the specific energy loss of a charged particle in the four layers of Xe/CO_2 gas mixture[1], as planned in the setup for the SIS100. The achievable dE/dx resolution will be sufficient to separate fragments. The charge information obtained by the TRD-dE/dx measurement can also be exploited in the tracking in order to determine the correct momentum for $Z = 2$ particles.

The averaged $\langle dE/dx \rangle$ signal measurable with a four layer TRD, requiring at least four reconstructed hits, is shown as a function of the true particle momentum in the left panel of Fig. 3.11. The different branches for protons, deuterons, tritons, ^{3}He and ^{4}He are clearly distinguishable. The right panel of Fig. 3.11 shows exemplary for the momentum interval $1.5 < p/Z < 2.0\,\mathrm{GeV}/c$ how a unique identification of d and ^{4}He can be performed by combining TOF and TRD information. Please note that here the reconstructed momentum is used, which in this case does not take into account the different fragment charges Z, such that the $\langle dE/dx \rangle$ branches for, e.g., deuterons and ^{4}He are moved closer in momentum in comparison to the situation in the left panel. While the m^2/Z^2 measurement alone, as provided by TOF, does not allow to separate these two fragments, the addition of the TRD-dE/dx signal results in a clear separation of the two. The energy loss measurement with the TRD also helps to reduce the background in the identification of other fragments, e.g. of ^{3}He. As can be seen in the lower left corner of the right panel of Fig. 3.11, the TOF measurement alone is still affected by a background, resulting from wrong track matches, which can be separated by combining it with the TRD-dE/dx information. This background rejection is illustrated in Fig. 3.12 in the TOF m^2/Z^2 spectrum by requiring a TRD-$dE/dx > 25\,\mathrm{keV{\cdot}cm^2/g}$. A suppression factor ~ 20 can be achieved for deuterons in the region above $p/Z > 1.5\,\mathrm{GeV}/c$. TRD-$dE/dx$ might even be used to clean up the particle identification of lighter hadrons, such as protons and kaons.

The distributions of the averaged energy loss signal $\langle dE/dx \rangle$ of deuterons and ^{4}He, as

[1] Alternatively, the TRD can be operated with a less expensive Ar/CO_2 gas mixture, if no electron identification is required in a special running scenario.

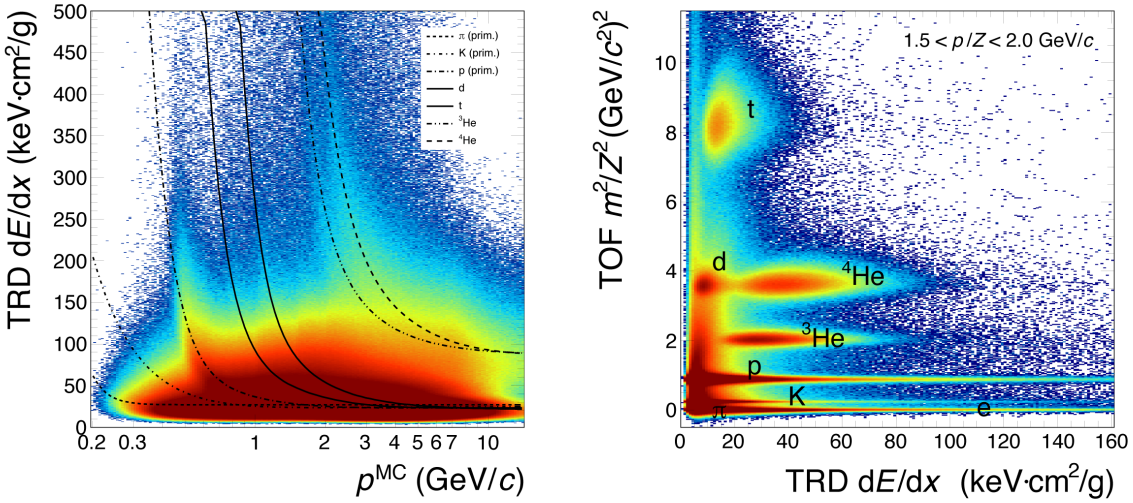

Figure 3.11: Left: The averaged $\langle dE/dx \rangle$ signal as reconstructed with the TRD as a function of the true momentum p^{MC}. The lines depict the expectations for the different particle species. Right: The TRD signal versus the mass squared as measured by the TOF in central (10 %) Au + Au collisions at 8 AGeV. Shown is the momentum interval $1.5 < p/Z < 2.0\,\mathrm{GeV}/c$, where p in this case is the reconstructed momentum.

reconstructed in the TRD for Au + Au collisions at 8 AGeV, are displayed in Fig. 3.13 for two different reconstructed momentum intervals. A clear separation of d and ^{4}He is visible at both momentum ranges. By fitting these $\langle dE/dx \rangle$ distributions with a modified Gaussian

$$f(x) = A\, e^{-(|x-\mu|/(\sigma\sqrt{2}))^{\beta}} \left(1 + \alpha\, \mathrm{erf}\left[\frac{|x-\mu|}{\sigma\sqrt{2}}\right]\right) , \tag{3.1}$$

which takes into account the non-Gaussian tails of the distributions via the parameters α and β, the momentum dependence of the corresponding energy loss resolution $\sigma(p/Z)/\langle dE/dx \rangle(p/Z)$ can be obtained, as shown in the left panel of Fig. 3.14 for different TRD setups comprising three, four and five layers. The typical dE/dx resolution achievable with a four layer TRD, requiring a measured hit in each of them, is around 23 % above $p/Z = 1\,\mathrm{GeV}/c$ and rises only slightly with increasing momentum. But since it always stays clearly below 30 %, this configuration would fulfil the performance requirements without problems. With a three layer setup a resolution close to ~ 30 % can be achieved, while five layers would always be below 25 %. The resolutions can be translated into a separation power, defined for the particle species i and j as

$$S_{ij}(p) = \frac{\langle dE/dx \rangle_i(p/Z) - \langle dE/dx \rangle_j(p/Z)}{\sigma_i(p/Z)} , \tag{3.2}$$

which is shown for deuterons and ^{4}He in the right panel of Fig. 3.14. A separation of deuterons and ^{4}He on a level of $\sigma \gtrsim 4$ should therefore be possible in the whole accessible momentum range with four layers. Around $p/Z \sim 1.3\,\mathrm{GeV}/c$ it even reaches values of ~ 5. Please note that the separation power can be improved even further in the lower momentum region, if the correct charge is taken into account in the momentum determination as it is possible after a proper identification of the fragments with the TRD.

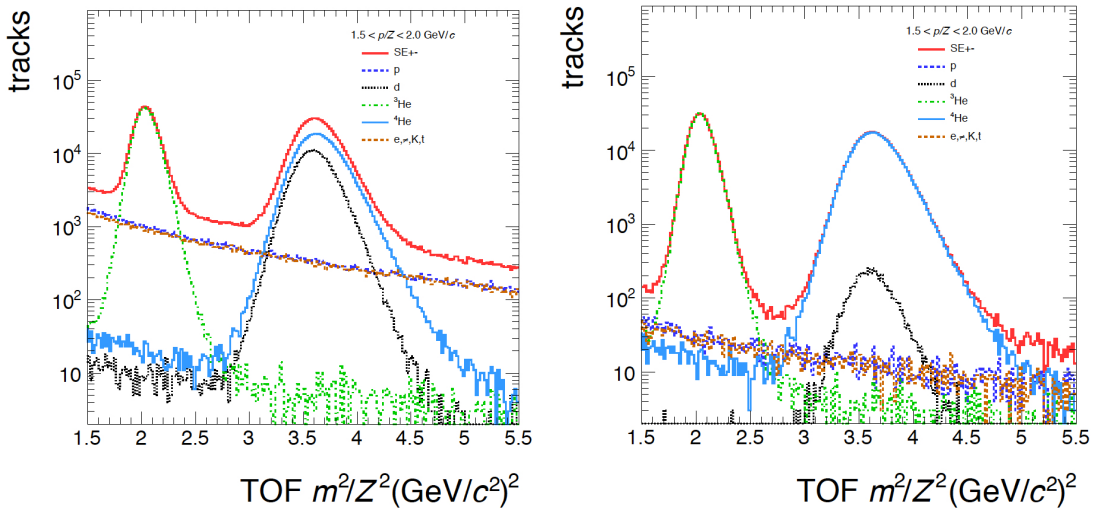

Figure 3.12: The m^2/Z^2 measurement provided by the TOF in the momentum interval $1.5 < p/Z < 2\,\mathrm{GeV}/c$ and the mass region of heavy fragments without (left) and with TRD PID selection on ^{4}He (right).

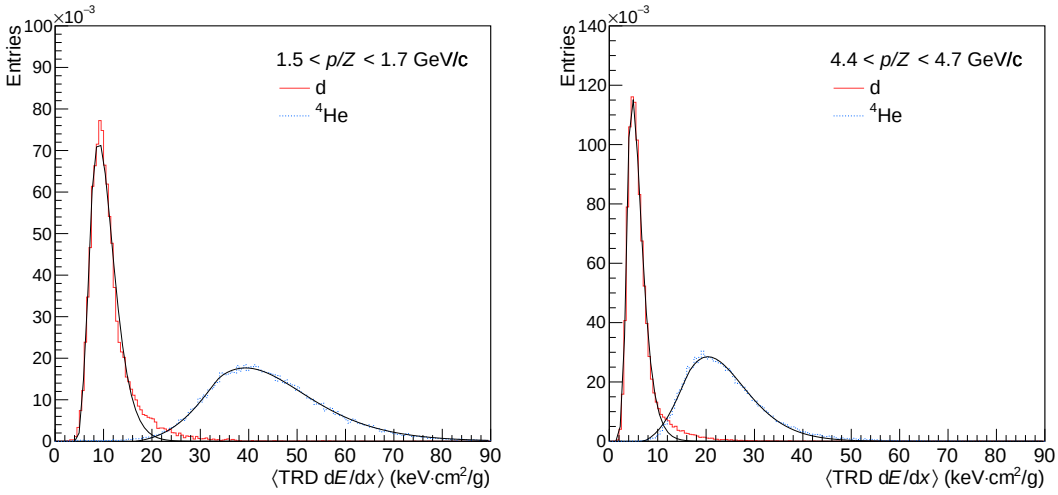

Figure 3.13: The averaged $\langle dE/dx \rangle$ distributions for the fragments d and ^{4}He as reconstructed with the TRD in central (10 %) Au + Au collisions at 8 AGeV, requiring at least four measured hits. Shown are the reconstructed momentum intervals $1.5 < p/Z < 1.7\,\mathrm{GeV}/c$ (left panel) and $4.4 < p/Z < 4.7\,\mathrm{GeV}/c$ (right panel). The results of the fit with the modified Gaussian are shown in black.

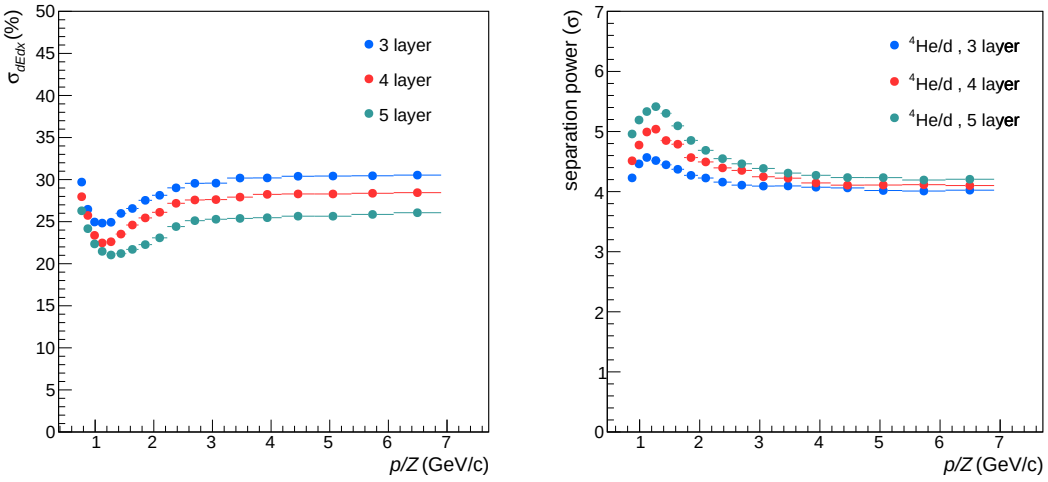

Figure 3.14: Left: The resolution of the averaged $\langle dE/dx \rangle$ as a function of the particle momentum reconstructed with the TRD for deuterons in central (10 %) Au + Au collisions at 8 AGeV, reconstructed with a setup of three, four and five TRD layers. Right: The corresponding separation power for deuterons and ^{4}He.

Chapter 4

The Transition Radiation Detector

In the following we outline the design for the CBM-TRD as it is foreseen for the various experimental setups of CBM at the SIS100. The configuration described here is based on an established and robust readout chamber design (see Chap. 5), which fulfills the performance parameters outlined in Sect. 2.3.

Another important aspect of the current design is its modularity and the reduction of the number of different components to a minimum. This facilitates mass production and allows for a flexible configuration of the detector geometry.

4.1 Working principle

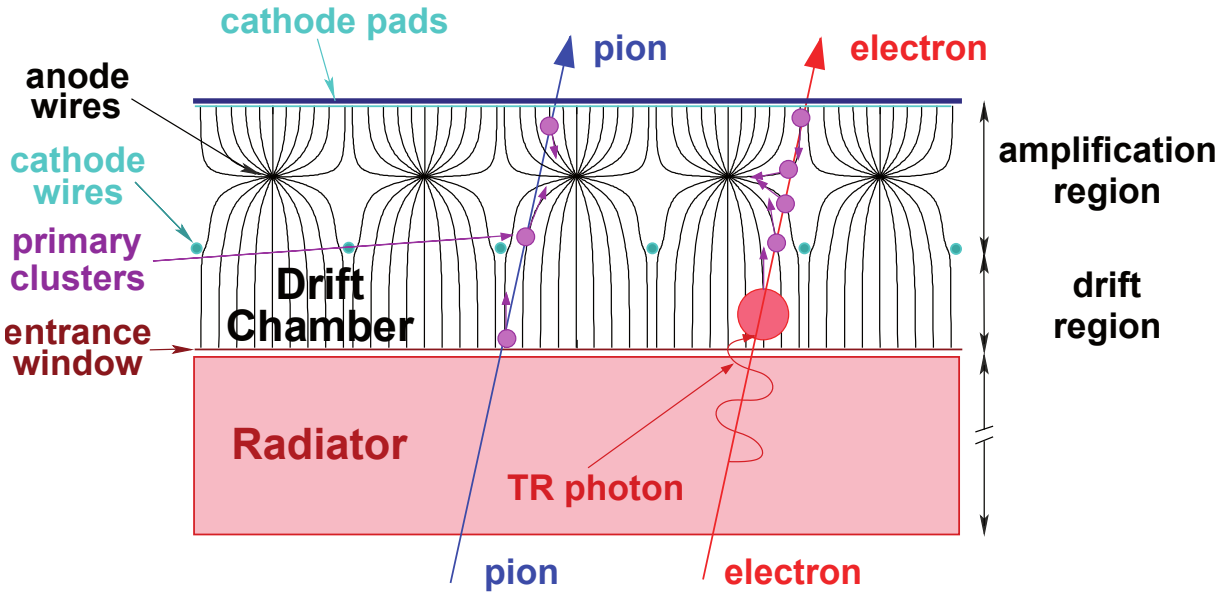

Figure 4.1: A schematic illustration of the working principle of the CBM-TRD.

The basic working principle of the CBM-TRD is illustrated in Fig. 4.1. The detector is essentially composed of two parts, the Read-Out Chamber (ROC) and the radiator. Transition Radiation (TR) photons are generated in the radiator by electrons with a given probability, while the heavier pions, being too slow, pass through without producing any TR. In order to efficiently absorb the TR-photons in the gas volume of the ROC, a xenon gas mixture, having a high absorption cross section for photons in the TR spectral range, is used as a counting gas. Thus, the TR-photons are predominantly absorbed in the region directly behind the entrance window.

On top of the TR-signal the ROCs also collect the charge released via the specific energy loss $\langle dE/dx \rangle$ caused by primary ionization processes in the gas. Differences in the $\langle dE/dx \rangle$ between electrons and pions additionally enhance the separation power between the two and also extend the electron identification towards lower charged particle momenta where no TR-photons are produced. Furthermore, the $\langle dE/dx \rangle$ measurement can be used to support the identification of nuclear fragments.

4.2 TRD station layout

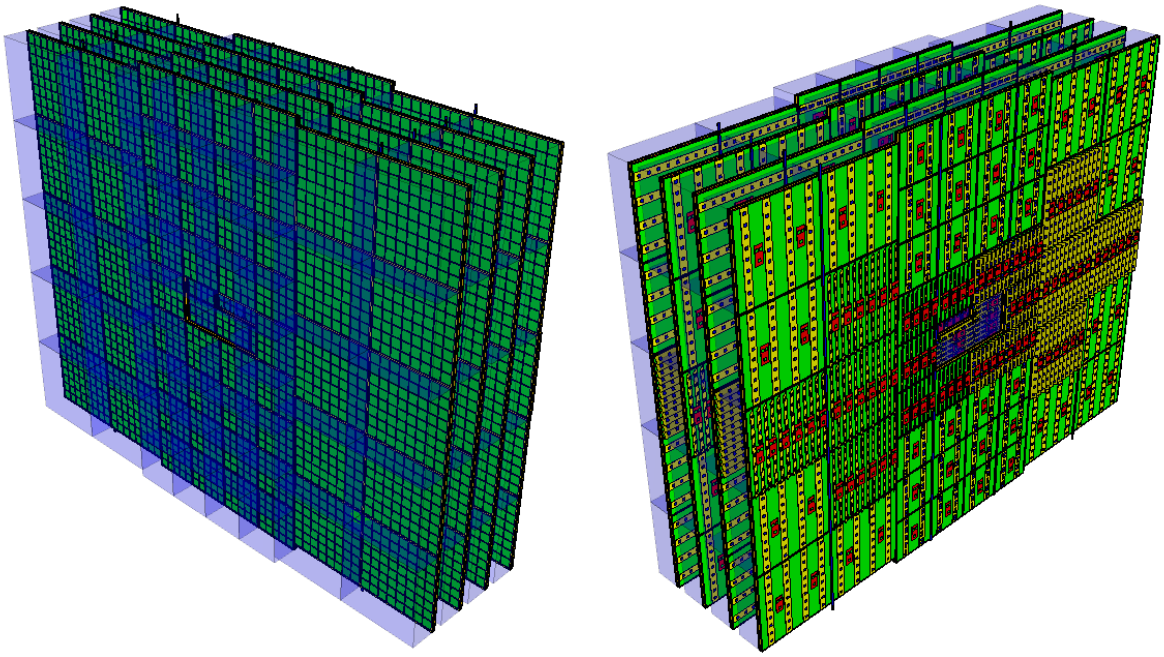

Figure 4.2: CBM-TRD geometry for SIS100 consisting of one station with four layers of detectors. Shown here is the implementation of the TRD geometry in the CBMROOT simulation framework. Visible are the ROCs with the radiator boxes in the front view (left), while the rear view (right) shows the backpanels of the ROCs together with the front-end electronics.

Module type	# Modules/plane	# Pads	Pad area (cm^2)
1	10	25,600	1.2
3	24	15,360	4.6
5	8	27,648	2.7
7	12	13,824	8.0
Total for one TRD layer	54	82,432	

Table 4.1: The number of different TRD module types per detector layer, together with the corresponding number of readout channels (pads).

The required performance parameter for the SIS100, as summarized in Sect. 2.3, can be achieved by a TRD consisting of four layers of radiators and ROCs as demonstrated in Chap. 3. For a possible use of the TRD at a future SIS300, this setup can easily be adapted by extending it to up to ten detector layers.

The TRD is designed such that the entire system can be built with modules of only two different sizes, see Fig. 5.8. The TRD modules are of quadratic shape with outer dimensions of $57 \times 57\,\mathrm{cm}^2$ (small module types) and $99 \times 99\,\mathrm{cm}^2$ (large module types). Given the CBM fixed target geometry we expect large hit rates at forward angles dropping over few orders of magnitude towards larger angles. The spatial distribution of the hit rates, as common for all fixed target experiments, falls exponentially with increasing distance to the beam axis, as discussed in Sect. 4.4. This requires a high detector granularity in the inner part equipped with the small modules, whereas the outer areas can be covered with large modules. To deal with the high hit rate a high granularity is realized by a small pad size in the inner part. Towards the outer regions the pad area is scaled up by almost one order of magnitude. The size of the largest commercially available single piece of Printed Circuit Board (PCB), which can be used for the pad plane, defines the maximum size of the small, innermost modules. The large modules will have to be equipped with pad planes assembled from several PCBs and special precautions in order to achieve gas tightness will have to be implemented in this case. The maximal size of the modules is further constrained by possible gain instabilities which can occur at the highest count rates, if the anode wires were too long and thus have to collect too much charge. The scaling of the pad size is implemented on pad planes with different layouts. All required pad sizes can be accommodated by four different pad plane types, two for the small and two for the large module types as described in Sect. 5.5.

A given module of the CBM-TRD consists of three different components: the ROC, the radiator, and the Front-End Electronics (FEE). The construction details of the ROCs are summarized in Chap. 5, the choice and the design of the radiator is described in Chap. 6, and details on the FEE implementation are given in Chap. 7.

The modules will be arranged in four layers, which together form a single TRD station with a common support structure (see Fig. 4.2). Figure 5.24 displays the arrangement of the ROCs and Front-End Boards (FEB) on two different TRD layers. Their orientation changes by 90° in each alternating layer, i.e. the long sides of the readout pads point vertically in layers one and three and horizontally in layers two and four. The orientation of the FEBs follows the one of the readout pads. This way an optimal tracking resolution in both dimensions can be achieved. Table 4.1 summarizes the numbers of different TRD module types needed to build one detector layer (see also Fig. 5.21) and the corresponding number of readout channels (pads). In total this results in 216 modules with 329728 readout channels for a complete TRD station with four detector layers.

The module arrangement allows for a vertical segmentation of a TRD layer in three parts, two outer ones, consisting each of two columns of large module types, and a central one, containing the small module types surrounding the rectangular hole for the beam pipe and six large ones on the top and bottom (see also Fig. 8.2). This segmentation will be useful during installation and maintenance, since it they can be moved and hoisted to the ground level separately.

The TRD modules will be mounted in a supporting structure that holds all four layers of the TRD station. It will comprise an outer frame to which the ledges that support the ROCs and the radiators will be attached and which will also allow the movement of the TRD with a crane. It also supports the gas supply, LV and HV services, as well as the cooling. A description of the layout of the supporting system and its mechanical structure and components can be found in Sect. 8.2.

4.3 General system layout

The complete setup of CBM as planned for SIS100 is displayed in Fig. 4.3. Shown are the following components from left to right:

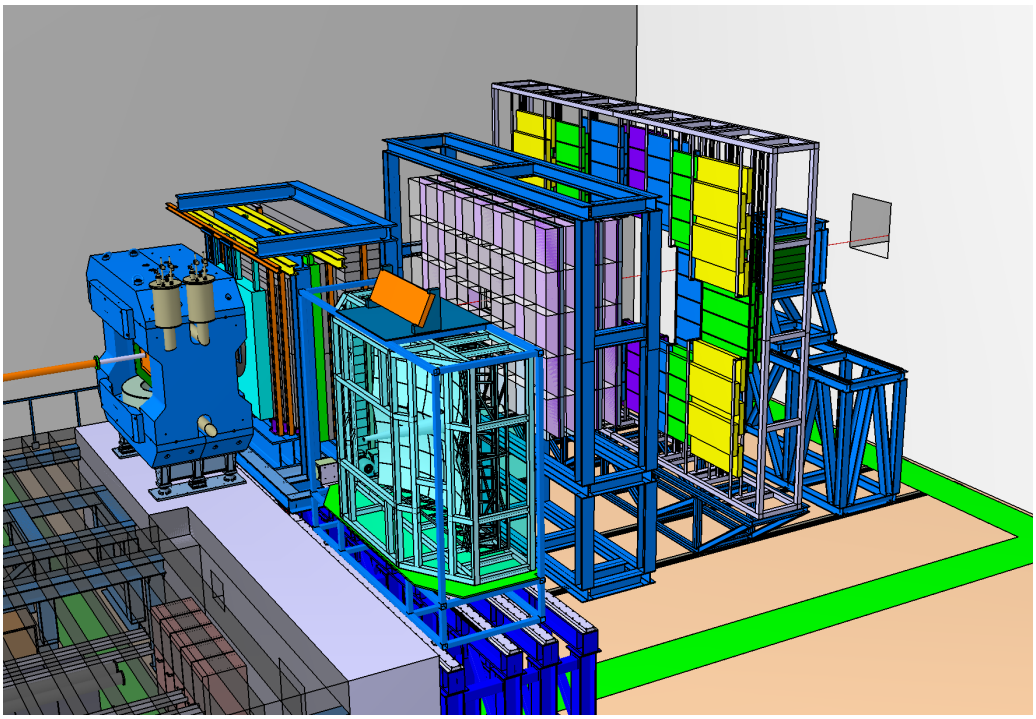

Figure 4.3: Drawing of the experimental setup of CBM for the SIS100. The four layer TRD station is shown as gray boxes positioned in beam direction behind the magnet and MUCH, respectively RICH, followed by the TOF wall and the PSD.

- The magnet surrounding the tracking detectors MVD and STS.
- The muon spectrometer MUCH situated directly behind the magnet and the RICH detector in its parking position next to it.
- The TRD with four layers of ROCs (gray boxes), together with its support frame.
- The TOF wall with different type of Resistive Plate Chamber (RPC) detectors (yellow, green, blue and violet boxes).
- The Participant Spectator Detector (PSD) for centrality and event plane determination.

Due to the modular structure of the CBM setup, the experiment can easily be configured in various ways by moving in and out different detector components, such that the setup can be optimized for different physics cases. The TRD will play an important role in three of these configurations. In the electron setup the TRD station will directly follow the RICH detector and bridge the region between RICH and TOF. In the muon configuration the RICH will be replaced by the muon arm MUCH, consisting of absorbers and tracking chambers, and the TRD will serve here as the last tracking device for muons. Finally, the TRD can also be used in a setup dedicated to hadron measurements only, where neither RICH nor MUCH are part of the setup.

4.3.1 TRD in the CBM electron setup

Figure 4.4 shows the CBM electron setup consisting of MVD, STS, RICH, TRD and TOF. In this configuration the RICH and TRD together will provide the electron identification necessary for the measurement of low and intermediate dielectrons (see Sect. 3.1.2). The tracking will be performed by the STS, while the MVD will be essential to reject conversion electrons.

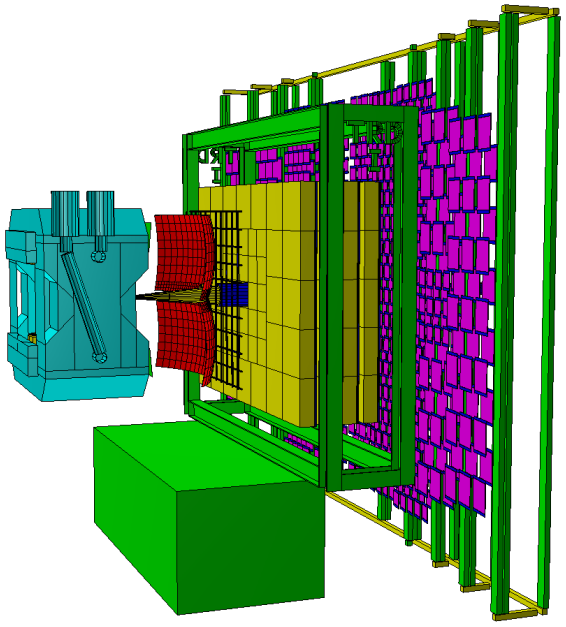

Figure 4.4: Sketch of the CBM electron setup for SIS100 with the TRD (yellow) as electron identification device. Please note that the RICH detector in this figure is only represented by its mirrors, shown in red.

4.3.2 TRD in the CBM muon setup

It is foreseen to employ the TRD as last tracking station in the configuration SIS100-C of the MUCH [42], as shown in Fig. 4.5. This configuration will therefore consist of two layers of GEM detectors, two layers of straw tubes, and the four layer TRD station. This setup will be complemented by a 60 cm carbon absorber in front of the first GEM layer and four iron absorbers between the consecutive tracking devices with a total thickness of 170 cm (see Tab. 2.1 in [42]). Tracking before the first absorber will be done with the STS. As the TRD station will be placed behind the last absorber, essentially only muons will pass through it and thus create only a very low hit rate in the TRD. The main physics case for this setup is the measurement of dimuons in the mass range between low mass vector mesons (ρ, ω and ϕ) and the J/ψ meson.

4.3.3 TRD in the CBM hadron setup

Another possible scenario in which the TRD can be included is the CBM setup for hadrons only. In this case, neither RICH nor MUCH is part of the experimental setup, but only MVD, STS, TRD and TOF (see Fig. 4.6). Tracking and secondary vertex reconstruction will be done by STS and MVD, while the hadron identification will be performed by TRD and TOF. Here the TRD will augment the time-of-flight measurement by its additional dE/dx information, as discussed in Sect. 3.5. To reduce the running costs, the TRD can in this scenario also be operated with an Ar/CO_2 mixture, instead of the much more expensive Xe/CO_2, because no TR-photon detection is needed in this case.

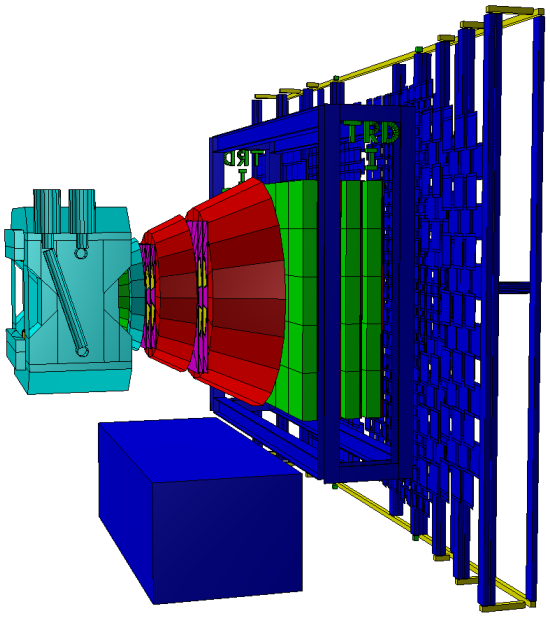

Figure 4.5: Sketch of the CBM muon setup SIS100-C with the TRD (green) as last tracking device of the MUCH.

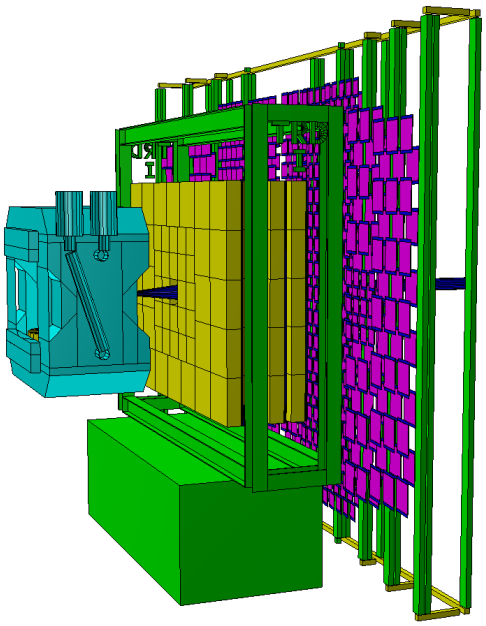

Figure 4.6: Sketch of the CBM hadron setup for SIS100 including the TRD (yellow).

4.4 Occupancy and hit rates

The TRD will be operated in the high multiplicity environment generated by Au + Au collisions at interaction rates up to 10 MHz. In the following the corresponding detector occupancy for central Au + Au collisions at 10 AGeV (SIS100) and 30 AGeV (SIS300), as well as hit rates at minimum bias Au + Au collisions at 10 AGeV are estimated, as simulated with the UrQMD event generator. These values also serve as a basis for a determination of the data rate produced by the CBM-TRD (see Sect. 7.3).

4.4.1 Occupancy simulation

The averaged occupancy seen by the TRD ROCs in the different detector layers is shown in Figs. 4.7 and 4.8 for central Au + Au collisions at 10 AGeV, respectively 30 AGeV. The granularity of the different ROCs corresponds to the pad sizes as described in Sect. 5.5 (see Tab. 5.4 and Fig. 5.21). Since the pad sizes are adjusted to the local track density, the resulting occupancy has very similar values in the different regions of the detector layers and ranges between 0.7 % and 5.5 % at 10 AGeV (1.2 % and 11.1 % at 30 AGeV). Generally, for the environment at the SIS100 the occupancy is relatively moderate and well within the requirements of $< 10\,\%$. It should therefore not pose any problem for the tracking and particle identification algorithms described in Sect. 9.3.

4.4.2 Hit rate simulation

The averaged hit rates per readout pad in the TRD ROCs of the different detector layers are shown in Fig. 4.9 for minimum bias Au + Au collisions at 10 AGeV, scaled to an interaction rate of 10 MHz. In this calculation the forced neighbor readout is assumed, as implemented in the SPADIC chip and described in Sect. 7.1. The granularity of the different ROCs corresponds to the pad sizes as described in Sect. 5.5 (see Tab. 5.4 and Fig. 5.21). Similar to the averaged occupancy, only small variations of the hit rate per readout pad over a given detector layer are visible. It is found to be around 50 kHz in most positions and only reaches values of maximally 120 kHz in very localized areas. Therefore, this detector configuration should overall be in accordance with the requirements specified in Tab. 2.1.

The hits rates per pad can be translated into hit rates seen by a single anode wire, which is a quantity relevant for the stability of chamber operation. In the highest hit density areas this results in maximal hits rates per wire of around 1.4 MHz.

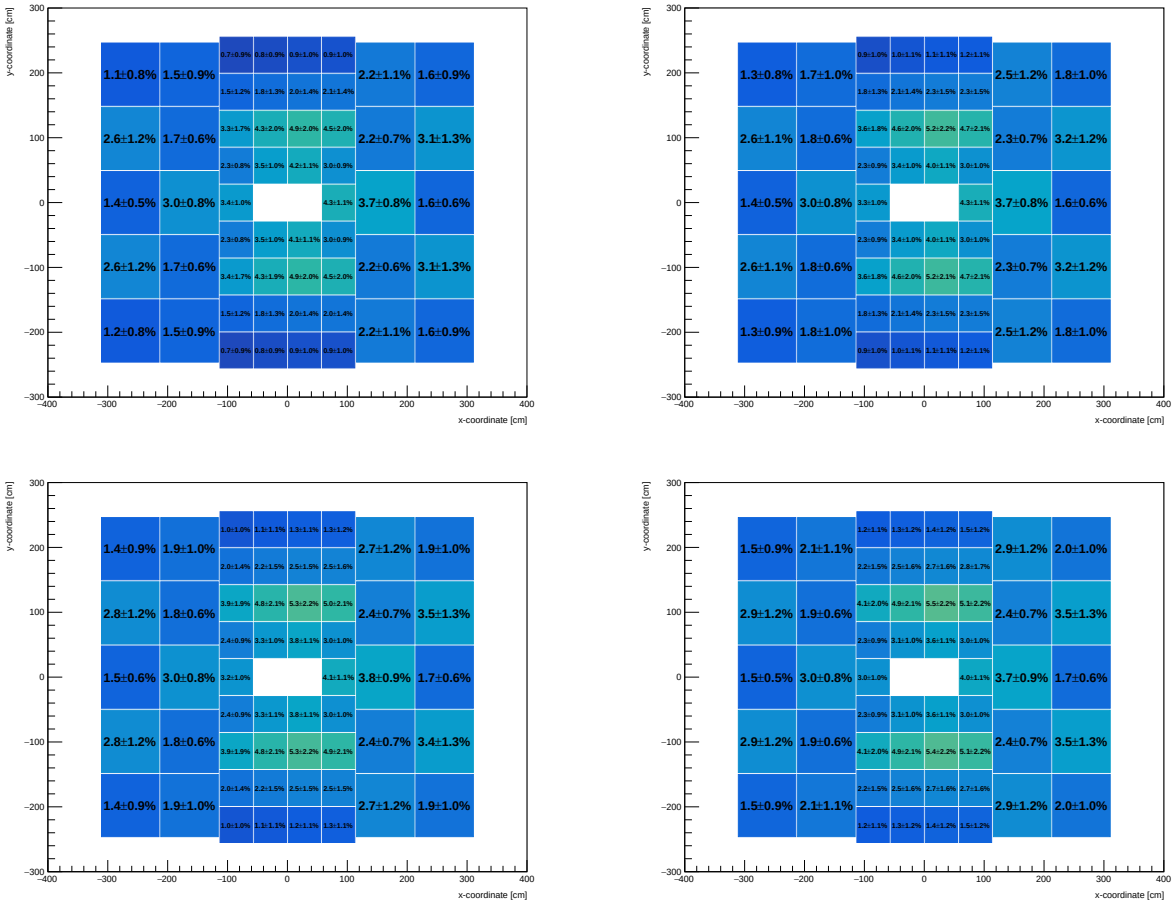

Figure 4.7: Averaged occupancy for central (10 %) Au + Au events at 10 AGeV. Shown are simulations for layer 1 (upper left), 2 (upper right), 3 (lower left) and 4 (lower right). The coordinate system covers a range of ±6 m in x- and ±5 m in y-direction. The color scale represents the mean occupancy and is:
blue: $\leq 2\,\%$, cyan: $\leq 4\,\%$, green: $\leq 6\,\%$, ocher: $\leq 8\,\%$, yellow: $\leq 10\,\%$, red: $> 10\,\%$.

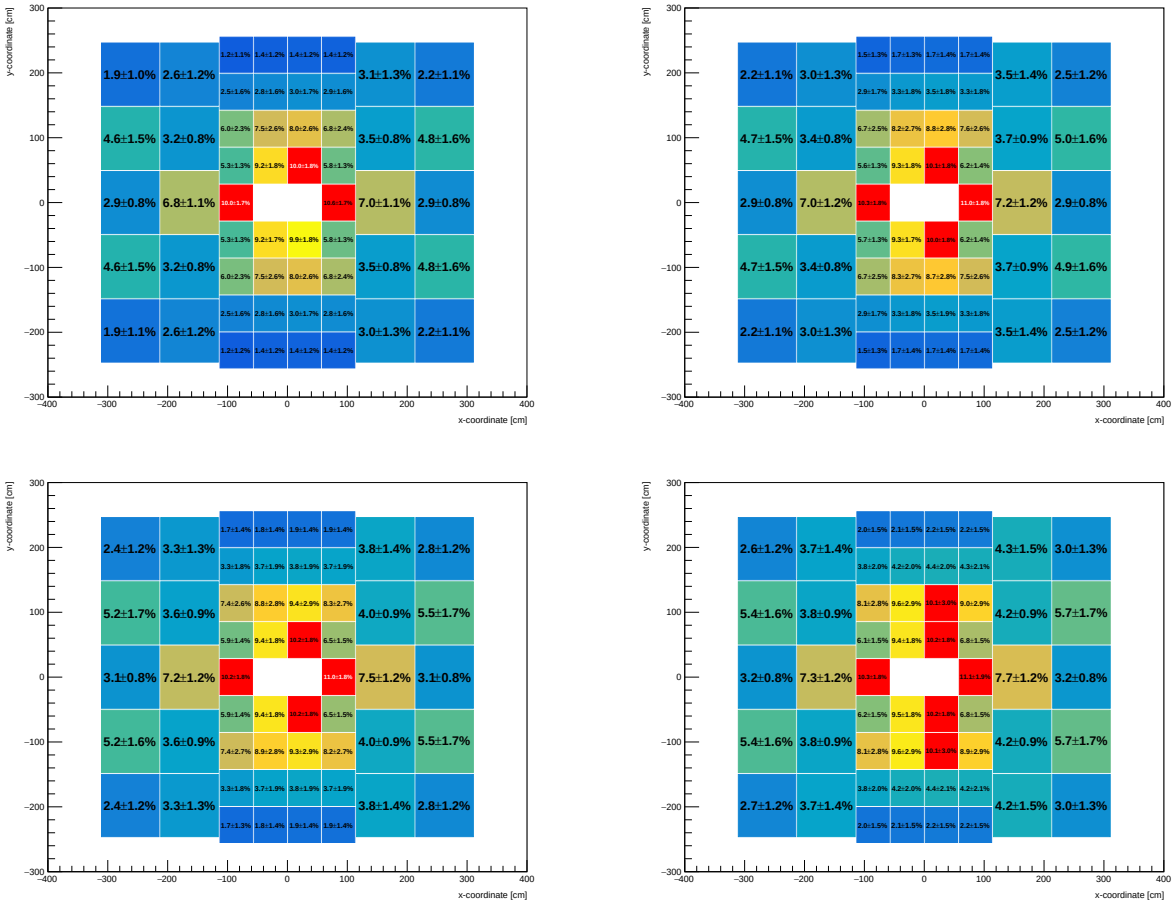

Figure 4.8: Averaged occupancy for central (10 %)) Au + Au events at 30 AGeV. Shown are simulations for layer 1 (upper left), 2 (upper right), 3 (lower left) and 4 (lower right). The coordinate system covers a range of ± 6 m in x- and ± 5 m in y-direction. The color scale represents the mean occupancy and is:
blue: $\leq 2\,\%$, cyan: $\leq 4\,\%$, green: $\leq 6\,\%$, ocher: $\leq 8\,\%$, yellow: $\leq 10\,\%$, red: $> 10\,\%$.

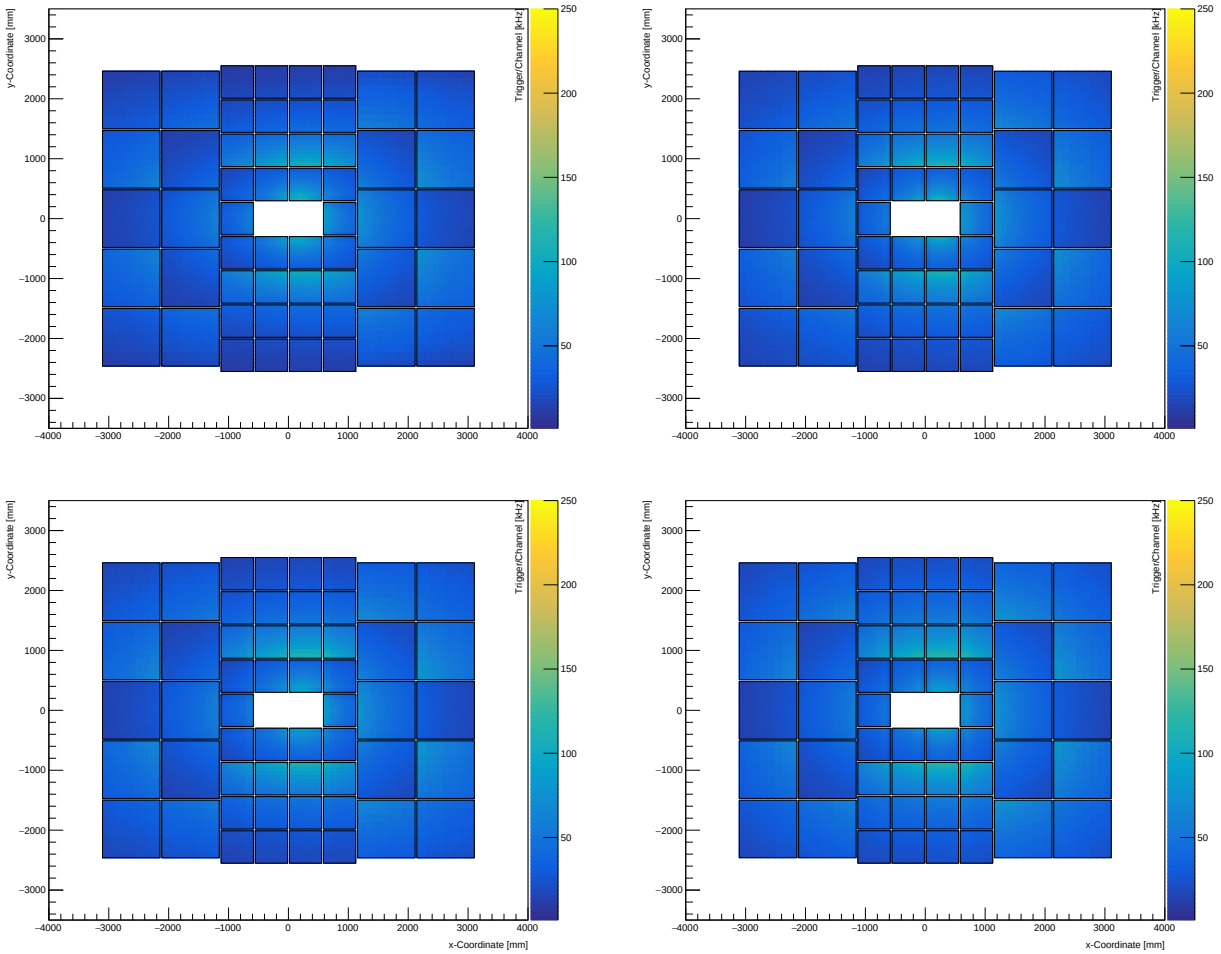

Figure 4.9: Average hit rate for minimum bias Au + Au events at 10 AGeV, scaled to an interaction rate of 10 MHz. Shown are simulations for layer 1 (upper left), 2 (upper right), 3 (lower left) and 4 (lower right). The coordinate system covers a range of ± 6 m in x- and ± 5 m in y-direction. Forced neighbor readout is included. The color scale represents the mean hit rate and is:
dark blue: $0 - 25$ kHz, blue: $25 - 75$ kHz, cyan: $75 - 125$ kHz, green: $125 - 175$ kHz, ocher: $175 - 225$ kHz, yellow: $225 - 250$ kHz, red: > 250 kHz.

4.5 Test beam results

In the following we present some results from the test beam campaigns performed with a mixed electron and pion beam at the CERN-PS, a heavy-ion beam at the CERN-SPS and at the Gamma Irradiation Facility GIF++ at CERN. They illustrate the performance of the TRD prototypes in terms of position resolution (CERN-PS) and in a high multiplicity environment (CERN-GIF++ and CERN-SPS).

4.5.1 Tests with electron and pion beams (CERN-PS)

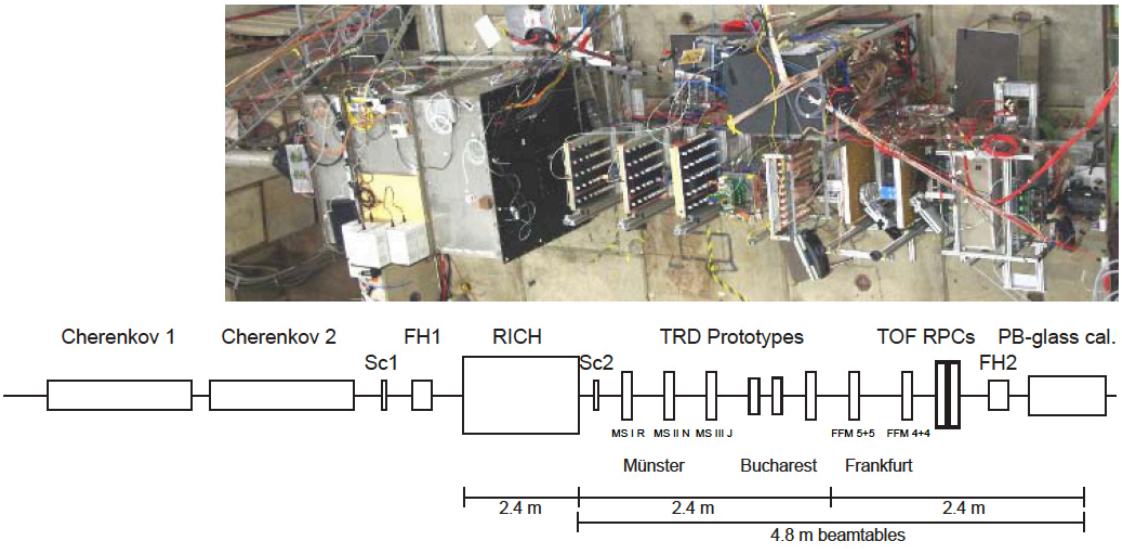

Figure 4.10: The test beam setup in 2012 at the T9 beam line at the CERN-PS. The photo has been rotated and shifted to match the sketch below. The beam is coming from the left through the second Cherenkov counter passing the first scintillator and the first fiber hodoscope. The first detector prototype in beam direction is a RICH prototype followed by the second scintillator. following downstream are eight TRD prototypes from Münster, Bucharest and Frankfurt. The last prototype detectors are two TOF RPC detectors from Bucharest followed by the second fiber hodoscope and the Pb-glass calorimeter.

The performance of several radiator options (for a discussion of the results see Sect. 6.3.1), as well as the position resolution of the small detector prototypes has been investigated during an in-beam test with electrons and pions at various momenta from the CERN-PS/T9 in a setup that included several other detector prototypes (RICH, TRD and TOF), and was thus quite similar in terms of material budget to the final the CBM SIS100 electron setup. The full setup is shown in Fig. 4.10 and was composed of the following detectors: two fiber hodoscopes (position reference), two air Cherenkov detectors, one CO_2 RICH prototype, six TRD and two TOF RPC prototypes, as well as one Pb-glass calorimeter (PID reference). The TRD prototypes were early versions of the small modules ($57 \times 57\,\mathrm{cm}^2$) and operated with a Xe/CO_2 (80/20) gas mixture (high voltage settings: anode 1775 V, drift -500 V). The readout electronics employed the first SPADIC prototype v0.3 in combination with triggered stand-alone DAQ system.

The position resolution has been estimated using an one-dimensional linear tracking algorithm based on the information from the two fiber hodoscopes and two TRD prototypes with the same pad plane orientation. The results are presented in the left panel of Fig. 4.11 as function of the beam momentum for a beam composed of electrons, muons and pions (open circles) and

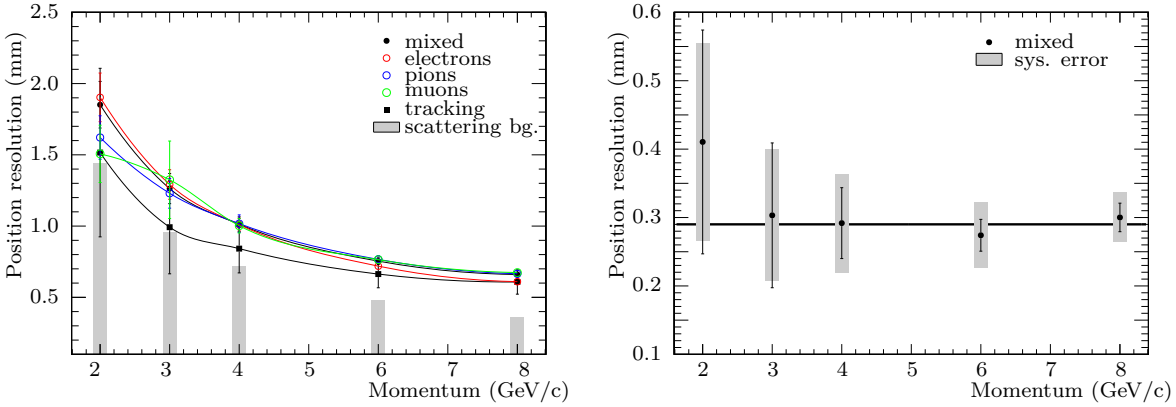

Figure 4.11: Left: Position resolution as function of particle momentum at an anode voltage of 1775 V and a drift voltage of 500 V determined via a PRF fit for different beam particles. The values represented by the squares include a misalignment compensation. Right: Position resolution using a PRF fit for the mixed particle beam after a misalignment correction and subtraction of the multiple scattering component (see text for details).

the mixed beam (black circle). The values for the position resolution were estimated with a linear track fit data from the two fiber hodoscopes as external position reference. The black squares show the results of the track fit including an iterative misalignment compensation based on the residuals seen in the first two identical TRD prototypes. An estimation of a homogeneous radiation length equivalent to the material present in the setup between the two hodoscopes (shown as gray boxes) was calculated using the modified Highland-Lynch-Dahl approximation:

$$\Theta_{\text{proj}}^{\text{rms}} = \frac{13.6\,\text{MeV}}{p\,\beta c}\, z \sqrt{\frac{X}{X_0}} \left[1 + 0.038 \ln\left(\frac{X}{X_0}\right)\right] \tag{4.1}$$

Here $\Theta_{\text{proj}}^{\text{rms}}$ is the width of the projected angle distribution (which has an approximately Gaussian distribution for small scattering angles), p, βc and z are the momentum, velocity and charge number of the incident particle, and X/X_0 is the true path length in units of radiation length.

A detailed simulation has been performed to estimate the broadening of the residual distribution measured in the detectors under test. The residuals have been calculated assuming a linear particle tracking. The material budget of the individual detector modules has been calculated as input for the simulation. The resulting contribution from multiple scattering is displayed as the gray boxes in the left panel of Fig. 4.11, while the right panel shows the unfolded position resolution after separating the scattering component. The resulting position resolution is in good agreement with 300 µm within the uncertainties over the full momentum range (see right panel of Fig. 4.11). This result agrees with the expectation from the full detector simulation as shown in Fig. 9.13, see Sect. 9.3.3.2.

4.5.2 Tests with heavy-ion beam (CERN-SPS)

During the CERN-SPS/T2-H4 high rate test beam, using Pb + Pb collisions at 30 AGeV, a setup combining two small type (i.e. $57 \times 57\,\text{cm}^2$) ROC prototypes was operated (the experimental setup is shown in Fig. 4.12). As gas mixture Ar/CO_2 (80/20) was used (high voltage settings: anode 1850 V, drift −500 V). The combination of the Pb-beam with a thick Pb-target allowed to generate hit rates of maximally ~ 2 kHz within the TRD chambers. A set of 32 channels grouped

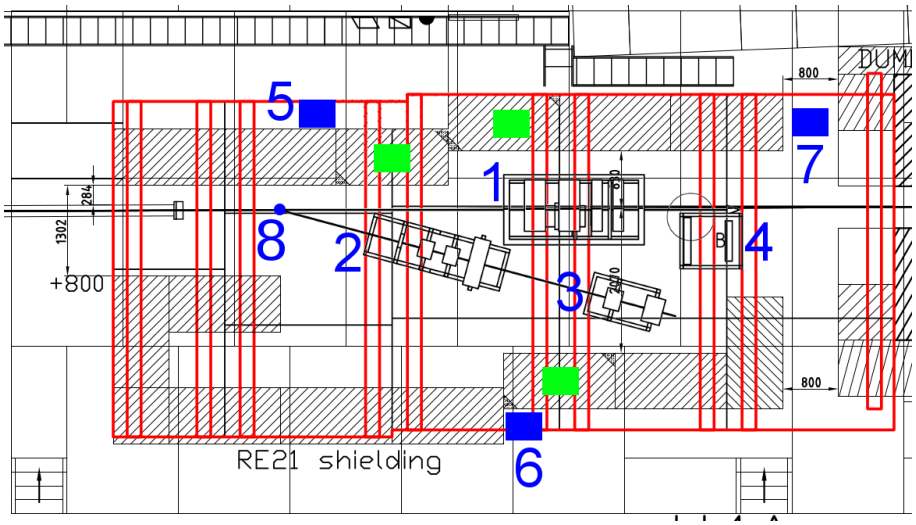

Figure 4.12: Sketch of the test setup at the CERN-SPS/T2-H4 beam in 2015. The Pb-target is located at position 8 and two TRD prototypes at pos. 4, with the supply and readout rack at pos. 7. The rest of the setup (pos. 1, 2 and 3) comprised TOF and MUCH prototypes.

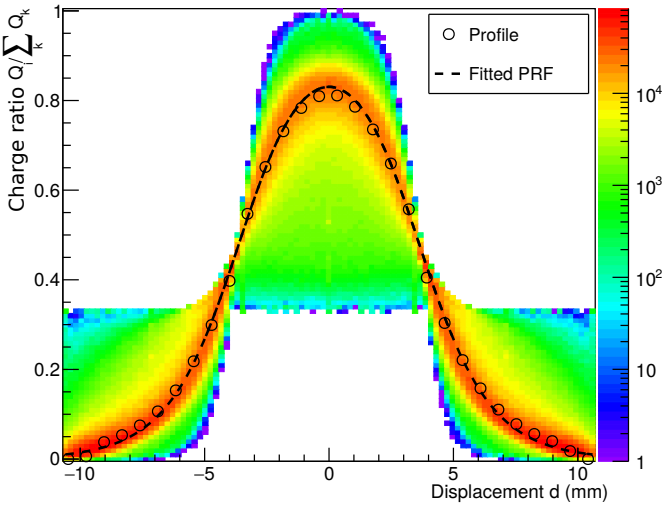

Figure 4.13: A measured PRF at the CBM high rate in beam test at CERN-SPS 2015 is presented. The one-dimensional projection of the distribution (black circles) is fitted using the Mathieson formula (Eq. 9.1). The extracted K_3 value is 0.388 ± 0.008 which is in good agreement with the theoretical prediction of 0.38 (compare to Fig. 9.5).

in 16 channels within two adjacent rows with an active area of $1\,\mathrm{cm}^2$ each have been read out per detector.

The data quality under these conditions has been assessed e.g. by comparing the measured Pad Response Function (PRF) to the theoretical prediction by Mathieson (Eq. 9.1). As shown in Fig. 4.13, a very good correspondance between the measurement and the theoretical expectation is observed, i.e. the detector performance in terms of signal-to-noise ratio and consequently the position resolution is as required. Generally, no deterioration of the data quality has been seen under the conditions present at the CERN-SPS.

4.5.3 Gamma Irradiation Facility (CERN-GIF++)

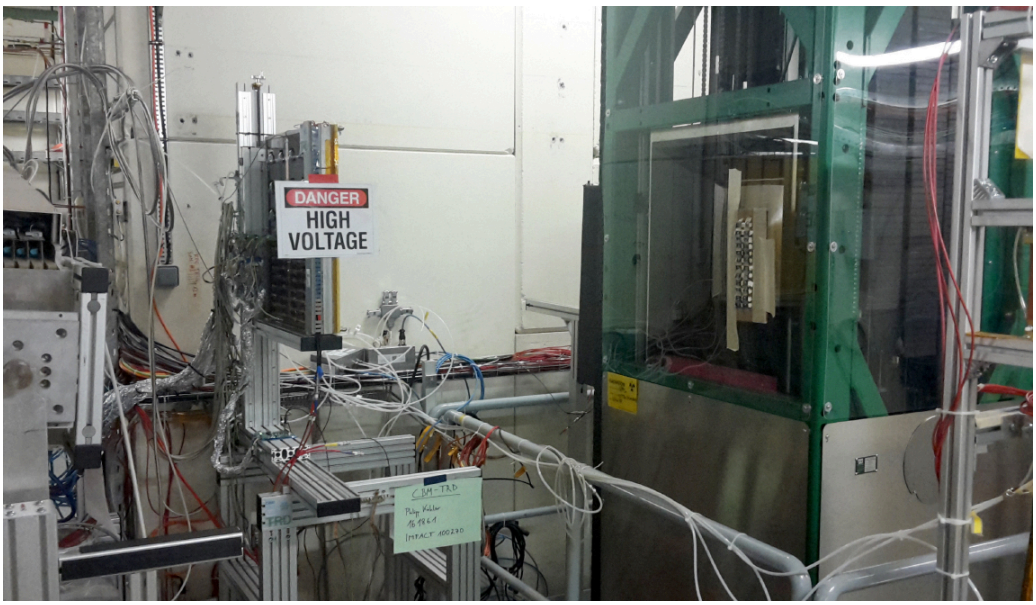

Figure 4.14: Picture of the CBM-TRD test setup at GIF++. Shown is the ROC prototype (left) together with the ^{137}Cs source (green structure on the right).

In order to study the performance of the TRD under realistic rates a dedicated test at the GIF++ facility at CERN [43] was performed in October 2017. This facility allows the irradiation of detectors by an intense (13.9 TBq) ^{137}Cs source. On top of the energy deposition due the direct absorption of the photons ($E_\gamma = 662\,\mathrm{keV}$) in the xenon gas of the TRD, charge will be released by Compton-scattering of the emitted photons in the counting gas and the detector material. The scattered electron will thus have a maximal energy of 478 keV.

Figure 4.14 shows the CBM-TRD test setup at GIF++. For this test a single small prototype chamber ($57 \times 57\,\mathrm{cm}^2$), operated with a gas mixture of Xe/CO_2 (80/20) at different anode high voltage settings, was placed at a distance of $\sim 1\,\mathrm{m}$ in front of the source. The GIF++ source provides a relatively homogeneous irradiation field in this area of the order of 10^7 photons/(cm^2 s). This photon flux can be reduced by different filters which provide a wide range of nominal attenuation factors between 1 and 46000. The TRD prototype was equipped with four SPADIC v2.0 chips, allowing to read out 128 pads, which were connected to the prototype FLES DAQ using AFCK boards (see Sect. 7.2.2).

The TRD prototype and its readout have been exposed to different levels of irradiation during the test. Irrespective of the photon flux, both, ROC and the SPADIC readout exhibited a stable performance without any directly observable problems. Please note, that the full, unattenuated photon flux already generates hit rates which are higher by more than an order of magnitude than what is to be expected during CBM operation. A more realistic scenario was achieved by

using the filter with a nominal attenuation factor of 10 (measured effective attenuation of 8.8), resulting in hit rates around $\sim 100\,\mathrm{kHz}$.

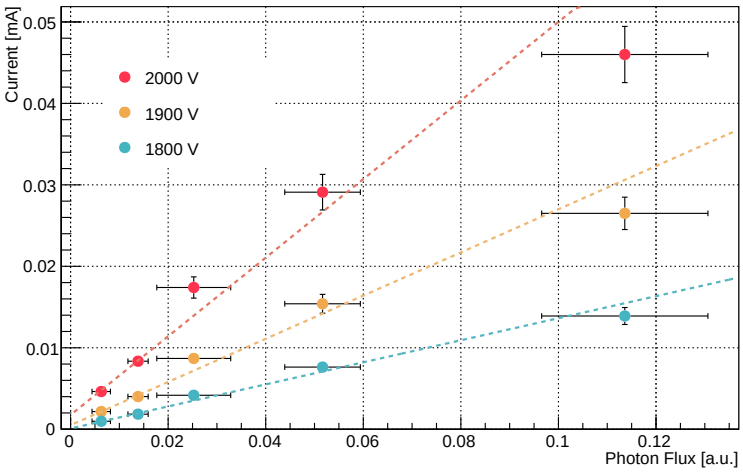

Figure 4.15: The currents measured at the anode wires for several voltages as a function of the estimated relative photon flux. The lines represent linear fits to the data points.

Figure 4.15 summarizes the measurements of the currents at the anode wires as a function of the relative photon flux calculated by using the effective attenuation factors as measured by the GIF++ crew for different filter selections [43]. Naturally, the currents increase with the irradiation level as more and more charge is released. A more solid understanding of the relation between the photon flux and the amount of charge created in the chambers will require a detailed simulation, taking into account the energy spectra of the photons and their modifications caused by the attenuation filters. Still, to first order the charge in the gas should be directly proportional to the incoming photon flux. In fact, it was found that the measured anode currents, being equivalent to the total charge after gas amplification, rise more or less linearly with the estimated relative photon flux[1]. For an anode voltage of 2000 V there might be a first indication for a less than linear increase towards the highest photon flux, corresponding to the hit rate distribution shown in the left panel, which could signal the onset of saturation effects in the gas amplification process due to space charge. However, a slight reduction of the anode voltage alleviates the effect already.

At GIF++ the performance of the detector can be further evaluated by measuring muons produced by the CERN-SPS under this high rate conditions created by the ^{137}Cs source. This requires an additional trigger in the muon beam which is currently being prepared for future measurements at GIF++ with the TRD. There it is planned to investigate the gas gain at different irradiation levels by measuring the pulse height distributions for the muon signals. GIF++ could potentially also be used to perform long term ageing tests (see Sect. 5.4.2.1).

4.5.4 Tests with electron beams (DESY)

The DESY accelerator in Hamburg allows to perform test beam experiments with electron beams of momenta between $1 - 5\,\mathrm{GeV}/c$. This facility was used in September 2017 for a systematic evaluation of the radiator performance and also to provide reliable reference data for the detailed

[1]The photon flux seen by the chambers after attenuation is relatively uncertain due to the fact that the filters strongly modify the photon spectrum and that different photon energies have substantially different absorption cross sections.

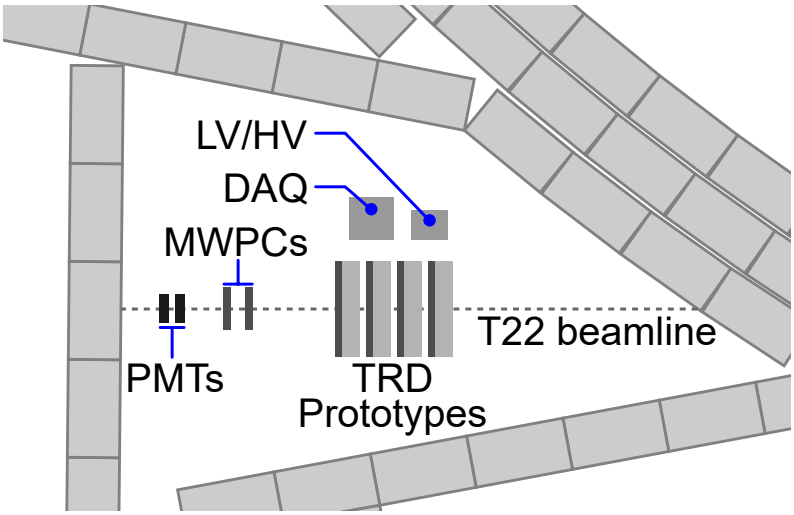

Figure 4.16: Floor plan of the setup at DESY. The beam is coming from the right. In the center the four large prototypes are shown.

detector simulation. Four large detector prototypes, measuring $95 \times 95\,\mathrm{cm}^2$ and thus being very close to the final design, have been the main part of the experimental setup (see Figs. 4.16 and 4.17). For each chamber a full size radiator made from polyethylene foam foil (radiator type H, see Sect. 6.3) has been produced. To provide a reference signal a ^{55}Fe source has been mounted close to the entrance window of the first chamber.

Further downstream two smaller MWPCs have been mounted for tracking and position resolution measurements (see Fig. 4.16), followed by two scintillation counters to allow for a measurement of the electron efficiency and energy loss spectrum. As detector gas a Xe/CO_2 (80/20) mixture was used for the four large detectors (high voltage setting: anode 2000 V, drift -500 V), and a Ar/CO_2 (80/20) mixture for the two smaller MWPCs.

At this test beam FEBs equipped with SPADIC 2.0, operated at a sampling frequency of 16 MHz, were used for data taking. Each chamber was equipped with one FEB. On the first chamber an additional FEB at the position of the ^{55}Fe source was mounted. For the readout of the scintillation counters a special FEB with LEMO connectors was manufactured. The total of eight FEBs where connected to AFCK boards via twisted pair copper wires. Each AFCK is equipped with an Xilinx Kintex-7 FPGA to emulate a GBTx. The further data transmission occurs via glass fibers to the DAQ-PC. Inside the DAQ-PC a FLES Interface Board (FLIB) transfers the data towards the First-Level Event Selector (FLES). The readout thus corresponds to the prototype layout described in Sect. 7.2.2 and was therefore involving all the essential components of the final readout chain.

For the systematic studies an electron beam with energies of 1, 2, 3 and 4 GeV was used. While the rate at 2 and 3 GeV was around 7 kHz, the measurements at 1 and 4 GeV needed more than 22 hours each to achieve the necessary statistics. The orientation of the first three chambers was chosen to be the same to allow for a measurement of the position resolution. The fourth chamber was rotated by 90° to measure the position resolution. In combination with the data from the two scintillation counters an energy dependent electron efficiency and energy loss spectrum can also be determined. The analysis of the data of this test beam campaign is currently in progress, but as an early result the measured pulse height spectra with and without radiator are shown in Fig. 4.18 in comparison. The additional contribution due to the absorption of transition radiation produced by the radiator type H (see Sect. 6.3.2) is clearly visible.

Figure 4.17: Picture of the four large TRD prototypes with radiators of type H in the experimental area at DESY.

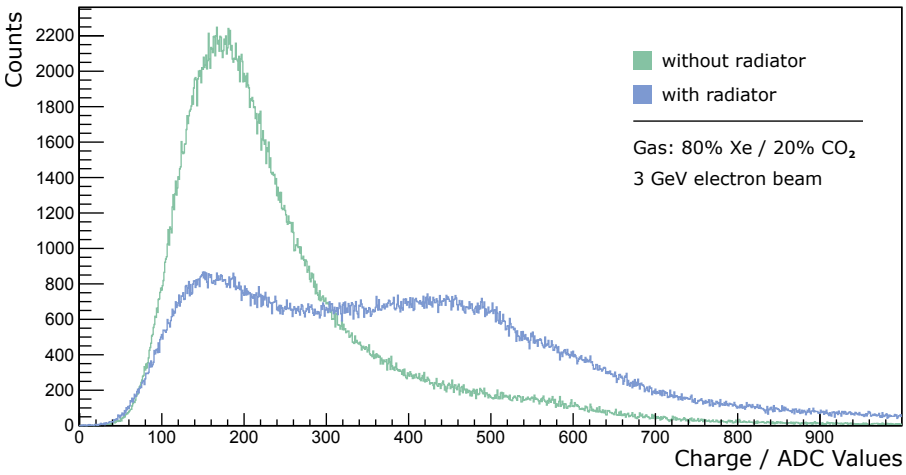

Figure 4.18: Pulse height spectra for a 3 GeV electron beam. Shown are the spectrum measured in a single detector layer with a radiator in front of the ROC (blue line) and without (green line). The additional contribution due to the absorption of transition radiation is clearly visible.

4.6 Radiation environment

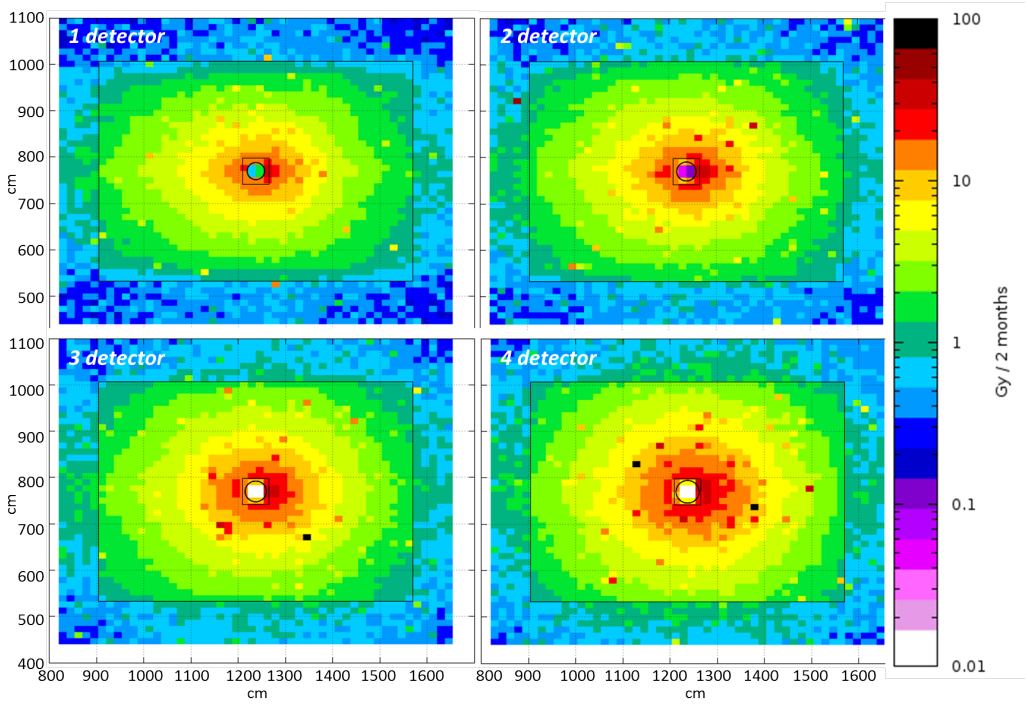

Figure 4.19: The total ionizing radiation dose expected in the four TRD layers. The calculation was performed with FLUKA [31] and corresponds to two months of Au + Au collisions at 10 AGeV with an interaction rate of 5 MHz.

The TRD will cover a region of polar angles between $\sim 3^\circ - 45^\circ$ over which the anticipated particle rates, and correspondingly also the radiation environment, changes drastically. In order to assess the radiation background in which the TRD will have to be operated, simulations using the FLUKA package [31] have been performed. The results corresponding to two months of Au + Au collisions at 10 AGeV with an interaction rate of 5 MHz are summarized in Figs. 4.19 – 4.21.

The total ionizing radiation dose is found to be below 10 Gy / (2 months) for the largest part of the detector area (see Fig. 4.19). In the innermost chambers close to the beam pipe a dose of about $20 - 40$ Gy/(2 months) might be expected. The total non-ionizing radiation dose should remain below 5×10^{11} NIEL/cm^2/(2 months) for the entire detector area (see Fig. 4.20), while the expected neutron density is not expected to exceed 2×10^{12} n/cm^2/(2 months) anywhere in the acceptance of the TRD (see Fig. 4.21).

Based on the presented simulated radiation doses, we prefer to keep the number of active electronic components as low as possible. The ASIC foreseen for the FEE, the SPADIC 2.1, is based on the UMC 180 nm technology (see Sect. 7.1) and is expected to work in the above described environment without problems.

4.7 Material Budget

The CBM-TRD is generally designed such to minimize the material inside the active area of the detector to limit multiple scattering and the production of secondary particles. This is in particular important for the matching of tracks from the TRD to the TOF, but also a prerequisite for a good performance of the TRD itself. The goal of a minimal material budget is achieved by

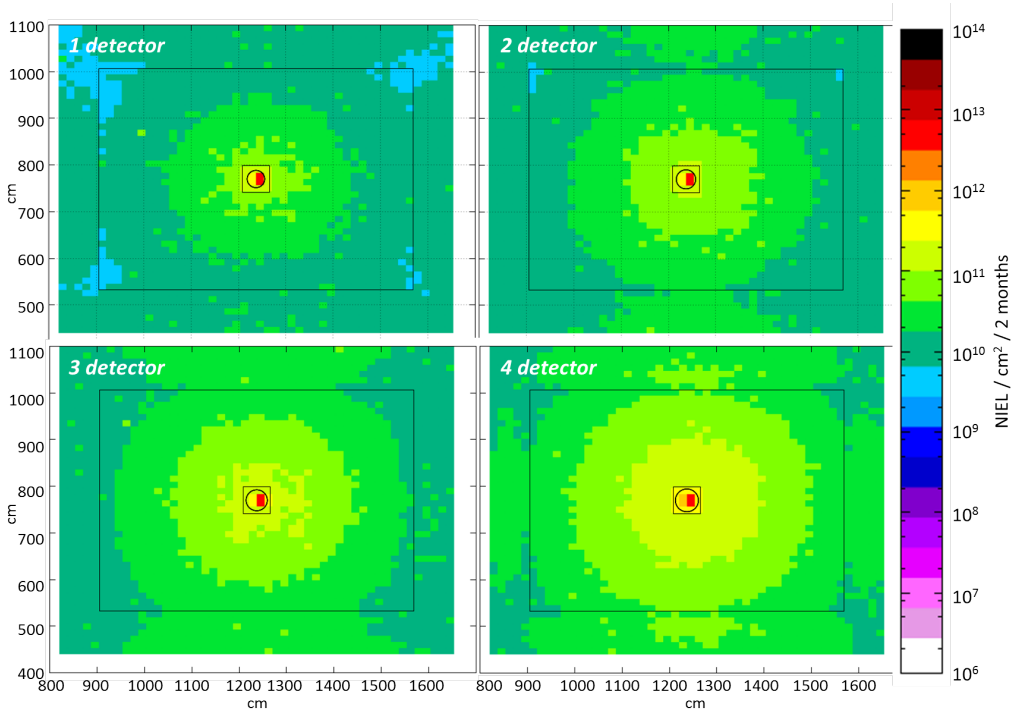

Figure 4.20: The total non-ionizing radiation dose expected in the four TRD layers. The calculation was performed with FLUKA [31] and corresponds to two months of Au + Au collisions at 10 AGeV with an interaction rate of 5 MHz.

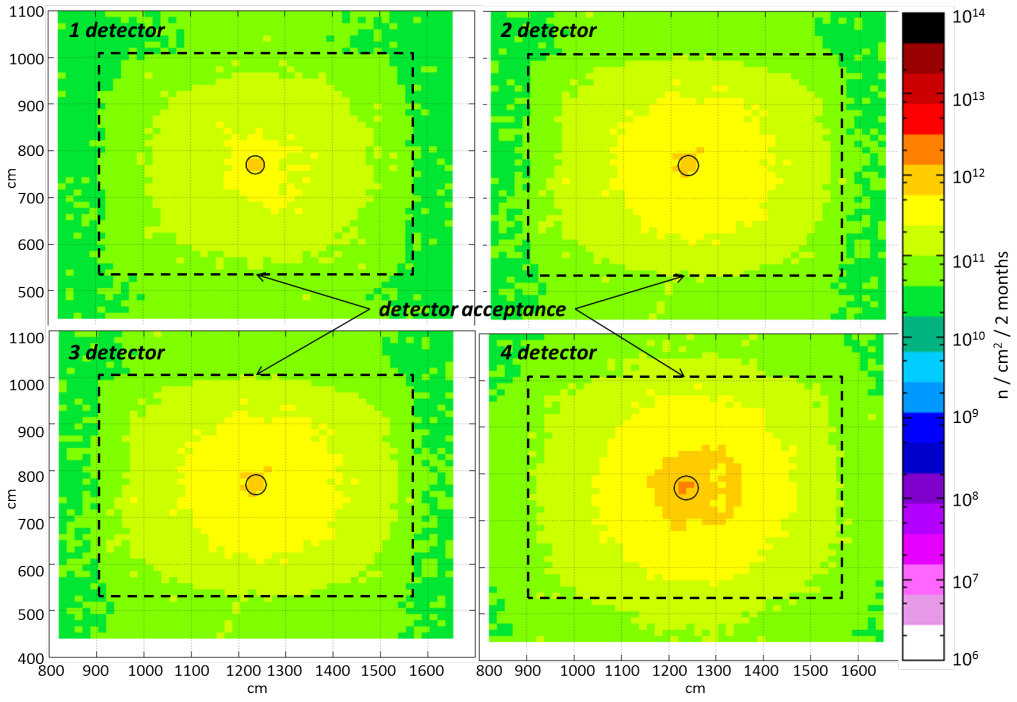

Figure 4.21: The total neutron density expected directly behind the four TRD layers. The calculation was performed with FLUKA [31] and corresponds to two months of Au + Au collisions at 10 AGeV with an interaction rate of 5 MHz.

using thin, lightweight MWPC as described above. In the following the contributions from the different detector components are described.

4.7.1 Material in front of TRD

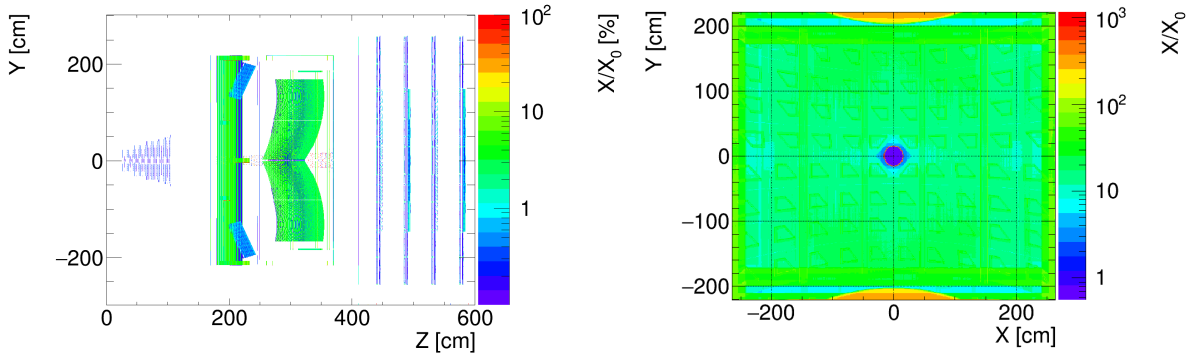

Figure 4.22: Left: the material budget distribution in y-z-direction (z = beam direction, y = vertical direction) for the four TRD layers and the detectors and support structures in front of the TRD as obtained from the CBMROOT geometry. Shown are the averaged percentages of radiation length X/X_0 calculated by following straight trajectories from the target through the TRD geometry as implemented in GEANT3. The averaging is done over ± 1 m in x-direction. Right: the integrated material budget distribution in x-y-direction. Here the integration has been performed over z covering all material in front of the TRD. x and y refer to the position of the straight trajectories on the first TRD layer.

The left panel of Fig. 4.22 presents a two-dimensional overview of the material distribution in front of the four TRD layers (displayed in the region $z > 430$ cm). Visible are, from left to right, the STS layers, the support structures of the RICH readout, the RICH mirrors and its housing. Most of the material seen by tracks entering the TRD is located in the RICH area and corresponds to $X/X_0 \sim 10\,\%$ averaged over ± 1 m in x-direction. The total material budget seen by particles following a straight trajectory before they enter the TRD is shown in the right panel of Fig. 4.22.

4.7.2 Radiator

Table 4.2 summarizes the material budget in terms of radiation length for three different radiator materials, G30, H and K++, which are under consideration. The baseline TRD design will employ the H radiator type. A detailed discussion on the various radiator types can be found in Sect. 6.3. Depending on the material and thickness of the radiator the material budget varies between $X/X_0 = 1.44 - 3.09\,\%$.

Prototype	Material	Density (g/cm^3)	Thickness (cm)	X/X_0 (%)
G30	PP fibers	0.064 – 0.074	12	1.70 – 1.96
H	PE foam	0.026	30	1.39 – 1.75
K++	POKALON		25	3.09

Table 4.2: The material budget of the different radiator options.

4.7.3 Frontpanel and gas window

A minimal amount of material between radiator and active gas volume can be achieved by using a single Kapton foil, stabilized by a CF support grid, as shown in Fig. 5.14. The resulting radiation lengths are presented in Tab. 4.3.

Material	Thickness (µm)	X/X_0 (%)
Aluminium	0.05	<0.001
Kapton	25	0.009
CF	10000	(4.215)
CF	15000	(6.323)
Sum		**0.010**
CF support grid		+ (4.215 – 6.323)

Table 4.3: The material budget of the frontpanel and gas window components.

The material budget seen by a particle passing perpendicularly through the full thickness of the CF support grid is naturally higher. However, only a very small fraction of the active area will be affected (see Fig. 5.11).

4.7.4 Gas volume

The second important component affecting the PID performance is the thickness of the active gas volume and the used gas mixture. The two noble gas mixtures which are under consideration are xenon and argon based as discussed in Sect. 5.2. The default counting gas mixture which will be used in the CBM-TRD is Xe/CO_2 (85/15), due to its higher TR-photon absorption cross section, whereas a Ar/CO_2 (80/20) mixture is used in some of the test beams and is considered as alternative for the cases where the TRD will be operated as a identification device for hadrons only (i.e. no electron-ID required) in order to reduce the costs. A total gas mixture thickness of 12 mm under operating conditions contributes with a radiation length of $X/X_0 = 0.065\,\%$.

4.7.5 Backpanel and pad plane

Material	Thickness (µm)	X/X_0 (%)
Honeycomb	22000	0.170
Air	22000	0.007
Epoxy	100	0.028
CF sheet	2×300	0.253
FR4	360	0.226
Cu	25	0.174
Aluminum frame	27000	(30.045)
Sum		**0.858**
Aluminum frame		+ 30.045

Table 4.4: Radiation lengths of the backpanel and pad plane components.

The radiation length for each subcomponent as well as the total radiation length in different regions of the backpanel (with and without aluminum frame) are listed in Tab. 4.4. The backpanel thus contributes the highest amount of material to the budget of a ROC (without radiator), while the gas window and the gas itself can be rather neglected.

4.7.6 Front end electronics

The FEBs can be installed at the backpanel with different tilting angle α, which will depend on the available space on a given module. Therefore, the amount of material introduced by the FEBs, as seen by a particle passing through a TRD module with perpendicular incidence angle, will depend on α and is listed in Tab. 4.5. The minimal and most uniform material distribution will be achieved when the FEBs are installed flatly on the backpanel (i.e. $\alpha = 0$) with $X/X_0 < 1.1\,\%$, as it is foreseen as default solution. Due to the requirements for cable routing and cooling tilting angles $\alpha > 0$ might be necessary. If the angle can be limited to $\alpha \leq 45^{\circ}$, this would imply only a moderate increase in radiation lengths to $X/X_0 \leq 1.51\,\%$. Larger angles, however, should be avoided since this would result in localized areas with relatively large material budget. The extreme case is $\alpha = 90^{\circ}$, which corresponds to $X/X_0 = 52.13\,\%$ at the FEB mounting positions but no material in the largest fraction of the active area.

Material	α (deg)	Thickness (cm)	X/X_0 (%)
FR4	0	0.170	1.068
	10	0.173	1.084
	45	0.240	1.510
	90	8.300	52.127

Table 4.5: Radiation lengths of the FEBs as function of their installation tilting angle α, estimated for perpendicular tracks.

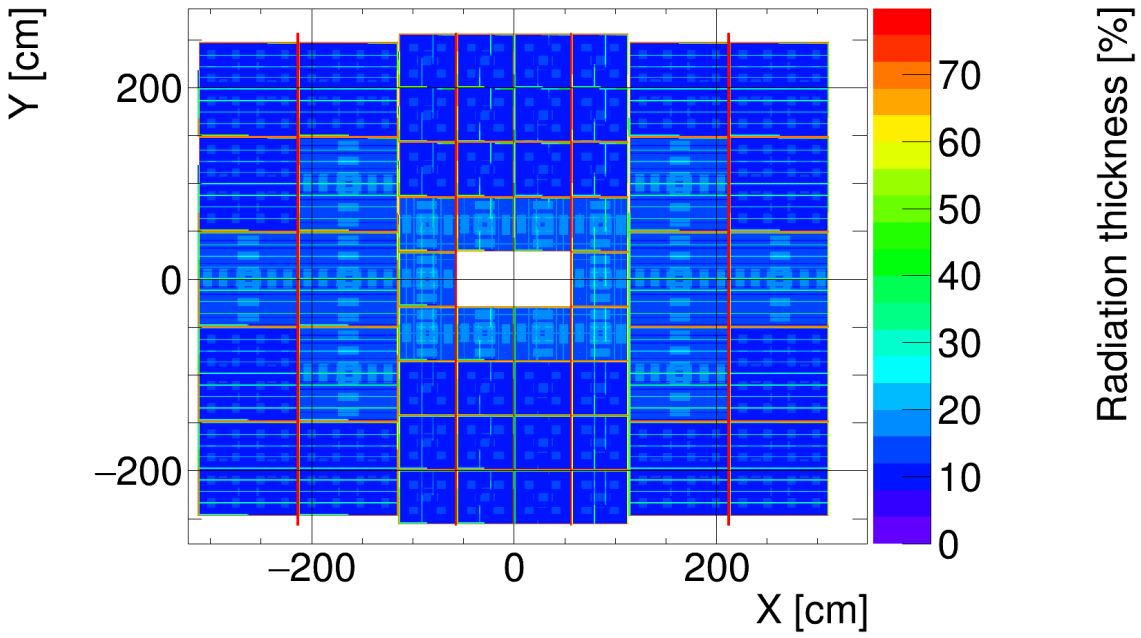

Figure 4.23: The material budget distribution for four layers of TRD-ROCs as obtained from the CBMROOT geometry. Shown are the percentages of radiation length X/X_0 calculated by following straight trajectories from the target through the TRD geometry as implemented in GEANT3.

4.7.7 Support structure

It is planned to construct the support structure from aluminum profiles of minimal cross section to keep the additional material as low as possible (see Sect. 8.2). Optionally, parts of the structure can be made of carbon sheets to reduce the material budget even further. Overall, the support structure will add not more than $X/X_0 = 40\,\%$ to the budget in very small and localized areas only, which is in the same order than the contribution of the ROC frames.

4.7.8 Total material budget

The total material budget of one detector layer inside its active region, including the default radiator H, varies therefore between a minimum of 2.33 – 2.69 % (empty regions between the CF grid) and 6.54 % (small module CF grid), respectively 8.65 % (large module CF grid) for particles passing perpendicularly through the full grid thickness. To this the material of the FEBs has to be added which amounts to $X/X_0 = 1.07\,\%$ for a default mounting angle of $\alpha = 0^{\circ}$. Thus, inside the active detector (CF grid excluded) area the material budget remains with maximally 3.8 % clearly below the design requirement of 5 % (see Tab. 2.1).

The chamber frame adds 43.58 % per detector layer in localized outer areas of the modules. A parallel projection of the material budget including the FEB material is presented in Fig. 4.23. In the largest fraction of the TRD area the budget is relatively moderate ($X/X_0 < 10 - 20\,\%$ for four layers) and well within specifications. Due to the non-projective arrangement of the modules in the different TRD layers, the material of the module frames and of the CF support grids is not seen under the same angles and is thus distributed over the whole detector area.

The total material budget of the TRD with four layers as shown in Fig. 4.23, averaged over the whole detector area, i.e. including ROC frames, but without support structure, is estimated as $X/X_0 = 19.4\,\%$.

Chapter 5

Readout Chamber

This chapter summarizes the design of the Read-Out Chambers (ROCs). It will be based on a Multi-Wire Proportional Chamber (MWPC) with an amplification region of 3.5+3.5 mm thickness, combined with a thin drift region (5 mm thickness) separated by a cathode wire plane. The entrance window to the drift region is defined by a aluminized foil, which also serves as cathode for the drift field. On the backpanel of the ROC a pad plane will be mounted, where the charge induced by the gas amplification around the anode wires is collected. Via the segmented pads a precise reconstruction of the position of the ionization processes is possible.

5.1 Parameters of ROC operation

Parameter	Default value
Leakage rate	< 1 ml/h
Signal-to-noise ratio (MIP)	≥ 30:1
Maximal signal collection time	0.3 µs
Drift field	1 kV/cm
Drift velocity (Xe/CO_2 (85/15))	3 cm/µm
Anode voltage (Xe/CO_2 (85/15))	1850 V
Anode voltage (Ar/CO_2 (80/20))	1800 V
Drift voltage	-500 V
Gas gain	~ 2000
Maximal gas pressure variation	± 1 mbar

Table 5.1: Summary of the operation parameters of the ROCs.

The main parameters relevant to the operation of the ROCs are summarized in Tab. 5.1. The gas gain is mainly determined by the anode voltage and the used gas mixture, as shown in the left panel of Fig. 5.1. Since electron identification is the main purpose of the TRD, the most important aspect in terms of stability is the need to reduce gain variations during data taking to a minimum. Therefore, the gas gain should be kept stable at least within ± 10 %, which in turn means that the differential gas pressure needs to be kept stable within ± 1 mbar (see discussion in Sects. 5.4.1 and 5.4.3). Also, the gas temperature needs to be controlled such that the gas gain is not affected too much. However, as illustrated in the right panel of Fig. 5.1, the temperature dependence is relatively weak such that it is sufficient to limit its variations to a few degrees K.

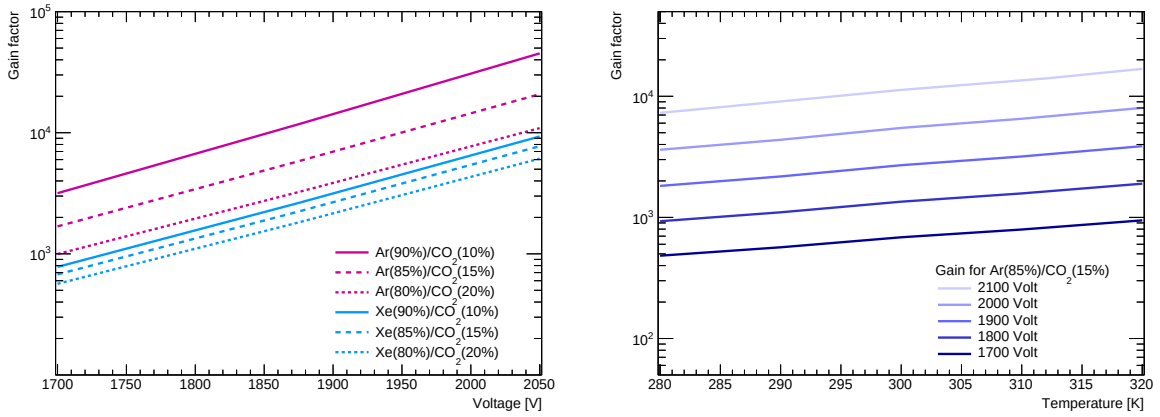

Figure 5.1: The gas gain as a function of the anode voltage (left panel) and of the gas temperature (right panel) as calculated with GARFIELD [44] for the default ROC geometry ($3.5 + 3.5$ mm amplification and 5 mm drift region) and for different gas mixtures.

5.2 Gas mixture

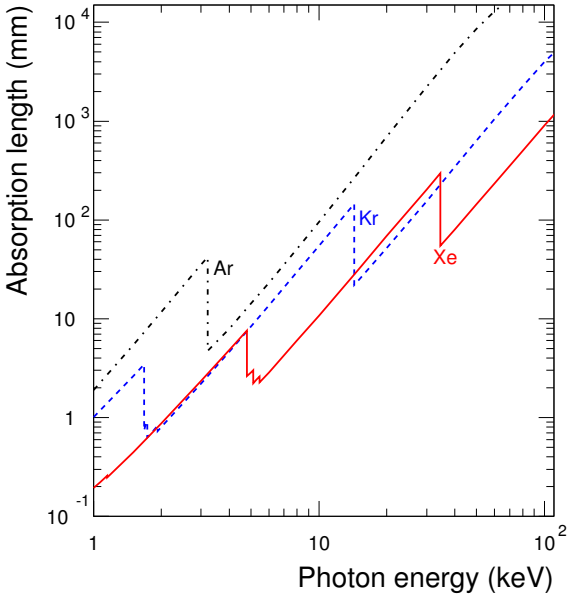

Figure 5.2: The X-ray absorption length in different noble gases [45].

In the standard operation scenario of the CBM-TRD a mixture of 85 % xenon and 15 % CO_2 is foreseen as counting gas. A sufficiently short absorption length for the TR-photons produced in the radiator is mandatory in order to achieve an efficient electron identification with gas detectors of limited thickness. From the comparison of X-ray absorption lengths of different noble gases, shown in Fig. 5.2, it is obvious that this goal can only be achieved with xenon as the main gas component. For a typical TR-photon energy below 10 keV xenon has an absorption length of less than 10 mm. Therefore, a MWPC with a gas thickness of similar dimensions is able to absorb the bulk of the photons, if the TR-spectrum is not too hard. A detailed discussion on the TR-photon absorption probabilities and the TR-photon spectra (see e.g. Fig. 6.3) can be found in Sect. 6.1.2. The transmission probability of argon and xenon gas mixtures (85 % noble

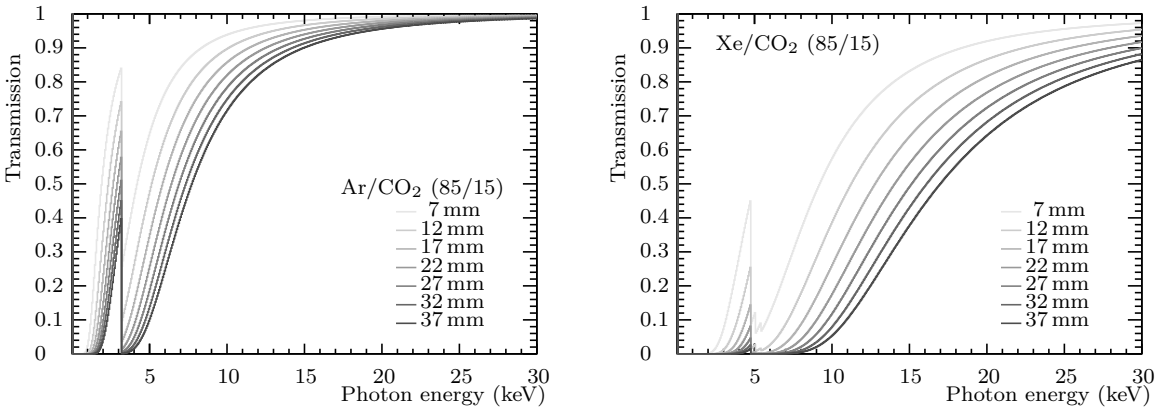

Figure 5.3: Transmission probabilities for argon (left) and xenon (right) based mixtures (85 % noble gas and 15 % CO_2) of different gas thicknesses: 7, 12, 17, 22, 27, 32, and 37 mm.

gas and 15 % CO_2) at different thicknesses are presented in Fig. 5.3.

The technical properties of the Xe/CO_2 gas mixture are discussed in Sect. 8.3.1. Two other important aspects are illustrated in Fig. 5.4: the drift velocity and the diffusion coefficients. It should be pointed out, that in [45] no significant dependence of neither the drift velocity, nor of the diffusion coefficients on the magnetic field was observed up to $B = 0.6$ T. Therefore, the simulations shown in Fig. 5.4 can also be applied to the CBM-TRD which is operated outside of the magnetic field.

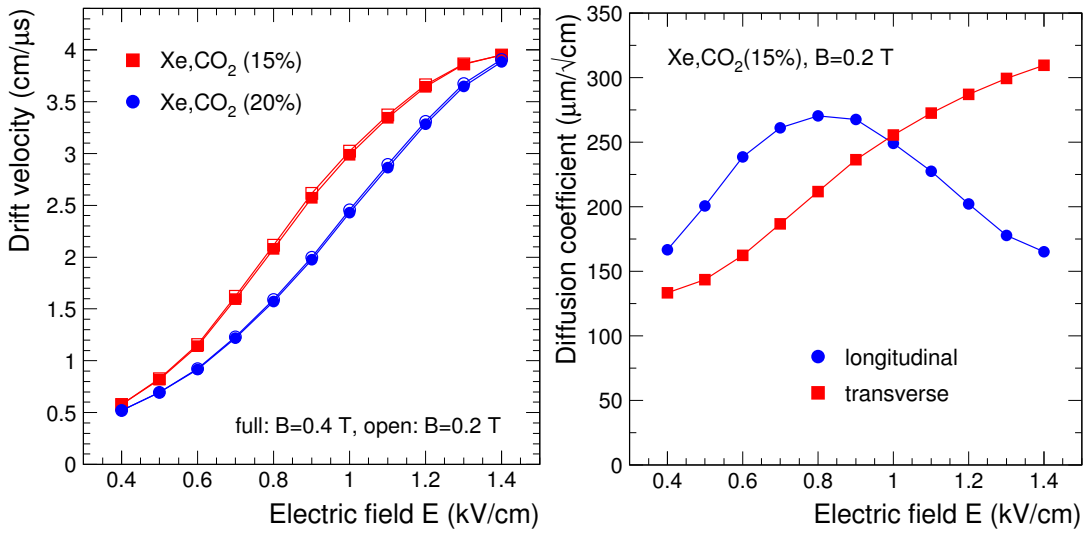

Figure 5.4: The drift velocity (left) and the diffusion coefficient (right) for Xe/CO_2 mixtures as calculated with GARFIELD for different electric drift fields [45].

For a default drift field of 1 kV/cm a drift velocity v_D of about 3 cm/µs can be expected for Xe/CO_2 (85/15). A high drift velocity is advantageous for the CBM-TRD, since the high interaction rates require short signal collection times. Since the TRD is not going to be operated as a real drift chamber, i.e. the drift time information is not being used in the space point reconstruction, a precise knowledge of v_D is not required, which facilitates the operation and calibration of the TRD.

At the default drift field of 1 kV/cm the diffusion coefficients are expected to be about 250 µm/$\sqrt{\text{cm}}$, both in longitudinal and in transverse direction, see right panel of Fig. 5.4. For

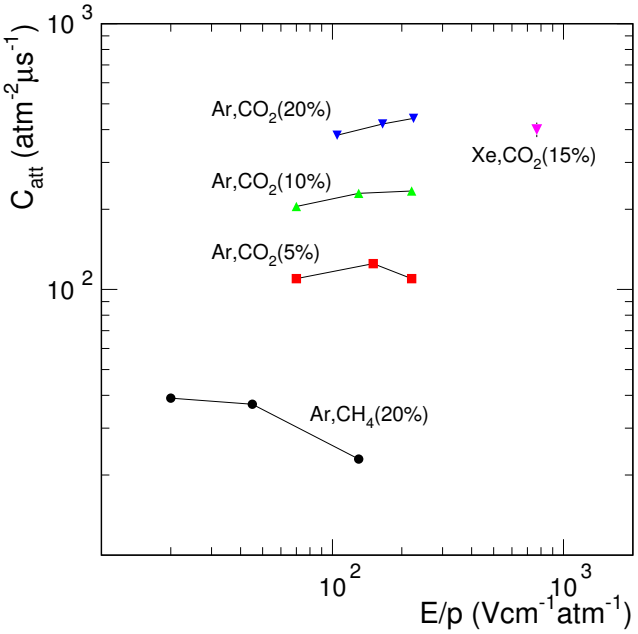

Figure 5.5: The electron attachment coefficient as a function of the reduced drift field for different gas mixtures [45].

the foreseen drift length of 0.5 cm this corresponds to maximum spread of an initially point-like electron cloud of $\sim 180\,\mu$m, which is small enough to not affect the position resolution and the signal shape.

The electrons produced in the ionization processes can be absorbed by gas impurities during their drift to the amplification region. In particular oxygen is of relevance here due to its electronegativity. The resulting signal loss follows an exponential behavior as function of drift time t_D and depends on the total gas pressure p, as well as the oxygen partial pressure $p(O_2)$:

$$N(t_{\text{drift}}) = N(0) \cdot \exp(-p \cdot p(O_2) \cdot C_{\text{att}} \cdot t_D) \tag{5.1}$$

Figure 5.5 summarizes the electron attachment coefficients C_{att} measured for different gas mixtures [45]. It is relative large for CO_2 mixtures due to its large number of low lying excitation levels. However, since the drift times in the CBM-TRD are short ($t_D < 0.2\,\mu$s), the resulting effect on the signal height will be only 1 % or less (for $C_{\text{att}} = 400\,\text{atm}^{-2}\mu\text{s}^{-1}$ and assuming $p(O_2) = 100\,$ppm).

5.3 Design optimization

The layout of the ROCs has been optimized based on results from test beam measurements at the CERN-PS. The measured electron and pion energy loss spectra have been used to estimate the full system performance within a simulation as a function of the number of detector layers and the total thickness of the Xe/CO_2 gas volume. The results are presented in Fig. 5.6 for an extended version of the default radiator solution H, labelled H++ (see also Sect. 6). The simulated dE/dx spectra have been tuned to in-beam test results measured with a TRD prototype comprising a 12 mm thick gas gap. Please note that the absolute values for the pion suppression in a more realistic environment, where also not every track has four points attached, are slightly lower than the values shown in Fig. 5.6 (see Tab. 9.1). Increasing the thickness further by additional 10 mm leads to a very moderate improvement of the pion suppression. However, regarding the fact that thicker gas volumes also cause an significant increase in signal collection time (see Fig. 5.7)

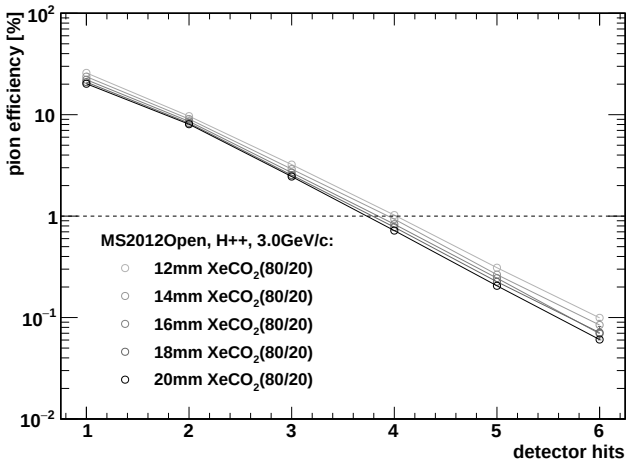

Figure 5.6: Simulated pion efficiency at 90 % electron efficiency as a function of the gas gap thickness, filled with $Xe/CO_2(80/20)$, for different number of TRD layers.

this is not a viable option in a high counting rate environment. Therefore, a gas thickness of 12 mm, subdivided into 7 mm amplification and 5 mm drift regions, has been identified as the best compromise.

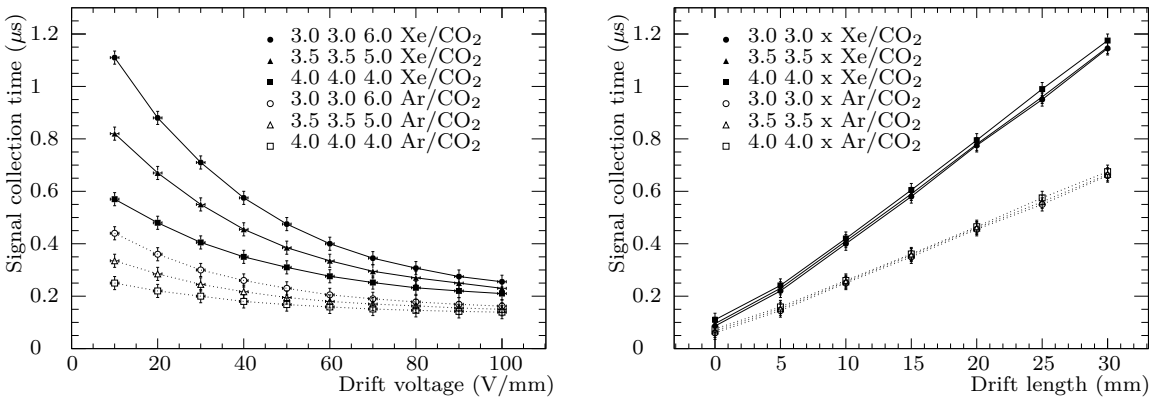

Figure 5.7: Signal collection time for a simulated electron signal as calculated with GARFIELD [44]. Data for Xe/CO_2 (80/20) are represented by filled symbols and for Ar/CO_2 (80/20) by open symbols. An anode voltage of 1675 V is applied for the geometries with $3.0 + 3.0$ mm thick amplification regions, 1800 V for those with $3.5 + 3.5$ mm thickness, and 1925 V for those with $4.0 + 4.0$ mm. The drift voltage scan is shown on the left and the drift length scan at 100 V/mm on the right hand side.

5.4 ROC design

The layout of the pad plane foresees rectangular pads, whose widths along a pad row (direction along the wires) are determined by the fixed distance between the pad plane and the anode wire grid. This way the pad response function can be adjusted such that it ensures an optimal charge distribution on adjacent pads (10 %/80 %/10 %) and thus a good energy and position resolution. In addition, the fixed pad width minimizes the numbers of different layouts of the FEBs. The

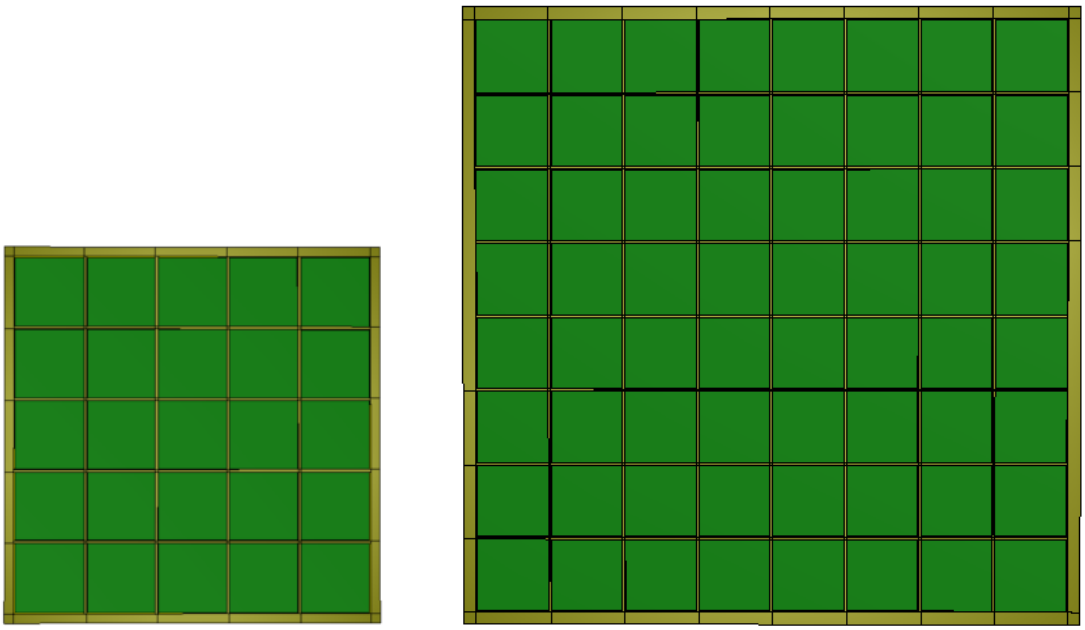

Figure 5.8: Sketch of a small (left panel) and large (right panel) CBM-TRD ROC (front view). The outer dimensions are $57 \times 57\,\mathrm{cm}^2$ for small and $99 \times 99\,\mathrm{cm}^2$ for large types. Shown here is the implementation of the module geometry in the simulation framework.

various pad sizes have therefore to be realized by scaling the long edge of the pads (i.e. orthogonal to the wires) accordingly. In this direction the position resolution will thus effectively be limited to the pad dimension, since the charge sharing between pad rows is marginal, at least for the larger pad sizes implemented in the outer detector regions. Therefore, it is foreseen to rotate the modules by 90° between each detector layer in order to achieve a good position resolution in x and y direction. However, this requires a quadratic shape of the TRD modules, if the number of different module types is supposed to be kept minimal.

5.4.1 MWPC description

A MWPC design with additional drift region is chosen as the default solution for the ROCs of the CBM-TRD. The additional drift region ensures a high TR absorption probability and it provides a higher gain stability of the ROC under external pressure variations. At the same time it allows to keep the size of the induced charge clusters small, which is determined by the distance between the anode wire plane and the readout electrode. A small cluster size is of special importance in the high occupancy environment of CBM. A potential drawback of a drift detector is a reduced signal collection speed (for electrons it is 0.1 µs for a symmetric $3.5 + 3.5$ mm MWPC and additional 0.125 µs in a 5 mm drift region with 100 V/mm field, see Fig. 5.17) and a possibly increased accumulation of space charge compared to a MWPC without drift region. Nevertheless, a signal collection time of below 0.3 µs should in any case be sufficient at trigger rates of ~ 100 kHz in the most inner part of the detector with a readout pad area of $1.2\,\mathrm{cm}^2$, corresponding to an average trigger separation in time of 10 µs. Therefore, the proposed ROC design should fulfil the requirements in terms of readout speed in all possible cases.

Figure 5.8 shows a front view sketch of a small and a large ROC, while Fig. 5.9 presents a

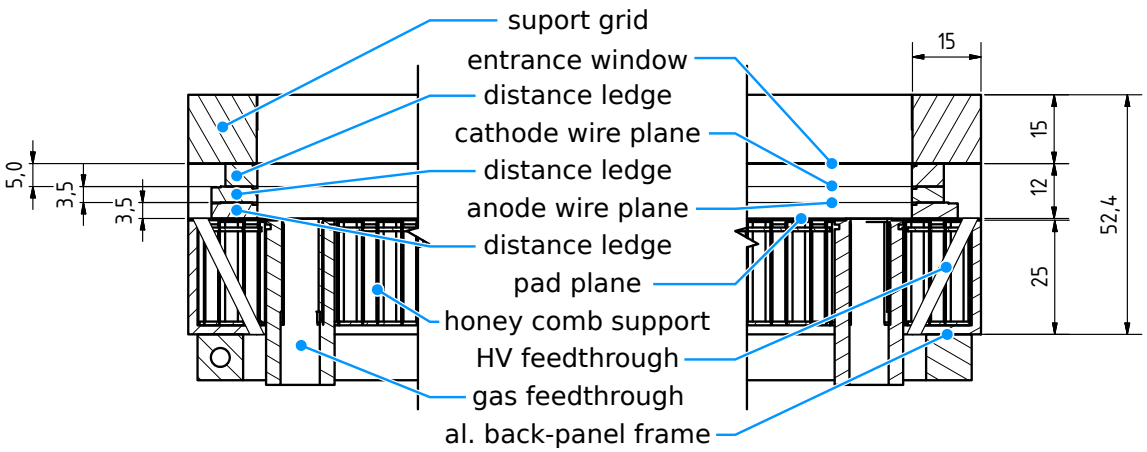

Figure 5.9: Cross section of the outer parts of a CBM-TRD ROC. All dimensions are in millimeter.

cross section of the outer region of one ROC together with the corresponding dimensions and positions. Shown are the different components, such as the honeycomb structure, the pad plane and the aluminum frame, which together form the backpanel, the different wire distance ledges together with the cathode and anode wire planes, and the entrance window with the carbon fibre support structure. The full chamber layout for a large module type is illustrated in Fig. 5.10 and the dimensions and basic parameters are summarized in Tab. 5.2.

ROC type	small	large
Module type	1, 3	5, 7
Outer dimensions	$57 \times 57\,\mathrm{cm}^2$	$99 \times 99\,\mathrm{cm}^2$
Active area	$2916\,\mathrm{cm}^2$	$9216\,\mathrm{cm}^2$
Total thickness	49.5 mm	
Thickness amplification region	3.5+3.5 mm	
Thickness drift region	5 mm	

Table 5.2: Summary of the dimensions of the two ROC layouts.

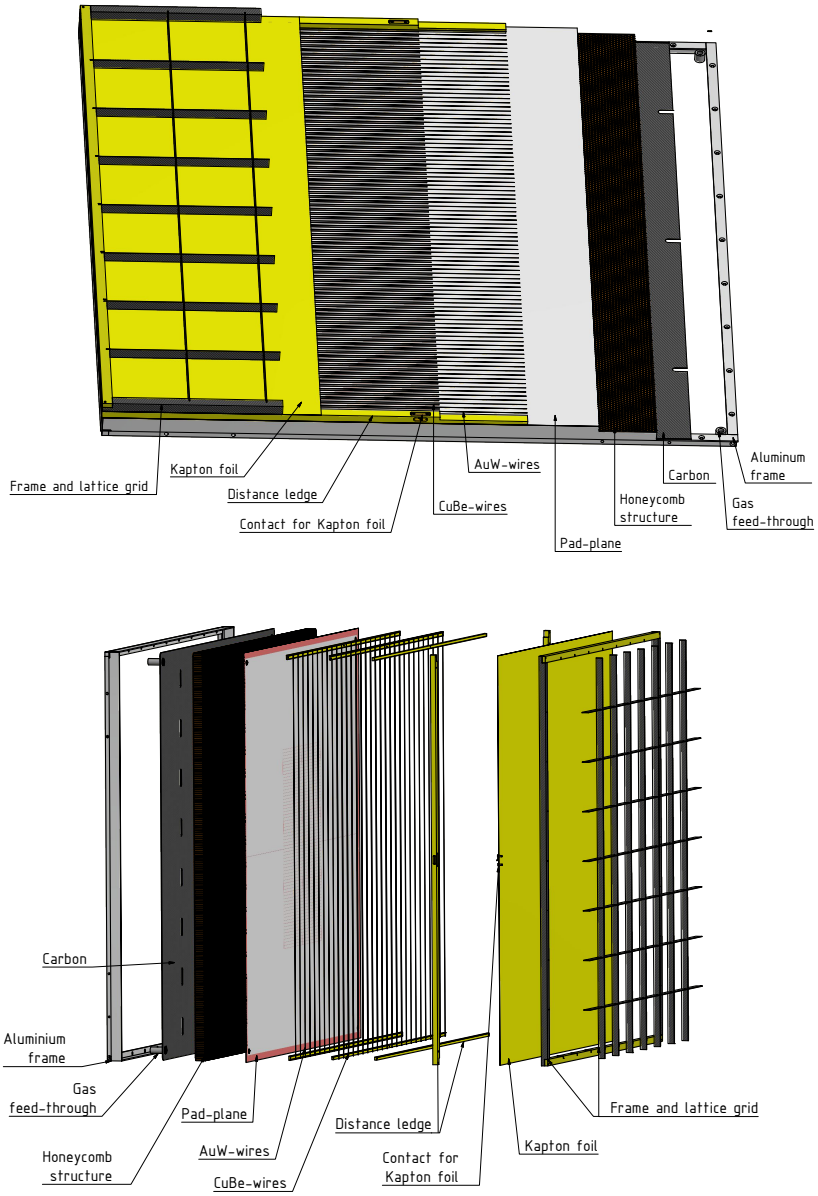

Figure 5.10: Upper panel: drawing of a full CBM-TRD ROC of the large module type. Visible are the different layers from left to right: frame and carbon support lattice, Kapton foil as entrance window, distance ledge with electrical contact for the foil, wire planes, pad plane, honeycomb structure, carbon layer, and outer aluminum frame. Also shown are the gas feedthroughs in the backpanel. Lower panel: Explosion view of the same ROC module.

The first detector component is the entrance window made from a 25 µm thick Kapton foil, coated with 0.05 µm aluminium on a single side. This foil can be stretched using a thermally expanding frame and is glued to a carbon lattice window support structure (a prototype is presented in Fig. 5.14). The production procedure is described in Sect. 5.4.2. The entrance window ensures gas tightness and acts at the same time as drift potential plane. The mechanical deformation has therefore to be limited to keep gain variations caused by pressure changes within a reasonable range. The maximally acceptable foil deflection due to an over- or under-pressure in the detector volume of 1 mbar has been estimated to be 1 mm based on GARFIELD simulations (see Sect. 5.4.3). The goal to limit the foil deflections to ±1 mm can not be reached with a single foil with a surface of up to 1 m^2 without additional mechanical support. This motivates the addition of a support grid in order to subdivide the surface into smaller areas inside which the mechanical properties of the stretched foil are sufficient to limit the deflection below 1 mm, including a safety margin for the deflection of the support structure itself. This critical size was determined in lab tests to be $10 \times 10\,cm^2$. Another important constraint for the lattice structure is that cross braces above readout pads should be avoided. For these reasons a rectangular grid design was chosen. The inhomogeneous lattice influences the PID performance in a negative way, since the parts of the active gas volume which are shadowed by it have a lower probability to be reached by TR-photons. The covered surface fraction can be reduced by using a lattice rip width as thin as 0.8 mm. The mechanical stability of the entrance window is not affected, since the stiffness perpendicular to the foil surface scales with rip height, which is 10 mm (15 mm) for the small (large) module type. The resulting surface coverage would in this case be of the order of 1 %, but depends on the impact angle as shown in Fig. 5.11. It is the lowest for particles with an impact angle of 0 °, where the shadowed fraction of the total surface is around 1 %, and reaches a maximum value of approximately 9 % for an angle of 35 ° in the case of a large module type. Figure 5.12 shows a drawing of the currently foreseen implementation of the grid, to be manufactured from carbon fibre material.

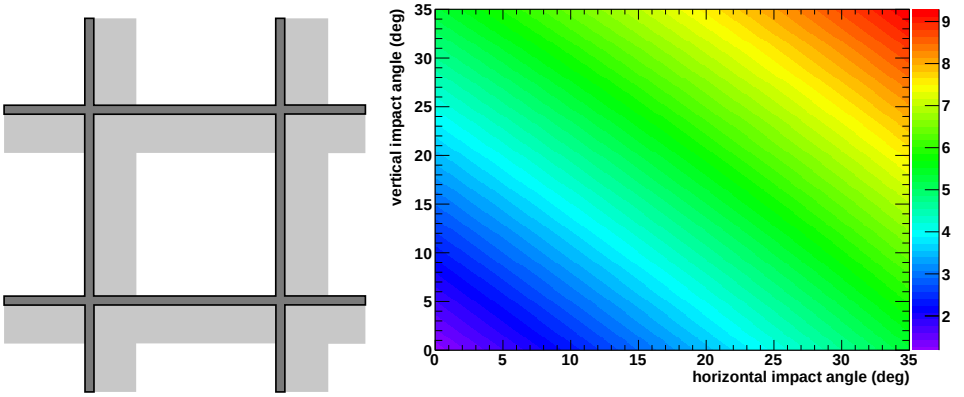

Figure 5.11: On the left side a schematic drawing of part of a support grid is shown. The dark gray area is covered by the lattice itself where the light gray area is the additionally shadowed area seen by particles coming from the upper left side. The light gray area varies as a function of the horizontal and vertical impact angle of the particle relative to the chamber surface. The shadowed active area fraction in percent calculated for one TRD module of $57 \times 57\,cm^2$ with 4×4 lattice rips of 0.8 mm width and a rip height of 10 mm as function of the horizontal and vertical impact angle is presented on the right side. The covered area is 1 % where the additional shadowed area fraction at maximum impact angles is 9 %.

The active gas volume is enclosed on the four sides by two end strips made from G11 and a stack of three wire distance ledges (5, 3.5 and 3.5 mm thick). The wire distance ledges define the

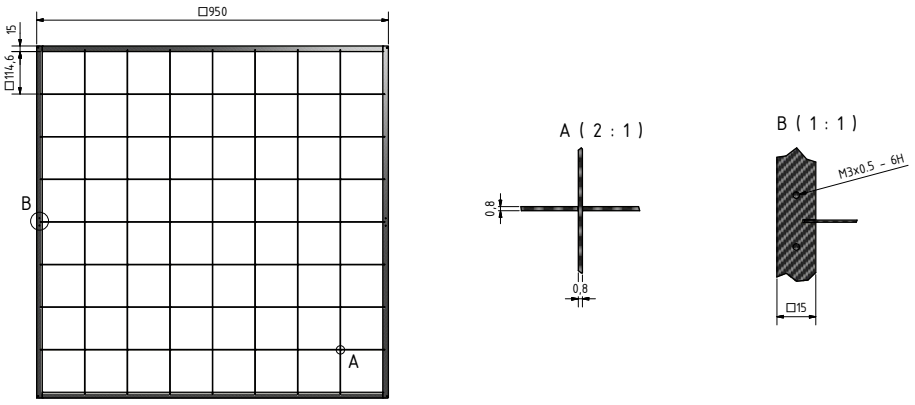

Figure 5.12: Drawing of the planned carbon support grid with a lattice rip of 0.8 mm and a height of 15 mm, as foreseen for a large module type.

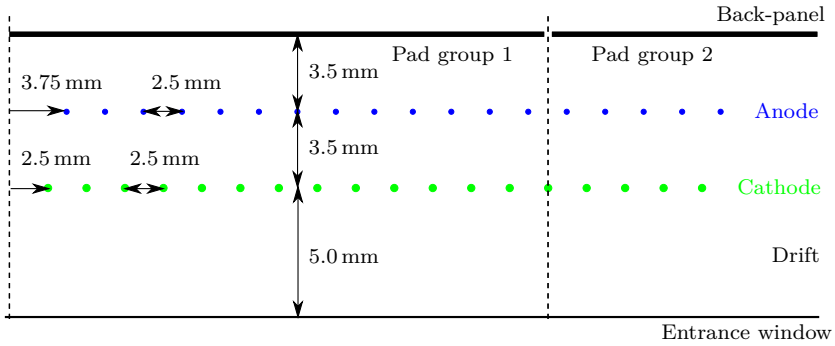

Figure 5.13: Schematic drawing of the anode and cathode wire grid positions relative to the pad plane and the entrance window.

distance between the two wire planes, whose geometrical arrangement is depicted in Fig. 5.13. A summary of a the parameters of wire planes is given in Tab. 5.3. The gas volume is closed on the bottom side by the readout electrode, the pad plane. This PCB layer is glued to a honeycomb carbon fiber sandwich [45], which is carried by an outer aluminum frame. The last two components define the mechanical stability of the detector and compensate the wire tension. The design of the detector is optimized to maximize the acceptance of each detector plane. Therefore all supplies are routed and connected from the backside of the detector, including high voltage, gas, and LV supply of the readout electronics. E.g. the gas feedthroughs are inserted into the backpanel as shown in Figs. 5.9 and 5.10.

5.4.2 ROC production

The following description of the production procedure for TRD ROCs is based on the extensive experiences with the ALICE-TRD production and on the special requirements for the construction of the prototypes for the CBM-TRD (see Fig. 5.9). The detector assembly starts with the aluminum backpanel support frame. A 23 mm thick honeycomb carbon fiber sandwich [45] is

	Anode wires	Cathode wires
Material	W (Au-plated)	Cu-Be
Diameter	20 µm	75 µm
Tension	50 – 55 cN	100 cN
Pitch	2.5 mm	2.5 mm

Table 5.3: Summary of the dimensions and parameters of the wire planes.

Figure 5.14: Gas foil window supported with the carbon lattice window support structure.

glued to this frame using Araldite AW 106 and the remaining gap between them is filled with AW 116. This combination will ensure the mechanical stability of the chamber and compensate the wire tension from the anode as well as the cathode wires. After hardening of the backpanel pad plane sandwich the missing reamed holes for the wire distance ledges and the eight anode HV cable feedthroughs are drilled next to the wire distance ledge position in regular spacing through the pad plane backpanel. The pad side of the pad plane backpanel sandwich is finally cleaned with isopropanol. The wire distance ledges are prepared with a 2.5 mm copper adhesive tape glued to the 0.2 mm deep groove on the top side. The ledges are connected to the backpanel using AW 106 and Nylon aligning pins parallel to the long pad size direction to adjust a precise distance of 3.5 mm between the pad plane and the anode wires. The anode wires (20 µm Au-plated W-wire) are winded to a wire transfer frame with a pitch of 2.5 mm and a tension of 50 – 55 cN. Technicoll is used to fix wires in position on the frame before dividing the frame in half. The wire grid is positioned and lowered to the wire ledges until the wires rest on top of the ledges. A schematic drawing of the anode and cathode wire grid position relative to the pad plane is presented in Fig. 5.13. The anode wire copper strip is subdivided into eight equal anode sectors. A thin film of AW 106 is applied on top of the wire ledges and a second wire ledge of 3.5 mm thickness is put on top of this film to keep the wires in position. The second distance ledge on the opposite side of the anode wire copper strip is prepared with another copper strip to connect the cathode wires later. After hardening of the glue the wires are soldered to the copper strip and cut off the transfer frame. The anode HV cables are coated with a thin Technicoll film and pitched through the backpanel feedthroughs. The glue film ensures gas tightness and mechanical load removal from the soldering point on the copper strip, to which the anode HV cables are soldered. The

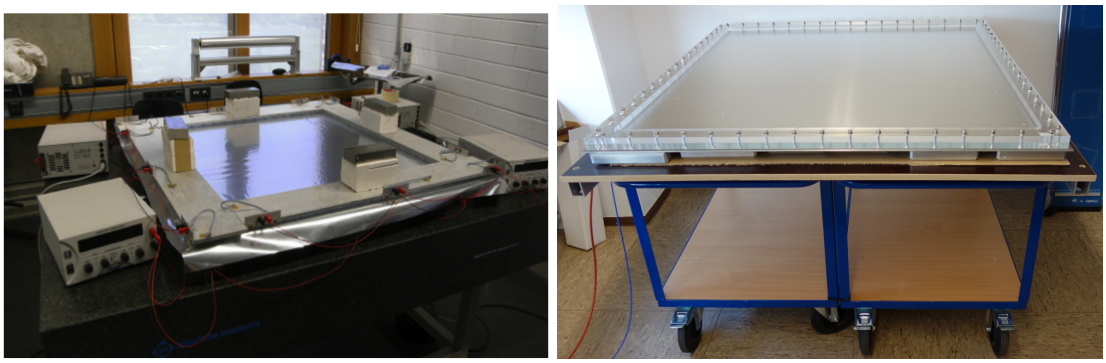

Figure 5.15: Devices to prepare the cathode foil for the entrance window at a well defined tension. The left picture shows the frame with heating coils and power supplies. A PMMA stretching frame on a aluminium heating plate for up to 1 m^2 foils is presented on the right figure.

cathode wires (75 µm Cu-Be) are winded with the same spacing and a tension of 100 cN. The second wire plane is positioned staggered relative to the anode wire grid. The glueing procedure is analog to the anode procedure. A last wire distance ledge of 5 mm thickness is put on top of the glue film. The cathode wires are cut away from the transfer frame after hardening of the glue and soldered to the copper strip on the opposite side of the wire ledge, to which the anode wires have been soldered previously. The cathode cable is soldered to the copper strip. The open sides are completed by the end strip which is adjusted by another set of Nylon aligning pins.

To the carbon lattice a foil of 25 µm Kapton with 0.05 µm aluminum on one side will be attached. The foil can be stretched by the thermal expansion of a Plexiglas, PMMA (PolyMethylMethAcrylate), frame from 20 °C to 50 °C. This procedure is based on a development for GEM foils and in principle described in [46]. A first version of a foil stretching device has already been used for the production of prototype TRD modules [47]. Figure 5.15 shows the device, which consists of an aluminum frame that is attached to the foil and can be heated by electrical heating elements to a well defined temperature (here typically 55° C). This approach can easily be applied to the large-scale production of the MWPCs of the CBM-TRD.

This gas window is glued to the chamber body to enclose the gas volume. The electrical connection to the aluminized Kapton gas window is realized by an overlapping part of the Kapton foil crimped over a copper strip covered on both sides with silver glue. The drift HV cable is soldered to this copper strip after hardening. The copper strip is afterwards covered by a Kapton adhesive tape to ensure electrical isolation to the outside. The chamber is closed by glueing the support grid gas window on top of the active detector volume. The gaps on the two wire ledge stack sides are filled with AW 106 to ensure gas tightness and increase mechanical stability.

5.4.2.1 Materials and Ageing

Due to the high interaction rates planned for the CBM experiment, the CBM-TRD will be exposed to a high radiation dose during its lifetime (see Sect. 4.6). Therefore, it has to be assured that the detector components do not suffer in this environment and thus cause performance degradations. This applies on one side to the materials used for the ROC construction and on the other side to the used gas mixture.

Concerning the ROC materials, especially those in direct contact with the gas volume, we make sure to use only those which have already been tested and certified for existing detectors (e.g. the ALICE-TRD). In particular this applies to the used glues (Araldite AW 106 and AW 116), the G11 ledges, the Kapton foil entrance window and the PCB of the pad plane. Therefore, no special problems in terms of ageing due to new and unknown material properties are in principle

to be expected.

The gas mixture foreseen for the CBM-TRD (Xe/CO_2 (85/15)) is non-organic, i.e. it does not contain any hydro-carbons (e.g. ethane) which tend to polymerize under high irradiation and thus cause depositions on the wires. Also, we do not intend to use any carbon-fluorides which can generate agressive hydro-fluorides in the presence of small H_2O contaminations, as observed in the ATLAS-TRT [48]. Thus, the gas mixture should be relatively inert under strong irradiation. However, it should nevertheless be ensured during operation that the gas contamination with H_2O and also Si is minimized. The latter can potentially be contained in lubricants present in components of the gas system and could cause depositions of Si-components on the wires.

Some guidelines on the effects of ageing can also be derived by the comparison with already existing TRDs. In terms of construction and materials the ALICE-TRD is very close to the proposed CBM-TRD design and its chambers have so far been operated since 2009 without any signs of ageing [49]. However, the accumulated radiation dose is in the ALICE situation still much lower than what is to be expected in the CBM case. A better benchmark is provided by the ATLAS-TRT, which has been operated at much higher interaction rates and is closer to the collision point. In fact, the accumulated charged particle dose and neutron fluence rate is very close to the expectations for the CBM-TRD [48]. For this detector it has been verified that the finally used gas mixture ($Xe/CO_2/O_2$ (70/27/3)), which is thus quite similar to the one foreseen for the CBM-TRD, causes no detrimental effects under this radiation environment [50].

Nevertheless, we still plan a series of further ageing tests, in order to rule out any unexpected behaviour. One option is the exposure of a ROC prototype to the high radiation environment available at the GIF++ facility at CERN (see Sect. 4.5.3) in order to mimic the operation within the CBM experiment in a realistic way. Other tests with sample materials and a small test chamber will be performed at the ageing test setup available at the GSI detector laboratory [51].

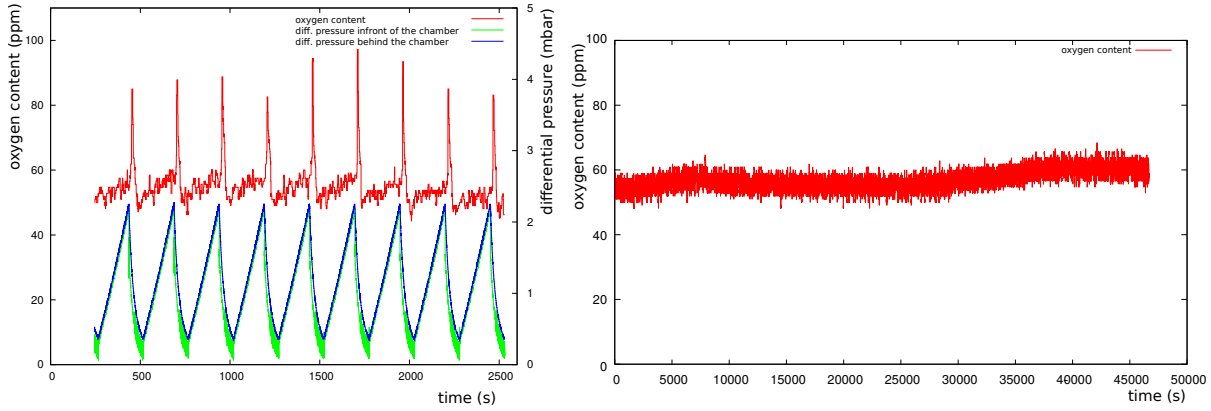

Figure 5.16: Left: A fraction of a 1.5 mbar pressure sequence is presented. The differential pressure in the gas system in front (blue) and behind (green) the chamber is shown in combination with the oxygen content (red) of the gas mixture after passing the chamber.
Right: The leakage rate of the detector under test has been tested after the full one year test sequence. The oxygen content is at the same level compared to a measurement before the stress test.

5.4.2.2 Entrance window stress test

Since the Kapton foil entrance window is the mechanically most fragile part of the detector, it had to undergo a one year mechanical stress test operation. The main mechanical stress to this component is provoked by pressure variations due to weather changes. An estimate on the distribution of air pressure variations within time windows of 10 min is given by a measurement

of the atmospherical pressure and have been extrapolated to a full year.

The differential gas pressure has been measured in front and behind the chamber. As observable for the condition of the foil window, the oxygen content of the gas mixture at the exhaust has been continuously monitored. The pressure variation was realized using an electric valve, closing the gas exhaust. An example for a 1.5 mbar overpressure sequence is presented in Fig. 5.16. The short spikes in the oxygen content at the exhaust of the chamber have been identified as gas backflow during the retain of the gas within the chamber. As result of this procedure, the chamber has been found to be in the same condition after one year of operation since the leakage test before and after the test showed the same level of oxygen contamination.

5.4.3 Electrostatic calculations

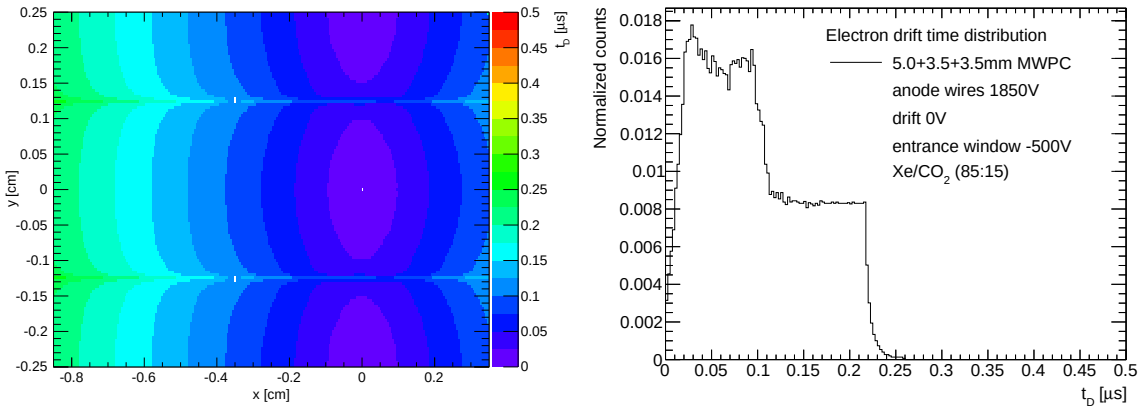

Figure 5.17: GARFIELD calculation of the electron drift times t_D in the default chamber geometry ($3.5 + 3.5$ mm amplification and 5 mm drift region) for an anode voltage of 1850 V and a drift voltage of -500 V. Shown is t_D as a function of the spatial coordinates x (drift direction) and y inside a drift cell (left) and the projected t_D distribution (right).

The GARFIELD simulation program [44] was used to determine the properties of the proposed ROC design. The default wire geometry of $3.5+3.5+5$ mm results in electron drift time distributions as shown in Fig. 5.17. Inside the amplification region the electrons are collected on the anode wires within 0.1 µs. To this the drift region adds further 0.125 µs. These drift times depend on the position of the primary ionization relative to the corresponding anode wire, as illustrated in the two-dimensional distribution shown in the left panel of Fig. 5.17.

An important point, that needs to be addressed with these calculations, is to which extend mechanical deformations of the entrance window foil modify the electric field and thus the corresponding gas gain. Figure 5.18 shows the field lines as simulated with GARFIELD. The middle panel displays the configuration for the nominal geometry, i.e. an 3.5+3.5 mm amplification and 5 mm drift region. To the left (right) the effect of a -1 mm and -2 mm ($+1$ mm and $+2$ mm) deformation of the entrance window is shown. As can be seen, a deformation of ± 1 mm already leads to visible distortions of the electric fields also inside the amplification region and thus alters the resulting gain. This effect is further quantified in Fig. 5.19, which displays the expected relative variation of the gain factor as a function of the displacement of the entrance window. A shift of its position by ± 300 µm results in gain variations of around ± 2 %. Restricting the deformations to below 1 mm will therefore ensure that local gain changes will be significantly smaller than 10 %. These remaining gain variations can easily be corrected by the corresponding calibration methode (see Sect. 9.4).

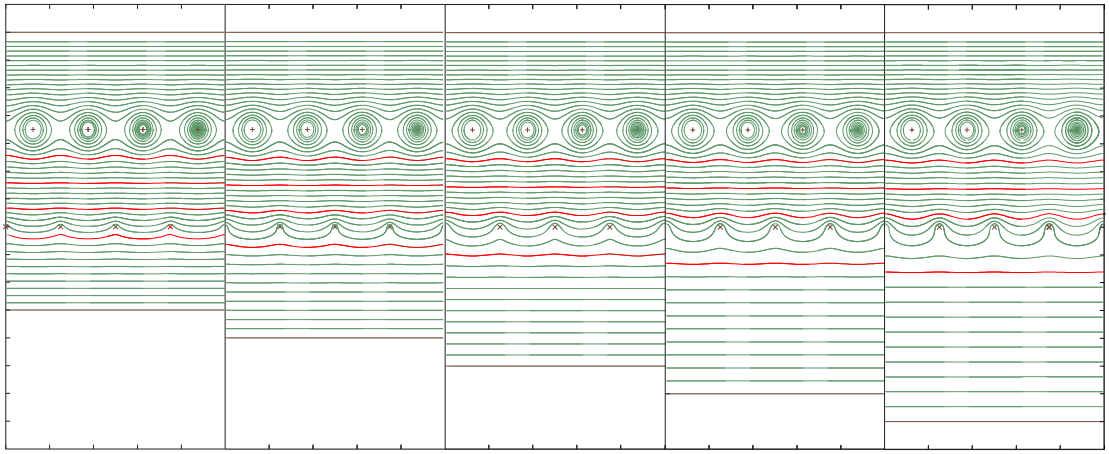

Figure 5.18: GARFIELD drift field scan for deformed gas windows of ±1 mm and ±2 mm for a constant drift voltage of −500 V. The nominal geometry is 3.5 + 3.5 + 5 mm (central panel). From left to right the deformation is −2 mm, −1 mm, 0 mm, +1 mm, and +2 mm. The potential lines for 0, 250, 500 and 750 V between the anode and cathode wire plane are highlighted in red.

5.5 Pad planes and front end boards

The charge generated in the amplification region induces a signal on the segmented pad plane, which constitutes the part of the TRD backpanel that faces the chamber interior. The signals seen by the individual pads are directly fed into the FEBs, which will be mounted on the outer side of the backpanels. The FEBs provide the readout and infrastructure for the SPADIC ASICs, as described in Chap. 7.

5.5.1 Pad plane layout

Module type	# Columns	# Rows	# Pads	Height (cm)	Width (cm)	Area (cm^2)
1	80	32	2560	1.75	0.68	1.18
3	80	8	640	6.75	0.68	4.56
5	144	24	3456	4.00	0.67	2.67
7	144	8	1152	12.00	0.67	8.00

Table 5.4: The parameters characterizing the pad plane layout for the different TRD module types. Given are the number of pads in row and column direction, as well as the corresponding pad dimensions.

The pad plane layout has to respect several constraints. While for the smaller modules in the inner detector regions they can still be produced as a single PCB, for the large modules they will have to be constructed from two or more separate PCB pieces, since they cannot be produced in the required size. The dimensions of the pads depend on the configuration of the wire grid. E.g. the length of the pads needs to be an integer multiple of the anode wire spacing. Also, it should be ensured that the length of the traces leading from the pads to the connectors is minimal in order to reduce cross talk. Therefore, the pads from two or four different pad rows will be grouped onto a single connector. In order to achieve the necessary channel integration for the different pad sizes 64 pads (*super density*, see left and middle panels of Fig. 5.20) and

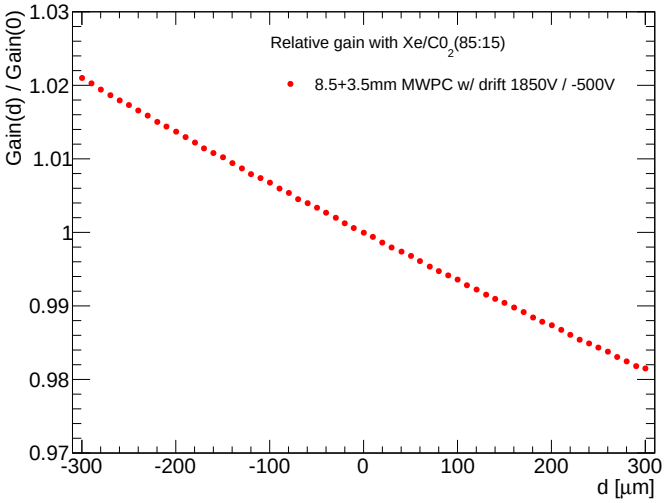

Figure 5.19: The relative gain variation as a function of the displacement d of the entrance window position as calculated with GARFIELD.

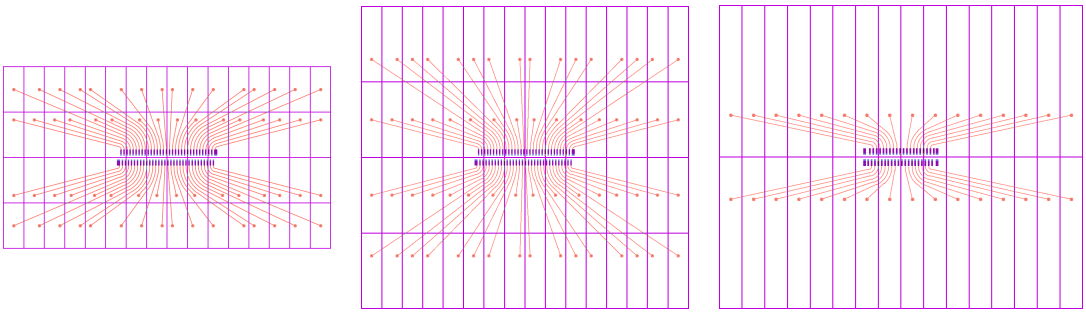

Figure 5.20: Layout of the different pad plane traces (shown at different scales). Left: 64 channel footprint, module type 1 (4 rows of 16 pads, *super density*). Middle: 64 channel footprint, module type 3 (4 rows of 16 pads, *super density*). Right: 32 channel footprint, module types 5 and 7 (2 rows of 16 pads, *regular density*).

blocks of 32 pads (*regular density*, see right panel of Fig. 5.20) are currently foreseen. The shown layouts provide the shortest possible trace lengths from the connector to the pad locations. By grouping the pads this way the number of pads in a given row will be fixed to a multiple of 16, while the connectors and cables will be for 32 or 64 channels.

The sizes of the readout pads have to be adjusted to the expected hit densities in the different areas of the CBM-TRD. Based on simulations using UrQMD events for Au + Au collisions at 10 AGeV, using the latest CBM geometry with a realistic material budget, the pad sizes have been determined such that the hit rates and occupancies always stay low enough (see Sect. 4.4). On the other side, one would like to avoid to have too many different pad plane layouts in the whole detector design in order to facilitate the module production. In the current design only four different pad planes are needed, two for the smaller modules (type 1 and 3) and two for the larger ones (type 5 and 7). The result of this optimization procedure is summarized in Tab. 5.4 and the arrangement of the different pad plane types in one CBM-TRD plane is shown in Fig. 5.21.

5.5.2 Front-end board arrangement

The FEB design has to reflect the different channel densities. One ASIC is designed for 32 channels. In the case of a 64 channel connector and cable two ASICs have to be grouped. To

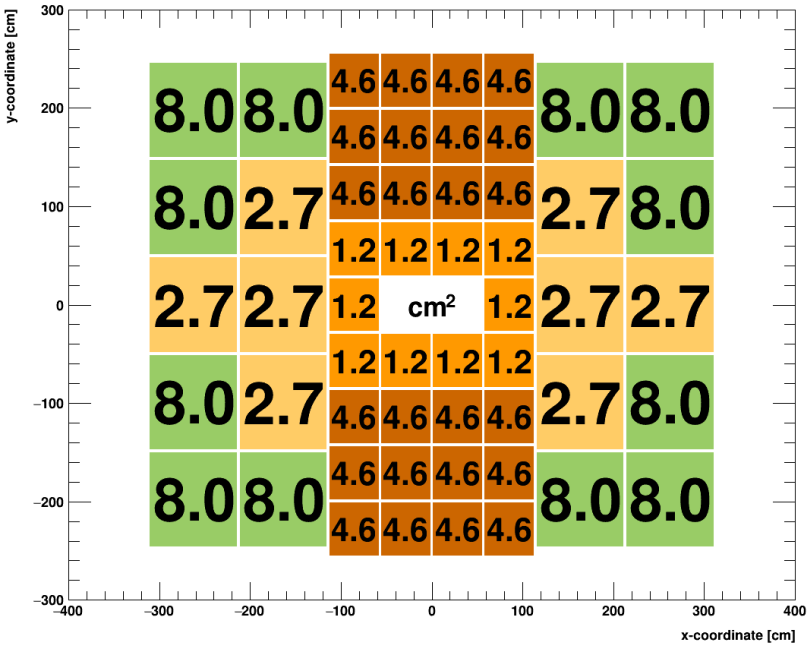

Figure 5.21: The distribution of pad sizes in the CBM-TRD geometry. The values correspond to the pad areas in cm^2.

minimize the amount of material introduced by the FEBs into the detector setup the number of channels per FEB should be chosen as high as technically possible. While for the small modules FEBs with super density are needed, for the large ones the regular density FEB is sufficient. Currently foreseen is one FEB type for the small modules with 320 channels (notation: FEB_10s) which supports 10 ASICS. For the large modules two types of FEBs with 160 (5 ASICs, notation: FEB_05n) and 128 channels (4 ASICs, notation: FEB_04n) are planned, which will be mounted next to each other. The four different module types of the CBM-TRD, together with their corresponding FEB types mounted on the back, are shown in Fig. 5.22. Table 5.5 summarizes the essential parameters of the different FEB types and also lists the number of FEBs and ASICs needed.

FEB type	Module types	ASICs/FEB	Channels/FEB	FEBs/module	No. of FEBs
FEB_10s	1 / 3	10	320	8 / 2	512
FEB_05n	5 / 7	5	160	12 / 4	576
FEB_04n	5 / 7	4	128	12 / 4	576
Total number of ASICs:		**10,304**			

Table 5.5: Summary on the different FEB types together with the total number of needed ASICs.

It is planned to directly mount the FEBs to the backpanel of the ROCs. Due to their relatively small area only lightweight holding structures will be needed, which can be glued directly to the backpanel. However, for the mounting of the FEBs different tilting angles α are in principle possible. If it is possible to realize a FEB design where the height of the PCB board does not exceed 3.0 cm, all TRD module types would provide enough space to install the FEBs flatly at the outer side of the backpanel (i.e. $\alpha = 0$, see Tab. 4.5) by mounting them with, e.g.,

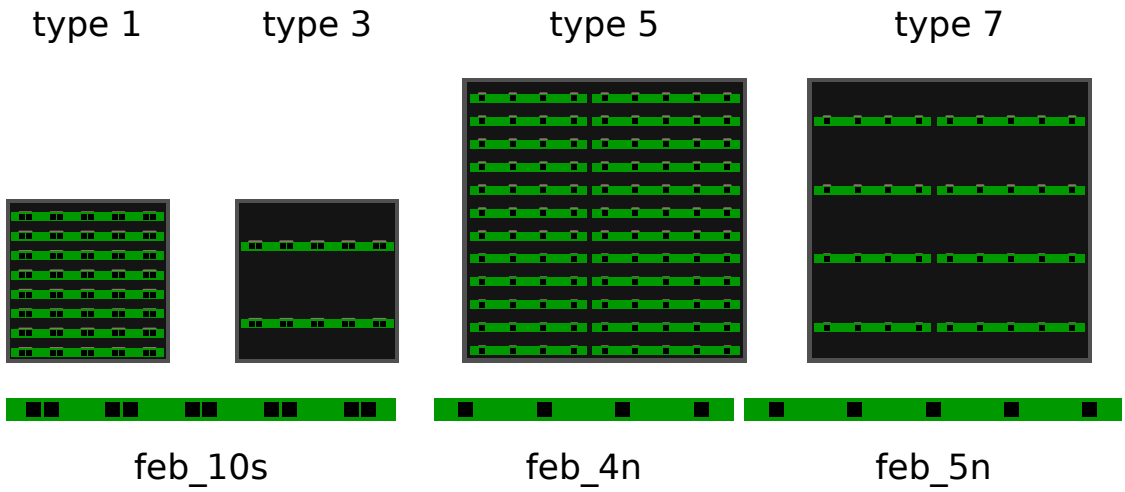

Figure 5.22: Rear views of the four different TRD module types, equipped with the corresponding FEBs shown in green. The three FEB types are shown again separately below the modules.

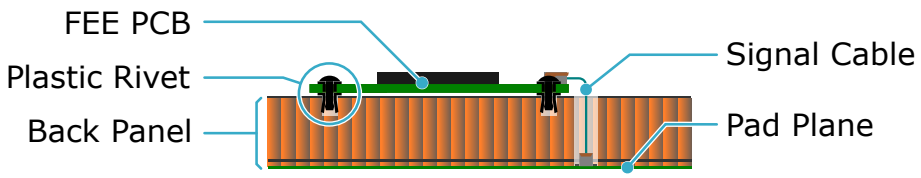

Figure 5.23: Mounting of the FEBs onto the backpanel.

plastic rivets as shown in Fig. 5.23. This arrangement would provide the most evenly distributed material budget. One prerequisite for FEBs of this size is to package the SPADIC chips as a BGA in order to reduce the real estate occupied by the chip to a minimum. However, if this turns out to be impossible or is prevented by issues like cable routing or cooling, the FEBs might have to be installed with a tilting angle $\alpha > 0$, especially for modules with a higher integration density, i.e. type 1 or 5, see Fig. 5.22. For these cases, α should be chosen such to ensure a minimal non-uniformity of the resulting material budget.

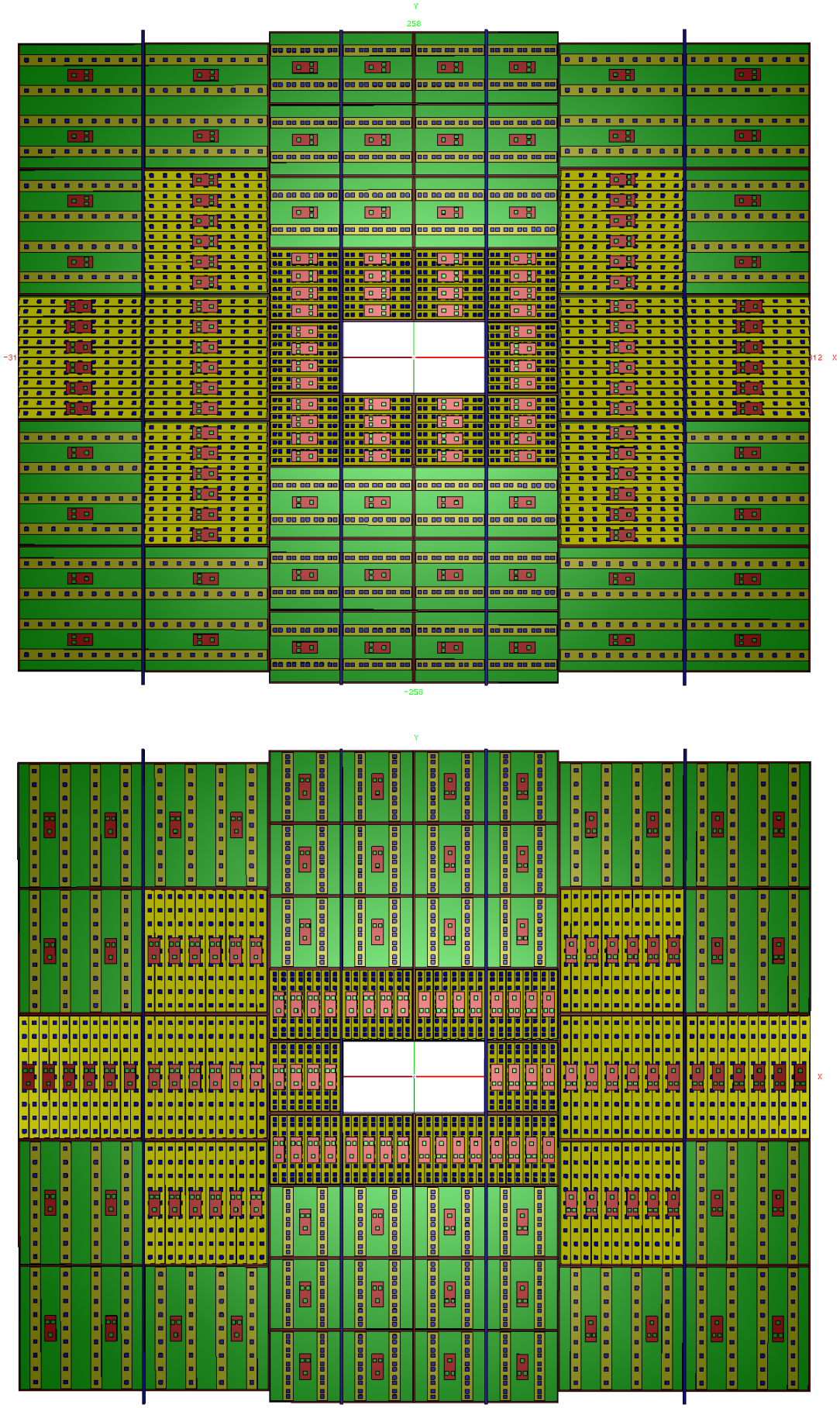

Figure 5.24: Rear view of two different TRD layers, illustrating the orientation of FEBs on the modules.

Chapter 6

Radiator

This chapter summarizes some theoretical approaches used to describe the different radiator types. These effective descriptions are on one hand the basis for the simulation of the TRD detector response, as described in Sect. 9.2. On the other hand, they have been employed to identify the optimal radiator solution and to match the design of the readout chambers to the spectral distribution of the produced TR-photons. Finally, the most promising radiator options for the CBM-TRD are presented and their properties, as well as their performance in test beam measurements, are discussed.

6.1 Theoretical description of radiators

Radiators are devices used to produce TR-photons emitted at periodic material boundaries between materials with different dielectric constants ϵ. Such boundaries can be realized in different ways: regular foil, foam and fiber radiators. The essential property of the radiator material is the plasma frequency ω_P. To calculate this property the average electron density n_e is needed, which is correlated to the average atomic number Z of the material. The Z, A (atomic mass number), ρ (density), and ω_P values of different materials can be found in Tab. 6.1. There are two main classes of radiators, the regular radiators mostly made from equally spaced foils and the irregular radiators made from foams or fiber mats. The regular radiators utilize coherent interference and produce a larger number of photons per incident electron and boundary, while the mean number of photons is lower in case of irregular radiators due to the missing coherent interference and/or the smaller structure size in foams or fiber mats. This lower number of photons and smaller mean photon energy can partially be compensated by a higher number of boundaries per unit length, since the average structure sizes are smaller.

6.1.1 Regular radiators

The simplest scenario of TR production by a relativistic particle with a Lorentz factor γ considers a single interface which is crossed by the charged particle. The expected double differential photon spectrum is

$$\left(\frac{d^2N}{d\omega d\vartheta}\right)_{\text{interface}} = \frac{\alpha}{\pi}\cdot\left(\frac{\vartheta}{\gamma^{-2}+\vartheta^2+(\omega_{P,1}/\omega)^2}-\frac{\vartheta}{\gamma^{-2}+\vartheta^2+(\omega_{P,2}/\omega)^2}\right)^2 \tag{6.1}$$

with the emission angle relative to the direction of motion ϑ, the foil ($i=1$) and gap ($i=2$) plasma frequency $\omega_{P,i}$ and the fine structure constant α. The plasma frequency is given by

$$\omega_{P,i} = \sqrt{\frac{n_e\cdot e^2}{\epsilon_0\cdot m_e}} = \sqrt{\frac{4\pi\alpha\, n_e\,\hbar c}{m_e/c^2}} \tag{6.2}$$

where α is the fine-structure constant and m_e is the electron mass [52]. The average electron density n_e can be calculated as follows

$$n_e = \frac{\rho \cdot N_A \cdot Z}{A} \tag{6.3}$$

where ρ is the density, N_A the Avogadro constant and A the average mass number. The average atomic number Z can be approximated for i materials by using the relative weighting factor w_i

$$Z = \sum_i w_i \cdot Z_i \tag{6.4}$$

This scenario can be extended to a foil with two surfaces

$$\left(\frac{d^2N}{d\omega d\vartheta}\right)_{\text{foil}} = \left(\frac{d^2N}{d\omega d\vartheta}\right)_{\text{interface}} \cdot 4\sin^2\left(\frac{l_1}{2z_1}\right) \tag{6.5}$$

with z_i being the formation zone (Eq. 6.6) for the two media [53]. Both, foil thickness l_1 and gap dimension l_2, should be greater than the formation zone z_i, which is typically of the order of 10 µm for plastic and 700 µm for gases like air. z_i is given by

$$z_i = \frac{2\beta c}{\omega} \cdot \left(\gamma^{-2} + \vartheta^2 + \left(\frac{\omega_{P,i}}{\omega}\right)^2\right)^{-1} \tag{6.6}$$

where ω is the photon frequency and ϑ the photon emission angle with respect to the particle trajectory. All formulas up to now do not include self-absorption within the radiator material. Self-absorption is relevant in the low energy part of the spectrum, i.e. below a few keV. The production probability for a photon at a single foil is of the order of $1/\alpha$. To increase the particle separation performance, the number of interfaces has to be enhanced within a given radiator. A periodic radiator with N_f layers of thickness l_1 and spacing l_2 can be described by

$$\left(\frac{d^2N}{d\omega d\vartheta}\right)_{\text{stack}} = \left(\frac{d^2N}{d\omega d\vartheta}\right)_{\text{foil}} \cdot \exp\left(\frac{(1-N_f)\sigma}{2}\right) \frac{\sin^2\left(\frac{N_f\,\phi_{12}}{2}\right) + \sinh^2\left(\frac{N_f\,\sigma}{4}\right)}{\sin^2\left(\frac{\phi_{12}}{2}\right) + \sinh^2\left(\frac{\sigma}{4}\right)} \tag{6.7}$$

with $\phi_{12} = \phi_1 + \phi_2$ and

$$\phi_i \simeq \frac{1}{2}\left(\gamma^{-2} + \vartheta^2 + \left(\frac{\omega_{P,i}}{\omega}\right)^2\right)\omega\, l_i \tag{6.8}$$

and σ being the total photon absorption cross section σ ($\sigma = \mu_1 \cdot l_1 + \mu_2 \cdot l_2$) for one foil and gas layer. The mass attenuation coefficient μ/ρ for different elements, compounds and mixtures can be found in the National Institute of Standards and Technology (NIST) XCOM database [54]. The emission angle ϑ integral of this formula can be approximated as:

$$\frac{dN}{d\omega} = \frac{4\alpha}{\omega(\kappa+1)} \frac{\left(1-e^{(-N\sigma)}\right)}{\left(1-e^{(-\sigma)}\right)} \cdot \sum_n \Theta_n \left(\frac{1}{\varrho_1+\Theta_n} - \frac{1}{\varrho_2+\Theta_n}\right)^2 \left[1-\cos(\varrho_1+\Theta_n)\right] \tag{6.9}$$

according to [55]. This equation includes coherent and incoherent effects as well as the self-absorption of gap and foil material. Therefore it was used to calculate the total yield per keV in the following section. Equation 6.9 provides an accurate description of the spectra within ±15 % [56]. It uses the relation

$$\varrho_i = \frac{\omega l_1}{2c}\left(\gamma^{-2} + \left(\frac{\omega_{P,i}}{\omega}\right)^2\right), \tag{6.10}$$

with the definitions

$$\kappa = \frac{l_2}{l_1} \tag{6.11}$$

and

$$\Theta_n = \frac{2\pi n - (\varrho_1 + \kappa\varrho_2)}{1+\kappa} > 0. \tag{6.12}$$

Systematic deviations between measurements and theoretical predictions arising from the material budget of the radiator and the MWPC and possible irregularities of the radiator can be compensated by introducing an attenuation factor a, defined in the range [0,1]:

$$\left(\frac{dN}{d\omega}\right)_{\text{measurement}} = a \cdot \left(\frac{dN}{d\omega}\right)_{\text{theoretical}} . \tag{6.13}$$

6.1.2 Irregular radiators

A spectral distribution of TR-photon production in an irregular radiator, consisting of parallel plates of random thickness, is given by Garibian et al. [57]. This formulation can be modified to take into account the presence of a material in the gap. However, the usage of this model is quite challenging, since it implies a perfect knowledge of the two distributions of the foil and gap thicknesses. A schematic drawing illustrating the characteristics of a liquid/gas or solid/gas foam bubble is presented in Fig. 6.1.

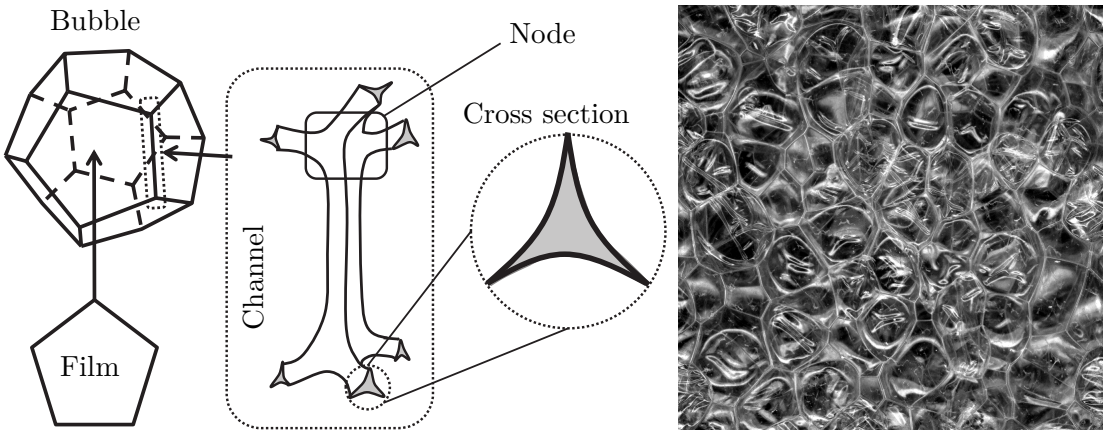

Figure 6.1: Left: Schematic of a dodecahedral bubble and the wall channel based on [58]. Right: Foam structure of a $19 \times 19\,\text{mm}^2$ and 5 mm thick cell-air polyethylene foam sample.

The films are thin sheets of liquid (solid, after hardening) separating two bubbles. The channels are thin liquid or solid columns formed at the intersection of three bubbles and are also known as plateau borders. The junctions where the channels intersect are called nodes and four channels meet at a single node [58]. This description implies a very complex inner structure of the foam with thin film structures, relatively thick channels and more or less spheric bubbles.

The description of the solid fiber or fleece components is in most cases easier. In [59] it was observed that the fiber diameters showed only a small variation within the same sample that was investigated, but at the same time have a broad spectrum of gap spacings as presented in Fig. 6.2. Nevertheless, the description of gap distributions is very complex in the case of fleece materials and depends on too many parameters such as fiber length, diameter, bendability and production process, and would thus demand a three dimensional measurement without any outer forces on the material disturbing the material properties.

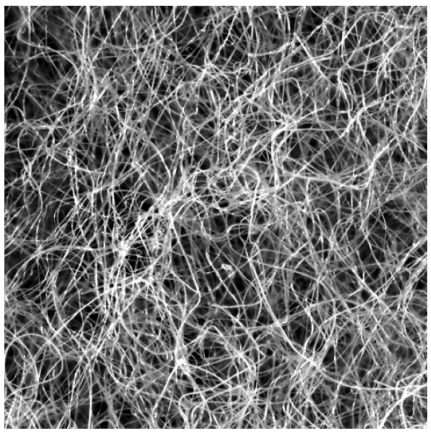

Figure 6.2: Fiber structure of a $10 \times 10\,\mathrm{mm}^2$ polypropylene fleece sheet.

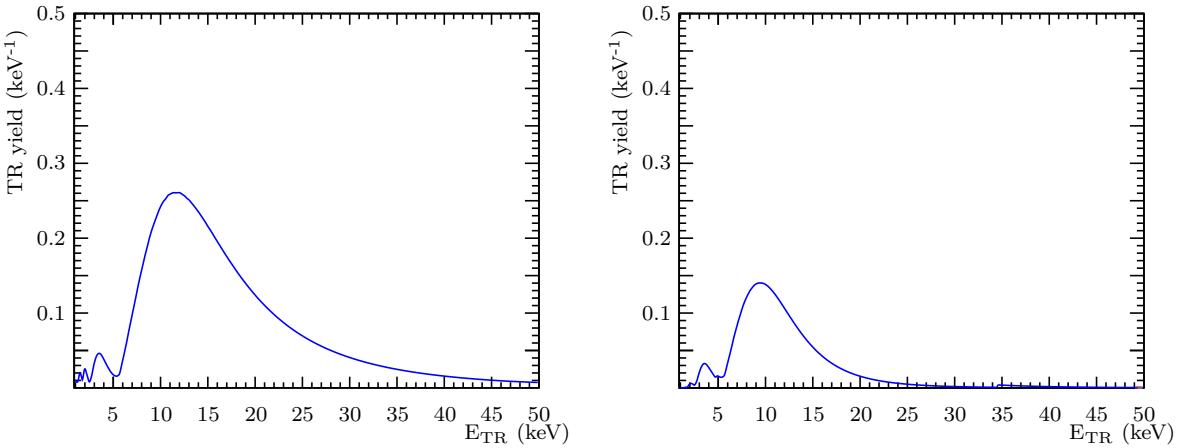

Figure 6.3: TR-photon emission (left) and absorption spectrum (right) for electrons at a momentum of $2.0\,\mathrm{GeV}/c$ for a POKALON N470 radiator with 24 µm foil thickness and 700 µm foil spacing, composed of 350 foils.

Based on the previous argumentation and the fact that the pure photon spectrum defies any attempt of direct measurement with a MWPC, a description of irregular radiators is not used here. Instead, the emission and absorption spectra, presented in the following, are based on a realistic material budget, but are calculated for a regular toy model radiator using Eq. 6.9 with average parameters $\langle l_1 \rangle$, $\langle l_2 \rangle$ and $\langle N_f \rangle$. The resulting spectra are scaled by a weighting factor a to describe the measured total energy loss spectra (dE/dx+TR) as good as possible. The full material budget between radiator and backpanel, i.e. the single sided aluminized Kapton foil, the wires and the Xe/CO_2 gas mixtures, are also taken into account. Simulated examples for emission and absorption spectra are presented in Fig. 6.3 for a POKALON based radiator. Comparing the two, the absorption probability distribution for a given detector configuration can be derived, as presented in Fig. 6.4. The absorption maximum $\omega_{\mathrm{max}}^{\mathrm{abs.}}$ of the 2012 prototypes is found to be around a photon energy of 5.66 keV.

It is essential to understand the influence of radiator parameters like material, number of foils and foil as well as gap thickness to optimize the TR-yield with respect to the absorbed spectrum seen by a readout chamber. The materials, which constitute the main components of possible radiators, have different properties like stability, conductivity, and cross section. The material properties, which are essential for this optimization, are shown in Tab. 6.1. The different

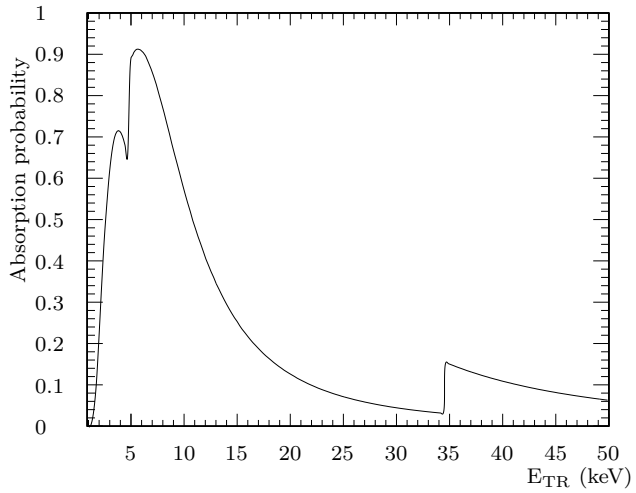

Figure 6.4: The photon absorption probability distribution for the 2012 chamber prototype including the transmission of the frontpanel components.

material parameters, such as density and plasma frequency, are chosen over a wide range of values, corresponding to the tested radiator prototypes.

Material	Z	A	ρ (g/cm^3)	ω_P (eV)
Air	14.49	29.02	$1.2 \cdot 10^{-3}$	0.71
Mylar	4.55	8.73	1.393	24.53
POKALON N470	4.06	7.71	1.15	22.43
Polyethylene (PE)	2.67	4.68	0.9	20.65
Polypropylene (PP)	2.67	4.68	0.9	20.65
Polymethylmethacrylate (PMMA)	3.18	5.89	1.18	22.99

Table 6.1: Gap and foil material properties: Z, A, ρ and ω_P at a pressure of 101.3 kPa and a temperature of 293.15 K. The properties of mixed materials are not presented in case of foams or fibers. The gaseous and solid components are presented separately within the first part of the table and are used as simulation input.

6.2 Optimization procedure

The optimal radiator parameters are strongly correlated with the detector characteristics. A good matching between the photon absorption probability spectrum (presented in Fig. 6.4) and the TR-photon production spectrum leads to an optimal PID performance of the entire detector system. The shape of the TR-spectrum is mainly influenced by the foil and gap thickness. The total yield can be modified by the used number of foils. A numerical approach has been chosen to optimize the energy loss due to TR-photon emission per electron as presented in Fig. 6.5 for different radiator materials.

The optimization was done numerically by varying the parameters l_1 in the range between 0 and 100 µm and l_2 between 0 and 10 mm. The resulting optimized parameters l_1^{opt} and l_2^{opt} for POKALON N470, PP and PE are listed in Tab. 6.2.

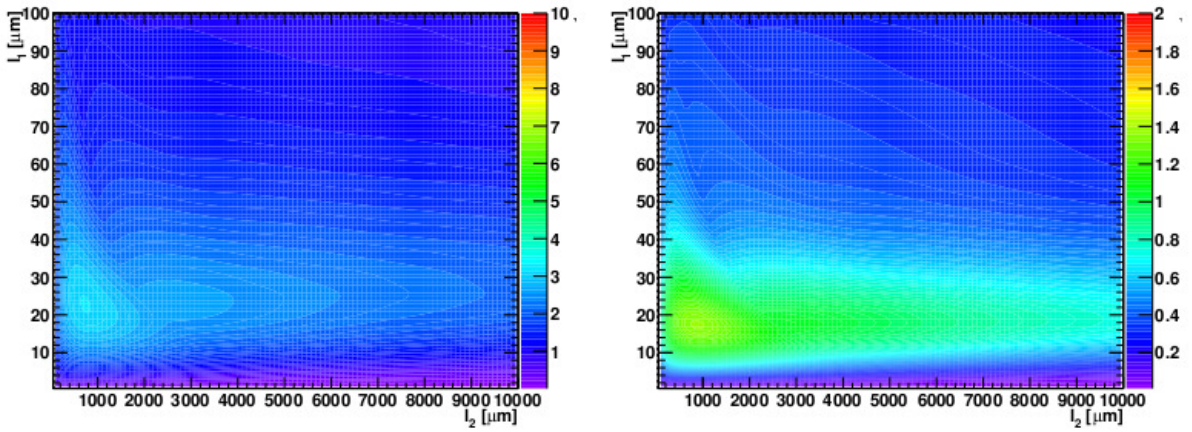

Figure 6.5: Integrated TR-yield emission spectrum (right) and spectrum of photons absorbed within the detector (left) calculated for 200 PE foils of variable foil thickness l_1 and gap thickness l_2 for electrons with a momentum of 2 GeV/c.

Material	l_1^{opt} (µm) ± 1 µm	l_2^{opt} (µm) ± 100 µm	l_1^{real} (µm)	l_2^{real} (µm)
POKALON N470	20	800	24	700
Polyethylene (PE)	20	800	12	900
Polypropylene (PP)	20	800	17	50

Table 6.2: Numerically optimized radiator parameters for a total number of foil layers of 200 at an electron momentum of 2 GeV/c. The parameters for the three most promising radiator materials are presented. The presented optimized values are rounded to commercially available material thicknesses. In the case of irregular materials the parameters of the prototype radiators are averaged values.

The granularity of the used histogram (compare Fig. 6.5) is the main origin of the uncertainties presented in Tab. 6.2. A variation of the chamber thickness resulting in a modification of the chamber absorption characteristic results in strong modification of the optimal radiator parameter l_1 and l_2. The exact matching of the parameters for the three most promising materials is therefore a special feature resulting from the absorption characteristic of our detector.

Since a too small foil thickness (l_1) can provide the same TR-yield as a too large foil thickness, the smaller parameter l_1 should always be preferred in order to minimize the material budget. A similar argument can be found for the foil spacing. In this case a shorter distance is leading to a more compact radiator and is therefore to be preferred if the optimal parameter can not be realized. In the end, the results of this optimization procedure have been used to classify new commercially available radiator materials into candidates worthwhile to be tested.

6.3 Radiator options

The following section describes what we currently consider to be the best radiator options. Pictures of the corresponding prototypes are presented in Fig. 6.6.

The best compromise between performance and mechanical feasibility was found for the following three radiator options:

H: PolyEthylene (PE) foam foil radiator. The stacks of 2.0 mm thick foam foils had the highest

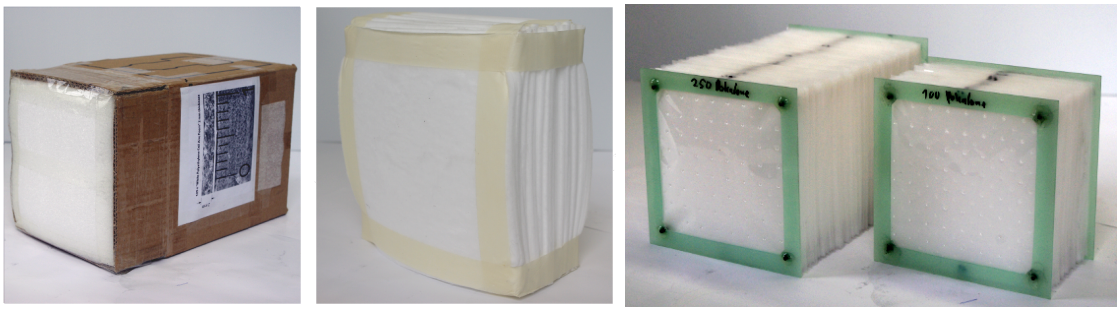

Figure 6.6: Prototypes of the three best radiator options. **H:** PE foam foils (left). **G30:** PP fiber fleece (type LRP 375 BK) layers (centre). **K++ :** self-supporting micro-structured POKALON foil (type N470) radiator (right).

performance among the irregular radiators which is also in reasonable agreement with simulations. The highest regularity of the bubble sizes, correlated to radiator parameters l_1 and l_2, was also observed for this material (see also Tab. 6.2).

G30: PP fiber radiator. This type is composed from 30 fiber fleece layers and also exhibited a good performance. The fiber diameter distribution is very uniform, while their spacing is completely chaotic. However, the relatively high price of the fibre material renders this option uneconomical.

K++ : Micro-structured self-supporting POKALON radiator. This is a low weight, frame-less option, made from 350 foil layers and combining the advantages of a regular radiator with the mechanical stability of an irregular radiator. Also here the comparatively high costs would constitute a significant disadvantage of this option.

6.3.1 Test beam results on radiator performance

A test of the particle identification (PID) performance was carried out at the CERN-PS using a mixed pion and electron beam (for details on the test beam setup see Sect. 4.5.1). For these measurements a combination of two identical MWPC prototypes ("MS I R" and "MS II N") with different radiators was used. They were performed with a Xe/CO_2 (80/20) mixture and a particle momentum of $3\,\mathrm{GeV}/c$. The electron and pion energy loss spectra were measured for each detector radiator combination using an external reference PID system composed of two air-Cherenkov counters and one lead-glass calorimeter. Based on the spectra measured in one TRD module, the final PID performance at a fixed electron efficiency can be extrapolated to a four layer detector by using the likelihood method on the total charge as described in Sect. 9.3.2.1. The approximated pion efficiency at 90 % electron efficiency with four detector hits (see Fig. 6.7) indicates a good agreement for most regular prototypes between simulation and measurement within the errors.

It can be seen that the most efficient radiator is a regular radiator made from PE-foil ("FFM0.7×350"), as expected. However, such a radiator is not an option for the CBM experiment, since the foil support frames would increase the material budget of the TRD to a value which can not be tolerated. Furthermore, it would be a non-trivial task to produce these kind of radiators in sufficient quantity and sizes. The best self-supporting candidates in terms of performance are G30 (PP-Fibers), H (PE foam foils) and K++ (regular micro-structured POKALON foil), as discussed above, where there are indications that the radiator type H overall performs best. In addition, a consideration of the pure material price would also exclude the PP-Fibers as well as the POKALON foil, thus leaving the radiator type H as the optimal choice.

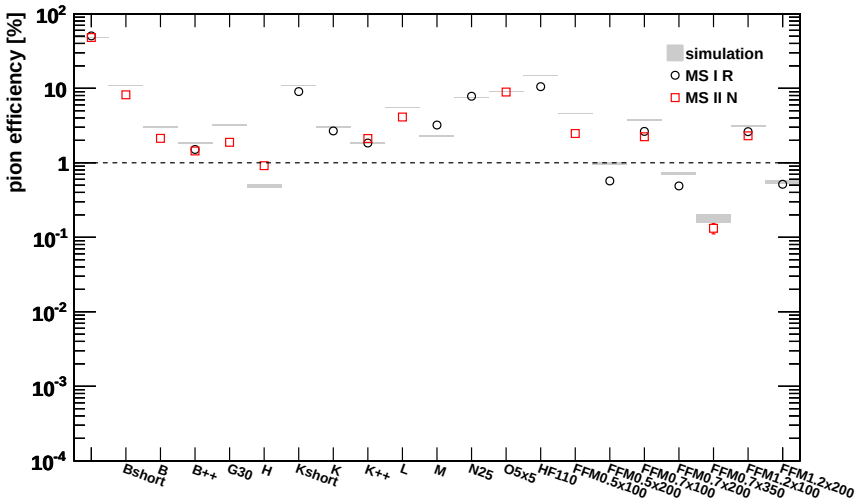

Figure 6.7: The pion efficiency at 90 % electron efficiency at $p = 3\,\mathrm{GeV}/c$, extrapolated to four measured detector hits per particle. Shown are different radiator prototypes.

6.3.2 Default radiator choice and mechanical layout

Following the considerations and test beam results outlined above, a radiator of type H will be the default solution. In order to provide mechanical stability and allow for an easy mounting, the foam foil layers will be enclosed in a box, such that each TRD module can be equipped with a separate, removable radiator. The radiator encasing will be composed of a hard foam box (PMMA, e.g. Rohacell HF71) of 8 mm thickness on five of its six surfaces, while the contact side towards the detector stays open. The transverse dimensions of the boxes are $57 \times 57\,\mathrm{cm}^2$ or $99 \times 99\,\mathrm{cm}^2$, corresponding to the sizes of the small and large TRD modules. The depth of the boxes is foreseen to be 30 cm. Table 6.3 summarizes the main parameters of the default radiator option. A prototype radiator, as tested at an electron beam at DESY, is presented in Figs. 6.8 and 6.9.

The boxes are glued with Araldite 2011 and filled with PE foam foil layers of 2 mm thickness each. The last foam foil layer is glued to the box outer frames to keep the inner foil layers in position. The small volumes within the carbon lattice in front of the ROCs entrance windows are also filled individually with the same foam foils (see Fig. 6.9). Both, the foam foils inside the carbon lattice and the ones inside the main radiator box, are mechanically stabilized on their open contact surface by using a polymer filament grid.

The box arrangement will thus provide a mechanically sturdy and effectively airtight encasing for the active radiator material (i.e. the foam foil layers). It will allow for an easy installation and handling of the individual radiators. In addition, it should also prevent any changes in the ambient atmosphere (e.g. air humidity or leakage of xenon from the ROCs) to severely affect the performance of the radiator.

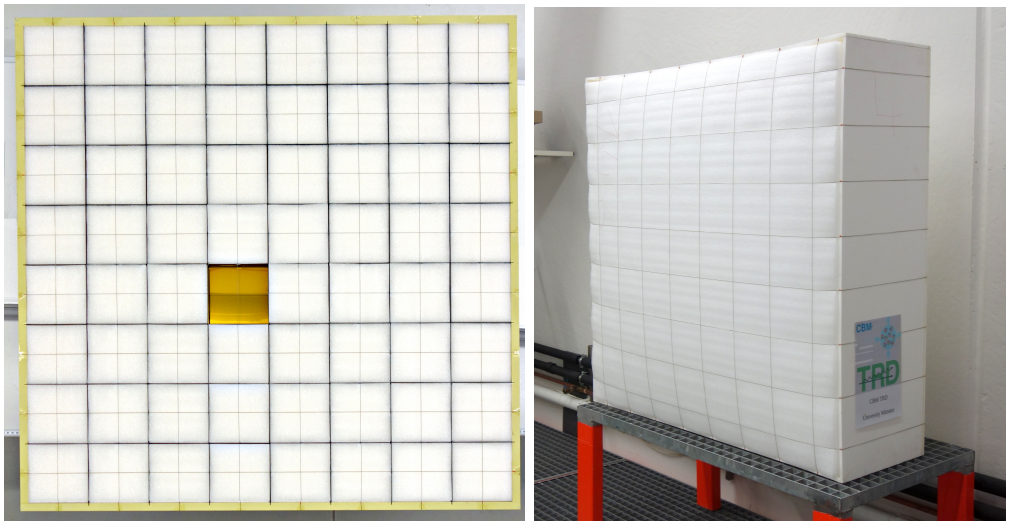

Figure 6.8: Full size radiator prototype of type H for the large ROCs. Left: ROC entrance area with PE foam foils inserted into the volumes between the carbon lattice, where one lattice cell was left free for test measurements. Right: radiator consisting of a PMMA hard foam box filled with PE foam foils. The shape of the radiator is stabilized by a polymer filament grid.

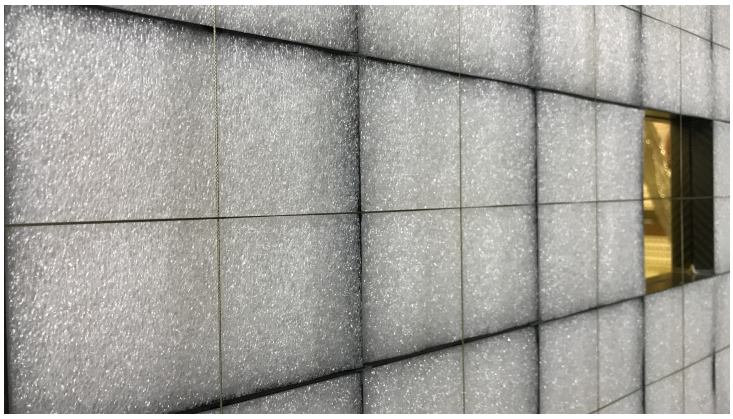

Figure 6.9: Close-up picture showing PE foam foils inserted into the volumes within the carbon lattice, held in place by a polymer filament grid.

	Parameter	Value
Radiator type H	Material	PE foam foils
	Thickness of foam foil	$\sim 2\,\mathrm{mm}$
	Number of foam foil layers	146
	Radiation length X_0	$44.8\,\mathrm{g/cm^2}$
	Density ρ	$0.026\,\mathrm{g/cm^3}$
Radiator box	Material	PMMA (Rohacell HF71)
	Wall thickness	8 mm
	Elastic modulus	92 MPa
	Radiation length X_0	$40.6\,\mathrm{g/cm^2}$
	Density ρ	$0.075\,\mathrm{g/cm^3}$
Outer dimensions	Module type 1 and 3	$57 \times 57 \times 30$ cm^3
	Module type 5 and 7	$99 \times 99 \times 30$ cm^3

Table 6.3: Summary of the main parameters of the default radiator option.

Chapter 7

Front End Electronics and Readout Chain

The TRD readout architecture is based on the SPADIC front-end ASIC, which will be operated on the Front-End-Boards (FEBs), directly mounted on the back of the readout chambers. From the front-end the data will be transported to the Read-Out Boards (ROBs) which integrate GBTx (GigaBit Transceiver) ASICs and VTTx (Versatile TransReceiver) / VTRx (Versatile Twin-Transmitter) as radiation hard optical link components. The ROB is used as transparent data combiner and to convert electrical to optical signals. The data is transported via optical fibers towards the FPGA based receiver cards called Common Readout Interface (CRI). After feature extraction and data pre-processing in the FPGAs of the CRIs, the preprocessed data is shipped via optical links to the FLIB/FLES data acquisition for further analysis and storage.

7.1 The SPADIC front-end ASIC

7.1.1 Overview

The SPADIC chip *(Self-triggered Pulse Amplification and Digitization ASIC)* is a mixed-signal readout ASIC with 32 input channels developed explicitly for the readout of the TRD of CBM [60]. Figure 7.1 shows a simplified block diagram: each channel contains a Charge Sensitive Amplifier (CSA), a continuously running ADC sampling the amplifier output, a programmable digital filter ('DSP') and a hit detection logic. When a hit occurs (the digital amplitude value crosses a programmable threshold or a steep slope is observed), the sampled data of the hit pulse shape is stored for later readout. The amount of data to read out per hit can be programmed in a very flexible way by choosing a set of sample values (relative to the trigger moment) with a programmable mask pattern. This flexibility allows a trade-off between data volume and detail of information. The selected data is then aggregated and distributed to two high speed serial links. Events are timestamped for later time event association and they contain some other meta-information and error checking bits. The chip is controlled with one serial control 'down' link, carrying configuration data and fast commands like test injections or timestamp synchronization signals.

The described architecture has been chosen, because it offers the possibility to analyze the shape of individual chamber pulses. This feature may allow a discrimination between different particle types, depending on the radiator design. As it was initially not clear which shape parameters are relevant, the pulse picking mechanism was introduced for a maximum of flexibility. No on-chip data processing (for instance a summation of ADC samples or the determination of the temporal pulse width) has been included yet, because such a dedicated hardware solution requires prior evaluation of the algorithm with real detector data.

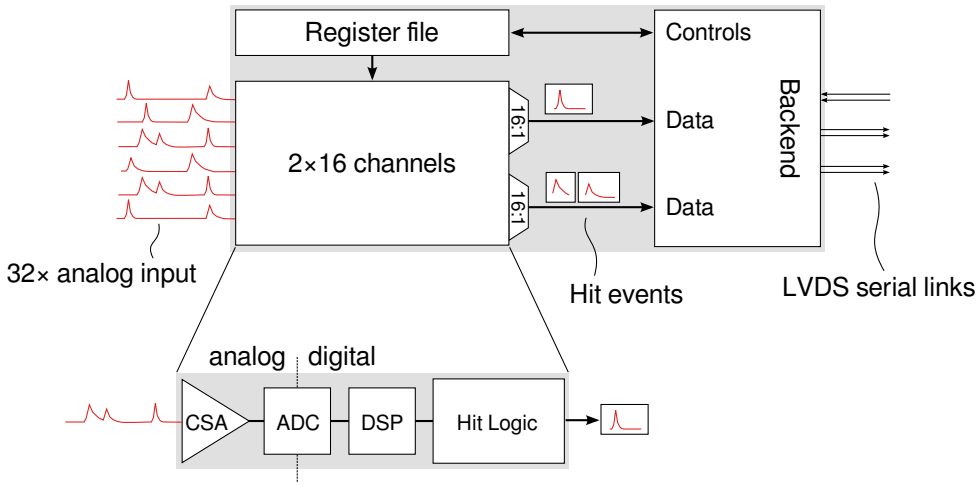

Figure 7.1: Conceptional block diagram of the SPADIC chip. The 'Backend' block is CBMnet in SPADIC 1.x and an E-link interface in SPADIC 2.x.

The programmable digital Infinite-Impulse-Response (IIR) filter has been included in order to pre-process possible complex detector pulse shapes. It may be used for ion tail cancellation or double hit discrimination.

Another important feature of SPADIC is a neighbor logic which allows to force trigger channels by hits in neighboring channels. The amplitude information of adjacent channels is used to improve position resolution so that also small amplitudes should be known. In a self triggered operation this would require very low thresholds so that data volume would be increased by noise hits. This First Neighbor Readout (FNR) mechanism allows to set a conveniently high threshold in all channels and still obtain the amplitude of neighbors (even below threshold) by force triggering. In order to provide a maximum flexibility for different pad plane designs, the neighbor association can be programmed to a large extent. SPADIC also allows to pass trigger information from chip to chip (which is not trivial due to signal propagation times) and therefore provides four neighbor trigger inputs and outputs at both the 'top' and 'bottom' sides of the chip.

Table 7.1 summarizes the most important chip properties, Fig. 7.2 shows the layout of the chip. A website has been set up to distribute information about the chips [61].

Parameter	Value
Chip size	$5 \times 5\,\mathrm{mm}^2$
Channels	32
Total power	600 mW
Peaking time of analogue part	80/240 ns
ADC resolution	9 bits
ADC sampling frequency	25/16 MHz
IIR filter stages (1st order)	4
Technology	UMC 180 nm
Transistor count	$\approx$ 2.5 M

Table 7.1: Most important parameters of the SPADIC chips. Multiple values refer to different chip versions.

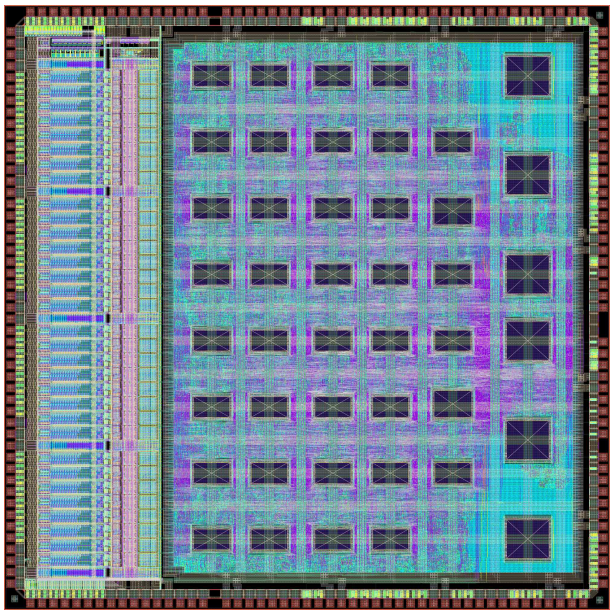

Figure 7.2: Top-level layout of the SPADIC 1.0 chip. The chip has a size of $5 \times 5\,\mathrm{mm}^2$. The 32 analog channels occupy the first quarter of the chip area from the left side, the synthesized digital part is to the right. The black boxes are larger memory blocks.

7.1.2 Chip versions and history

After prototyping five test chips with few channels, the first full size chip SPADIC 1.0 has been submitted end of 2011 [62, 63]. The analogue shaper in that chip has a peaking time of 80 ns, the ADC samples at 25 MSps, and the digital interface uses the CBMnet protocol [64] (this part has later been used as a basis for the digital interface of the first STS-XYTER chip [65]). Apart from few minor bugs, SPADIC 1.0 is fully functional and has been used for intensive lab characterizations. A small number of chips has been packaged into 176 pin ceramic carriers (Fig. 7.3) which were then mounted on various versions of the FEBs used to read out detector prototypes. Several test beam campaigns were carried out with these packaged chips.

Because no more SPADIC 1.0 chips were available at some point, a slightly updated version, SPADIC 1.1, has been submitted in 2015. The three known bugs (instability in analogue part, unwanted behavior of comparator under certain conditions, timing issue in serial output stream) were fixed. This chip has been used already in 2016 for test beam measurements at the CERN-SPS.

After CBM had decided to move from the special CBMnet protocol to a format using the GigaBit Transceiver chips (GBT) from CERN, the entire digital interface of the SPADIC 1.x chips had to be exchanged. This has been carried out in late 2015 and early 2016 (very much based on an E-link implementation for the STS-XYTER developed by the group in Krakow [66, 67]) and the new chip SPADIC 2.0 has been submitted in June 2016 on an engineering run together with other CBM ASICs. While the major change is an 'E-link' compatible data/control interface, the opportunity was used to change a few chip parameters: the peaking time of the analogue part has been increased to 240 ns to match the longer drift paths in the latest TRD chambers, the ADC sampling rate has been slowed down correspondingly to 16 MSps (this is also driven by changes in the clock speeds of the CBM DAQ) and the number of 'pre-samples' (ADC values *before* trigger has occurred) has been increased.

A further iteration SPADIC 2.1 was submitted in August 2017, which introduces changes in both the analogue and digital part, most notably a switchable low-gain mode, a switchable additional shaping order (if turned on, the peaking time remains at 240 ns, if turned off it is

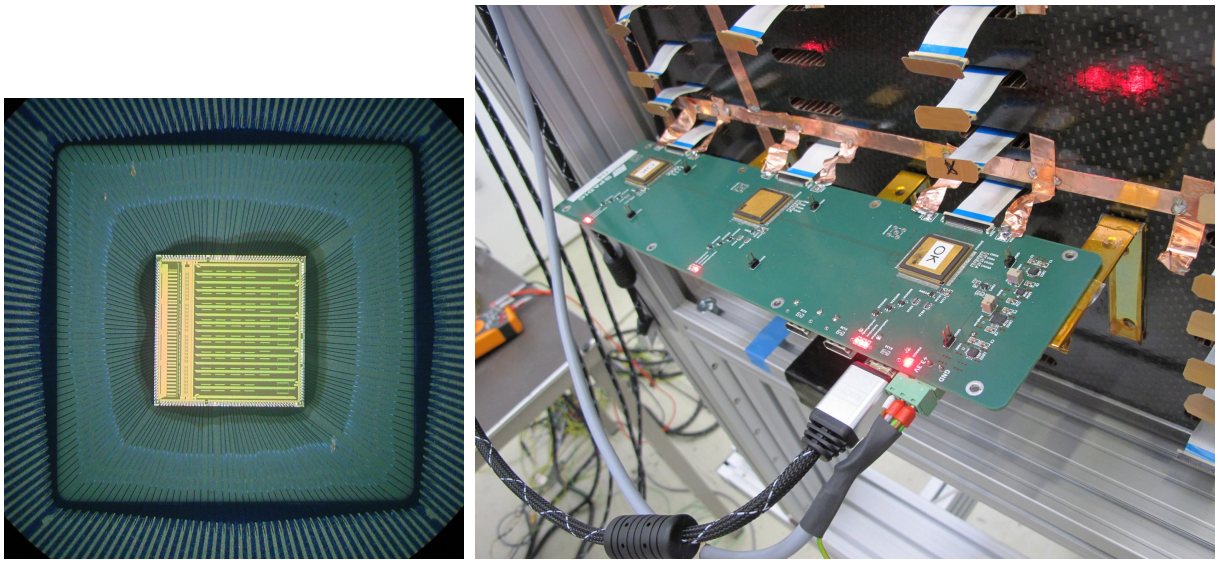

Figure 7.3: Left: Bonding detail of a SPADIC 1.0 mounted in a QFP176 ceramic carrier. Right: FEB using packaged chips during a beam test.

120 ns), a power-down pin and improved overload recovery for the analogue part, a more efficient digital data format, and a digital baseline tracking feature. In order to reduce the size of the FEBs, SPADIC 2.1 will be assembled in BGA instead of QFP packages. It is expected that mass production for the full detector will be based on SPADIC 2.1. Table 7.2 shows some key parameters of the different chip versions.

	SPADIC 1.0	SPADIC 1.1	SPADIC 2.0	SPADIC 2.1
Year	2011	2015	2016	2017
Peaking time	80 ns	80 ns	240 ns	240/120 ns
ADC sampling frequency	25 MHz	25 MHz	16 MHz	16 MHz
Master clock	250 MHz	250 MHz	160 MHz	160 MHz
Interface	CBMnet	CBMnet	E-Link	E-Link
Package	QFP176	QFP176	QFP208	BGA196
Notes	first full size chip	bug fixes	new interface	production design

Table 7.2: Comparison of the different full size SPADIC versions.

7.1.3 Charge Sensitive Amplifier (CSA) and ADC

The analogue front-end consists of a classical arrangement of a CSA, a pole-zero compensation network and a shaping amplifier. The overall structure shown in Fig. 7.4 generates a pulse of shape

$$f(t) = A \cdot \frac{t}{\tau} \cdot \exp\left(-\frac{t}{\tau}\right) \quad (\text{for} \quad t \geq 0)$$

with peaking times $\tau = 80/240/120$ ns for SPADIC 1.x, SPADIC 2.0, and SPADIC 2.1, respectively. For SPADIC 2.1, an additional shaping order is switchable for which the pulse shape becomes

$$g(t) = A \cdot \left(\frac{t}{\tau}\right)^2 \cdot \exp\left(-\frac{t}{\tau}\right) \quad (\text{for} \quad t \geq 0)$$

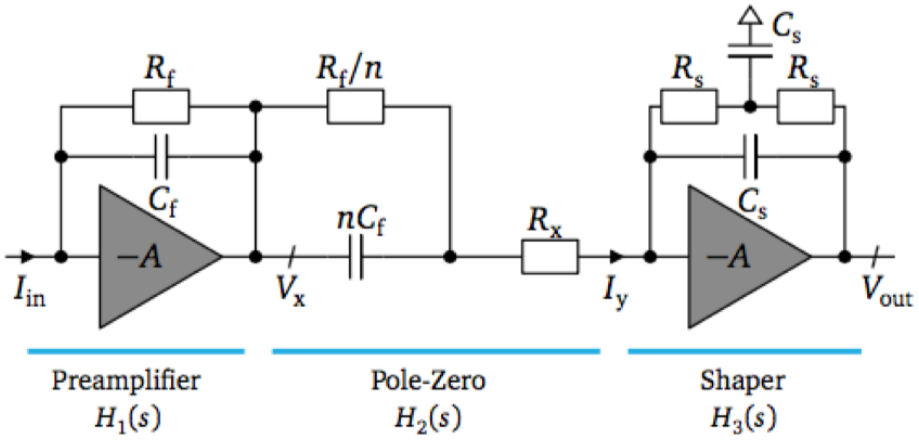

Figure 7.4: Principle of the charge amplification, pole-zero correction and shaping in the SPADIC.

with a peaking time of 240 ns given $\tau = 120$ ns. Pulses digitized with the internal ADC at a sampling rate of 20 MHz[1] are shown in Fig. 7.5. The pulse shape matches very well the prediction.

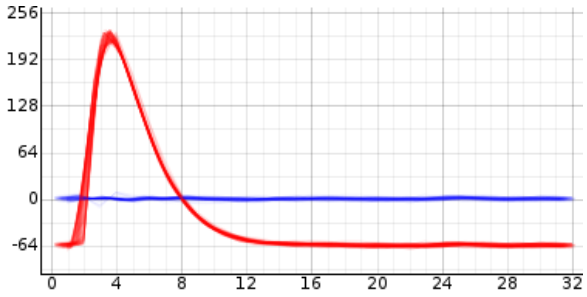

Figure 7.5: Digitized pulses generated by test injection. The flat blue lines are the residuals of fits to the predicted pulse shape.

The amplifier/shaper has been optimized for positive inputs signals. It consumes a power of ≈ 5 mW. In order to be able to also process negative signals from other detector types a less power-optimized front-end for negative input signals is available, consuming ≈ 10 mW. The type of front-end to be used can be configured by software.

The input referred noise expressed in electrons, i.e. the equivalent noise charge (ENC) has been determined on test chips as a function of input capacitance. Figure 7.6 shows simulations and measurements for a range of lengths of the input transistor. The best performance of $\approx 200\,e^- + 20\,e^-/pF$ is obtained for a length of 320 nm (dark blue curve with crosses). This choice is used for all later SPADIC versions.

The ADC is a custom pipelined design based on an special current memory cell [68]. It digitizes the shaper output with 9 bits at a rate of up to 25 MHz. The effective resolution, considering differential nonlinearities, is roughly 8 bits. The gain of the CSA in combination with the dynamic range of the ADC has been chosen so that a charge of ≈ 75 fC leads to a full scale ADC signal. In SPADIC 2.1, a low-gain mode is switchable, for which the gain is reduced by a factor of two.

Table 7.3 summarizes the most important parameters of the CSA/ADC part.

[1]The sampling rate is linked to the master clock frequency which was limited in the test setup.

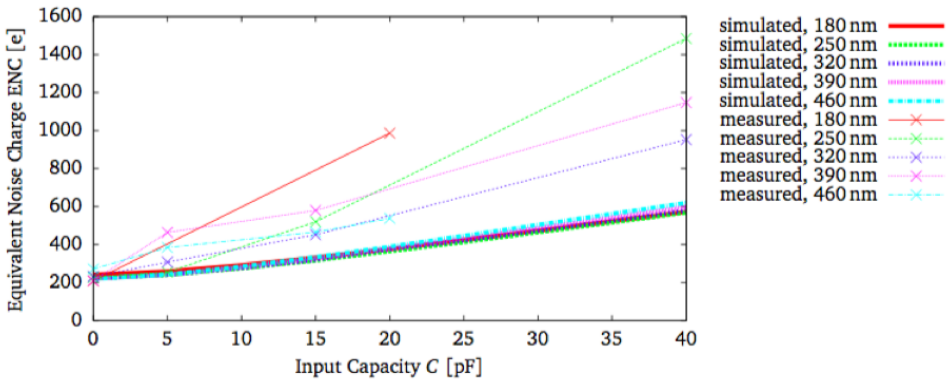

Figure 7.6: Simulated and measured ENC measured in SPADIC prototype chips for various lengths of the input transistor. The simulations (lower, solid curves) predict lower values than the measurements (upper curves with crosses). The observation that no dependence on transistor length is predicted by the simulations while a clear effect is measured indicates that the provided noise simulation models are inaccurate.

Parameter	Value
Shaper Type	CR-RC / CR-RC^2
Pulse shape	$\propto t \exp(-t/\tau)$ / $\propto t^2 \exp(-t/\tau)$
Peaking time	$\tau = 80/120/240$ ns
Noise	$\approx 200\,e^- + 20\,e^-/pF$
Input range	≈ 75 fC
Front end power	3.8 mW
Max. sampling frequency	25 MHz
Resolution	9 bits
ENOB	≈ 8 bits
ADC power	4.8 mW

Table 7.3: SPADIC Parameters of CSA and ADC.

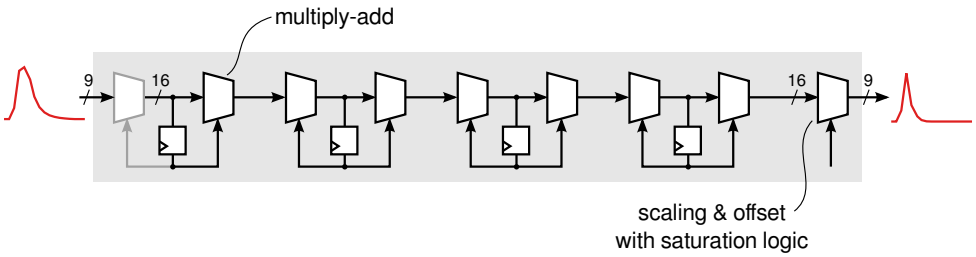

Figure 7.7: Topology of the IIR Filter. The first coefficient is hard-wired to zero, reducing the number of poles by one.

7.1.4 Digital signal processing

The digitized data is filtered by a digital IIR filter with the topology shown in Fig. 7.7. Four first order stages are followed by a final stage which scales and shifts the signal into a suited range and which handles overflow signals. Intensive simulations have been carried out to determine a good choice of the internal resolutions (affecting significantly the required hardware resources, in particular for the multiplier blocks) [69]. The main parameters of the filter are given in Tab. 7.4.

Parameter	Value
Order	4 zeros, 3 poles
Internal resolution	16 bits
Width of coefficients	6 bits
Available coefficients	$-1 \ldots 0.96875$ (in steps of $\frac{1}{32}$)
Width of scaling factor	9 bits
Available scaling factors	$-8 \ldots 7.96875$ (in steps of $\frac{1}{32}$)
Width of offset value	9 bits
Available offset values	$-256 \ldots 255$

Table 7.4: Properties of the digital filter part.

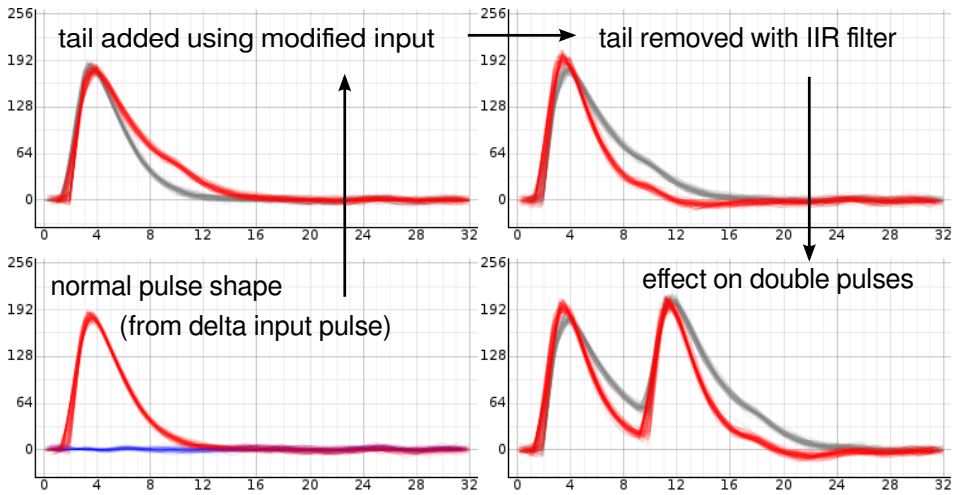

Figure 7.8: Measured pulse shape improvement achieved by the IIR filter (see text).

An example of filter action is shown in Fig. 7.8: the bottom left curve shows a digitized pulse obtained with standard charge injection. The upper left pulse shape is obtained by degrading the pulse intentionally with an additional injection. The shape of this distorted pulse can be improved by choosing suited coefficients in the IIR filter. The resulting signal (a real chip output is shown) is shown in the upper right curve. The lower right curve shows the filter action on a distorted double pulse.

The filtered digital signal is fed to a discriminator section which detects hits. A fixed threshold can be set, or the slope of the pulse (obtained as the difference of consecutive samples) can be used. Triggers from neighbor channels arriving either chip-internally or through dedicated chip pins can initiate a pulse readout as well. When a pulse is detected several sampled data values (up to 32) are tagged for readout. The pattern of values ("selection mask") is freely programmable so that a compromise between information content and data volume can be found. Figure 7.9 shows this unique pulse picking feature for two cases. For *multi-hits*, which are triggered in short

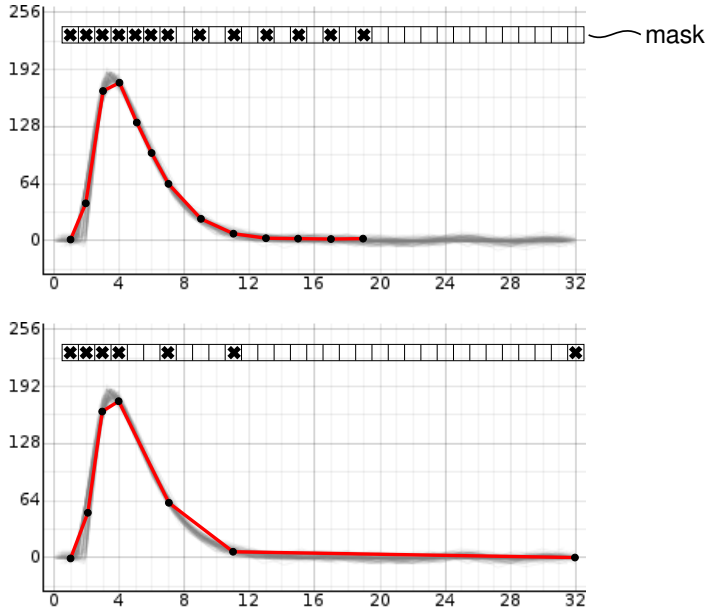

Figure 7.9: For each detected hit, a freely programmable set of signal samples are read out. Two examples sets are shown.

succession after a previous hit, an alternate selection mask is used that can be programmed independently. Such hits are flagged to distinguish them from isolated single-hits.

Furthermore, a running average of the digital signal is continuously calculated. The calculation is suspended while there is a hit. The resulting average baseline value can be included in the hit messages instead of the first regular sample which would indicate the instantaneous baseline value.

Field	Size (Bits)	Purpose
Channel number	4	Identify one channel within a group of 16 channels
Timestamp	8	Event time within one 'epoch'
No. of samples	2	Cannot be unambiguously determined from the event size
Hit type	2	Trigger source (e.g. self, neighbor)
Multi-hit flag	1	Indicates potential pile-up

Table 7.5: Metadata contained in a regular hit event.

Apart from the pulse shape information, further data like a timestamp or the trigger type that caused the hit is combined to a hit message (see Tab. 7.5), which consists of several 24-bit *Hit frames* as defined in the data format of the STS-XYTER, with customized payload usage. The shortest possible message consists of two 24-bit frames and can contain up to two samples. For additional samples included in the event, the message length increases according to the formula shown in Tab. 7.6, up to a maximum length of 14 frames for 32 samples contained.

The hits are buffered in a FIFO in each channel. 16 of these FIFO data streams are merged to one serial data stream, two of these streams leave the chip via the CBMnet or E-link interface. CBM has requested that the events leaving the chip are ordered according to their hit-time. This complicates the merging of the FIFO information into a single data stream (a simple round-robin arbitration is not possible). A special time ordering FIFO has been introduced to control the event selection. This circuitry, sketched in Fig. 7.10, is quite complicated, because it has to cope

Number of samples	Message length (24-bit frames)
$0 \leq N \leq 2$	2
$1 \leq N \leq 32$	$\lceil \frac{9N+20}{22} \rceil$
32	14

Table 7.6: Hit message length as a function of the number N of requested samples per hit. The minimum message length is 2 frames. For each additional sample, 9 more bits must be contained in the message, while each additional frame allows 22 more bits. There is a 20-bit offset which consists of the metadata and headers.

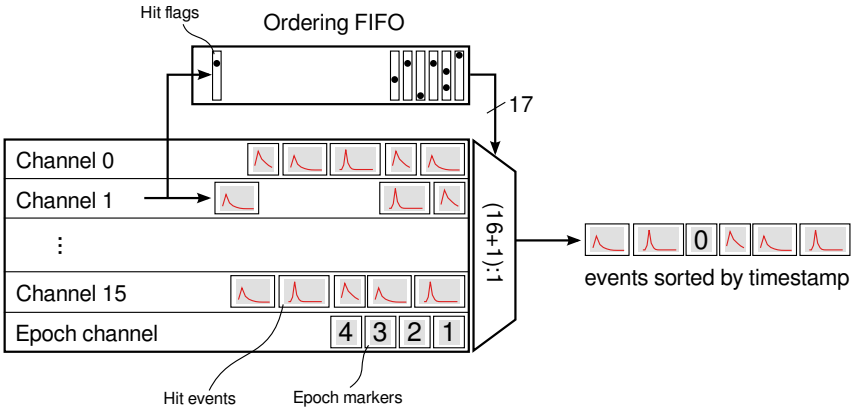

Figure 7.10: Principle of the time-ordering feature of events, implemented per group of 16 channels.

with different event sizes, with multiple events per timestamp and it must correctly react and recover from FIFO overflow conditions.

It is ensured that if a wraparound of the local timestamp counter occurs (one "epoch" has passed), an epoch marker is sent, such that all hit messages generated in one epoch are framed between two epoch markers, which allows that the absolute event times can later be reconstructed unambiguously. The size of the timestamp contained in each hit message (8 bits) is chosen to balance the message size with the rate of epoch markers that necessarily occupy the link.

Besides the regular hit events and epoch markers, there are other types of messages defined, which can notify about exceptional conditions like missed events due to full buffers.

7.2 The readout chain

7.2.1 TRD readout concept

The general concept of the TRD readout chain is summarized in the Figs. 7.11 and 7.12. The main components are the FEBs, ROBs and the input nodes containing the CRI boards. The communication between those main blocks is made by different data transport links that depend on the hardware used. The FEBs are mounted directly on the detector modules and convert the TRD signals into discrete messages. As presented before in Sect. 7.1, the SPADIC v2.1 chip, as the main component of the FEBs, will be used as front-end ASIC for the TRD.

The FEBs are directly connected to the ROBs via E-links (two per ASIC), which are also located on the TRD modules. The ROBs employ GBTx chips to provide the optical link connection between the TRD modules and the CRI boards. While their main task is to transport the data from the ASICs to the CRI boards via the uplinks, they also provide downlinks which

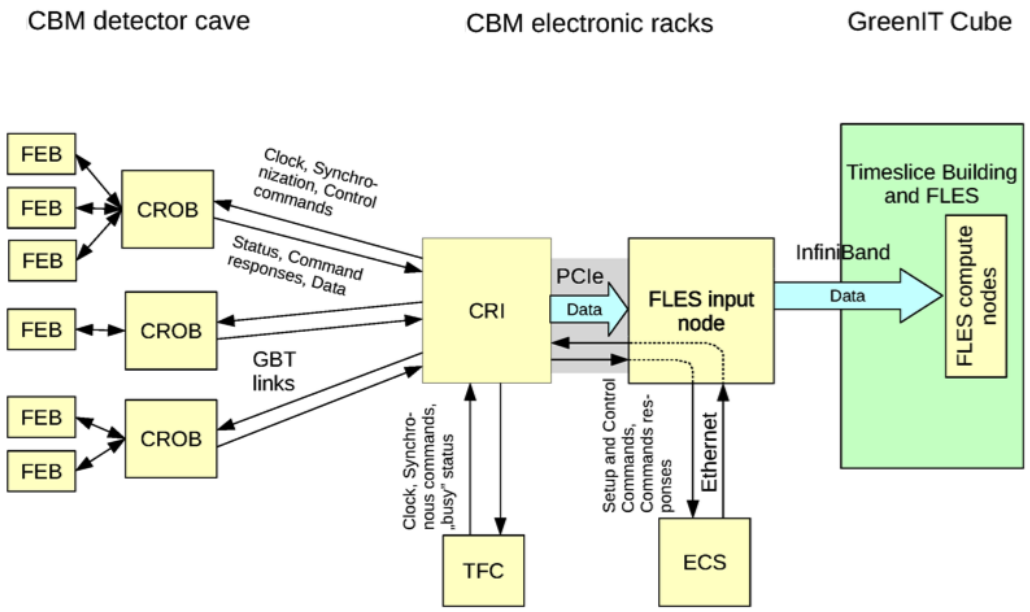

Figure 7.11: Schematic view of the CBM readout concept.

allow to send control commands to the SPADIC chips and take care of the clock distribution and synchronization.

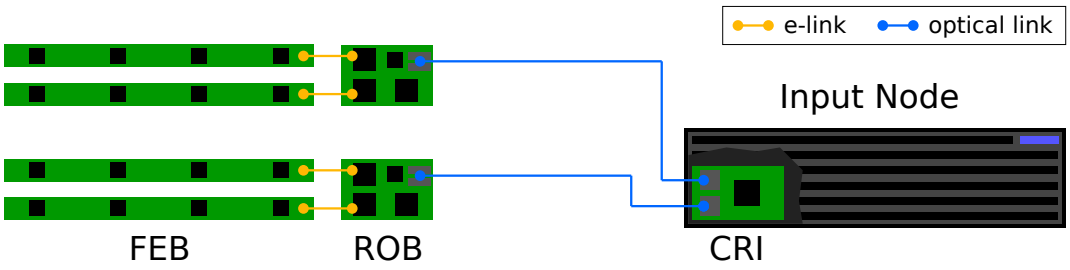

Figure 7.12: Schematic view of the TRD readout chain up to the CRI input nodes.

The TRD geometry and readout scheme has been optimized such that only one type of readout board, namely ROB3, is required. These boards feature the following components: $2 + 1$ GBTx chips, four optical links, one VTRx and one VTTx. The GBTx chips have been developed at CERN for the LHC upgrade program and are designed to reliably transport data, timing and control signals between the experiment and the off-detector electronics in an environment with very high levels of radiation and magnetic field [70].

Module type	1	3	5	7
Number of modules	40	96	32	48
FEB type	10s	10s	04n / 05n	04n / 05n
ASICs/FEB	10	10	$4+5$	$4+5$
FEB/module	8	2	2×12	2×4
ROB3/module	4	1	6	2
Number of optical fibers	640	384	786	384

Table 7.7: DAQ components required for the full TRD readout.

The numbers of components needed for the TRD readout chain are summarized in Tab. 7.7. The optical fibres listed there connect the ROBs with patch panels at a given detector layer. These in turn will be connected to the CRI boards via additional 2176 simplex fibers, subdivided into 544 downlink (46 × 12-fold MPO) and 1632 uplink (136 × 12-fold MPO) fibers. Each CRI board will be equipped with 24 transceiver (CRI-24), so that it can connect to eight ROB3. Thus, overall 68 CRI boards will be needed to receive the data from in total 544 ROB3 boards.

The CRI boards are operated in dedicated input nodes which are located outside of the CBM cave. They contain a FPGA that acts as a readout controller between the FEE and the First-Level Event Selector (FLES) input nodes. The communication between CRI and FLES is realized with PCIe bus. Finally, the data will be transported via Infiniband to the FLES compute node located in the GreenITCube computing center. A detailed description of the current common DAQ system development will be available in the CBM Online TDR [71].

The CRI boards also provide a data preprocessing stage, in the following called feature extraction, which will allow for a further reduction of the data volume. The feature extraction stage implements preprocessing algorithms in order to extract a relevant set of features from the input signals, such as cluster finding and the extraction of the total cluster charge. A description of the feature extraction is presented in Sect. 7.4.

7.2.2 TRD readout prototype

Figure 7.13: TRD readout chain using the SPADIC v2.0 ASIC and AFCK boards.

In order to verify the readout concept in the laboratory and during test beam campaigns, several prototype configuration have been implemented. The latest of these developments combines SPADIC v2.0 chips with so-called AFCK boards as receiver cards (see Fig. 7.13). This readout chain is the first one compatible with the final GBTx based readout scheme as presented in the previous section. It has already been used successfully for test beam measurements at the CERN-SPS in 2016 and at DESY in 2017 (see Sect. 4.5.4).

A detailed overview on the internal structure of the AFCK is shown in Fig. 7.14. Similar to the planned CRI boards it contains a FPGA which allows to implement a feature extraction stage at the receiving end of the GBTx optical link. It therefore also allowed to develop and test several feature extraction algorithms, as described in Sect. 7.4, even though the final readout chain is still under development.

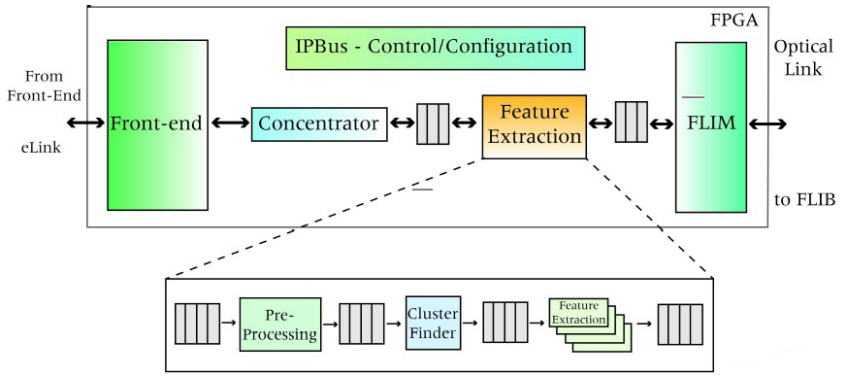

Figure 7.14: Detailed view of the components implemented on the AFCK boards. The front end transfer link is based on GBTx and the back end is based on FLIM.

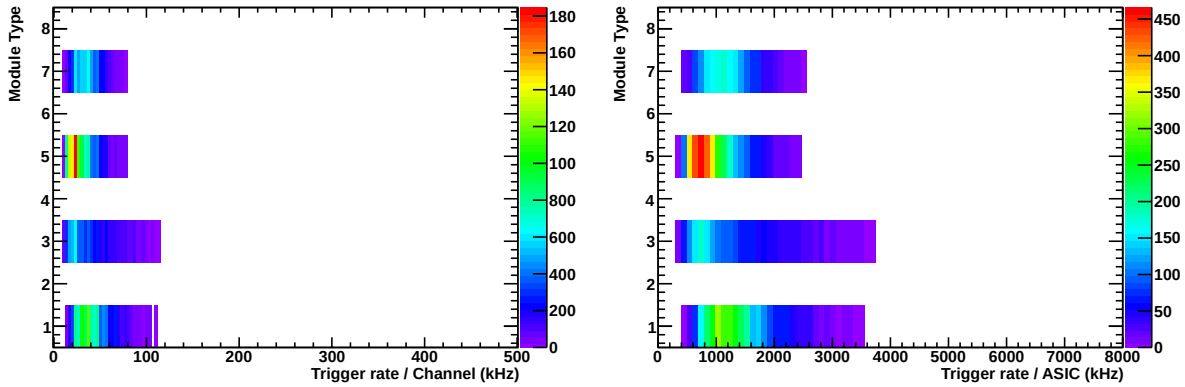

Figure 7.15: Hit rate simulation for 10 AGeV Au + Au collisions (compare to Fig. 4.9) including FNR trigger logic in anode wire direction of one adjacent channel per primary trigger for the different module types. Shown is the trigger rate per channel (left panel) and the trigger rate per ASIC (right panel).

7.3 Data transport and bandwidths

The TRD readout chain, as outlined above and summarized in Tab. 7.7, has been configured such that for the initial phases of detector operation at reduced interaction rates an uncompressed data stream can be transported in order to be able to fully debug the system. Therefore, this chain will on one side allow the transmission of the data rate expected at the SIS100 after moderate online reduction without problems, but on the other side would also still be sufficient for an operation at the SIS300. In the following we discuss the data rates expected in different configurations in relation to the available bandwidth.

The expected hit rates per channel and per ASIC, corresponding to Au + Au collisions at 10 AGeV as shown in Fig. 4.9, are summarized in Fig. 7.15. For the small modules of type 1 and 3 the hit rates per channel stay below 120 kHz and for the larger types 5 and 7 they are even below 80 kHz. The calculation of the hit rate per ASIC is based on the SPADIC data format (see Tabs. 7.5 and 7.6) and includes epoch messages and meta data. Based on this number one can then calculate the expected distributions for the data rate per ASIC for different numbers of transmitted signal samples, as shown in Fig. 7.16 for the different modules types. The upper bandwidth limit of the foreseen readout chain will be 640 Mbps, since each ASIC is connected via two E-links providing 320 Mbps each. For the small module types 1 and 3 this bandwidth

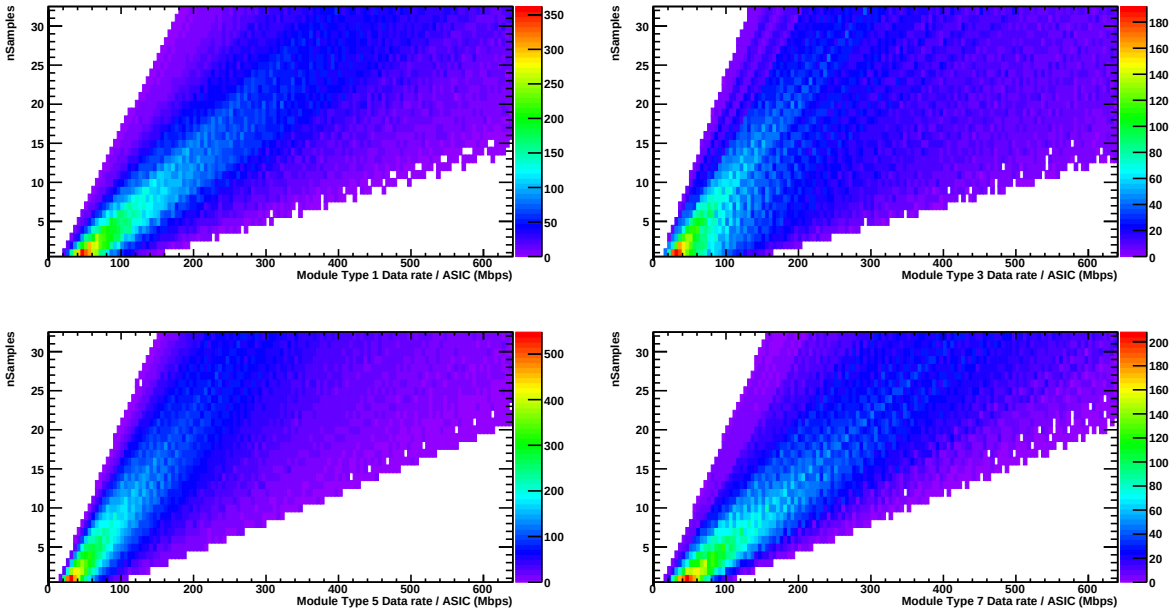

Figure 7.16: Resulting data rate for the four used module types as a function of the number of transmitted pulse shape samples.

will be exhausted for about 13 signal samples at full interaction rate, while for the large ones (5 and 7) 20 samples can still be accommodated. In practice, one would reduce the number of samples to values around seven. This configuration will still allow a good characterization of the signal shape and its baseline at a reduced data volume which fits comfortably into the available bandwidth. Figure 7.17 presents the data rates for the ASICs positioned at different positions on the four module types, assuming seven transmitted signal samples. In this configuration all ASICs stay well below the bandwidth limit of 640 Mbps. Based on this results with seven signal samples, a maximal data rate of 1.3 Tbit/s for 10 MHz minimum bias Au + Au collisions at 10 AGeV is expected for the full TRD with four layers.

7.4 Feature extraction

Feature extraction is the data preprocessing stage of the TRD DAQ chain. It aims at delivering event-filtered and bandwidth reduced data to the FLES. For this purpose it employs multiple processing algorithms which find and extract regions of interest within time series signals. For the requirements of the TRD the relevant signal processing stages are baseline correction and cluster finder. Possible applications and their implementations are described in the following subsections.

The feature extraction is based on the information provided by the SPADIC message format. A SPADIC message is composed of multiple message words, as explained in Sect 7.1, and contains a couple of metawords (e.g. timestamp, channel ID, group ID, and hit type) and the raw data from the ADC, which can be configured to provide a maximum of 32 samples.

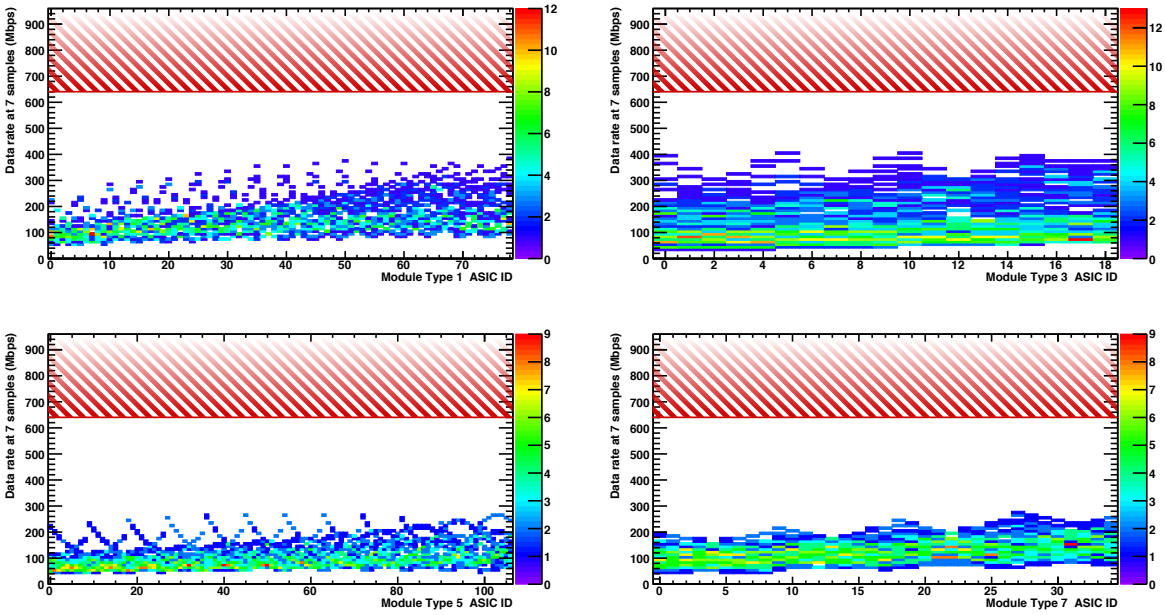

Figure 7.17: Resulting data rate for the four used module types for the different ASICs positioned on these modules, assuming seven transmitted signal samples. The upper bandwidth limit is illustrated by the red areas.

7.4.1 Applications

7.4.1.1 Baseline correction

The purpose of the baseline correction is to decrease the noise and systematic effects. The module has three operation modes:

a Fixed mode: A constant value stored in a register is subtracted.

b Bin dependent: For every value of the current message, a value stored in a memory is subtracted.

c.1 Variable: The last three time bins of the time dependent signals are averaged. This average value is then subtracted from all the message time bins. The calculation is performed for every message independently.

c.2 Variable: The first sample in front of the rising edge is subtracted from all the message time bins. The calculation is performed for every message independently.

Depending on the SPADIC message or, more precise, message stop type there are different default methods to be applied in order to perform a robust online baseline subtraction. The default case is a normal message stop type. These messages have a predefined number of samples (between 1 and 32). The minimal required number is two, i.e. one sample of the amplitude maximum and one to measure the current baseline of each individual channel, either as a pre-sample or a sample at a maximal distance relative to the amplitude maximum. For sample numbers larger than that the pre- or last message sample(s) can be used to calculate and subtract the up-to-date channel baseline.

The second case is the so-called multi-hit scenario (compare to Sect. 7.1). These messages have a number of samples smaller than the normal predefined one. This is due to the appearance

of a new detector signal during the message building within the predefined hit time window. The second signal is therefore positioned on top of the ion-tail slope of the previous one. A subtraction of the last time bins average would lead to an overcompensation of the baseline. This can be avoided by three different approaches:

- Subtraction of the pre-sample.
- Subtraction of a fixed measured baseline value.
- Subtraction a fitted baseline offset using the SPADIC response function.

However, the described effect can be reduced by applying the digital IIR filter as mentioned in Sect. 7.1. Therefore, it is also an option to avoid online processing of multi-hits within the CRI layer and to just transport them into the FLES for detailed analysis.

7.4.1.2 Signal preprocessing

Online data compression can be achieved by preprocessing the signal shapes within the CRI layer. By integrating the signal amplitude over a fixed number of samples the data volume will be reduced by a corresponding factor. Another alternative is to fit of the measured signal samples with the SPADIC response function to extract the exact position in time of the amplitude maximum, its amplitude value and the baseline offset. This approach would in addition also allow the separation of multi-hits in time direction, where the signal of the second hit sits on top of the tail of the previous one.

The complexity of the preprocessing algorithms which can be afforded on the FPGAs of the CRI boards of course depends on which fraction of the available resources is free for this purpose and not used for other data acquisition processes.

7.4.1.3 Cluster finder

The cluster finding in space and time is a promising option for data preprocessing, since the data from each SPADIC is already time sorted. The memory consumption for the cluster finding in time direction can be efficiently reduced compared to other type of ASICs which do not support time sorted data transport. The FNR trigger logic guarantees an equal time stamp for the messages of a physical charge cluster measured by a single ASIC. The ability of cluster merging between different ASICs of the same FEB or even the full chamber within the CRI layer is being investigated in details. An online cluster finding would create the possibility of further data compression by calculating the hit position based on the full charge information of the cluster.

7.4.2 Performance study

The following studies were done with a simulation chain emulating the prototype readout as described in Sect. 7.2.2. Even though there still will be differences to the final DAQ chain as the CRI-boards will be equipped with a different type of FPGA, these studies should nevertheless give a good impression about what precision can be achieved with the feature extraction at the CRI stage.

The simulation chain is shown in Fig. 7.18. A SPADIC 2.0 data generator uses as input GARFIELD [44] simulations for different types of TRD chambers. The GARFIELD data are processed by a software representation of the SPADIC 2.0 ASIC processing blocks to correctly generate a stream of hit messages as output. An emulated shaper applies the SPADIC 2.0 peaking time. The PRF is computed following the approximation of Mathieson [72] (see Eq. 9.1) to generate a representation of the charge deposition along the pad plane. An ADC model quantizes

the signals to 9-bit resolution. Finally, the signals are packed into SPADIC 2.0 hit messages. The corresponding meta data that is included in a hit message, e.g. time stamp, channel ID, group ID and stop type, are internally handled by the SPADIC data generator to simulate as close as possible the behaviour of the ASIC. The simulation engine runs three types of simulations, as illustrated in Fig. 7.18:

1 Hardware simulation: The data is continuously sent to the Data Processing Board (DPB) by a second DPB that acts as a SPADIC 2.0 emulator called *Streamsim*. In this sense the DPB sees no difference between the SPADIC 2.0 emulator and the real SPADIC 2.0 ASIC. The FLIB/FLES receives microsclices containing the feature extraction data computed by the preprocessing algorithms on the DPB. The data is then stored as a TimeSlice Archive (TSA) file.

2 HDL simulation: In scenarios where no DPB/Streamsim devices are available the HDL sources can be simulated by a third party simulator (Xilinx Vivado Simulator, XSIM). In order to provide a simulation as close as possible to the FPGA implementation, the Xilinx Simulator Interface (XSI) is used to provide the correct stimuli to the HDL design by its C/C++ Application Programming Interface (API). No microslice building is available at this level, therefore a time slice builder (*TSA builder*) is used to generate a TSA file from the simulation output.

3 Direct interface to CBMROOT: The data generated from the SPADIC data generator simulation engine is packed into a TSA file by the *TSA builder*. This is used by CBMROOT for reconstruction and analysis against the hardware and HDL simulation data.

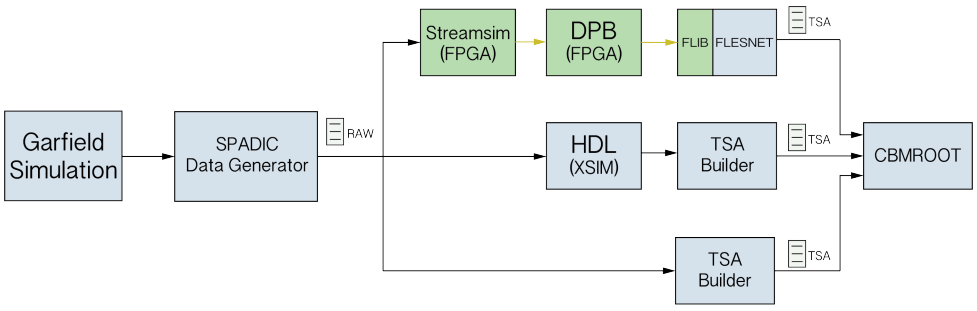

Figure 7.18: Feature extraction simulation chain. Green blocks represent operations implemented in hardware (FPGA), while blue blocks are operations implemented in software. The yellow line between the DPB and the FLIB represents an optical 10 Gbps data transmission interface.

The last step in the simulation chain is the the CBMROOT analysis. At this moment at least two TSA files are available (the unprocessed SPADIC 2.0 data and the feature extraction data). The CBMROOT engine would apply similar feature extraction algorithms to the unprocessed SPADIC 2.0 stream and then compare the results with the feature extraction data.

Figure 7.19 shows an example the performance of the feature extraction algorithm. The minimum amount of information computed by the feature extraction is the total cluster charge (with a resolution of 12 bit or 8 bit), the cluster time (12 bit) and spatial position (12 bit). Without considering any data transmission header, the feature extraction delivers a total amount of data of 36 bit with a cluster charge resolution of 12 bit or alternatively 32 bit for a cluster charge resolution of 8 bit. The performance was evaluated by comparing the values calculated in the feature extraction stage to the ones reconstructed with the offline software (see Sect. 9.3) using the full offline information.

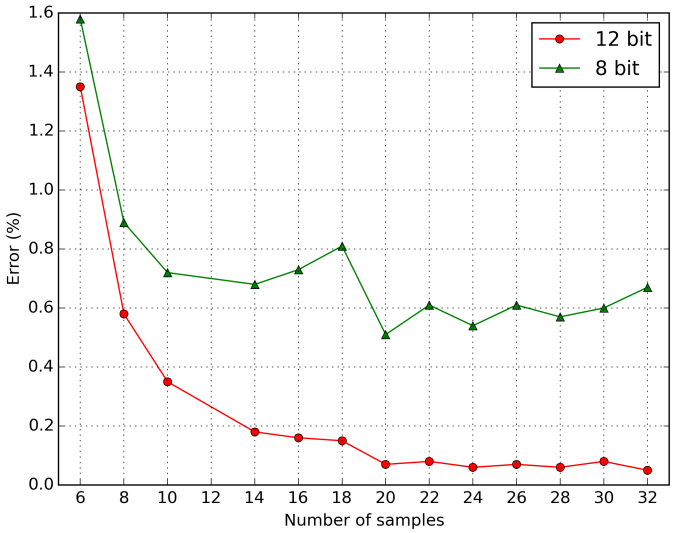

Figure 7.19: Performance study of the feature extraction algorithms using simulated data. Shown is the accuracy of the online reconstructed total cluster charge, determined by comparing the results of the online and the offline cluster finder as a function of the numbers of signal samples. The values represent a charge calculation resolution of 12 bit and 8 bit, respectively.

The online determined cluster charge depends naturally on the amount of information, i.e. number of signal samples evaluated and on the cluster charge resolution. Fewer samples transferred to the DPB layer result naturally in a less precise charge determination, as does a reduced (8 bit instead of 12 bit) resolution. However, the online values are always very close to the offline value, i.e. the deviations always stay below 2.0 %, even in the case of only six signal samples and 8 bit resolution of the algorithm (see Fig. 7.19). As the foreseen bandwidth easily allows to transfer at least seven signal samples (see Fig. 7.17), an accurate preprocessing of the data in the DPB layer should therefore be possible with sufficient accuracy.

Chapter 8

System Integration and Services

This chapter summarizes the services needed for the operation of the CBM-TRD, such as mechanical support structure, gas system, Low Voltage (LV), High Voltage (HV) and cooling. A description of the individual design options and their construction is given.

8.1 CBM-TRD commissioning and installation

After the ROCs have been built and tested, they have to be equipped with the FEE components. These will be mounted on the chambers and first tests of the fully equipped detector modules will be performed. The tested modules are then shipped to the CBM location on the FAIR area, to be integrated into layer segments. This structures are composed of $2 \times 5 = 10$ large modules in each of the outer two segments (light gray area shown in Fig. 8.2) and $12 \times 4 - 2 = 44$ small modules in the inner segment (dark gray area shown in Fig. 8.2). The segment integration will be done at the ground level of the CBM building (see Fig. 8.1).

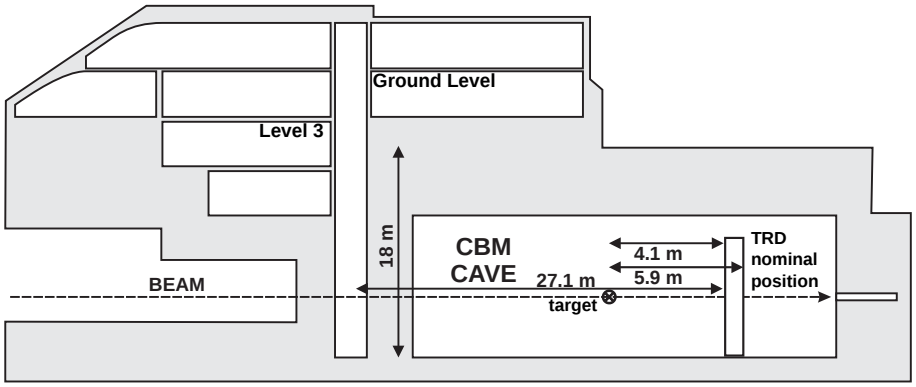

Figure 8.1: Schematic layout of the CBM building.

A temporal mounting structure is needed in this area to build the segments in a hanging position, since a segment is constructed such that it will support the load only in a vertical orientation. First gas tightness tests will also be performed here. The TRD gas system constructed for the test beams will be used for this purpose and installed during the installation time on the ground level of the CBM building. A minimal HV/LV and DAQ system will also be needed at this location. As additional infrastructure a lifting platform will be required as well. The finally assembled and tested segments are craned from the ground level of the CBM building into the cave and there integrated into full layers. The radiator box modules are mounted afterwards in a separate mechanical structure in front of each layer.

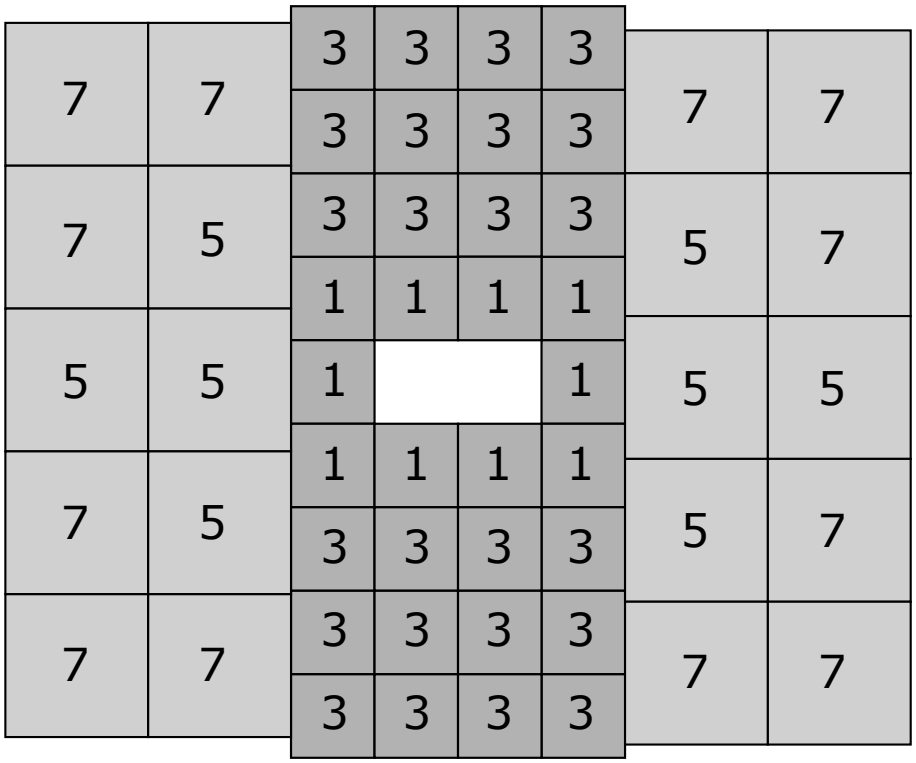

Figure 8.2: The arrangement of the different module types in one TRD layer. A layer can be separated into three vertical segments, two outer ones (shown in light gray) consisting of large modules, and a center one (shown in dark gray) containing only small modules.

8.2 Mechanical structure

The TRD components, whose weight can already now be determined relatively accurately, are the ROCs, which contribute with 1.51 t, and the radiators that will weigh 1.06 t. In addition, there will be the front-end electronics ($\sim$ 250 kg), cables, screws and other materials whose contribution is more difficult to estimate. However, a reasonable assumption on the the total weight of the TRD modules should be around ~ 3.4 t. This weight has to be supported by the frame structure, which has to be stable within ± 1 mm.

Figure 8.3 shows in the left and middle panel the foreseen support structure for one TRD segment based on KANYA profiles. This arrangement provides the necessary stability, while keeping the material in the active region of the CBM detectors at a relatively low level. The cross section of the two side bars ($30 \times 50\,\mathrm{mm}^2$), which run vertically in the middle of the structure, has been chosen such that they effectively have a material budget of $X/X_0 = 17\,\%$ only. However, it is planned to systematically evaluate the options with the help of a mock-up structure in the laboratory, in order to determine for instance whether the side bars can be made from even thinner profiles (e.g. $30 \times 30\,\mathrm{mm}^2$) without reducing the stability. A further reduction of the material can be achieved by replacing the aluminum side bars by carbon sheets, as presented in the lower right panel of Fig. 8.3.

The above described support frame will be mounted inside an outer support structure, which will be located outside of the active area of the CBM experiment. Therefore, it can be composed of relatively rigid and heavy steel beams. This structure should allow the independent movement of the each TRD layer along the beam direction within a range of about 1 m, so that an easy access to the backside of each layer is possible, e.g. for a replacement of front-end electronics components. This would require a rail structure on the support platform of the TRD along

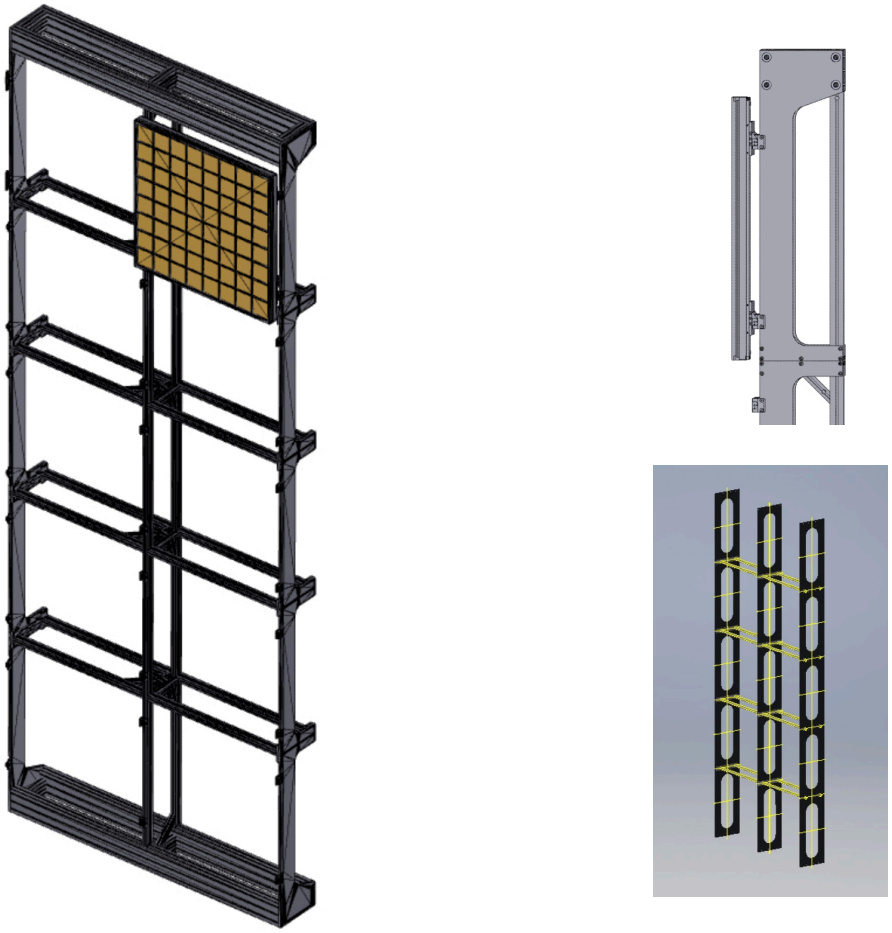

Figure 8.3: Drawing of the support structure for one TRD segment with large modules (left panel). A detailed side view is shown in the upper right panel, while the lower right panel displays a possible alternative for the side bars made from carbon.

which the support structure can be moved back and forth.

8.2.1 ROC mounting

The mounting of the individual TRD modules onto the support structure should allow for an easy removal of any given module without the need to dismount the adjacent ones. This can be realized with a system as depicted in Fig. 8.4. The modules, which are equipped with the mounting structure shown in turquoise, will be pushed from the front onto the connecting part on the support structure. By tightening the two screws on the side, the mounting structure will be held tight by the outer clamps shown in dark gray. By allowing for a 2 mm distance between the modules they can be mounted and removed individually, using a special handling device without affecting the neighbouring ones. This will allow for a fast replacement of malfunctioning modules during shutdown periods.

8.2.2 Radiator mounting

A hard foam is used to build an individual radiator nesting (five sides closed) for each module with a depth of 30 cm for the radiator type H. The box provides mechanical support and, being

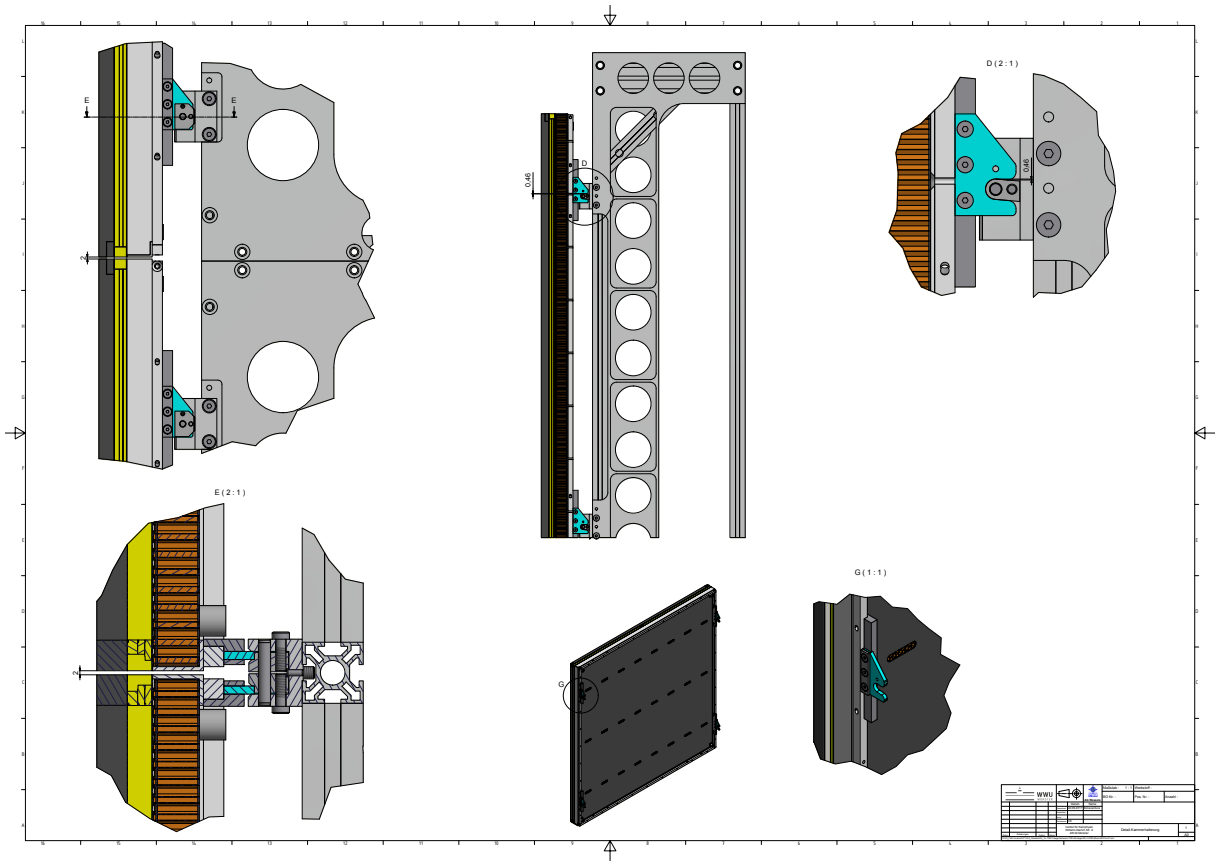

Figure 8.4: Details on the mounting of the modules to the support structure.

a foam, acts to some extend as a radiator at the same time. The foam foil stack is piled inside of the box. The open side of the box is orientated towards the entrance window of the chamber and the support grid, which keeps the first foil in position. At the same time the radiator box limits the flexibility of the support grid in direction of the radiator. This construction provides additional mechanical protection to the entrance foil window, the most fragile component of the detector. Also, it provides a quite flexible and modular design, since every ROC will be equipped with its own radiator box which can easily be removed.

It is planned to mount each radiator box individually to the TRD support structure. Since the solid foam encasing provides a basic mechanical stability to each radiator box, it can be attached to the ROCs by thin clamps which are wrapped around the outer edges of the radiator and extend through the 2 mm gap between the ROCs towards their back. These will be pulled tight in order to position the radiators as close as possible to the ROCs. However, in order to avoid possible deformations of the ROCs, they should not carry the whole weight of the radiators, especially in the case of the large modules 5 and 7. Therefore, an additional thin supporting device at the front of the radiators can be foreseen. This might simply be realized by thin Nylon threads hanging from above and holding the front of the radiators.

8.2.3 FEB mounting

In order to distributes the FEB material as homogeneously as possible on the back of the ROC, it is foreseen to mount them flatly onto the back panel (i.e. at an angle $\alpha = 0$, see Tab. 4.5). This also facilitates the design of a needed support structure, which could in this case just be simple plastic screws, and simplifies the cooling since the heat exchange can be realized by laminar air

flow. For the modules types 3 and 7 such an arrangement can be realized without problems as the distances between the readout cable holes is relatively large. However, for module type 1 and 5 the space between the cables will be very limited (see Fig. 5.22), which therefore puts special constraints on the FEB design.

8.3 Gas system

The CBM-TRD has an overall gas volume of $1.36\,\mathrm{m}^3$ in the SIS100 configuration with four layers. The total number of gas enclosures (detector modules) in the system is 216. There are two different module sizes $57 \times 57\,\mathrm{cm}^2$ and $99 \times 99\,\mathrm{cm}^2$ (see Sect. 4.3). The total gas depth in z-direction is 12 mm for both module types. This results in a rather disadvantageous, from the gas tightness point of view, volume-to-surface ratio of $1.36\,\mathrm{m}^3/122.6\,\mathrm{m}^2 = 0.012\,\mathrm{m}$. For this reason, special provisions have to be taken in order to minimize gas leakage (see Sect 5.4). In addition, a low-mass construction of the detectors is needed to reduce multiple scattering and TR-photon absorption in the material between radiator and active gas volume. The light construction mechanically limits the relative overpressure of the chambers to 2 – 3 mbar. In order to avoid electrostatic distortions due to deformation of the enclosing drift and pad electrodes, the overpressure at which the chambers are operated is limited to 1 mbar.

8.3.1 Gas choice

The choice of xenon as the noble gas in the mixture used for standard operation is determined by its large absorption, and subsequent ionization, cross section for transition radiation X-rays produced in a suitable radiator material. Because xenon is a high-cost gas (ca. 12 Euro/l), recirculation in a closed loop with a purification stage is mandatory. Optionally, one can foresee a recovery station in order to remove in particular nitrogen contaminations (see Sect. 8.3.2.4). The frequency in which the recovery would need to be performed depends on the in-flow rate of contaminants, but would be of the order of once per year. Thus, the cost of recovery plant needs to be put into relation with the price of new xenon fillings. In addition, xenon is a rather heavy gas (density 5.58 g/l). The density difference between the chamber volume and the surrounding air is 4.67 g/l. This means that the overpressure gradient of 0.46 mbar/m over a volume which extends over a height of 4.94 m is 2.28 mbar.

In order to avoid significant deformations of the thin entrance foil and pad plane structure, and to achieve an uniformity of operation of the whole system in terms of E/p (see Sect. 5.4 and Fig. 8.7), the maximum overpressure in each individual chamber should not be higher than 1 mbar. Thus, a suitable segmentation of the pressure regulation along the height of the detector is imposed by the choice of the noble gas. The typical quencher used in other TRD systems is methane, since its well known transport and quenching properties makes it a rather convenient choice. However, safety aspects, neutron interactions, and lifetime considerations make CH_4 a gas to be avoided. Therefore, the quencher of choice is CO_2, because it is non-flammable, contains no hydrogen, is a low-cost gas, and performs adequately. The concentration of quencher will be chosen as 15 %, as it has been operated in the ALICE-TRD. Because the maximum drift distance in a TRD module is only 5 mm, problems associated with electron attachment due to oxygen contamination in the presence of CO_2 are expected to be negligible. Concentrations of O_2 as high as 100 ppm are therefore affordable, since such a contamination would only affect the signal by $< 10\,\%$ (see discussion in Sect. 5.2). Another contaminant that needs to be monitored is H_2O. Following the ALICE-TRD experiences, the gas flow should be adjusted high enough that the H_2O intake remains on an affordable level (< 200 ppm).

Module (Manufacturer)	Purpose
Series 8B (VON ROHR)	Flow regulating valve
Pluto 22E 45-26 (HAUG)	Compressor
ZR800 (SYSTECH)	O_2 Analyzer
MGA3000 (ADC)	CO_2 Analyzer
DMT242 (VAISALA)	H_2O Sensor

Table 8.1: List of possible components for the TRD gas system and their purpose.

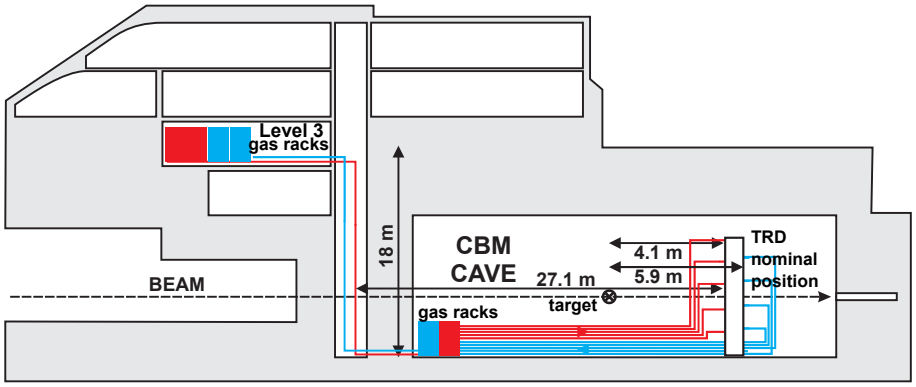

Figure 8.5: Schematic layout of the TRD gas system, showing the location of the different modules.

8.3.2 Layout

As explained in the previous section, the use of a high-cost gas makes a closed loop circulation system mandatory. The proposed system will consist of components that have been designed as standardized units for LHC gas systems. Table 8.1 lists as examples some components that have been used for the ALICE-TRD gas system. The mixing, purifying, and optional gas recovery are located in the gas handling area of the CBM building on level E30. The component sizes and ranges will be adapted to meet the specific requirements of the TRD gas system. An overview of the distribution system can be seen in Fig. 8.5. The basic function of the gas system is to mix the components in the appropriate proportions and circulate the gas through the TRD chambers at a pressure of < 1 mbar above atmospheric pressure. Some of the basic parameters of the TRD gas system are given in Tab. 8.2

Parameter	Values
Total gas volume	$1.36 + 0.5\,\mathrm{m}^3$
Gas mixture	Xe/CO_2 (85/15) (optionally Ar/CO_2 (80/20))
Working overpressure	1 mbar

Table 8.2: Basic parameters of the TRD gas system.

8.3.2.1 Mixing unit

Fresh gas that has to be added to the system will be provided by the mixing unit. The composition of the gas will be regulated by mass flow controllers for the separate components (see Fig. 8.6). They should have an absolute stability of 0.3 % over one year, and a medium term stability of 0.1 % under steady state conditions [45]. The estimated necessary fresh gas flow at operating conditions, which depends strongly on the leak rate, is expected not to be higher than 0.1 l/h. In

fact, in case of the ALICE-TRD even much lower values have finally been achieved ($< 20\,\mathrm{ml/h}$ [49]) and due to the conceptional similarities a comparable performance should also be possible with the CBM-TRD. Filling of the detector will be done in a closed loop circulation mode, where the purging gases O_2 and H_2O are continuously removed by the corresponding purifiers. Under normal operating conditions the mixing unit will replenish the gas which is lost from the system during the purification process or by leaks within the circuit.

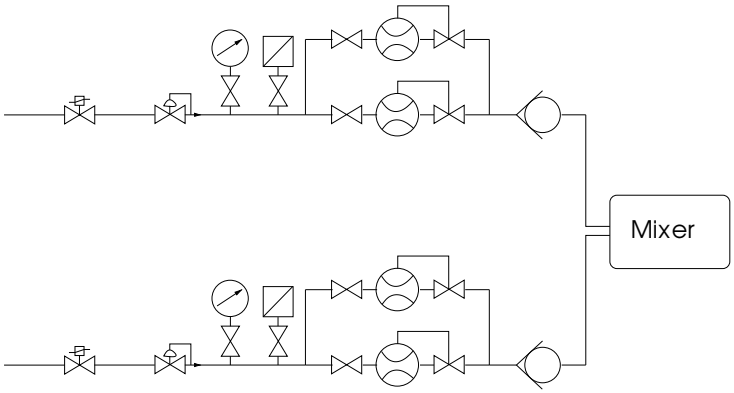

Figure 8.6: Gas mixing unit located in the gas handling area of the CBM building. The substantially different gas flows in the filling and running modes are controlled by two different mass flow controllers per gas line [45].

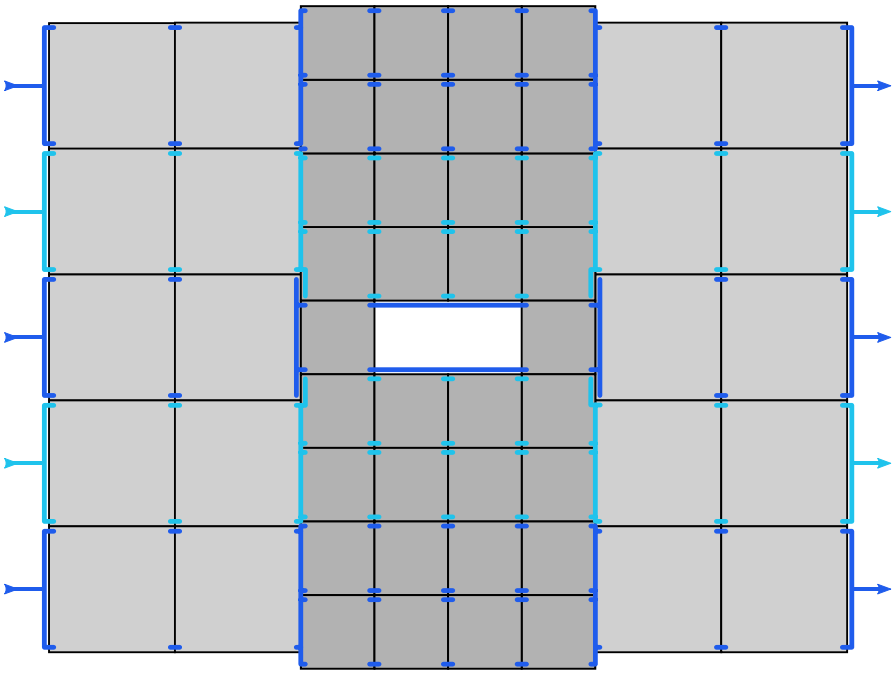

Figure 8.7: Sketch of the TRD gas supply chain. The layers will be divided vertically into five sections which are connected to individual supply and return lines.

8.3.2.2 Circulation and purification system

The gas mixture is circulated in a closed loop as shown in Fig. 8.5. Return gas from the detector must be compressed well above atmospheric pressure to pump it back to the gas handling area where it will be recycled through the purifier. The hydrostatic pressure over the total height of

the detector is approximatively 2.28 mbar. Since the detector working pressure is limited due to mechanical reasons to 1 mbar, a subdivision of the full detector into height sections is necessary. Furthermore, the flow and pressure regulation must be done in each section independently. In particular, the sensor for the pressure regulation must be as close as possible to the detector in order to minimize hydrostatical and hydrodynamical pressure differences between the chamber and the sensor. On the other hand, due to space limitations around the experimental setup, it is desirable to place as much hardware as possible in other areas. Taking into account these considerations, the following layout of the gas system is proposed and shown in Fig. 8.8.

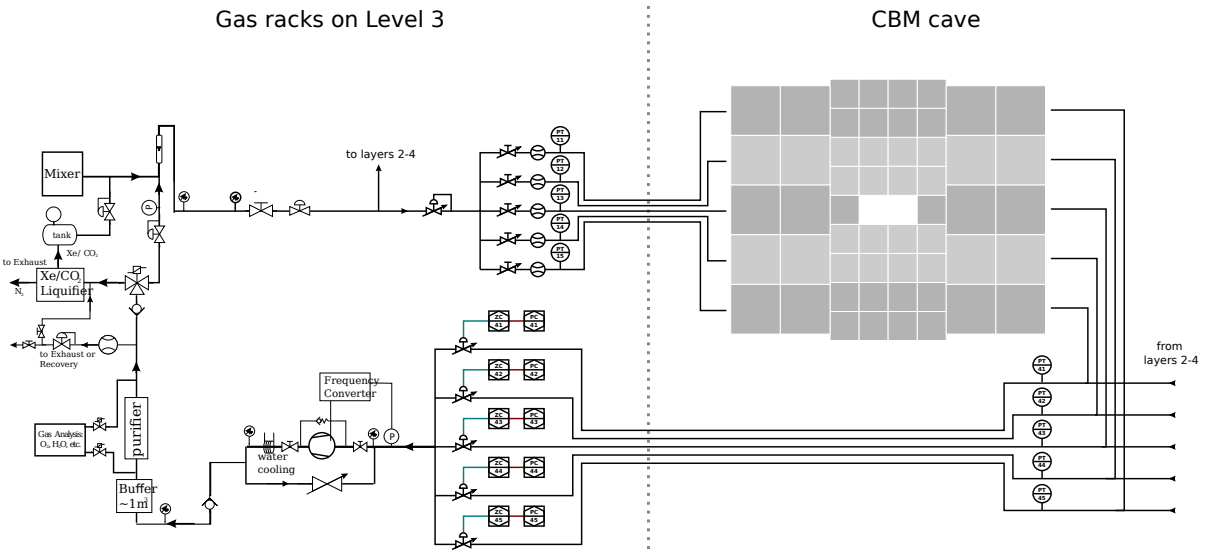

Figure 8.8: General layout of the gas loop [45].

Gas is distributed through a 20-line manifold (5 capillaries per detector layer), where the capillaries going to the detector are thin enough (around 6 mm inner diameter) to achieve a uniform, substantial pressure drop of almost 100 mbar. If all the lines have the same length and their flow resistance is the dominant fraction of the total flow resistance, the flow will be distributed evenly among the lines and an individual flow regulation is not necessary. Each line serves one sub-circuit consisting of 12, respectively 6, chambers per layer at approximately the same height (see Fig. 8.7). The feedthrough from chamber to chamber is foreseen to be realized by a short ($\sim$ 15 cm) pipe with an inner diameter of 8 mm, which results in a negligible total impedance to the gas along the 12 (6) served chambers. The four outlets of a given sub-circuit (corresponding to the four detector layers) are merged into one return line. The pressure sensor for a sub-circuit is located at this position. Therefore, a total of 5 return lines will run up to an accessible area, where the rest of the instruments for flow and pressure regulation will be installed. The pressure of each return line is accurately regulated by a flow valve. In addition, gas losses are compensated for by acting on the mixing unit flowmeters according to a pressure sensor located at the high pressure buffer after the compressor.

The purification system will remove oxygen and water contamination in the gas. This will be done with cartridges filled with activated copper. Two parallel purification units allow to run gas through one purification cylinder while the other one is being regenerated. Regeneration is done by heating the cartridges to 200 $^{\circ}$C under an Ar/H_2 (7 %) (Noxal) mixture.

8.3.2.3 Backup system

In case of a malfunctioning of the pressure regulation, for example due to a power failure, the two-way safety bubblers, located near the detectors, shall ensure that the maximum over- and

under-pressures that the detectors would be exposed to do not exceed 2 – 3 mbar. However, this mechanism should be regarded as the ultimate safety measure for the system. In case of an increase of the atmospheric pressure during such periods, the safety bubblers would allow air to be sucked into the detectors thus deteriorating the purity of the operating gas. The purifiers and the recovery station might therefore get rapidly saturated. In order to prevent air from entering the gas loop, a backup system for cases of failure has been foreseen. It consists of a permanent flow of CO_2 towards an exhaust, which passes one side of the bubblers. Thus, positive fluctuations of the ambient pressure result in an enrichment of CO_2 in the mixture, which, however, can be gradually compensated for by the fresh gas injection mechanism as the experiment is restarted. Negative fluctuations of the ambient pressure will lead in any case to a loss of some xenon.

8.3.2.4 Recovery station

Nitrogen, which enters the recirculation loop through leaks, cannot be removed by the purification system. Thus, a separation station is needed in order to extract the N_2 from the system and recover the xenon for recycling. This can be achieved with a special cryogenic recovery unit as sketched in Fig. 8.9.

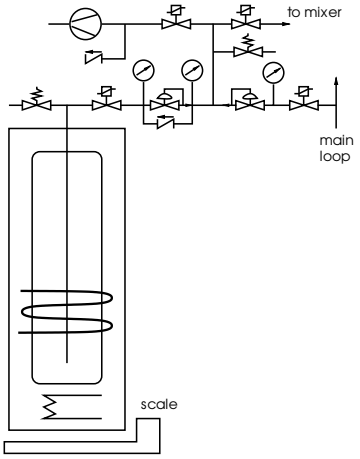

Figure 8.9: Schematic layout of a cryogenic plant for the separation of nitrogen from the gas mixture [45].

Gas	Freezing point (°C)	Boiling point (°C)
N_2	-209.86	-195.8
Xe	-111.9	-108.1
CO_2	-78.4 (subl.)	

Table 8.3: Freezing and boiling points of some gases relevant to the TRD gas system.

This concept has already been used by the ALICE experiment. The operating principle is based on the selective distillation of the gas by cooling it down to nearly the temperature of liquid nitrogen (LN_2). Because the freezing points of both, xenon and CO_2, are above the one of nitrogen, as listed in Tab. 8.3, one can freeze the xenon and the CO_2 by cooling down the gas mixture with LN_2 in a storage vessel, while keeping the nitrogen in the gas phase. A scale that weighs the vessel is used to control the amount of gas that enters the vessel. Once the desired amount has been frozen, the gas left in the vessel is pumped and vented out until the pressure

drops to essentially zero. Then, the vessel is brought back to room temperature. Usually, this kind of procedure is repeated once per year during shut-down periods.

8.4 Low voltage system

8.4.1 Power consumption

Component	Power consumption (W)
SPADIC	0.75
FEB_10s	7.5
FEB_04n	3.0
FEB_05n	3.75
GBTx	2.20
VTRx	0.63
VTTx	1.00
ROB3	8.23

Table 8.4: Estimated LV power consumption of individual readout components.

Component	Power consumption (W)			
Module type	1	3	5	7
FEBs	66	16	89	30
ROB3s	33	8	49	16
Module (A)	99	24	138	46
Module (B)	141	35	198	66

Table 8.5: LV power consumption per module. The values are given with (B) and without (A) 30 % heat dissipation in the DC-DC converters.

All following values are estimated based on the current prototype DAQ components. The final versions will be further optimized and the power consumption is expected to be lower. For the CBM-TRD it is mainly caused by the components listed in Tab. 8.4, resulting in a electric power consumption per module as listed in Tab. 8.5 and shown in Fig. 8.10. Here it is assumed that the SPADIC ASICs are operated at 1.8 V while the ROB3s will be operated at 1.5 V (GBTx), respectively 2.5 V (VTTx and VTRx).

In order to reduce the material introduced by the power bus bars to a minimum, we plan to use DC-DC converters placed on each ROC and FEB close to the load. In this case, the LV distribution can operate on a higher voltage of 12 V so that the cross sections of the power bus bars can be kept quite low. This reduces the material budget of the detector system and also minimizes the weight that needs to be carried by the support structure. However, the converters should not introduce additional noise and must be able to operate in a high radiation environment. Therefore, the preferred option are the FEAST DC-DC converters, which have been designed at CERN for exactly this purpose [73]. First tests in the laboratory also confirmed that their noise level is tolerable, in particular when an additional low pass filter is added.

For the estimates of the power consumption given in Tab. 8.5 as “Module (B)” we assume a 70 % efficiency of the DC-DC converters, i.e. 30 % of the power will be lost due to heat dissipation. After summing up the values for all the modules in the setup, the total power consumption of the full detector system is estimated as 18.5 kW (4.6 kW per detector layer).

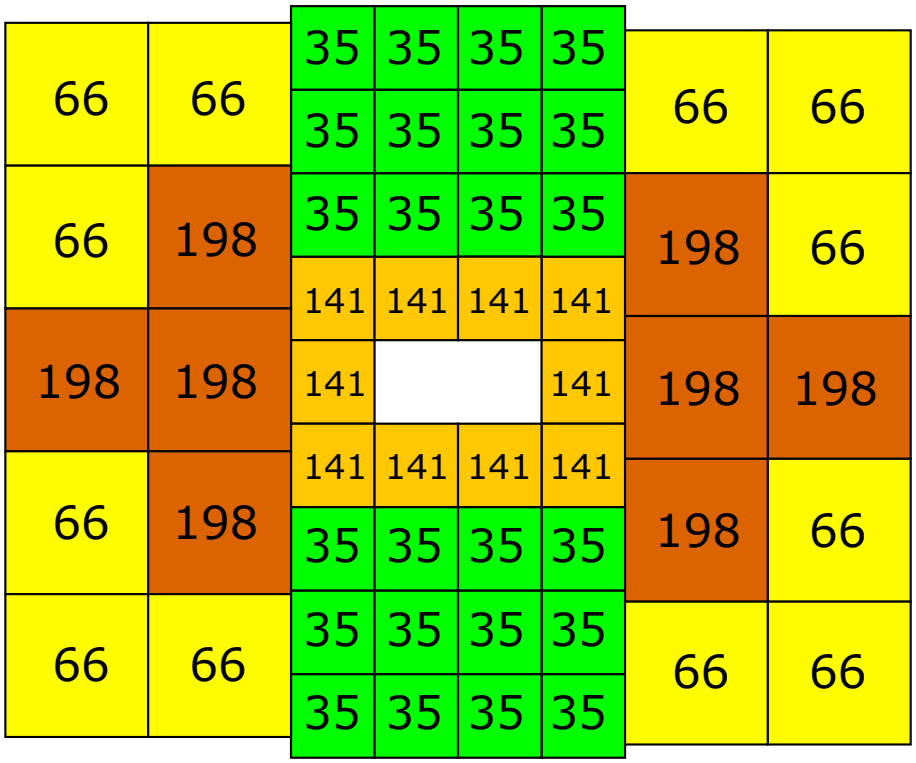

Figure 8.10: Power consumption of the readout electronics (FEBs, ROBs and DC-DC converters) for the different modules in one layer (see also Tab 8.5). The values are given in units of Watt.

8.4.2 LV distribution

The low voltage system will be subdivided into independent low voltage channels. The actual number of 64 LV channels is a compromise between cost and performance. Each of them will power half a vertical segment of a full layer, that corresponds to 2.5 – 4.5 chambers (see Fig. 8.11). The power supplies will be located inside of the cave beneath the magnet platform in an area not accessible during beam operation (see Fig. 8.12).

In this scenario a cable length of about 30 m is needed from the power supplies to the actual copper power bus bars. The cables should have an adequate cross section, e.g. for 100 mm^2 we estimate a maximum power dissipation of below 10 W over 2×30 m. The corresponding parameters of the bus bars are summarized in Tab. 8.6. Their cross section have been chosen such that the dissipated power always stays below 2 W.

Bus bar type	No.	I (A)	S (mm^2)	L (m)	W (kg)	R (mΩ)	P_{con} (W)	P_{diss} (W)
A and H	16	3.21	15	2.5	0.34	2.83	231	1.10
B and G	16	6.24	35	2.5	0.78	1.21	363	1.17
C and F	16	7.30	30	2.6	0.70	1.47	317	1.08
D and E	16	8.55	20	2.6	0.46	2.21	246	0.98

Table 8.6: Characteristics of the power bus bars as shown in Fig. 8.11. Listed are the transported current I, the cross section S, the length L, the weight W, the resistance R, the power provided to the consumer P_{con} and the power dissipated on the bus bars P_{diss}. The calculation assumes a voltage of 12 V on the LV distribution system.

Each of the listed LV bus bars (A – H) is needed 16 times (one supply and one return bar in the upper and lower half of each layer) and for each bus bar a supply cable is installed between

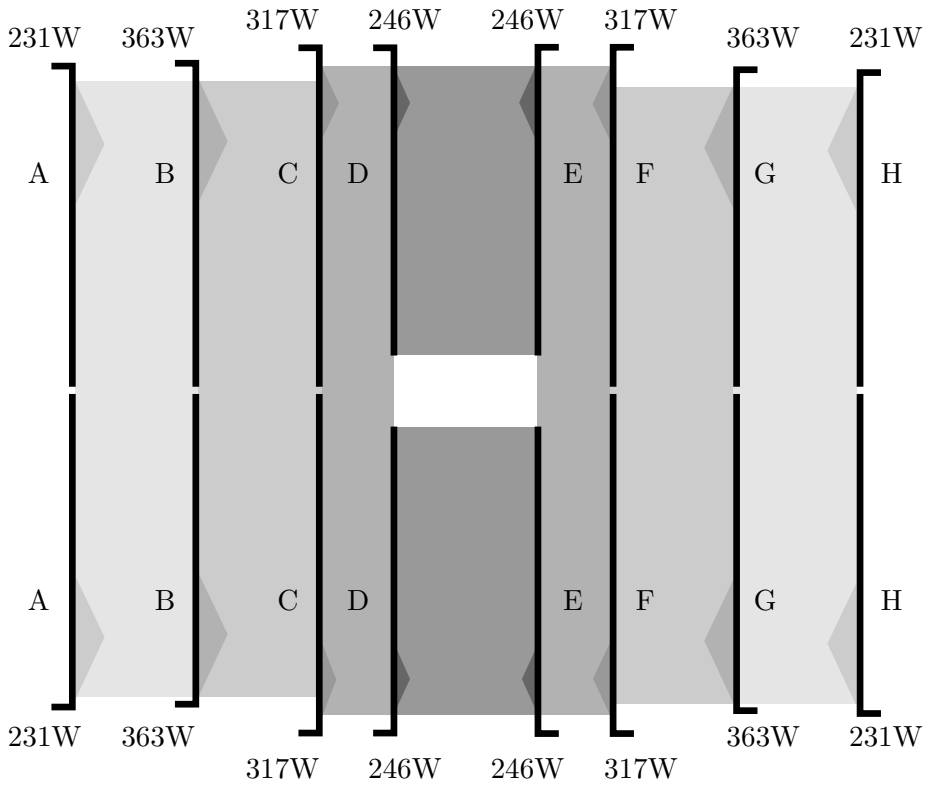

Figure 8.11: Schematic drawing of the LV power bus bars. The power consumption corresponds to the values shown in Fig. 8.10 and Tab. 8.5.

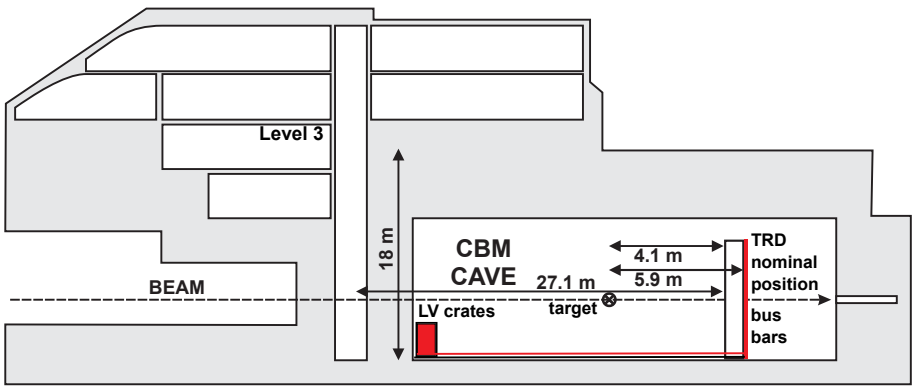

Figure 8.12: Schematic layout of the TRD LV system, showing the location of the different components.

the power supply and the bus bar. The total weight of the altogether 128 bus bars for the CBM-TRD is therefore 78 kg and thus only a minor contribution ($< 2.5\,\%$) to the total weight of the detector. The total amount of required LV components is listed in Tab. 8.7.

Number	Device	Length (m)	Comment
64	LV power supply channels		
128	LV supply cables	30	between power supplies and detector
128	LV copper bus bars	2.5 – 2.6	the on backside of each layer
3264	DC-DC converter (FEAST)		2176 for FEBs and 1088 for ROBs
4352	LV-FEB cables	0.6 – 1.0	between bus bars and FEBs

Table 8.7: Main components of the LV distribution system.

8.5 High voltage system

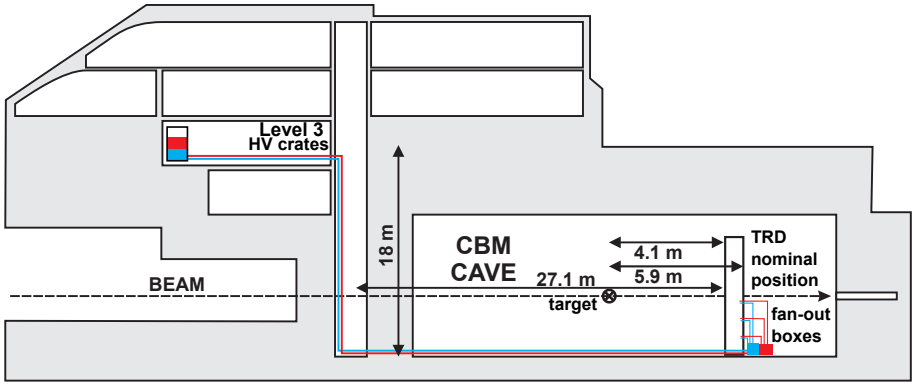

Figure 8.13: Schematic layout of the TRD HV system showing the location of the different modules.

The foreseen chamber design requires two HV potentials, one for the gas amplification and one for the drift region. The first is in the range of $1700 - 2200$ V with positive and the second 500 V with negative polarity, depending on the type of operation (Xe or Ar gas mixture). The negative potential is applied to the Kapton entrance foil window, while the positive potential is connected to the anode wires. To operate 216 individual detector modules 216 positive and 216 negative HV power supply channels are needed. In order to achieve a maximum channel utilization a 48 channel power supply would be the favored option. A cost efficient low noise power supply for this purpose is the ISEG HV EDS 301 30p/05n (48 channels). Therefore, five ISEG HV EDS modules with 48 channels with positive and five with negative polarity powered by one ISEG ECH 54 A (10 slot) crate are a possible solution for the CBM-TRD.

The interconnection of the HV power supplies positioned on Level 3 of the CBM building and the modules in the cave is done via $48 \times 0.14\,\mathrm{mm}^2$ 3 kV HT cables (with 48 litz wires each), as presented in Fig. 8.13. The 48 channels are split into individual channels using fan-out boxes positioned close to the nominal position of the TRD in the cave. From there the connection to the individual TRD modules is made via 2×216 coaxial HV cables (5 kV). The main components of the HV system are summarized in Tab. 8.8.

A low pass HV filter board close to the chamber will be used to enhance the potential stability and reduce external noise. At the same time it allows to decouple eight anode wire segments, thus enhancing the failure tolerance of the module with respect to mechanical and/or electrical

Number	Component	Length (m)	Comment
1	ISEG ECH 54 A		10 slots
1	ISEG CC 24		MMS crate controller
5	ISEG HV EDS 301 30p		48 channels/module (positive)
5	ISEG HV EDS 301 05n		48 channels/module (negative)
10	$48 \times 0.14\,\mathrm{mm}^2$ cable	45 – 50	48 channels
10	HV fan-out boxes		48 channels
432	Coaxial HV cables	15	single channel
216	HV filter boards		up to 9 anode segments & 1 drift

Table 8.8: Main components of the HV system.

anode wire problems. This will result in segments of 27 (48) wires for the small (large) module types, with a corresponding capacity of 83.5 pF (264.0 pF) per segment. Each segment will be connected to an external capacitor of 2.2 nF on the HV filter board, as already implemented for the ALICE-TRD.

The electrical interconnection between the HV filter board and the drift electrode/anode wires segment is realized using coaxial high voltage cables which are transferred through holes at the edges of the honeycomb backpanel and the pad plane. The gas tightness is ensured by the usage of Araldite glue.

8.6 Cooling

The cooling system needs to be able to remove the heat generated by the FEBs which comprise the SPADIC chips and the DC-DC converter as the main heat producer. For a given TRD layer this will amount to a total heat dissipation of 4.6 kW. This amount of heat should be removed to a level that keeps on one side the electronics in a comfortable environment and on the other side does not expose the surrounding detectors to any excessive temperatures.

Since an active water cooling system requires an additional complex infrastructure and will on top introduce a significant amount of extra material to the overall detector material budget, as well as additional costs, this option should only be followed if an air cooling system turns out to be insufficient. This might be the case for the innermost part of the detector with the highest integration density. Therefore, a dedicated water cooling system (see Sect. 8.6 below) is still being evaluated. However, as default solution air cooling is foreseen.

It is planned to evaluate the cooling needs in detail with a detector mock-up, using real ROC prototypes and electronics as well as additional adjustable heat sources. This will allow to measure the heat distribution in a realistic geometrical arrangement under various conditions and to validate the cooling concept.

8.6.1 Air cooling

Assuming an air flow of $600\,\mathrm{m}^3/\mathrm{h}$, which corresponds to an air velocity of 0.32 m/s for the geometry of the TRD (width of one layer × gap between layers = 6.65 m × 0.1 m), ~ 5 kW of heat can be transported out of the volume between the TRD layers with laminar air flow and inlet and outlet temperatures of 20 °C and 40 °C. This should be sufficient to cope with the overall expected heat dissipation of the TRD electronics. If this flow cannot be achieved by convection alone, additional fans can be mounted on the top of a detector layer. These can be coupled to heat exchangers in order to assure that the heat can be safely removed from the cave environment.

However, it needs to be assured that in this scenario no local hot spots and too steep temperature gradients develop. This is planned to be studied in the mock-up geometry mentioned above. Also, it has to be investigated whether dedicated cooling bodies are needed to transfer the heat from the electronic components to the flowing air. These would introduce additional material into the active zones of the detector and thus should be used only if necessary.

8.6.2 Optional water cooling

In the case that an additional water cooling is unavoidable for the inner part of the detector, a possible implementation could look as follows: The pipes used to bring the cool water to the ROCs as well as the return lines will be positioned between the beam pipe and the inner modules of type 1, which might have to be actively cooled. Eight FEBs of type 10s are mounted on the chamber with four ROB3, resulting in a minimum cooling pipe length per module of around 5.0 m. The heat radiator and pumping system will be positioned in the cave below the HADES platform. This results in additional 27 m pipes between the modules and the service station in average. The supply and return lines between the service station and the individual detector layers will be covered by aluminum pipes with a diameter of 32 mm for each layer. The pipes within each layer will be aluminum with an outer diameter of 6 mm. The full system has to be driven by underpressure to avoid a damage of the electronic in case of a cooling system leak.

8.7 Monitoring and detector control

The Detector Control System (DCS) is supposed to monitor and control the operation of the CBM-components such as the TRD. For a safe and stable operation of the TRD, the DCS should therefore provide the following functionalities:

- Switching on and off the detector or components of it.
- Allow to set and modify detector control parameters.
- Monitoring detector parameters essential for its operation and for the later data analysis.
- Logging and archiving of detector parameters, as well as providing trending displays.
- Issuing of alarms if predefined threshold values are exceeded and providing operator instructions.
- Safely switching off critical components or take other appropriate safety measures if necessary.

8.7.1 Implementation and communication

There are two different categories of systems to be controlled. One essentially comprises the readout related aspects, such as switching on and off individual FEBs or ASICs and monitoring their temperatures. This part could either use the E-link infrastructure or the available configuration register of the GBTx-chip for communication and will only be used when the readout system is operational.

The other category includes all the rather safety relevant topics. The system employed for this purpose will thus be implemented in the overall CBM-DCS framework, which is currently being developed. It will be based on DCS boards controlled via Ethernet, which can be operated independently from the GBTx-based readout chain. This is essential in order to be able to monitor and control safety critical parameters, e.g. gas pressure or HV, independently of the data acquisition.

The implementation of the DCS system will be based on the EPICS set of software tools and applications which provide a software infrastructure for use in building distributed control systems to operate devices such as large experiments [74]. EPICS uses Client/Server and Publish/Subscribe techniques to communicate between the various computers.

8.7.2 Detector parameters

Table 8.9 summarizes the main parameters of the TRD to be controlled and monitored by the DCS. It lists the foreseen location of the sensors, the controlled parameters, the number of sensors, the link type to connected to the DCS and the type of control. The section on FEB cooling applies in the case an active water cooling needs to be implemented.

Subsystem	Location	Controlled parameters	Number	Link type	Parameters	Control
FEB control	ROC	FEB temperature	1664	E-link	temperature	read
	ROC	FEB on/off	1664	E-link	bit pattern	read/write
FEB LV	Cave	FEB power supply (PS)	64	serial	current	read/write
	Cave	FEB PS temperature	12	analog	temperature	read
	Cave	FEB PS status/enable word	64	serial	bit pattern	read/write
	ROC	FEB voltage regulation	64	bus	current/voltage	read/write
	Detector layer	Connector and cable temperature	64	analog	temperature	read
ROC	ROC	ROC environment temperature	216	analog	temperature	read
Drift HV	Level 3	HV supply on/off	216	serial	voltage	read/write
	Level 3	HV settings and readings	216	serial	complex	read/write
Anode HV	Level 3	HV supply on/off	216	serial	voltage	read/write
	Level 3	HV settings and readings	216	serial	complex	read/write
Gas system	Level 3	H_2O content	1	serial	complex	read
	Level 3	CO_2 content	1	serial	complex	read
	Level 3	O_2 content	1	serial	complex	read
	Level 3	Inlet gas flow	20	analog	flow	read
	Cave	Return line pressure	5	analog	pressure	read
	Detector layer	Inlet and outlet gas temperature	25	analog	temperature	read
FEB cooling	Detector layer	Inlet and outlet water temp.	24	analog	temperature	read/write
	Detector layer	Inlet and outlet water pressure	24	analog	pressure	read
	Level 3	Safety switch	1	binary	voltage	on/off

Table 8.9: Main parameters of the detector control system for the TRD.

8.8 Safety aspects

The CBM-TRD detector will follow the GSI/FAIR safety rules and codes. Specifically, the following risks and actions are to be considered and will be discussed with the GSI/FAIR Technical Inspection and Safety commission:

- The gas mixtures for the TRD, Xe/CO_2 and Ar/CO_2, are non flammable and have UN classification 2.2 (non-toxic and non-flammable substances). Due to the non-negligible quantity of these gases in the CBM cave, the TRD volume is about $1.36\,m^3$, and the high densities of xenon (5.58 g/l), argon (1.78 g/l) and CO_2 (1.98 g/l), oxygen deficiency meters will be installed near to the detector.
- The TRD detector will be operated with an overpressure of a 1 mbar above the atmospheric pressure and is designed for a maximum over-pressure of 2 – 3 mbar. Thus, the TRD modules are not classified as pressure vessels.
- The high pressure part of the gas system is located in E30, near the surface. The gas system will be constructed according to the appropriate rules.
- The MWPCs will operate with high voltages at around 2 kV, the total current for each individual supply line will be limited to few mA. The low voltage supply to the detector readout is below 50 V. The total power dissipation on the detector is below 20 kW. Appropriate interlocks and current monitoring systems will be installed enabling to interrupt power at the source.
- Work will occasionally be done in the electronics area inside the CBM cave in E10, close to the detector. After beam shut down adequate waiting times are necessary to ensure that the air activation is below 3 µSv/h.

Chapter 9

Simulation and Reconstruction

The software developments for the simulation of the TRD detector and for the reconstruction of its data are presented in the following. A detailed and realistic description of the detector response in mandatory for reliable studies of the detector performance and is therefore based on input from test beam measurements as much as possible. In the following the TRD simulation and reconstruction procedures, as well as results on the tracking and electron identification performance are presented.

9.1 Simulation framework

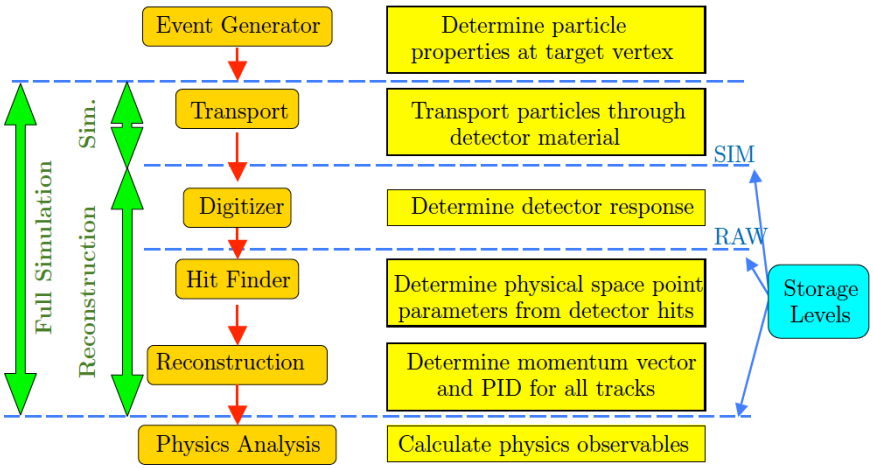

Figure 9.1: Summary of the different simulation and reconstruction steps implemented in the CBMROOT framework (picture taken from [59]).

The simulations presented here were performed within the CBMROOT framework, which contains all components necessary to perform a full detector simulation and reconstruction (see Fig. 9.1). As standard event generator UrQMD [11] is used. The detector setup used in the simulations is the same as described in Chap. 3. The particle transport through the geometry is performed with GEANT3 [29]. The details of the TRD response simulation, which describes the signal generation related to the specific energy loss and TR-photon absorption, and the details of the hit finding and reconstruction step are described in the following sections.

9.2 Detector simulation

The fundamental processes responsible for the signal creation and evolution within a TRD can in principle be included in all microscopic details in a MC detector response simulation framework, however, at the price of a relatively high CPU time consumption. To achieve an adequate compromise between a detailed physics simulation and an efficient detector response, both parts are decoupled in the CBMROOT simulation framework. The particle production and transport, as well as all relevant energy loss effects, except TR-photon production, are calculated within the simulation part. Only the total energy loss per active detector volume is stored. The detector response, DAQ, data transport, event building and the physics analysis is done in the second step, the reconstruction part. The output of the simulation is pure MC information, like the ionization energy loss or the position of the entrance and exit points of particle trajectories crossing active detector volumes.

9.2.1 Energy loss in the detector gas

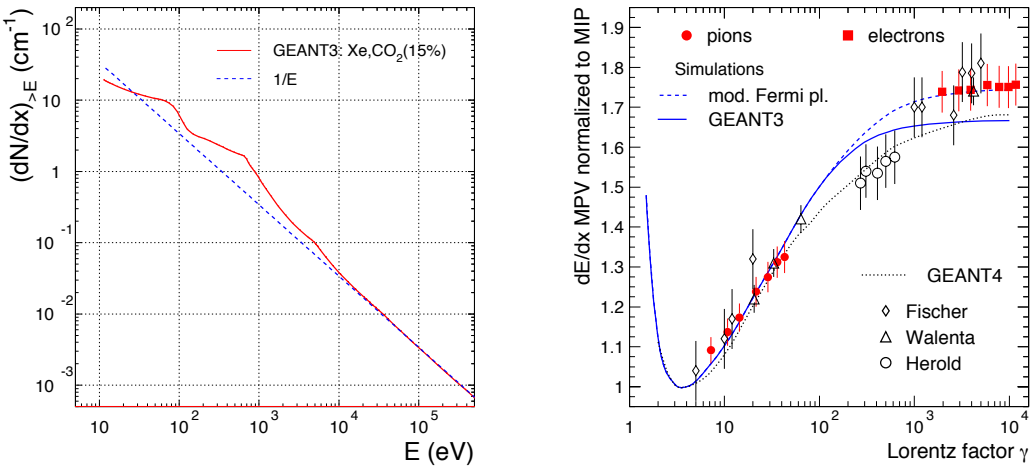

Figure 9.2: Left: The integral spectrum of the energy transfer in primary collisions of charged particles simulated with GEANT3 (red line). Right: The MPV of the energy loss, normalized to the MIP value, as a function of the Lorentz-factor γ. Both figures are taken from [75].

The energy loss of all particles, including δ-electron production, is calculated in the simulation step using GEANT3. In the context of the developments performed for the ALICE-TRD, the performance of GEANT3 in terms of energy loss for xenon as counting gas was evaluated [75]. The left panel of Fig. 9.2 displays the energy spectrum of primary electrons released in inelastic collisions of a minimum ionizing particle (MIP, $\gamma = 4$) with a Xe/CO_2 (85/15) mixture. GEANT3 uses an implementation of the photo-absorption ionization model [76] to calculate this process. The structures correspond to the atomic shells of xenon. For comparison also the Rutherford spectrum is shown, which, in its integral form, corresponds to a $1/E$ dependence. Both shown distributions start at the first ionization potential of xenon, $I_{\mathrm{pot}} = 12.1\,\mathrm{eV}$, and extend up to the energy above which the released primary electrons are treated as δ-rays that are transported as separate tracks by GEANT3. The threshold for this transition was chosen as 10 keV.

A comparison of the GEANT3 result for the most probable value (MPV) of the dE/dx (blue solid line) to data is shown in the right panel of Fig. 9.2. Generally, a good agreement was found up to the relativistic rise, while the unmodified GEANT3 slightly under-predicts the

measurements in the region of the Fermi-plateau.

9.2.2 Transition radiation

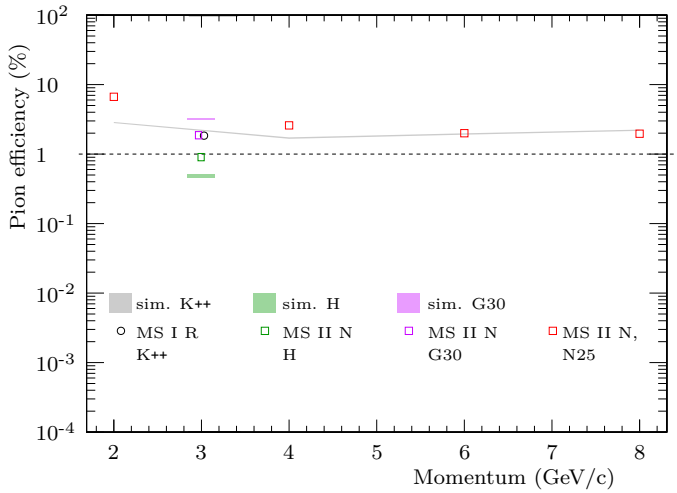

Figure 9.3: The pion efficiency, i.e. the probability to misidentify pions as electrons, for a TRD with four detector layers as a function of the particle momentum. Shown are test beam results for four different radiator types (K++, H, G30 and N25) in comparison to simulations [59]. The labels "MS I R" and "MS II N" refer to two different ROC prototypes.

The simulation of the TR-photon production is done based on Eq. 6.9 as described in Chap. 6.1. The self-absorption of the radiator is taken into account as well as the absorption of the aluminized entrance window and the active gas volume. Losses due to TR-photon absorption within the FR4 lattice grid between the radiator and the entrance window foil are also implemented. The final deposited energy due to TR-photon absorption within the sensitive gas volume is added to the ionization energy loss coming from the simulation part. The radiators which have been tested in beam up-to-now are all implemented in the framework and modeled according to the in beam test results. Figure 9.3 shows a comparison of pion efficiencies measured in beam tests and simulated with the above described approach.

Since for the radiators H and G30 the momentum dependence of their performance has not yet been experimentally determined, we rely in the performance studies on the momentum dependent prediction for the K++ type, tuned to the measurement at 3 GeV/c (gray band in Fig. 9.3). The radiator K++ is a self-supporting regular foil stack type. At a momentum of 3 GeV/c its performance is very similar to the radiator G30 and slightly worse than the radiator H, which are both discussed in Sect. 6.3 in detail. For the TRD setup radiator type H is currently foreseen as the default solution.

The comparison with the measurements for the radiator N25, which is an irregular type (PE foam) with properties similar to H (PE foam foils) and K++, illustrates that the calculated momentum dependence used here should be realistic, also for an irregular radiator. In any case, only a moderate change of the pion suppression factor with increasing momenta is expected, while the evolution towards lower momenta is rather dominated by the contribution from the energy loss due to ionization. The measurement for the radiator type H at 3 GeV/c might indicate that our currently employed model is even underestimating the achievable performance of the final detector design and that therefore the performance studies discussed in the following and in Chap. 3 can be considered as conservative.

9.2.3 Signal generation

The signal generation is partitioned into three stages: digitization, clustering and hit production.

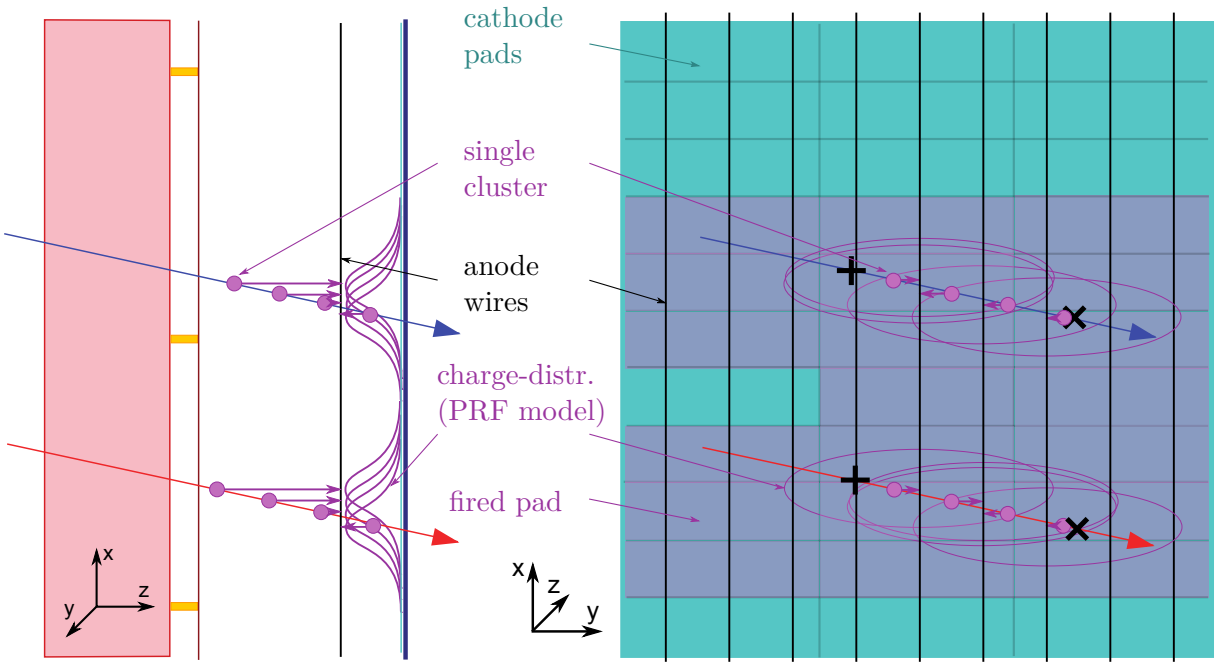

Figure 9.4: Schematic view of the CBM-TRD detector response simulation as implemented in CBMROOT. The algorithm splits the total MC energy loss into several equal single clusters per unit track length inside the active detector volume. These single clusters are transported towards the closest anode wire position. The induced charge fraction as function of the displacement of the single cluster position with respect to the center of the underlying pad is calculated in x- and y-direction based on the PRF model (Eq. 9.1). The product of the x and y charge fraction per pad is multiplied with the single cluster charge to evaluate the induced charge on each pad. The signal of two or more single clusters of the same or different MC tracks within the same event are summed up.

9.2.3.1 Digitization

The digitization comprises the detector response up to the charge distribution on the pad plane and charge integration and/or preprocessing by the ASIC. Up to now, there is no detailed time evolution of the signal and further detailed ASIC features implemented. The charge distribution is estimated based on the Pad Response Function (PRF)

$$\begin{aligned} PRF(d/h) &= \int_{d/h-W/2}^{d/h+W/2} \rho(d'/h)\; d(d'/h) \\ &= -\frac{\arctan\left(\sqrt{K_3}\tanh\left(\pi(\sqrt{K_3}-2)\cdot\frac{W-2\cdot d}{8h}\right)\right)}{2\,\arctan(\sqrt{K_3})} \\ &\quad -\frac{\arctan\left(\sqrt{K_3}\tanh\left(\pi(\sqrt{K_3}-2)\cdot\frac{W+2\cdot d}{8h}\right)\right)}{2\,\arctan(\sqrt{K_3})}. \end{aligned} \tag{9.1}$$

which uses the spatial integral of the charge density distribution $\rho(d/h)$ derived by Mathieson [77]

$$\rho(d/h) = q_a \cdot \frac{\frac{\pi}{2} \cdot \left(1 - \frac{\sqrt{K_3}}{2}\right)\sqrt{K_3}}{4 \arctan\left(\sqrt{K_3}\right)} \cdot \frac{1 - \tanh^2\left(\frac{\pi}{2} \cdot \left(1 - \frac{\sqrt{K_3}}{2}\right)\frac{d}{h}\right)}{1 + K_3 \tanh^2\left(\frac{\pi}{2} \cdot \left(1 - \frac{\sqrt{K_3}}{2}\right)\frac{d}{h}\right)}. \tag{9.2}$$

Equation 9.1 describes the normalized induced charge fraction as a function of a parameter representing the chamber geometry K_3, the pad width W, the distance between anode wire plane and pad plane h and the displacement d of the cluster relative to the pad center. Values of K_3 are presented in Fig. 9.5 for different values of the ratio h/s, where s is the wire pitch, and the ratio r_a/s, where r_a is the diameter of the wires. For the CBM-TRD ROCs the following values apply: $h = 3.5\,\text{mm}$, $s = 2.5\,\text{mm}$, $h/s = 1.4$ and $r_a = 20\,\mu\text{m}$, resulting in $K_{3,\parallel} \approx 0.35$ and $K_{3,\perp} \approx 0.38$

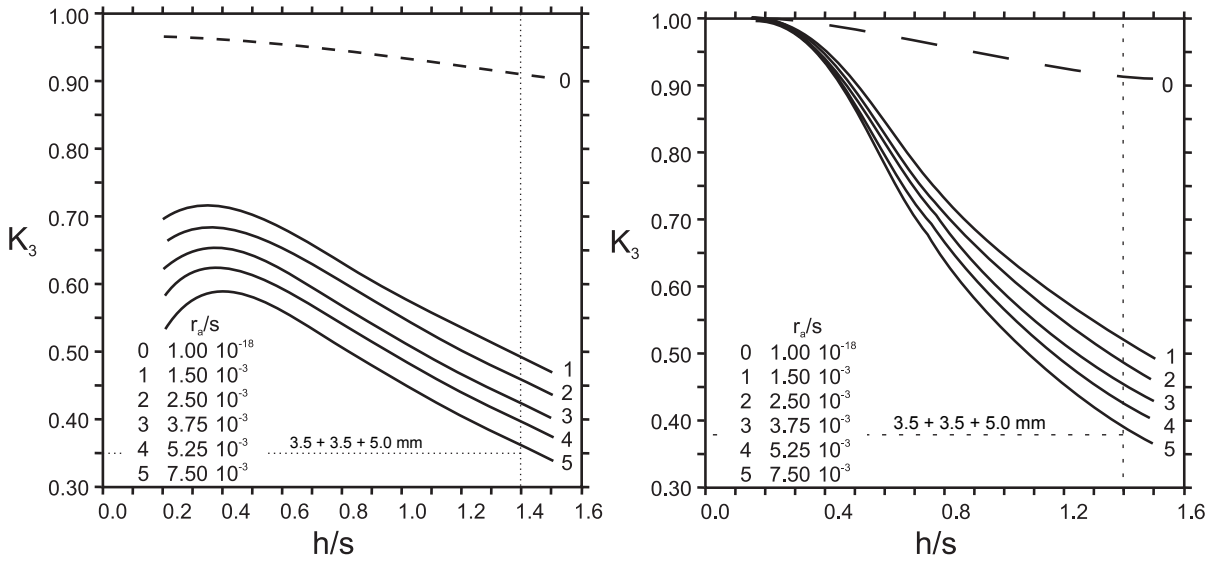

Figure 9.5: Values of K_3 as a function of the ratio h/s for various values of r_a/s parallel (left) and perpendicular (right) to the anode wire direction based on [77].

This description is valid parallel and perpendicular to the anode wire direction for rectangular pad geometries and is therefore used to calculate the charge sharing on adjacent pads in the CBM-TRD. Since the simulation stores only the total energy loss per particle track segment, the clustering of the primary ionization processes along the particle trajectory has to be recovered in the reconstruction step to obtain a realistic detector response in a MWPC, specially for tracks with a large impact angle. The total energy loss is therefore subdivided into n equal fractions, which is also done for the track path in the active volume. The individual primary ionization clusters are projected towards the closest anode wire. The induced charge fraction is calculated based on Eq. 9.1, multiplied by the primary cluster energy loss fraction and summed up on the channel ("digi") level. The fired digis are summed up after each event, since a given pad can be fired by more than one track in a collision.

9.2.3.2 Clustering and hit reconstruction

In a following step the continuous and mixed digi stream is sorted. This is done based on a detector and channel unique ID. This analysis step corresponds to ASIC (time sorting) and

the DPB/FLES (spatial sorting) in the experiment. All digis above a threshold of 1 keV total energy loss are used as cluster seed. All digis sharing at least one edge along the anode wire direction with a seed digi are merged into a cluster, where different seeds can share digis. Since the detector design is optimized for an average cluster size of 2.5 channels per cluster in anode wire direction, only first neighbor generation digis are merged to the seeds. This feature is also realized in the SPADIC by a neighbor channel triggered readout. This algorithm allows therefore for detailed detector studies, including occupancy and physics performance. The DPB readout layer is also implemented. It is foreseen to merge clusters of adjacent rows which overlap in column, if the weighted center of charge of both agree within a fixed window. The procedure reduces significantly the amount of ghost hits in the last step.

A hit corresponds to a charge cluster with a position information assigned to it. The position in the x-y-plane is determined by calculating the center-of-gravity of the charges associated with a given cluster. The z-position of the hit is set to to the z-position of the pad plane of the corresponding chamber.

9.3 Reconstruction routines

This section describes technical details and performance tests on the hit and track reconstruction routines implemented in CBMROOT which are the basis for all physics feasibility studies and TRD performance simulations presented in the physics performance chapter (see Chap. 3). The main challenge of the hit reconstruction and track recognition in the CBM-TRD detector results from the large multiplicity in heavy-ion collisions, which leads to a high track and hit density in the TRD detector.

9.3.1 Track reconstruction

The track reconstruction algorithm developed for the TRD is based on a track following algorithm using the tracks reconstructed in the STS as seeds. The STS tracking employs the cellular automaton method [78] and the STS track parameters are used as a starting point for the following track prolongation. This track following is based on the standard Kalman filter technique [79] and is used for the estimation of track parameters [80] and trajectory recognition. The main logical components are track propagation, track finding, track fitting and, finally, a selection of good tracks. Each of these steps will be described in the following in more detail.

9.3.1.1 Track propagation

The track propagation algorithm estimates the particle trajectory and its errors, while taking into account three physics processes which influence the trajectory: energy loss, multiple scattering and the magnetic field. The effect of the material on the track momentum is taken into account by calculating the expected average energy loss due to ionization (Bethe-Bloch formula) and bremsstrahlung (Bethe-Heitler formula) [81]. The influence of multiple scattering on the error, which is propagated via the covariance matrix, is included by adding process noise in the track propagation. Here, a Gaussian approximation employing the Highland-Lynch-Dahl formula (Eq. 4.1) [81] is used to estimate the average scattering angle. The propagation of the trajectory is done according to the equation of motion. If the track passes a magnetic field the equation of motion for a charged particle is solved applying the 4^{th} order Runge-Kutta method [82]. If it passes a field free region a straight line is used for propagation and transport matrix calculation. The transport matrix is calculated by integrating the derivatives along the so-called zero trajectory [83]. A detailed description of the track propagation developed for the TRD can be found in [84].

9.3.1.2 Track finding

In the track finding algorithm hits are attached to the propagated tracks at each detector station using two different methods. Either just the nearest hit is attached to the track, or all hits within a certain environment are included in the branching method. For the first method, only one track is propagated further. The branching method allows for several track branches to be followed, one for each attached hit. Techniques common to both methods are the above described track following, the Kalman filter and the calculation of the validation region for hits.

The assignment of new hits is done step by step at each detector station. After the track has been propagated to the next station, possible hits are attached and track parameters are updated by the Kalman filter. For the attachment of hits a validation gate is calculated in order to allow for a high degree of confidence in the hit-to-track assignment. The validation gate is defined based on the residual vector r (distance between the fitted track and the hit) and the residual covariance matrix R. In the context of Kalman-based tracking filters, a validation gate can be expressed as $v = r\,\mathbf{R}^{-1}\,r^T < d$. The cut value d is chosen such that a defined probability of rejecting the correct hit is achieved, here this probability is chosen to be 0.001. Values for d are taken from χ^2 tables, determined as a function of the number of effective degrees of freedom. The algorithm takes into account the possibility of hits missing due to detector inefficiencies, dead zones in the detector, inefficiencies of the hit finder algorithm, and other effects.

The two methods that are used to assign hits to tracks differ in the way how they treat the situation in which several hits lie within the validation gate. In case of the branching method, a new track branch is created for each hit lying within the validation gate. Since the number of branches can grow exponentially, the χ^2 value is calculated for each track branch and unlikely ones are rejected. For each input track seed the number of created branches is also calculated and, if it exceeds a certain limit, the tracking continues by using the nearest neighbor approach instead. For the second method no track branches are created. The nearest neighbor method attaches the hit with the smallest v, if it is lying in the validation region at all.

9.3.1.3 Track selection

After track finding so-called clone tracks (consisting of very similar sets of hits) and ghost tracks (consisting of a random set of hits) have to be rejected while keeping correctly found tracks with high efficiency. The selection algorithm works in two steps. First, tracks are sorted by their quality, which is defined by the track length and their χ^2. Then, starting with the highest quality tracks, all hits belonging to a track are checked. In particular, the number of hits shared with other tracks is calculated and the track is rejected, if more than 15 % of its hits are shared.

9.3.2 Electron identification

The goal of the electron identification algorithms is to distinguish electrons and pions using a set of energy loss measurements. The simulated signal distributions in a single TRD layer are displayed for two different momentum intervals in Fig. 9.6. The values are corrected for the different path lengths the tracks can have when passing through the gas volume at different incidence angles. The distributions for pions reflect the deposited charge due to energy loss alone. As the pion momentum increases, the average of the distribution move to slightly higher values due to the increase of the specific energy loss dE/dx in the relativistic rise region of the Bethe-Bloch curve. For electrons the distributions have a more complex shape, since in addition to the specific energy loss also the TR component contributes and causes the second maximum at higher momenta. While the specific energy loss of electrons is already in the plateau region of the Bethe-Bloch curve throughout the whole relevant momentum range and thus the position

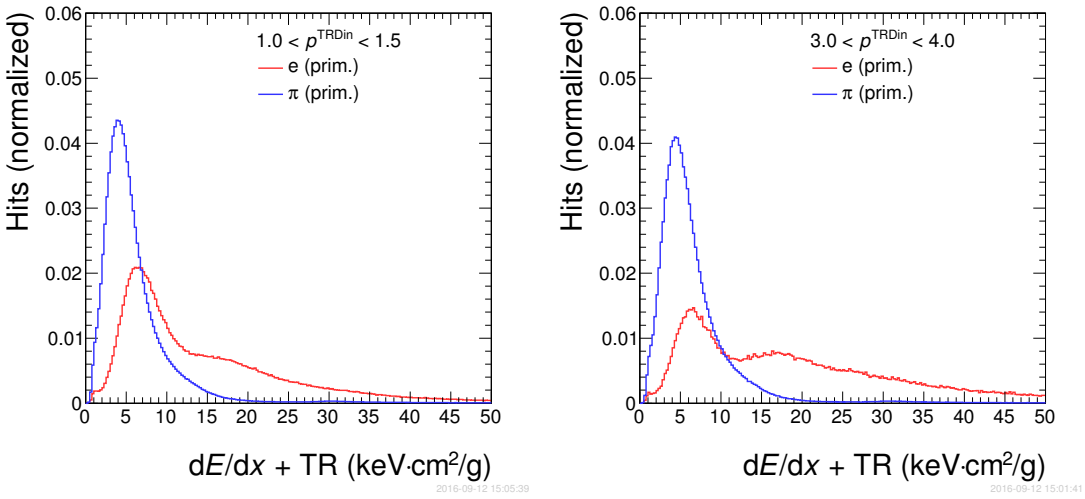

Figure 9.6: The simulated signal distributions for a single TRD layer in two different momentum intervals. Primary electrons are shown in red and pions in blue color.

of the first peak does not change, the TR contribution still rises between the two momentum intervals shown.

The TRD in the SIS100 configuration will deliver up to four independent measurements of the dE/dx + TR signals. The distributions of the averaged signals for tracks with at least three hits is shown in Fig. 9.7. Even though a clear separation of electrons and pions is visible in both momentum intervals, applying simple cuts on the average signal for all layers usually does not provide a sufficiently high pion suppression level, so that more sophisticated algorithms have to be used. For this purpose several methods for electron identification were implemented. The two main algorithms, which are mainly used as identification methods in the analyses, are the Likelihood Function Ratio (LFR) and an Artificial Neural Network (ANN). Other methods, that were also implemented and tested, are Ordered Statistics (Median) and an algorithm based on the usage of a Boosted Decision Tree (BDT) classifier. However, since it turned out that they do not offer any performance benefits or other practical advantages in comparison to the other two methods, they are not further evaluated in detail here.

9.3.2.1 Likelihood function ratio

As the default electron identification method, which is also used for the simulations prepared for the performance studies shown in Chap. 3, the LFR is used. The likelihood for a measured track to be an electron is defined as

$$L = \frac{P_e}{P_e + P_\pi}, \tag{9.3}$$

where P_e is the probability that the track is an electron and P_π its probability to be a pion.

$$P_e = \prod_{i=1}^{N} P(E_i|e), \quad P_\pi = \prod_{i=1}^{N} P(E_i|\pi). \tag{9.4}$$

Here, $P(E_i|e)$ and $P(E_i|\pi)$ are the probabilities that the energy deposit in the ith layer was produced by an electron or a pion, respectively. N is the number of hits assigned to a given track.

The right panel of Fig. 9.8 shows the distributions of the likelihood values for electrons and pions. The cut on the likelihood values defines a certain electron identification efficiency.

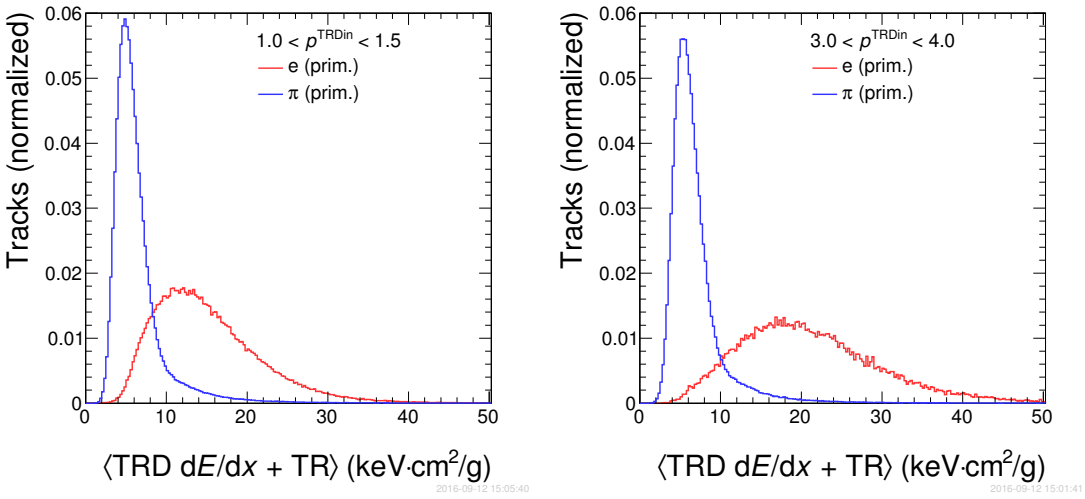

Figure 9.7: The simulated distributions of the average energy loss signal for tracks reconstructed with at least three hits in the TRD for two different momentum intervals. Primary electrons are shown in red and pions in blue color.

Depending on the pion suppression needed in a given analysis, different values can be selected (e.g. 90 % or 80 %). Lower efficiencies result in higher pion suppression factors at the expense of a lower accepted fraction of electrons.

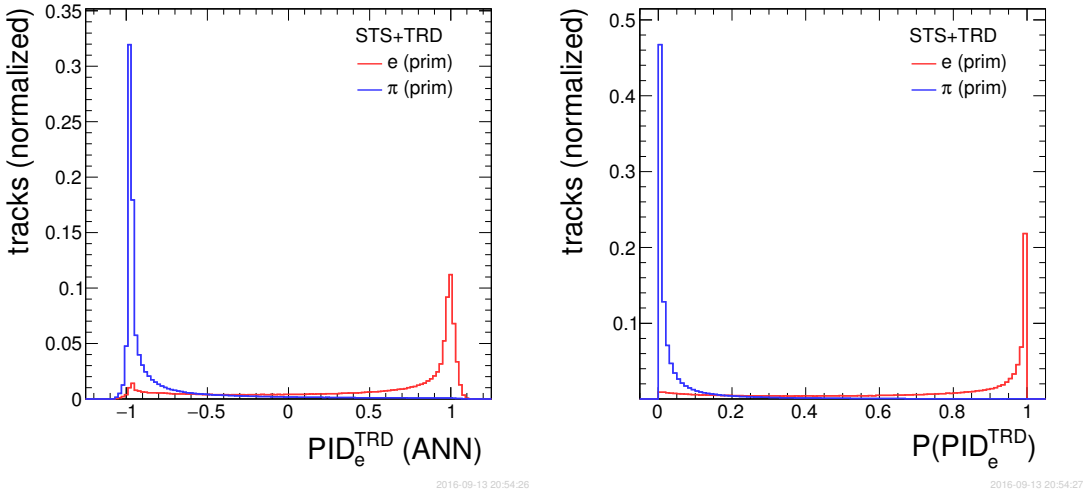

Figure 9.8: Left: The distributions of the ANN output values for electrons and pions, integrated over all momenta. Right: The momentum integrated distributions of the likelihood values for electrons and pions. Electrons are shown in red, pions are shown in blue color.

9.3.2.2 Artificial neural network

As an alternative method for electron identification the ANN can be employed. Here the ANN implementation of the multilayer perceptron type from the ROOT package [28] was used. The number of input neurons corresponds to the number of energy loss measurements (number of hits in a track). The number of neurons in the hidden layer is the doubled number of the input neurons. The ANN has one output neuron. Simply using a set of energy loss measurements as

input to the ANN did not allow to train the ANN in a robust way and to obtain reasonable pion suppression factors. To solve this problem it was proposed [85] to transform the initial energy loss measurement set to a new set of variables λ_i, according to the equation:

$$\lambda_i = \frac{E_i - E_{\mathrm{mp}}}{\xi} - 0.225, \tag{9.5}$$

where E_i is the measured value of energy loss in the ith TRD station, E_{mp} is the most probable value, and ξ corresponds to $\frac{1}{4.02}\ FWHM$ of the distribution of energy loss for pions. The sample of the obtained λ_i values is sorted according to their magnitude and for each of them the corresponding values of a Landau distribution function $\varphi(\lambda)$ are calculated. This new set of is used as the input to the ANN.

The left panel of Fig. 9.8 illustrates the distributions of the ANN output values from the training sample for electrons and pions. A cut on the ANN output value defines the required electron identification efficiency.

9.3.2.3 Boosted decision tree

First a preparation step is performed in order to construct Probability Density Functions (PDF), which are needed for the energy loss transformation. PDFs are obtained separately for pions and electrons in the following way: for each TRD track the assigned set of energy loss measurements is sorted from the lowest value to the highest one. Then a set of histograms is filled such that the lowest energy loss value goes to the first histogram, the next one to the second and so on. Finally, these histograms are normalized to an integral of unity and kept for the further analysis.

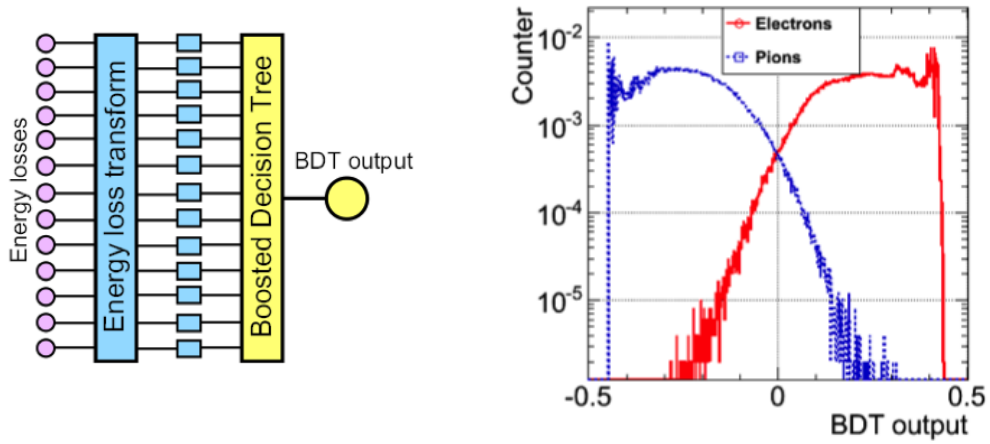

Figure 9.9: Left: Diagram illustrating the BDT working principle. Right: Example of BDT outputs for simulated electrons and pions.

During the reconstruction step the array of measured energy loss values, assigned to a given track, is sorted by its magnitude. Then for each energy loss E_i a new "normalized" value L_i is calculated according to the equation:

$$L_i = \frac{PDF_i^{\pi}(E_i)}{PDF_i^{\pi}(E_i) + PDF_i^{e}(E_i)}\ , \tag{9.6}$$

where $PDF_i^{\pi}(E_i)$ corresponds to the value of the PDF for pions and $PDF_i^{e}(E_i)$ to the value of the PDF for electrons for the i-th energy loss. The resulting array of "normalized" energy

losses is used as input for a BDT classifier [28]. The cut on evaluated BDT output value is set assuming 90 % electron identification efficiency. Figure 9.9 shows a sketch of the BDT-principle (left) and an example of the BDT output for pions and electrons (right).

9.3.2.4 Ordered statistics (median)

For each reconstructed TRD track the median value of the corresponding array of energy loss measurements is calculated by rearranging all the measurements from the lowest to the highest value and selecting the middle one. If there is an even number of measurements, the median is defined to be the mean of the two middle values. Using a cut on the median value one can distinguish between electrons and pions. The main advantage of this algorithm is its simplicity and extremely fast calculation speed, while at the same time it gives reasonable results. The median method is more robust in comparison to a simple cut on the sum of energy loss measurements, as it helps to overcome difficulties with long tails of the energy loss distributions.

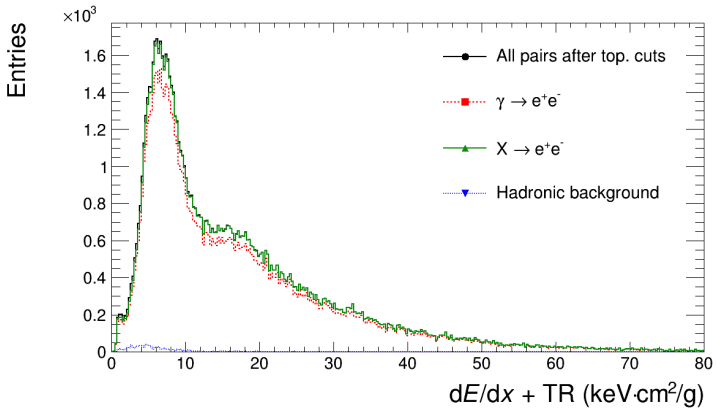

Figure 9.10: Simulated energy deposition spectra for the 10 % most central Au + Au UrQMD events at 8 AGeV, integrated over all momenta. Shown are electron candidates selected via the topological cut method (black line), together with the contribution from real electrons ($X \rightarrow e^+e^-$, green line) and the remaining hadronic background (blue line). The electrons originating from photon conversions are also shown separately ($\gamma \rightarrow e^+e^-$, red line). A purity of the electron sample of ~ 99 % can be reached with the chosen cuts [86].

9.3.2.5 Preparation of reference samples

Most of the electron identification methods described above (LFR, ANN and BDT) need samples of cleanly identified electrons and pions in order to generate reference probability distributions (LFR and BDT) or to train the ANN. From real data these samples can either be prepared by employing the particle identification capabilities of the other detectors in CBM (i.e. RICH and TOF) or by using topological cuts to separate particles from weak decays (e.g. pions from $K^0_s \rightarrow \pi^+ + \pi^-$) or from photon conversions in the target and first STS layers (electrons from $\gamma \rightarrow e^+ + e^-$). However, the first method has the disadvantage that it can only be used in the lower momentum region, where RICH and TOF can provide an efficient electron and pion identification. Since the TRD is supposed to identify electrons in particular in the higher momentum region, e.g. above $p \approx 6\,\mathrm{GeV}/c$, the second method is the preferred option. This method is also successfully being applied in the case of the ALICE-TRD [49].

A detailed study of the topological cut method was performed in [86]. It was shown that a very clean electron sample can be obtained by selecting photon conversions via cuts on the opening angle between the positive and negative pair tracks, the pointing angle of their summed

momentum vector relative to the main interaction vertex or the distance between main and secondary vertex positions, as illustrated in Fig. 9.10. Since the efficiency of this identification method is relatively low (typically in the order of a few percent, depending on the applied cuts) a significant event statistics is required in order to generate reference distributions in several momentum intervals with sufficient precision. However, estimates based on simulated UrQMD Au + Au events at 8 AGeV show that the necessary statistics can be easily obtained within normal running time. E.g. $\sim 5 \times 10^9$ minimum bias events, corresponding to 50 days of data taking at 50 kHz interaction rate, would be sufficient to accumulate enough statistics in the momentum region above 5 GeV/c [86].

9.3.3 Performance of the tracking and electron identification.

The results presented in this section are based on studies performed with standard simulations for central Au + Au collisions at 8 AGeV beam energy. Events were generated with the UrQMD event generator [11] to which various dielectron sources have been added as described in Sect. 3.2.2. The detector setup which is described in Sect. 3.2.1 was used for simulations.

9.3.3.1 Requirements

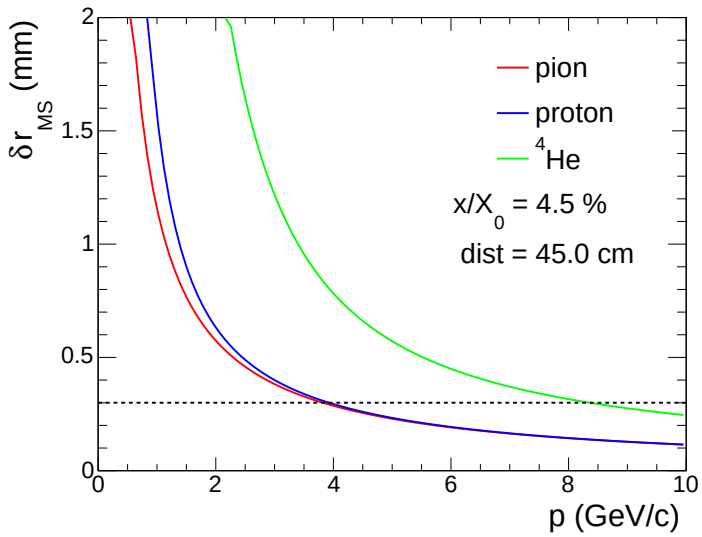

Figure 9.11: The position error δr_{MS} seen by a given TRD layer caused by the multiple scattering induced by the material of the downstream layer as a function of particle momentum p. δr_{MS} has been calculated for pions, protons and ^{4}He using the Highland-Lynch-Dahl formula (Eq. 4.1), assuming a material budget of $x/X_0 = 4.5\,\%$ for a single layer and a distance of 45 cm between layers.

In terms of tracking, the TRD is supposed to help matching tracks reconstructed in the STS to hits measured by TOF. Since it is located outside of the magnetic field, it will not contribute significantly to the momentum determination. In fact, multiple scattering, which on one side occurs between STS and the first TRD layer in the material of the RICH and on the other side in each TRD layer, will be the dominating contribution in this region of the CBM setup. This is illustrated in Fig. 9.11, where the multiple scattering contribution caused by one TRD layer to the measurement in the subsequent one has been calculated with the Highland-Lynch-Dahl formula (Eq. 4.1). For all relevant momenta ($p < 4\,\mathrm{GeV}/c$) the multiple scattering will cause a distortion of the track position on the next layer δ_{MS} that is larger than the required point

resolution of the TRD of $\sigma_{x,y} = 300\,\mu m$. Thus, a further increase of the point resolution will not improve the momentum resolution significantly. Rather, it is mandatory that the tracking algorithm is able to uniquely assign the measured points to the right tracks in a high multiplicity environment by taking the multiple scattering into account, as it is implemented in the employed Kalman filter.

9.3.3.2 Reconstruction efficiency and resolution in the TRD

The performance of the reconstruction algorithms was determined using information on the MC input. For the efficiency calculation the level of correspondence between found and simulated tracks is estimated. A track is defined as correctly found, if more than 50 % of the reconstructed hits match to hits of a MC track. The track reconstruction efficiency is defined as $\epsilon = N_{rec}/N_{acc}$, where N_{rec} is the number of tracks correctly reconstructed in the TRD and N_{acc} is the number of reconstructable tracks lying in the TRD acceptance, i.e. having a minimal number of MC hits in the TRD. They should also be reconstructed in the MVD and the STS with at least four points in total, of which one has to be in the first MVD layer. In addition, they must fulfil the requirement to point to the primary vertex with a $\chi^2/ndf < 3$.

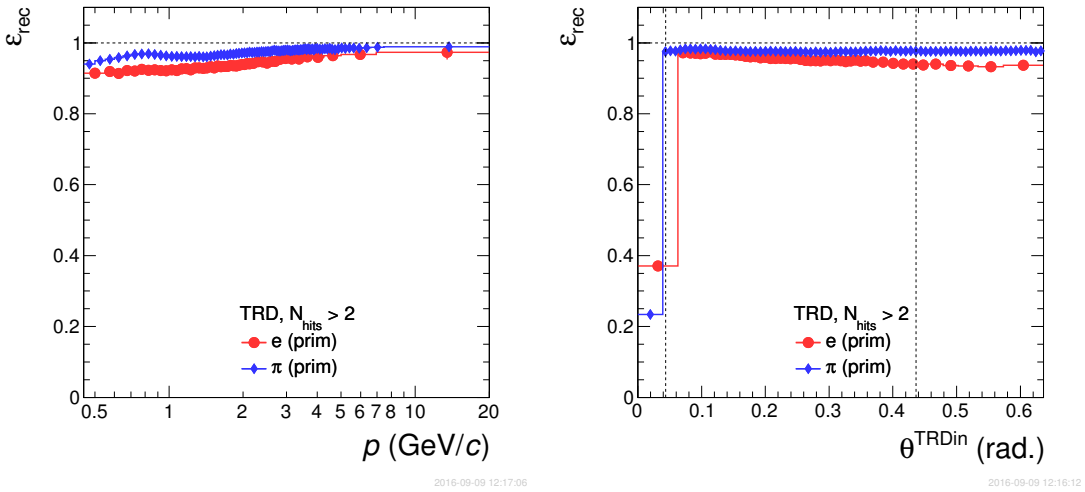

Figure 9.12: Reconstruction efficiency for primary $e^{\pm}$ (red) and pion (blue) tracks measured with at least three points in the TRD as a function of their momentum (left) and polar angle at the first TRD layer (right) in Au + Au collisions at 8 AGeV. The vertical dashed lines indicate the nominal CBM acceptance ($2.5° - 25°$).

Figure 9.12 shows the track reconstruction efficiencies for the TRD as a function of their momentum and polar angle at the first TRD layer θ^{TRDin} in Au + Au collisions at 8 AGeV beam energy. It is defined for tracks inside the TRD acceptance (producing at least three MC hits) and a minimal number of reconstructed TRD points of three. The efficiencies are well above 90 % at all momenta and θ^{TRDin}. A slight increase towards higher momenta and smaller angles is visible. These dependencies are more pronounced for the electrons than for pions. This difference is caused by the fact that electrons, in addition to multiple scattering, suffer from bremsstrahlung in the detector material in front of the TRD. This effect significantly alters their trajectories and cannot directly be incorporated in the treatment of the track errors within the Kalman filter approach, due to its highly non-Gaussian energy loss distribution as described by the Bethe-Heitler formula. However, overall the differences between the electron and pion efficiency are not very large (maximally 5 %).

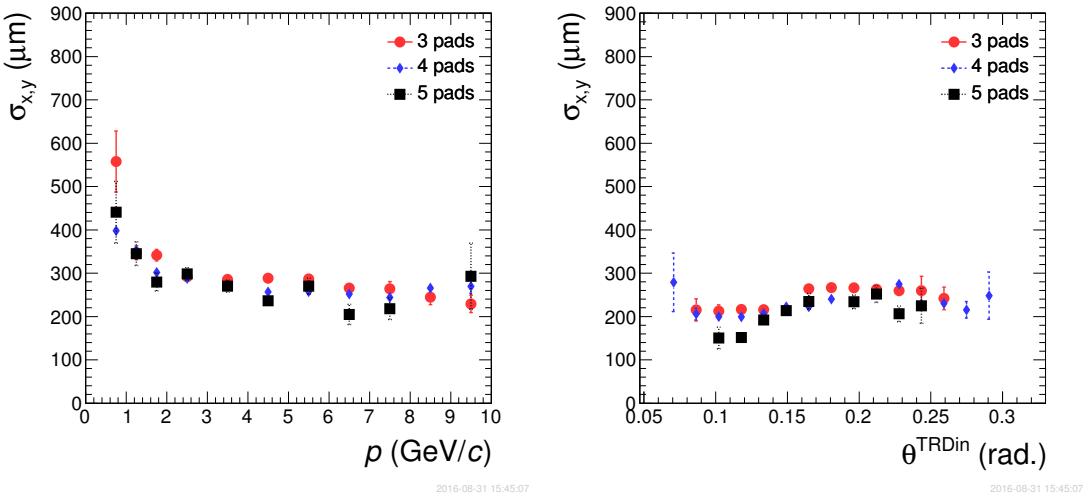

Figure 9.13: Point resolution for different cluster sizes ($3-5$ pads) as a function of momentum and polar angle at the first TRD layer of the tracks reconstructed in the innermost, small TRD modules in central Au + Au collisions at 8 AGeV.

The spatial resolution of reconstructed points is displayed in Fig. 9.13. It is obtained by comparing the reconstructed cluster ($3-5$ pad cluster) position along a pad row to the one of the corresponding MC point. For the innermost modules (small module types 1, 2 and 3) a very good position resolution below 300 µm for $p > 2\,\mathrm{GeV}/c$ is found, irrespective of the incidence angle of the track on the first TRD layer and of the cluster size. For the larger outer modules (module types 6, 7 and 8) the position resolution is found to be slightly worse and is $\sim 400\,\mu\mathrm{m}$.

In the current CBM global track reconstruction scheme the TRD points are not included in the momentum fits. Therefore, the momentum resolution is entirely determined by the STS alone and the TRD has no impact here.

9.3.3.3 Matching efficiency between TRD and TOF

An important question that needs to be addressed is whether the additional material introduced by the TRD will affect the matching efficiency between the tracks reconstructed by STS and TRD and the corresponding points found in the TOF detector. The additional multiple scattering caused by the TRD material should ideally at least be compensated by the additional point measurements with the TRD.

The results of a dedicated study are displayed in Fig. 9.14. A high matching efficiency for pion tracks (filled blue diamonds) of $\epsilon_{\mathrm{rec}} > 97\,\%$ is obtained with a TRD geometry including the complete material budget. This efficiency exhibits no strong dependence on momentum or polar angle. For electrons (filled red circles) it is found to be slightly less at low momenta and larger polar angles, but also never drops below 97 %.

To investigate whether the material introduced by the TRD outweighs the improvement of the pointing accuracy due to the TRD points, an additional calculation was performed where the TRD geometry was completely removed from the simulation. The results, which now correspond to the efficiencies for matching tracks reconstructed by STS alone to TOF points over the empty space between the two detectors, are shown as the open symbols in Fig. 9.14. For low momenta ($p \lesssim 1\,\mathrm{GeV}/c$), the TRD in fact causes a slight deterioration for pions. However, for higher momenta no effect is seen for pions while the electron matching efficiency is significantly improved by the presence of the TRD at all momenta. This can be explained by the effect of Bremsstrahlung on the electron trajectories in the STS and RICH material, which can to some

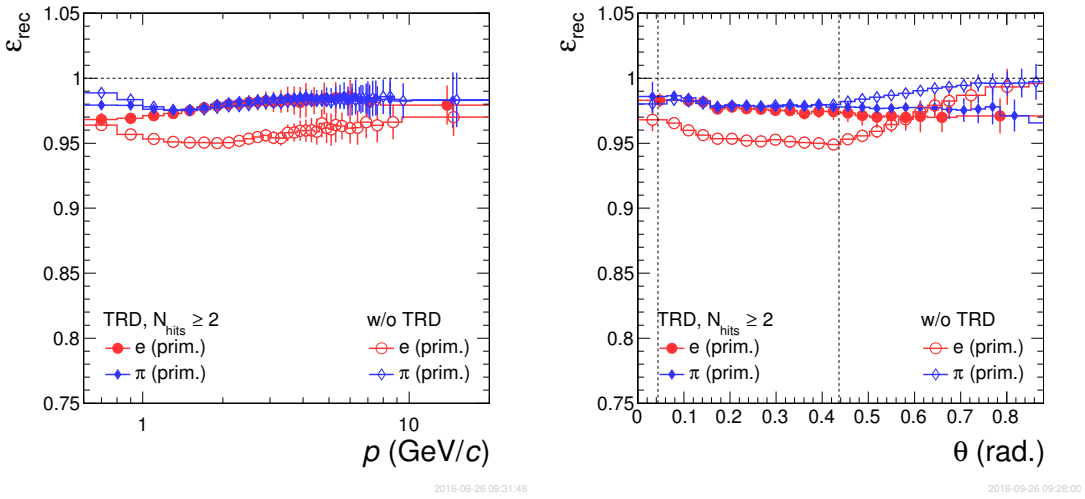

Figure 9.14: The efficiency to match tracks reconstructed in STS and TRD with at least three reconstructed TRD points to hits found in TOF for primary $e^{\pm}$ (red) and $\pi^{\pm}$ (blue) as a function of momentum (left) and polar angle (right) in Au + Au collisions at 8 AGeV beam energy (filled symbols). The vertical dashed lines indicate the nominal CBM acceptance ($2.5° - 25°$). Also shown is the matching efficiency between STS and TOF alone, without a TRD in between (open symbols).

extend be corrected by adding the intermediate point measurements of the TRD.

9.3.3.4 Electron identification efficiency

The electron identification efficiency is defined as the number of electrons which were correctly identified in the detectors STS(+RICH)(+TRD), divided by the number of electrons being properly reconstructed in the corresponding detectors. In this analysis the tracks are required to have the following minimal number of reconstructed points: $N_{\text{hits}}^{\text{STS}} \geq 6$, $N_{\text{hits}}^{\text{RICH}} \geq 6$ and $N_{\text{hits}}^{\text{TRD}} \geq 3$.

The pion suppression factor is defined as the number of pions which were reconstructed in the STS and TRD, divided by the number of pions identified as electrons in the corresponding PID detectors. The electron identification in the TRD applies a momentum dependent cut on the electron likelihood in order to achieve a momentum independent electron efficiency. The left panel of Fig. 9.15 shows as an example the case for 80 % electron efficiency. Similarly, a momentum dependent cut on the ANN-output of the RICH is applied such that a constant electron efficiency of 90 % up to $p = 9\,\text{GeV}/c$ results. For tracks above this momentum the RICH information is not used, since it does not significantly improve the electron identification there and would just reduce the efficiency.

The pion suppression factor as a function of momentum together with the corresponding electron efficiency is summarized in the right panel of Fig. 9.15 and in Tab. 9.1 for Au + Au collisions at 8 AGeV beam energy. The TRD alone, in its standard four layer configuration, will provide in the high momentum region ($p > 8\,\text{GeV}/c$) a pion suppression factor of up to ~ 23 (~ 45) at 90 % (80 %) electron efficiency. In this momentum region the addition of RICH and TOF information increases this value further to ~ 80, however at a reduced electron efficiency of ~ 70 %, due to the combination of the inefficiencies of the contributing detectors.

In addition to the standard TRD configuration with four layers, also setups consisting of three or five identical detector layer were investigated. Since these layouts will provide different numbers of measurements of the energy loss and TR production for a given track, they will

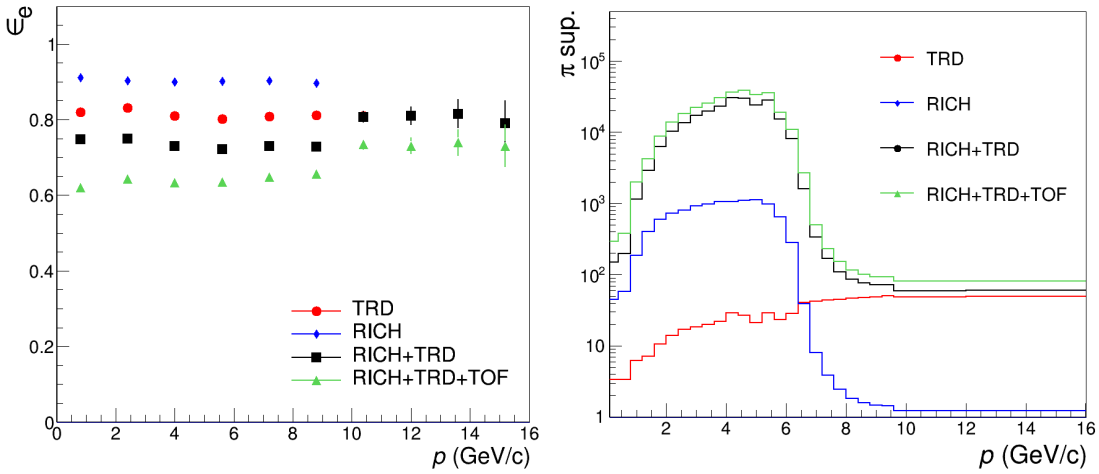

Figure 9.15: The electron identification efficiency (left panel) and the pion suppression factor (right panel) as a function of momentum. Both are calculated with the likelihood ratio method for the 10 % most central Au + Au collisions at 8 AGeV beam energy. Shown is the performance for different detector combinations.

naturally result in a worse, respectively better electron identification capability of the TRD. The resulting numbers on the pion suppression factors for the two setups are summarized in in Tab. 9.2 and presented as a function of momentum in Fig. 9.16. They are lower by about a factor of three in the case of three layers and higher by roughly the same factor for five layers, both in comparison to the default geometry with four layers.

Detector combination	Momentum region	TRD $e^{\pm}$-efficiency	Pion suppression factor
TRD	$2-8\,\mathrm{GeV}/c$	80 %	30
	$>8\,\mathrm{GeV}/c$	80 %	45
	$2-8\,\mathrm{GeV}/c$	90 %	20
	$>8\,\mathrm{GeV}/c$	90 %	23
RICH+TRD+TOF	$2-8\,\mathrm{GeV}/c$	80 %	3×10^3
	$>8\,\mathrm{GeV}/c$	80 %	80

Table 9.1: The pion suppression factors for different electron identification efficiencies in different momentum intervals and for different detector combinations. The electron efficiency of the RICH has been adjusted to 90 % in all cases. The values are given for the default TRD geometry with four layers.

9.3.4 Reconstruction efficiency of the TRD in the muon setup

As described in Sect. 4.3.2, the TRD is also foreseen as part of the CBM muon setup together with the MUCH detectors (see Fig. 4.5). In the SIS100-C configuration, muons will be reconstructed by the STS in combination with MUCH, consisting of one carbon (60 cm thickness) and three iron absorbers (20 cm, 20 cm and 30 cm thickness), instrumented with three GEM stations, followed by the four layer TRD station as final tracking station. Additional muon identification will be provided by the TOF detector.

Figure 9.17 illustrates that the TRD is indeed very well suited as tracking device in the muon spectrometer. Shown is the invariant mass distribution for muon pairs from ω mesons embedded into UrQMD events reconstructed with the MUCH setup employing the four layer TRD station

# Layers	Detector combination	Momentum region	Pion suppression factor
3	TRD	$2-8\,\mathrm{GeV}/c$	10
		$>8\,\mathrm{GeV}/c$	13
	RICH+TRD+TOF	$2-8\,\mathrm{GeV}/c$	1×10^3
		$>8\,\mathrm{GeV}/c$	20
5	TRD	$2-8\,\mathrm{GeV}/c$	70
		$>8\,\mathrm{GeV}/c$	145
	RICH+TRD+TOF	$2-8\,\mathrm{GeV}/c$	8×10^3
		$>8\,\mathrm{GeV}/c$	240

Table 9.2: The pion suppression factors for different electron identification efficiencies in different momentum intervals and for different detector combinations. The electron efficiency of the TRD has been adjusted to 80 % and the one of the RICH to 90 % in all cases. Shown are the numbers for alternative TRD geometries with three and five layers.

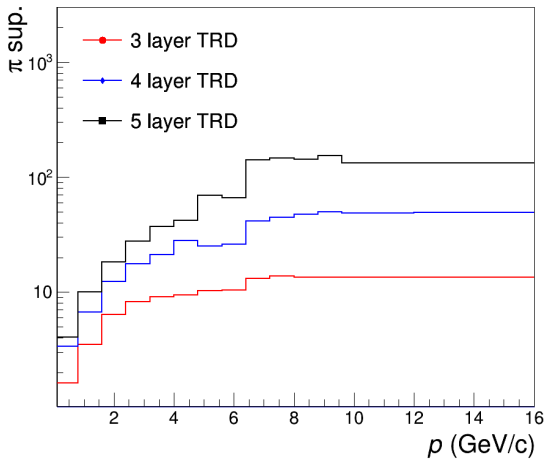

Figure 9.16: The pion suppression factor as a function of momentum for different numbers of TRD layers. All values are calculated with the likelihood ratio methode for the 10 % most central Au + Au collisions at 8 AGeV beam energy.

as final tracking device. The muon tracks were selected by requiring at least seven hits in the STS, eight in the MUCH tracking stations and two in the TRD. Further selection criteria are on the matching quality of the extrapolated tracks to the main interaction vertex, $\chi^2_{\mathrm{vertex}} < 2$, and to the hits reconstructed in the three MUCH tracking layers, $\chi^2_{\mathrm{MUCH}} < 1.25$, respectively in the four TRD layers, $\chi^2_{\mathrm{TRD}} < 3$. For the particle identification in TOF a cut at $m^2 < 0.01\,(\mathrm{GeV}/c^2)^2$ is imposed in addition. With this setup and cut selection, a reconstruction efficiency of $\epsilon_{\mathrm{rec}} = 4\,\%$ and a mass resolution of $14\,\mathrm{MeV}/c^2$ is obtained for the ω, with a signal-to-background ratio of ~ 0.5. By relaxing the selection criteria χ^2_{MUCH} and χ^2_{TRD} the efficiency can be significantly increased, however, at the expense of a reduced signal-to-background ratio. Depending on the applied criteria around $10^6 - 10^7$ ω mesons can thus be recorded in two months assuming an interaction rate of 1 MHz.

Figure 9.18 illustrates that the four layer TRD station matches the acceptance of the MUCH quite well. The acceptance, shown here as blue diamonds, is defined by muon tracks reconstructed in more than seven layers of the MUCH tracking detectors which generate at least one MC point in one of the TRD layers. While tracks below $p \approx 3.2\,\mathrm{GeV}/c$ are stopped in the last absorber, those above this momentum are all findable with the TRD. For these tracks also the efficiency has been determined (red dots in Fig. 9.18) by requiring that at least two matching hits have

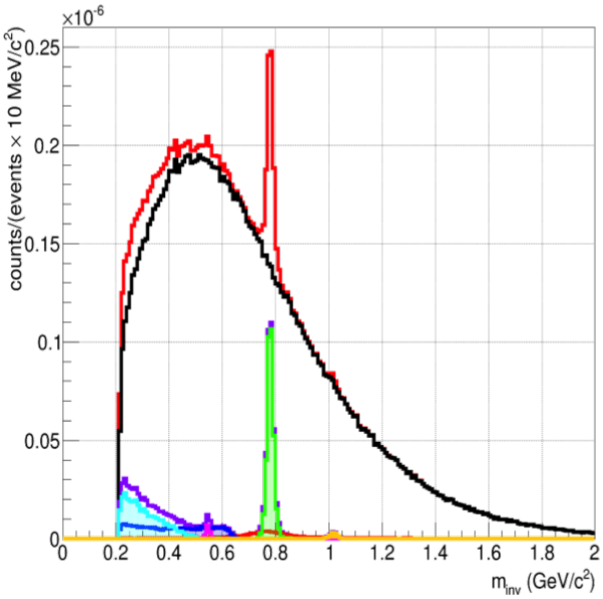

Figure 9.17: Invariant mass distribution of dimuon pairs in 10 % most central Au + Au collisions at 8 AGeV. Shown is a full simulation using as input a vector meson cocktail embedded into UrQMD events for the muon arm geometry with TRD as last tracking station. All pair combinations are represented by the red line, while the combinatorial background is displayed in black. The different components of the vector meson cocktail are also shown at the bottom of the figure.

to be reconstructed in the TRD. It is found to be $\sim 95\,\%$ and independent of the muon track momentum.

9.4 Calibration and alignment

An important prerequisite for a good reconstruction performance is the availability of accurate calibration and alignment procedures. With respect to the envisaged PID capabilities of the TRD, especially the gain stability is of crucial importance. Therefore, we address in this section in particular the possible strategies for gain calibration, which will be the main challenge depending on the chosen readout chamber type. In the high rate environment of CBM a proper alignment of the different TRD chambers is also essential to ensure a high matching efficiency between STS, TRD, and TOF. For both, calibration and alignment, one can build on the large amount of experience gathered in the recent years with the ALICE-TRD.

9.4.1 Gain calibration procedures

The gain of the TRD readout chambers will be influenced by several factors. Parameters such as temperature and pressure of the gas mixtures will have a direct effect on the overall gain, but can in principle be controlled to a certain extend by the gas system. Still, residual time dependent changes will remain, which need to be corrected within the reconstruction procedure. On top of this, every chamber will have a local variations of the gain that need to be known in order to achieve a uniform performance. Time dependent pressure differences between the inside and the outside of the chambers will modify these gain uniformities, since they can deform the entrance window that also serves as a cathode plane. E.g. for the ALICE-TRD variations of

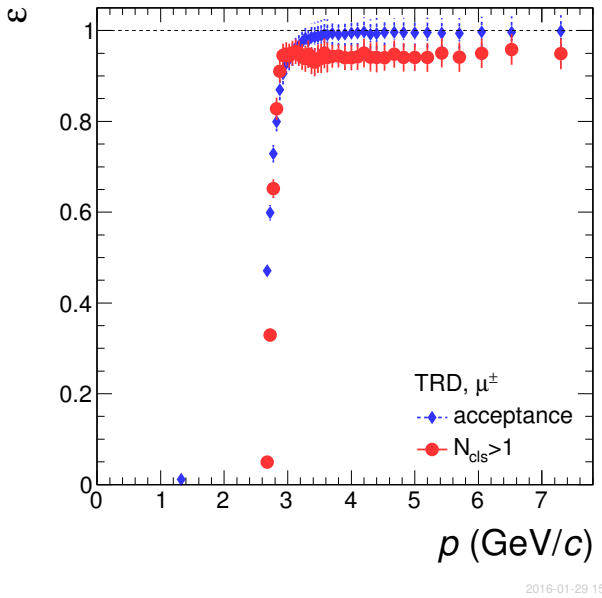

Figure 9.18: Acceptance (blue diamonds) and matching efficiency (red dots) of the TRD as part of the MUCH setup SIS100-C as a function of muon momentum for minimum bias Au + Au collisions at 8 AGeV. The efficiency is determined for tracks inside the acceptance having at least two reconstructed hits in the TRD.

the gain factors over one year of ±7 % were observed [49]. Therefore, a careful gain calibration strategy is mandatory and we foresee the procedures outlined in the following.

9.4.1.1 Krypton calibration

The local gain variations of the chambers can be mapped during a dedicated run where ^{83}Kr is added to the gas mixture. This procedure is well established and has been employed several times to calibrate TPCs [87, 88], as well as the ALICE-TRD [89, 90]. The procedure requires the introduction of solid ^{83}Rb into the gas system, which decays by electron capture into gaseous Kr. Hereby also the isomer state ^{83m}Kr is populated, which has an excitation energy of 41.6 keV, a half-life of 1.8 hours and decays into the ground state by the emission of electrons. By reconstructing the energy deposited by them inside the gas of the chambers a local gain calibration can be achieved. Previous experiences with the ALICE-TRD show that several days of measurement with a ^{83}Rb source of 5 MBq intensity are sufficient to register in the order of thousand counts per pad. This allows to establish two-dimensional gain factor maps with high enough accuracy ($\sim 1\,\%$), which can then serve as a starting point for a time-dependent gain calibration procedure. The Kr-calibration procedure would at least be required after each new module installation or rearrangement.

9.4.1.2 Online gain monitoring

A first correction of time dependent gain variations should be possible based on the online measurement of the pressure differences between inside and outside of the readout chamber. This measurement can be used to calculate variations of the gain factor by combining its known effect on the deformation of the entrance window and the induced change of the electric field. This online gain correction can serve as a starting point for a first reconstruction pass.

9.4.1.3 Calibration with data

A further refinement of the gain calibration can be achieved by a calibration using collision data. By analyzing the pulse height spectra collected within a given time interval, a time dependent calibration can be performed. As a minimal option, this will allow to calculate one pad averaged gain factor per readout chamber which can be used to correct the two-dimensional gain factor maps obtained by the Kr-calibration by a time dependent correction factor. For the ALICE-TRD a precision of 1.4 % was achieved with this kind of procedure [49]. However, the high interaction rates measured with CBM might allow to accumulate much higher statistics than available to ALICE within the relevant time intervals (typically in the range of $1 - 6$ hours). Therefore a time dependent calibration of more local regions of a given ROC (groups of pads or even single pads) could be possible.

In addition to the gain calibration, this procedure will allow to monitor time depending variations of the status and noise level of a given readout channel and thus will be an essential part of the data quality assurance.

9.4.2 Alignment procedure

The alignment of the TRD chamber relative to each other and relative the STS can be performed using either tracks from cosmic rays or from collisions in the target. The procedure is in principle based on a minimization of space point residuals with respect to reconstructed tracks, as can be implemented within. e.g., the MILLIPEDE package [91]. Since the tracks passing through the TRD layers are straight, due to the absence of any magnetic field in this region, this minimization procedure should pose no principal problems. Generally, the alignment should be updated before each data taking period, especially if the detector setup has been modified.

Using cosmic ray tracks has the advantage, that an alignment can be performed before the actual data taking. This is important for the online data reconstruction, whose performance will otherwise be limited. A possible disadvantage of this approach is that it might be difficult to obtain sufficient statistics for cosmic ray tracks that pass horizontally through all detector layers. In any case, this requires a dedicated trigger setup (using e.g. the TOF detector). With the ALICE-TRD a typical precision of the relative chamber alignment with cosmic ray tracks of 0.13 mm was achieved, requiring a statistics in the order of 10^3 tracks per chamber [49].

A higher accuracy of the alignment will be achievable with real collision data, since a much higher statistics of usable tracks will be available. However, this procedure will only be possible during or even after the data taking. An online implementation of the procedure might allow to determine the alignment parameter iteratively before any online reconstruction and might also be used to monitor time dependent variations of the relative chamber alignment.

Chapter 10

Mass Production

As described in Chap. 4 the CBM-TRD for SIS100 will consist in total of 216 individual detectors (not including spares), which need to be constructed, tested, and finally installed in the experimental setup of CBM. These tasks can naturally not be handled by a single institution. Therefore, it is necessary to involve several major construction sites in the assembly of the individual detectors or major parts of it. In order to keep the production fast and cost efficient, it is planned to use industrial pre-produced components as often as possible. The production of the individual ROCs can be subdivided into three major component groups: entrance window, wires and FR4 ledges and backpanel. This modularity opens up the possibility to assembly subcomponents at individual institutes. Alternatively, the production can be subdivided according to ROC module types (see e.g. Fig. 5.22). Further work packages are the production of the radiators, as well as the electronics integration and test.

10.1 Production equipment

For the production and test of the ROCs the following basic equipment is required:

- **Clean room:** The mounting and adjusting of the wires should be performed in a room which provides a sufficiently dust free environment.
- **Granite or glass table:** Tables with sufficient planarity (precision below 50 µm) are required for the ROC frame assembly.
- **Winding machine:** Special machines for the production of wire planes with controlled wire tension are needed. The wires are wound onto aluminum frames of sufficient rigidity, which then can be transferred to the ROC frames to allow glueing of the wires onto the frames.
- **Optical alignment and tension measurement devices:** In order to properly align the wires with a precision better than 10 µm a setup with a microscopic device is required. After glueing, the tension of the wires needs to be measured by an additional setup.
- **Plexiglas frame:** These frames are needed to stretch the Kapton foils for the ROC entrance windows. The frames are heated, e.g. by an oven of sufficient size providing temperatures up to 60 $^{\circ}$ C, and therefore expand, thus providing the necessary tension to the foils.
- **Test stand:** For a first performance test of the completed ROCs they are scanned with an ^{55}Fe-source in a special test stand. This requires the availability of a simplified gas system and a data acquisition in order to operate the chambers in the laboratory under realistic conditions.

- **Storage space:** Appropriate space for storage of raw materials and finished detector modules should be available at the construction sites.

10.1.1 Existing laboratory infrastructure

It is foreseen to distribute the ROC production between the laboratories in Bucharest, Frankfurt and Münster. All sites were already involved in the construction and integration of chambers of the ALICE-TRD. Therefore, they have not only collected a considerable experience in the mass production of MWPCs, but also have already installed fully equipped detector laboratories for this purpose.

10.1.1.1 Bucharest laboratory

The laboratory for gas detectors at the Hadron Physics Department "Horia Hulubei" National Institute of Physics and Nuclear Engineering, Bucharest (HPD/IFIN-HH) has originally been set up for the construction of ROCs for the ALICE-TRD and provides all the necessary equipment. Its infrastructure consists of five clean rooms (2 × ISO6, 1 × ISO7 and 2 × ISO8), one wire winding machine, two vacuum tables, one glass table, and the necessary devices for mounting and adjusting the wires and for measuring their tension. For testing the completed chambers a special chamber test stand available in a separate room.

10.1.1.2 Frankfurt laboratory

The laboratory for gas detectors at the Institut für Kernphysik, Frankfurt (IKF) has originally been set up for the construction of readout chambers for the ALICE-TRD and provides all the necessary equipment. Its infrastructure consists of a clean room equipped with a wire winding machine, a portal crane for the transport of the wire frames, and the necessary devices for mounting and adjusting the wires and for measuring their tension. In a second room a granite table (dimensions: 180 cm × 120 cm × 25 cm) with a mechanical precision below 12 µm underneath an airflow box is available for the final assembly of a given chamber. For testing the completed chambers a special test stand has been set up in a separate room, which allows to scan the chambers in two dimensions with a radioactive or a X-ray source. In addition, other rooms are available for preparing the chamber frames and backpanels and for performing tests of the mounted frontend electronics. All the described equipment is free to be used for the chamber production for the CBM-TRD.

10.1.1.3 Münster laboratory

The laboratory for gas detectors at the Institut für Kernphysik, Münster (IKP) has originally been set up for the integration of readout chambers for the ALICE-TRD into so-called super-modules and provides all the necessary equipment for final integration and hardware tests. Its infrastructure consists of a test gas system, a portal crane for the transport of larger chamber structures, and a water cooling system. In a second room a granite table with a mechanical precision below 12 µm underneath an airflow box is available for the final assembly of a given chamber. It is planned to move a wire winding machine from Heidelberg ALICE-TRD equipment to Münster for the time of the detector production for CBM. A cleanroom, which was used for the production of wire frames for the KATRIN experiment, will then be available for the final chamber assembly. In addition, other rooms are available for preparing the chamber frames and backpanels and for performing tests of the mounted frontend electronics. All the described equipment is free to be used for the chamber production for the CBM-TRD. Cooperations with local industries have been established and developed further during the prototype production.

10.2 Production timeline

10.2.1 Human resources

The available human resource in the three institutions participating in the module construction is estimated in Tab. 10.1. The total working hours per week of 745 h has to be divided corresponding to the construction tasks described below and the project plan given in Sect. 11.3.

Institute	Phys.	Tech.	Pdocs	PhD	MSc	PTE
Bucharest	3.00	5.00	0.00	1.00	1.00	0.00
Frankfurt	1.00	1.25	1.00	2.00	3.00	3.00
Münster	1.00	3.50	1.00	2.00	4.00	2.00
WHPD	8.50	8.50	8.50	8.50	8.50	2.00
scale factor	0.75	0.75	0.50	0.33	0.33	1.00
WHPW	159.20	310.80	42.50	70.10	112.20	50.00
CBM-TRD WHPW						**744.8**

Table 10.1: Working Hour Per Day (WHPD) and Working Hour Per Week (WHPW) based on the available human resource of the participating institutes. We distinguish permanent stuff physicists (Phys.), technicians and engineers (Tech.), Postdocs (Pdocs), PhD students (PhD), master students (MSc) and part time employees (student helpers, etc.) (PTE).

10.2.2 Time consumption

We have relatively good estimates on the time consumption for the production of ROCs based on experiences with the ALICE-TRD ROC mass production and CBM-TRD prototype construction. From this we estimate the total production time for one ROC including wire position and tension tests, as well as final HV stability and gas tightness tests done by two persons to be 77 hours and 170 hours for hardening of the glue. This breaks down into three main building blocks: entrance window, backpanel, wire plane and ledges. Since the most time consuming part of the ROC production is the hardening of the glue (12 h) and the wire winding (4 h) and each wire winding process results in two identical wire planes it is more efficient to build two ROCs in parallel. For the following estimations we will use abbreviation for Glueing Hours (GH) and Working Hours (WH). With an adequate work planning it is possible to move most of the GH towards night which makes production more efficient.

10.2.2.1 Entrance window

The production of one entrance window composed of a single sided aluminized Kapton foil, outer FR4 frame and CF lattice takes for two persons three days or 17 WH and 36 GH. The parallel production can only be realized if critical infrastructure like the oven for thermal stretching of the foil and the Plexiglas stretching frame is also available two times.

10.2.2.2 Backpanel

The production of one backpanel composed of aluminum frame, honeycomb and pad plane takes for two persons five days or 35 WH and 48 GH. A vacuum table with a sufficient surface is necessary for the parallel production of two backpanels.

10.2.2.3 Wiring and glueing to ledges

The final completion of the ROC, joining of the two pre-produced building blocks, wiring and glueing of the wired distance ledges takes for two persons seven days or 25 WH and 86 GH.

10.2.2.4 Radiator

In addition to the ROC also the radiator boxes need to be prepared. Due to their relatively simple construction their construction mainly requires the glueing of the boxes and the application of the support filaments, once the necessary pieces have been prepared in the required dimensions. This is estimated to require 3 WH and 36 GH. However, these activities can be done in parallel to the ROC production and thus will not substantially add to the overall required time.

10.2.2.5 Front-End Electronics

The production of the FEBs will be done in external companies once all the ASICs are available. Therefore, no additional manpower is needed for this purpose. However, the produced boards will of course require a thorough testing before installation on the TRD modules. This task will have to be performed by the involved institutes. Once a defined testing program is in place, these procedures can be run in parallel to the chamber production and could be operated by $2-3$ additional student helpers (PTE).

10.2.2.6 Total production time

This results in a total time consumption for two ROCs built by two persons of 15 days, composed of 77 WH and 170 GH. Including the assumption of 250 working days per year we come up with an estimated production time for three participating production sides producing two ROCs in parallel of two years in total. The detailed project time plan can be found in Sect. 11.3.

Chapter 11

Project Organization

The CBM-TRD project is organized as follows: in addition to a project leader (Christoph Blume), a deputy project leader (Mihai Petrovici) and a project technical coordinator (Cyrano Bergmann, before David Emschermann), seven sub-projects have been defined:

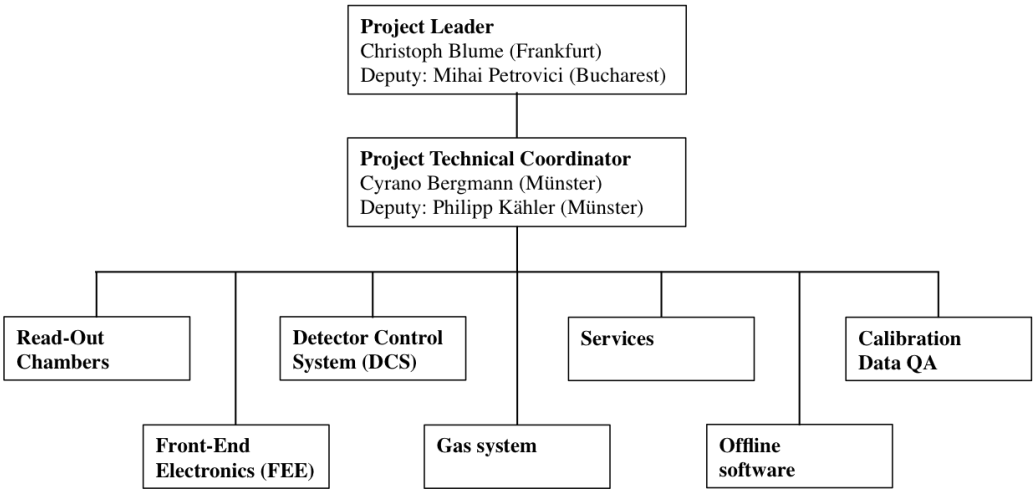

These sub-projects encompass the following activities and responsibilities, which should be organized by one dedicated coordinating person:

- **Read-out chamber:** Installation, commissioning, and operation of the readout chambers, including the radiators.
- **Front-End Electronics (FEE):** Integration, commissioning, and operation of the TRD FFE and the following readout chain. Implementation and maintenance of feature extraction and other online signal processing algorithms.
- **Detector Control System (DCS):** Integration of the TRD in the CBM-DCS.
- **Gas system:** Development, installation, and operation of the TRD gas system.
- **Services:** Installation and maintenance of the LV, HV, and cooling system.
- **Offline software:** Implementation and maintenance of the TRD offline software. This includes the detector specific simulation software, as well as the TRD related reconstruction algorithms (tracking, PID).

- **Calibration:** Implementation and operation of the TRD calibration algorithms (e.g. gain calibration). Also, included are procedures to perform a quality assessment of the raw and reconstructed data.

11.1 Responsibilities

11.1.1 Participating institutes

The following institutions are participating in the development and construction of the CBM-TRD:

- Bucharest, Romania, National Institute of Physics and Nuclear Engineering (IFIN-HH).
- Frankfurt am Main, Germany, Institut für Kernphysik (IKF), Goethe-Universität.
- Frankfurt am Main, Germany, Institut für Informatik, Infrastruktur und Rechnersysteme in der Informationsverarbeitung (IRI), Goethe-Universität.
- Heidelberg, Germany, Institut für technische Informatik (ZITI), Ruprecht-Karls-Universität.
- Münster, Germany, Institut für Kernphysik (IKP), Westfälische Wilhelms-Universität.

In addition, there is an expression-of-interest to join the project by a group at the Wigner Research Centre for Physics in Budapest, Hungary.

11.1.2 Sharing of tasks

The following table summarizes how the responsibilities for the construction of the TRD will be shared. It reflects the current assignments for the TRD part od the CBM hardware components list, which is being prepared as a basis for a future memorandum of understanding.

Item	Institutions
ROCs	Bucharest (IFIN-HH)
	Frankfurt (IKF)
	Münster (IKP)
Radiators	Münster (IKP)
ASICs	Heidelberg (ZITI)
FEBs	Frankfurt (IKF)
ROBs	Münster (IKP)
Gas system	Münster (IKP)
Cooling	Münster (IKP)
LV system	Frankfurt (IKF)
HV system	Münster (IKP)
On-detector & environment monitoring	Frankfurt (IKF)
CRI layer (firmware design)	Frankfurt (IRI)
Offline software	Frankfurt (IKF)

11.2 Costs

The following calculation is based on the costs (netto) estimated for the prototype production in 2017. Also, the costs for the external support structure and additional external services are not included here.

11.2.1 Single readout chamber and FEE

The cost estimates for a single readout chamber (w/o readout electronics) are based on the experiences with the construction of CBM-TRD prototypes and ALICE-TRD modules.

Item	Cost (Euro)			
Module-type	1	3	5	7
Honeycomb	610	610	1,320	1,320
Pad plane	450	450	1,490	1,490
Gas plugs	50	50	50	50
Aluminum frame	50	50	90	90
FR4 ledges	540	540	900	900
Kapton single sided aluminum sputtered	40	40	40	40
Carbon lattice	60	60	120	120
Araldite glue	20	20	20	20
Anode wire	20	20	40	40
Cathode wire	30	30	80	80
Radiator foam foil CellAir 2 mm	50	50	70	70
Radiator box 10 mm Rohacell HF71	110	110	220	220
Signal cable 40-pin			20	20
Signal cable 64-pin	30	30		
Expendables	260	260	410	410
Total	2,320	2,320	4,870	4,870
Sum				**705,120**

The costs for the TRD readout electronics, covering the full readout chain, includes in addition to the front-end electronics (ASICs and FEBs) the infrastructure for the data collection, namely the common readout interface boards CRI-24, ROBs and optical fibres. For the total number of 329,728 channels, the following costs have been estimated:

Item	Cost (kEuro)
ASICs (incl. 10 % spares)	158
FEBs (incl. 10 % spares)	279
CRI-24 boards	816
ROBs	55
Optical fibers	104
Total	**1,412**

Relating this cost estimate to the total number of readout channels results in 4.15 Euro/channel, including all readout components but without spares.

11.2.2 Total TRD setup

Based on cost estimate for a single ROC and the readout electronics presented above, the total cost for the CBM-TRD is estimated. For the SIS100 configuration (four layers) we thus arrive at the following values:

Item	Cost (kEuro)
ROC (216 chambers + 10 % spares)	776
Readout electronics	1,412
Xe/CO_2 (initial filling)	40
HV PS	75
LV PS (FEB & ROB)	100
HV cables & infrastructure	40
LV cables & bus bars	40
DC-DC converter	135
Gas system	500
Cooling	250
Support structure	194
Total	**3,562**

11.2.3 Project funding

The TRD project will be funded mainly by German and Romanian agencies. In the case of the involved German universities this will be BMBF "Verbundforschung", while the Romanian contribution will be provided in form of an in-kind contract between FAIR, IFIN-HH and the Romanian funding agency. Here, we quote the numbers communicated by the CBM collaboration to the FAIR Resource Review Board (RRB) at its 7th meeting in Nov. 2017. The numbers in italics are currently not considered as secured yet, but rather an expression-of-interest.

Source	Amount (MEuro)	
Germany (BMBF, university funding)	1.00	+ *0.59*
Romania (In-kind contract)	1.73	
Hungary	0.20	+ *0.05*
Total	2.93	+ *0.64*

11.3 Schedule

The overall TRD construction and milestone plan is shown in Figs. 11.1 and 11.2. It is based on the current FAIR planning and assumes that the CBM cave will be available for detector installation in Dec. 2021 and envisages that the first TRD modules can be installed from January 2023 onwards. The schedule is planned such that the complete TRD support structure with all services will be available in the CBM cave at that moment and can then subsequently be equipped with fully tested and instrumented TRD modules. It is also adjusted to the envisaged funding profile for the project and embedded in the official FAIR planning scheme. Here it is assumed that Romanian in-kind contract will be signed in Dec. 2019, while the German BMBF-funding can be expected for the coming funding period starting in Oct. 2018.

The plan foresees a detailed list of milestones, including the following Conceptual Design Reviews (CDR), Production Design Reviews (PDR) and Production Readiness Reviews (PRR):

Milestone	Date
Chamber support CDR	28.06.2019
SPADIC ASIC PDR	01.11.2018
SPADIC ASIC PRR	12.12.2018
FEB PRR	27.12.2019
Large modules PDR	28.06.2019
Small modules PDR	27.12.2019
Radiator box PDR	27.12.2019
Gas system CDR	28.06.2019
HV system CDR	13.07.2018
LV system CDR	13.07.2018
Mainframe CDR	26.06.2020
Support and mainframe PDR	25.06.2021

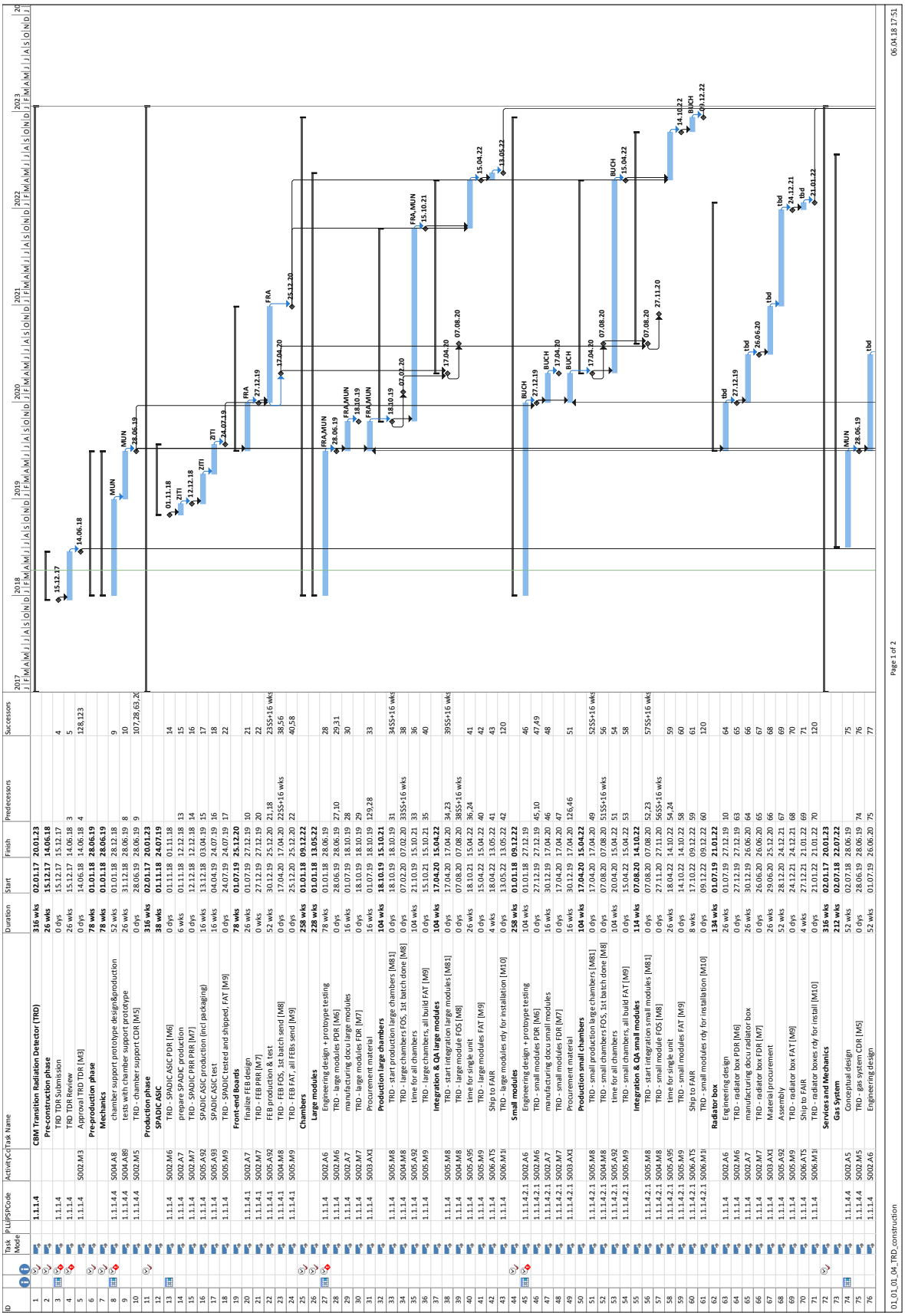

Figure 11.1: Project plan outlining the production schedule and the corresponding milestones (part 1).

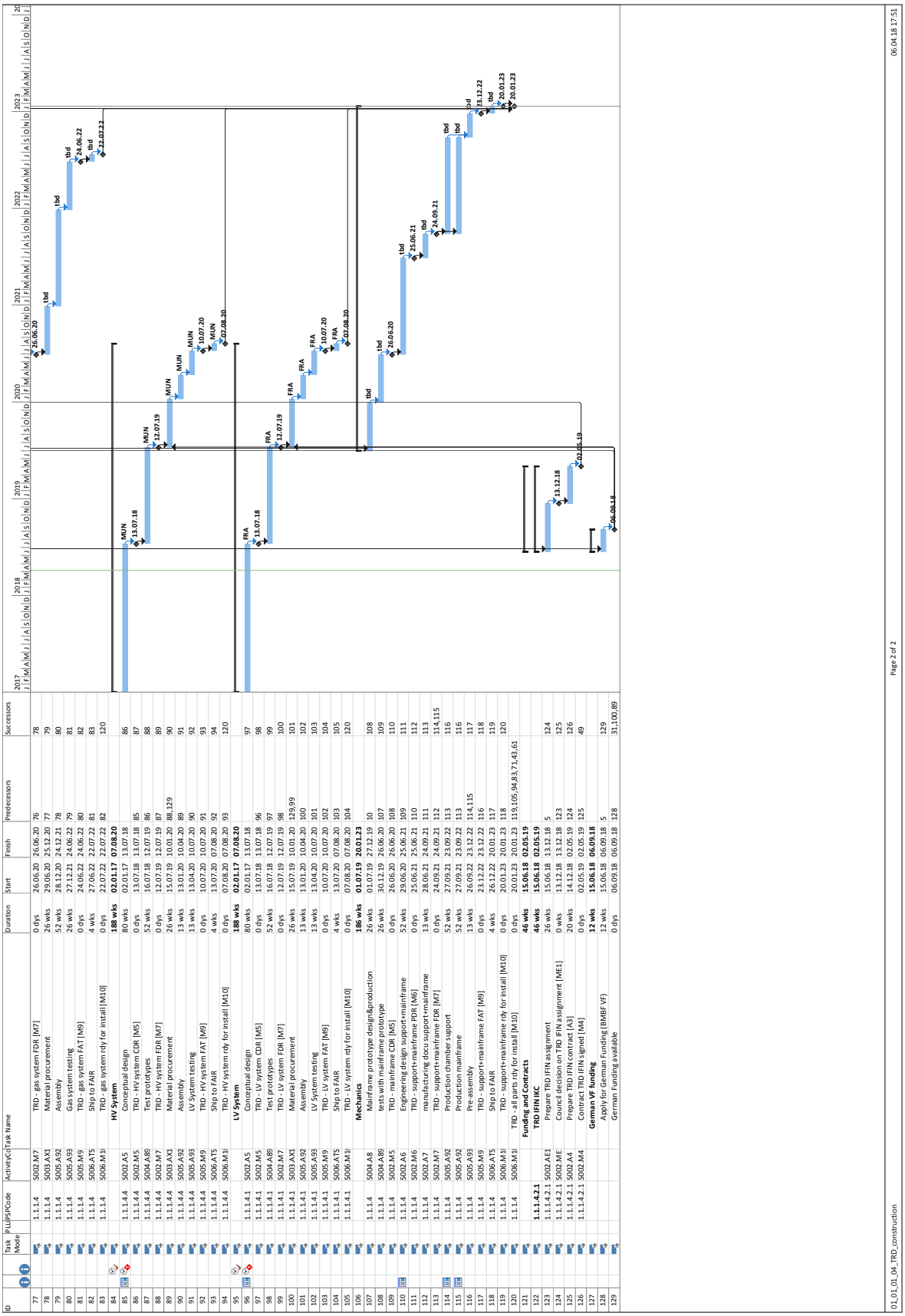

Figure 11.2: Project plan outlining the production schedule and the corresponding milestones (part 2).

Appendix A

The CBM Collaboration

T. Ablyazimov[1], A. Abuhoza[2,61], R.P. Adak[3], M. Adamczyk[4], K. Agarwal[5], M.M. Aggarwal[6], F. Ahmad[7], N. Ahmad[8], S. Ahmad[7], A. Akindinov[9], P. Akishin[1], E. Akishina[1], T. Akishina[1], V. Akishina[10,1,2], A. Akram[11], M. Al-Turany[2], I. Alekseev[9], E. Alexandrov[1], I. Alexandrov[1], S. Amar-Youcef[12], M. Anđelić[13], O. Andreeva[14], C. Andrei[15], A. Andronic[2], Yu. Anisimov[16], H. Appelshäuser[12], D. Argintaru[17], E. Atkin[18], S. Avdeev[16], R. Averbeck[2], M.D. Azmi[8], V. Baban[17], E. Badura[2], S. Bähr[19], T. Balog[2], M. Balzer[19], S. Bandyopadhyay[20], E. Bao[11], N. Baranova[21], D. Bartoş[15], S. Bashir[7], M. Baszczyk[22], O. Batenkov[23], V. Baublis[24], M. Baznat[16], J. Becker[19], K.-H. Becker[25], S. Belogurov[1], A. Belousov[10], D. Belyakov[1], J. Bendarouach[26], I. Berceanu[15], A. Bercuci[15], A. Berdnikov[27], Y. Berdnikov[27], R. Berendes[28], G. Berezin[16], C. Bergmann[28], D. Bertini[2], O. Bertini[2], C. Beşliu[17], O. Bezshyyko[29], P.P. Bhaduri[2,30], A. Bhasin[31], A.K. Bhati[6], B. Bhattacharjee[32], A. Bhattacharyya[20], T.K. Bhattacharyya[33], S. Biswas[3], T. Blank[19], D. Blau[34], V. Blinov[2], C. Blume[12], Yu. Bocharov[18], J. Book[12], J. Brzychczyk[4], A. Bubak[35], T. Bus[12], V. Butuzov[18], A. Bychkov[16], A. Byszuk[36], M. Călin[17], Ping Cao[37], G. Caragheorgheopol[15], I. Carević[13], V. Cătănescu[15], A. Chakrabarti[20], Sanatan Chattopadhyay[20], Subhasis Chattopadhyay[30,3],A. Chaus[38], Jianping Cheng[39], V. Chepurnov[16], H. Cherif[12,2], A. Chernogorov[9], M.I. Ciobanu[2,62], G. Claus[40], F. Constantin[15], M. Csanád[41], Supriya Das[3], Susovan Das[5], J. de Cuveland[10], B. Debnath[32], D. Dementiev[16], Wendi Deng[42], Zhi Deng[39], H. Deppe[2], I. Deppner[11], O. Derenovskaya[1], C.A. Deveaux[26], M. Deveaux[12], K. Dey[32], V. Dobyrn[24], D. Doering[12], Sheng Dong[42], A. Dorokhov[40], A. Drozd[22], A.K. Dubey[30], S. Dubnichka[16], Z. Dubnichkova[16], M. Dürr[26], L. Dutka[4], M. Dželalija[13], V.V. Elsha[16], D. Emschermann[2], H. Engel[43], V. Eremin[44], T. Eşanu[17], J. Eschke[45,2], Xingming Fan[46], O. Fateev[16], Shengqin Feng[47], S.P.D. Figuli[19], I. Filozova[1], D. Finogeev[14], P. Fischer[48], H. Flemming[2], J. Förtsch[25], U. Frankenfeld[2], V. Friese[2], E. Friske[5], I. Fröhlich[12], J. Frühauf[2], J. Gajda[22], T. Galatyuk[49,2], G. Gangopadhyay[20], C. García Chávez[43],J. Gebelein[43], P. Ghosh[12,2], S.K. Ghosh[3], S. Gläßel[12], M. Goffe[40], L. Golinka-Bezshyyko[29], V. Golovatyuk[16], S. Golovnya[50], V. Golovtsov[24], M. Golubeva[14], D. Golubkov[9], A. Gómez Ramírez[43],S. Gorbunov[10], S. Gorokhov[50], D. Gottschalk[11], P. Gryboś[22], F. Guber[14], K. Gudima[16], M. Gumiński[36], A. Gupta[31], Yu. Gusakov[16], Dong Han[39], H. Hartmann[10], J. Hehner[2], N. Heine[28], A. Herghelegiu[15], N. Herrmann[11], B. Heß[5], J.M. Heuser[2], A. Himmi[40], C. Höhne[26], R. Holzmann[2], Dongdong Hu[37], Guangming Huang[42], Xinjie Huang[39], D. Hutter[10], A. Ierusalimov[16], M. Irfan[8], D. Ivanischev[24], M. Ivanov[2], P. Ivanov[18], Valery Ivanov[1], Victor Ivanov[1], Vladimir Ivanov[24,18], A. Ivashkin[14], K. Jaaskelainen[40], H. Jahan[8], V. Jain[30], V. Jakovlev[23], T. Janson[43], Di Jiang[37], A. Jipa[17], I. Kadenko[29], P. Kähler[28], B. Kämpfer[46,63], V. Kalinin[23], J. Kallunkathariyil[4], K.-H. Kampert[25], E. Kaptur[35], R. Karabowicz[2], D. Karmanov[21], V. Karnaukhov[16], K. Kasiński[22], G. Kasprowicz[36], M. Kaur[6], A. Kazantsev[34], U. Kebschull[43], G. Kekelidze[16], M.M. Khan[8], A. Khanzadeev[24,18], F. Khasanov[9], A. Khvorostukhin[16], V. Kirakosyan[16],

A. Kiryakov[50], M. Kiš[2], I. Kisel[10], P. Kisel[12,2,1], S. Kiselev[9], T. Kiss[51], P. Klaus[12], R. Kłeczek[22], Ch. Klein-Bösing[28], V. Kleipa[2], V. Klochkov[2,12], P. Kmon[22], K. Koch[2], L. Kochenda[24,18], P. Koczoń[2], M. Kohn[28], B. Komkov[24], M. Korolev[21], I. Korolko[9], R. Kotte[46], A. Kovalchuk[38], S. Kowalski[35], M. Koziel[12], G. Kozlov[10,1], V. Kozlov[24], V. Kramarenko[16], P. Kravtsov[24,18], E. Krebs[12], I. Kres[25], D. Kresan[2], G. Kretschmar[12], M. Krieger[48], A.V. Kryanev[1,18], E. Kryshen[24], M. Kuc[52], W. Kucewicz[22], V. Kucher[10], L. Kudin[24], A. Kugler[53], A. Kumar[30], L. Kumar[6], A. Kurepin[14], N. Kurepin[14], A. Kurilkin[16], P. Kurilkin[16], V. Kushpil[53], S. Kuznetsov[16], V. Kyva[38], V. Ladygin[16], C. Lara[43], P. Larionov[12,2], A. Laso García[46,63],E. Lavrik[5], I. Lazanu[17], A. Lebedev[2,1], S. Lebedev[26,1], E. Lebedeva[26], J. Lehnert[2], Y. Leifels[2], Qiyan Li[12,42], Xin Li[37], Yuanjing Li[39], V. Lindenstruth[10,2], B. Linnik[12], Feng Liu[42], I. Lobanov[50], E. Lobanova[50], S. Löchner[2], P.-A. Loizeau[2], S.A. Lone[7], J.A. Lucio Martínez[43],Xiaofeng Luo[42], A. Lymanets[2,38], Pengfei Lyu[39], A. Maevskaya[14], S. Mahajan[31], T. Mahmoud[26], P. Maj[22], Z. Majka[4], A. Malakhov[16], E. Malankin[18], D. Malkevich[9], O. Malyatina[18], H. Malygina[12,2,38], S. Mandal[30], V. Manko[34], A.M. Marin Garcia[2], J. Markert[2], S. Masciocchi[2], T. Matulewicz[52], L. Meder[19], M. Merkin[21], V. Mialkovski[16], J. Michel[12], N. Miftakhov[24], L. Mik[22], K. Mikhailov[9], V. Mikhaylov[53], V. Militsija[38], M.F. Mir[7], D. Miskowiec[2], I. Momot[12,2,38], T. Morhardt[2], S. Morozov[14], W.F.J. Müller[45,2], C. Müntz[12], S. Mukherjee[3], C.E. Muñoz Castillo[43],Yu. Murin[16], C. Nandi[30], E. Nandy[30], L. Naumann[46], T. Nayak[30], V.S. Negi[30], W. Niebur[2], V. Nikulin[24], D. Normanov[18], A. Oancea[43], Kunsu Oh[54], Yu. Onishchuk[29], G. Ososkov[1], P. Otfinowski[22], E. Ovcharenko[1], S. Pal[30], I. Panasenko[5,38], N.R. Panda[55], S. Parzhitskiy[16], V. Patel[25], C. Pauly[25], D. Peshekhonov[16], V. Petráček[56], M. Petri[12], M. Petriş[15], A. Petrovici[15], M. Petrovici[15], A. Petrovskiy[18], O. Petukhov[14], D. Pfeifer[25], K. Piasecki[52], J. Pietraszko[2], R. Płaneta[4], V. Plotnikov[9], V. Plujko[29], J. Pluta[36], A. Pop[15], B.V.K.S. Potukuchi[31], K. Poźniak[36,52], A. Prakash[53], S.K. Prasad[3], M. Prokudin[9], M. Pugach[10,2,38], V. Pugatch[38], S. Querchfeld[25], L. Radulescu[15], S. Raha[3], W. Raja[7], F. Rami[40], R. Raniwala[57], S. Raniwala[57], A. Raportirenko[1], J. Rautenberg[25], J. Rauza[22], R. Ray[3], S. Razin[16], S. Reinecke[25], A. Reinefeld[58], A. Reshetin[14], C. Ristea[17], O. Ristea[17], A. Rodriguez Rodriguez[2], F. Roether[12], R. Romaniuk[36], A. Rost[49], E. Rostchin[24,18], I. Rostovtseva[9], J. Rożynek[52], Yu. Ryabov[24], R. Sahoo[59], P.K. Sahu[55], S.K. Sahu[55], J. Saini[30], S. Samanta[3], S.S. Sambyal[31], V. Samsonov[24,18,27], O. Sander[19], S. Sarangi[33], S. Sau[20], C. Schiaua[15], F. Schintke[58], C.J. Schmidt[2], H.R. Schmidt[5], J. Scholten[12], K. Schweda[2], F. Seck[49], S. Seddiki[2], I. Selyuzhenkov[2], A. Semennikov[9], A. Senger[2], P. Senger[2,12], A. Shabanov[14], A. Shabunov[16], Ming Shao[37], A.D. Sheremetiev[16], Shusu Shi[42], N. Shumeiko[16], V. Shumikhin[18], I. Sibiryak[34], B. Sikora[52], A. Simakov[18], C. Simon[11], C. Simons[2], A.K. Singh[33], B.K. Singh[60], C.P. Singh[60], V. Singhal[30], M. Singla[2], P. Sitzmann[12], K. Siwek-Wilczyńska[52],L. Škoda[56], I. Skwira-Chalot[52], I. Som[33], Guofeng Song[37], D. Soyk[2], P. Staszel[4], M. Strikhanov[18], S. Strohauer[12], J. Stroth[12,2], C. Sturm[2], R. Sultanov[9], Yongjie Sun[37], D. Svirida[9], O. Svoboda[53], R. Szczygieł[22], Zebo Tang[37], M. Tanha[12], J. Tarasiuk[52], O. Tarassenkova[24], M.-G. Târzilă[15], M. Teklishyn[45,38], T. Tischler[12], P. Tlustý[53], T. Tölyhi[51], A. Toia[2,12], N. Topil'skaya[14], M. Träger[2], I. Tsakov[16], Yu. Tsyupa[50], N.G. Tuturas[17], F. Uhlig[2], E. Usenko[14], I. Valin[40], D. Varga[51], I. Vassiliev[2], O. Vasylyev[2], E. Verbitskaya[44], A. Veshikov[23], R. Visinka[2], S. Volkov[24], A. Volochniuk[29], A. Vorobiev[50], Aleksey Voronin[16], Alexander Voronin[21], V. Vovchenko[10], M. Vznuzdaev[24], Dong Wang[42], Xi-Wei Wang[47], Yi Wang[39], M. Weber[19], C. Wendisch[2], J.P. Wessels[28], M. Wiebusch[12], D. Wielanek[36], A. Wieloch[4], A. Wilms[2], N. Winckler[2], M. Winter[40], K. Wiśniewski[52], Gy. Wolf[51], Sanguk Won[54], Ke-Jun Wu[47], J. Wüstenfeld[46], Changzhou Xiang[42], Nu Xu[42], Junfeng Yang[2,37], Rongxing Yang[37], Zhongbao Yin[42], In-Kwon Yoo[54], B. Yuldashev[16], I. Yushmanov[34], W. Zabołotny[36,52], Yu. Zaitsev[9], N.I. Zamiatin[16], M. Zhalov[24], Yifei Zhang[37], Lei Zhao[37], Jiajun Zheng[37], Sheng Zheng[47], Daicui Zhou[42], Jing Zhou[47], Xianglei Zhu[39], A. Zinchenko[16], M. Żołądź[22], P. Zrelov[1], V. Zryuev[16], P. Zumbruch[2], M. Zyzak[2]

[1]Laboratory of Information Technologies, Joint Institute for Nuclear Research (JINR-LIT), Dubna, Russia
[2]GSI Helmholtzzentrum für Schwerionenforschung GmbH (GSI), Darmstadt, Germany
[3]Department of Physics, Bose Institute, Kolkata, India
[4]Marian Smoluchowski Institute of Physics, Jagiellonian University, Kraków, Poland
[5]Physikalisches Institut, Eberhard Karls Universität Tübingen, Tübingen, Germany
[6]Department of Physics, Panjab University, Chandigarh, India
[7]Department of Physics, University of Kashmir, Srinagar, India
[8]Department of Physics, Aligarh Muslim University, Aligarh, India
[9]Institute for Theoretical and Experimental Physics (ITEP), Moscow, Russia
[10]Frankfurt Institute for Advanced Studies, Goethe-Universität Frankfurt (FIAS), Frankfurt, Germany
[11]Physikalisches Institut, Universität Heidelberg, Heidelberg, Germany
[12]Institut für Kernphysik, Goethe-Universität Frankfurt, Frankfurt, Germany
[13]University of Split, Split, Croatia
[14]Institute for Nuclear Research (INR), Moscow, Russia
[15]Horia Hulubei National Institute of Physics and Nuclear Engineering (IFIN-HH), Bucharest, Romania
[16]Veksler and Baldin Laboratory of High Energy Physics, Joint Institute for Nuclear Research (JINR-VBLHEP), Dubna, Russia
[17]Atomic and Nuclear Physics Department, University of Bucharest, Bucharest, Romania
[18]National Research Nuclear University MEPhI, Moscow, Russia
[19]Karlsruhe Institute of Technology (KIT), Karlsruhe, Germany
[20]Department of Physics and Department of Electronic Science, University of Calcutta, Kolkata, India
[21]Skobeltsyn Institute of Nuclear Phyiscs, Lomonosov Moscow State University (SINP-MSU), Moscow, Russia
[22]AGH University of Science and Technology (AGH), Kraków, Poland
[23]V.G. Khlopin Radium Institute (KRI), St. Petersburg, Russia
[24]National Research Center "Kurchatov Institute" B.P.Konstantinov, Petersburg Nuclear Physics Institute (PNPI), Gatchina, Russia
[25]Fakultät für Mathematik und Naturwissenschaften, Bergische Universität Wuppertal, Wuppertal, Germany
[26]Justus-Liebig-Universität Gießen, Gießen, Germany
[27]St. Petersburg Polytechnic University (SPbPU), St. Petersburg, Russia
[28]Institut für Kernphysik, Westfälische Wilhelms-Universität Münster, Münster, Germany
[29]Department of Nuclear Physics, Taras Shevchenko National University of Kyiv, Kyiv, Ukraine
[30]Variable Energy Cyclotron Centre (VECC), Kolkata, India
[31]Department of Physics, University of Jammu, Jammu, India
[32]Department of Physics, Gauhati University, Guwahati, India
[33]Indian Institute of Technology Kharagpur, Kharagpur, India
[34]National Research Centre "Kurchatov Institute", Moscow, Russia
[35]Institute of Physics, University of Silesia, Katowice, Poland
[36]Institute of Electronic Systems, Warsaw University of Technology, Warsaw, Poland
[37]Department of Modern Physics, University of Science & Technology of China (USTC), Hefei, China
[38]High Energy Physics Department, Kiev Institute for Nuclear Research (KINR), Kyiv, Ukraine
[39]Department of Engineering Physics, Tsinghua University, Beijing, China
[40]Institut Pluridisciplinaire Hubert Curien (IPHC), IN2P3-CNRS and Université de Strasbourg, Strasbourg, France

[41]Eötvös Loránd University (ELTE), Budapest, Hungary
[42]College of Physical Science and Technology, Central China Normal University (CCNU), Wuhan, China
[43]Institute for Computer Science, Goethe-Universität Frankfurt, Frankfurt, Germany
[44]Ioffe Institute, Russian Academy of Sciences, St. Petersburg, Russia
[45]Facility for Antiproton and Ion Research in Europe GmbH (FAIR), Darmstadt, Germany
[46]Institut für Strahlenphysik, Helmholtz-Zentrum Dresden-Rossendorf (HZDR), Dresden, Germany
[47]College of Science, China Three Gorges University (CTGU), Yichang, China
[48]Institut für Technische Informatik, Universität Heidelberg, Mannheim, Germany
[49]Institut für Kernphysik, Technische Universität Darmstadt, Darmstadt, Germany
[50]Institute for High Energy Physics (IHEP), Protvino, Russia
[51]Institute for Particle and Nuclear Physics, Wigner Research Centre for Physics, Hungarian Academy of Sciences, Budapest, Hungary
[52]Institute of Experimental Physics, University of Warsaw, Warsaw, Poland
[53]Nuclear Physics Institute of the Czech Academy of Sciences, Řež, Czech Republic
[54]Pusan National University (PNU), Pusan, Korea
[55]Institute of Physics, Bhubaneswar, India
[56]Czech Technical University (CTU), Prague, Czech Republic
[57]Physics Department, University of Rajasthan, Jaipur, India
[58]Konrad-Zuse-Zentrum für Informationstechnik Berlin (ZIB), Berlin, Germany
[59]Indian Institute of Technology Indore, Indore, India
[60]Department of Physics, Banaras Hindu University, Varanasi, India
[61]also: King Abdulaziz City for Science and Technology (KACST), Riyadh, Saudi Arabia
[62]also: Institute of Space Science, Bucharest, Romania
[63]also: Technische Universität Dresden, Dresden, Germany

Appendix B

List of Acronyms

A:	ADC	Analog-to-Digital Converter
	AFCK	AMC FMC Carrier Kintex
	AGS	Alternating Gradient Synchrotron
	ALICE	A Large Ion Collider Experiment
	AMC	Advanced Mezzanine Card
	ANN	Artificial Neural Network
	API	Application Programming Interface
	ASIC	Application Specific Integrated Circuit
	ATLAS	A Toroidal LHC ApparatuS
B:	BDT	Boosted Decision Tree
	BGA	Ball Grid Array
	BNL	Brookhaven National Laboratory
	BR	Branching Ratio
C:	CBM	Compressed Baryonic Matter
	CDR	Conceptual Design Report
	CERN	Conseil Européen pour la Recherche Nucléaire
	CF	Carbon Fibre
	CLK	CLocK
	CPU	Central Processing Unit
	CRI	Common Readout Interface
	CSA	Charge Sensitive Amplifier
D:	DAQ	Data AcQuisition
	DCS	Detector Control System
	DPB	Data Processing Board
	DSP	Digital Signal Processor
E:	ECAL	Electromagnetic CALorimeter
	ECS	Experiment Control System

	ENC	Equivalent Noise Charge
	ENOB	Effective Number Of Bits
	EPICS	Experimental Physics and Industrial Control System
F:	FAIR	Facility of Antiproton and Ion Research
	FEB	Front-End Boards
	FEE	Front-End Electronic
	FIFO	First In First Out
	FLES	First Level Event Selector
	FLIB	FLES Interface Board
	FLIM	FLES Interface Module
	FMC	FPGA Mezzanine Card
	FNR	First Neighbor Readout
	FPGA	Field Programmable Gate Array
	FWHM	Full Width Half Maximum
G:	GBT	GigaBit Transceiver
	GEANT	GEometry ANd Tracking
	GEM	Gas Electron Multiplier
	GH	Glueing Hours
H:	HDMI	High-Definition Multimedia Interface
	HDL	Hardware Description Language
	HSD	Hadron String Dynamics
	HT	High Tension
	HV	High Voltage
I:	ID	IDentification
	IIR	Infinite Impulse Response
	IMR	Intermediate Mass Region
	ISO	International Organization for Standardization
J:	JINR	Joint Institute of Nuclear Research
L:	LFR	Likelihood Function Ratio
	LHC	Large Hadron Collider
	LQ	Likelihood derived from charge (Q) measurement
	LV	Low Voltage
M:	MADC	Multiplexed Analog-to-Digital Converter
	MAPD	Multi-Avalanche Photo-Diodes
	MAPS	Monolithic Active Pixel Sensors
	MAPT	Multi-Anode Photomultiplier Tubes
	MC	Monte Carlo

	MIP	Minimum Ionizing Particle
	MPO	Multi-fiber Push On connector
	MPV	Most Probable Value
	MRPC	Multi-gap Resistive Plate Chambers
	MSV	Modularized Start Version
	MUCH	MUon CHambers
	MVD	Micro Vertex Detector
	MWPC	Multi-Wire Proportional Chamber
N:	NICA	Nuclotron-based Ion Collider fAcility
	NIEL	Non-Ionizing Energy Loss
	NIST	National Institute of Standards and Technology
P:	PASA	Pre-Amplifier Shaping Amplifier
	PC	Power Consumption
	PCB	Printed Circuit Board
	PCIe	Peripheral Component Interconnect express
	PDF	Probability Density Function
	PDR	Production Design Review
	PE	PolyEthylene
	PID	Particle IDentification
	PMMA	PolyMethylMethAcrylate
	PP	PolyPropylene
	PRF	Pad Response Function
	PRR	Production Readiness Review
	PS	Power Supply
		Proton Synchrotron
	PSD	Participant Spectator Detector
	PTE	Part Time Employees
Q:	QDC	Charge-to-Digital Converter
	QFP	Quad Flat Package
	QGP	Quark-Gluon Plasma
R:	RHIC	Relativistic Heavy-Ion Collider
	RICH	Ring Imaging CHerenkov
	RPC	Resistive Plate Chamber
	RRB	Resource Review Board
	ROB	Read-Out Board
	ROC	Read-Out Chamber
S:	SF	Spectral Function
	SIS	Schwer-Ionen Synchrotron
	SPADIC	Self-triggered Pulse Amplification and Digitization ASIC

	SPS	Super Proton Synchrotron
	ST	Shaping Time
	STAR	Solenoidal Tracker At RHIC
	STS	Silicon Tracking System
T:	TFC	Timing and Flow Control system
	THR	THReshold
	TID	Total Ionizing radiation Dose
	TOF	Time-Of-Flight
	TR	Transition Radiation
	TRD	Transition Radiation Detector
	TRT	Transition Radiation Tracker
	TSA	TimeSlice Archive
U:	UrQMD	Ultra-relativistic Quantum Molecular Dynamics
	UMC	United Microelectronics Corporation
	UV	Ultra-Violet
V:	VTR	Versatile TransReceiver
	VTT	Versatile Twin-Transmitter
W:	WH	Working Hours
	WHPD	Working Hour Per Day
	WHPW	Working Hour Per Week
	WLS	WaveLength Shifter
X:	XSI	Xilinx Simulation Interface
	XYTER	X-Y-Time-Energy Readout

Bibliography

[1] **Wuppertal-Budapest** Collaboration, S. Borsanyi *et al.*, "Is there still any T_c mystery in lattice QCD? Results with physical masses in the continuum limit III", *JHEP* **09** (2010) 073, arXiv:1005.3508 [hep-lat].

[2] A. Bazavov *et al.*, "The chiral and deconfinement aspects of the QCD transition", *Phys. Rev.* **D85** (2012) 054503, arXiv:1111.1710 [hep-lat].

[3] Y. Aoki *et al.*, "The order of the quantum chromodynamics transition predicted by the standard model of particle physics", *Nature* **443** (2006) 675–678, arXiv:hep-lat/0611014 [hep-lat].

[4] Z. Fodor and S. D. Katz, "Critical point of QCD at finite T and μ_B, lattice results for physical quark masses", *JHEP* **04** (2004) 050, arXiv:hep-lat/0402006 [hep-lat].

[5] A. Andronic *et al.*, "Hadron production in ultra-relativistic nuclear collisions: quarkyonic matter and a triple point in the phase diagram of QCD", *Nucl. Phys.* **A837** (2010) 65–86, arXiv:0911.4806 [hep-ph].

[6] K. Fukushima and T. Hatsuda, "The phase diagram of dense QCD", *Rept. Prog. Phys.* **74** (2011) 014001, arXiv:1005.4814 [hep-ph].

[7] **STAR** Collaboration, A. Schmah *et al.*, "Highlights of the beam energy scan from STAR", *Central Eur. J. Phys.* **10** (2012) 1238–1241, arXiv:1202.2389 [nucl-ex].

[8] **NA61** Collaboration, A. Aduszkiewicz *et al.*, "NA61/SHINE at the CERN SPS: plans, status and first results", *Acta Phys. Polon.* **B43** (2012) 635, arXiv:1201.5879 [nucl-ex].

[9] D. Blaschke *et al.*, "Topical issue on exploring strongly interacting matter at high densities - NICA white paper", *Eur. Phys. J. A* **52** no. 8, (2016) 1.

[10] W. Ehehalt and W. Cassing, "Relativistic transport approach for nucleus nucleus collisions from SIS to SPS energies", *Nucl. Phys.* **A602** (1996) 449–486.

[11] S. A. Bass *et al.*, "Microscopic models for ultrarelativistic heavy ion collisions", *Prog. Part. Nucl. Phys.* **41** (1998) 255–369, arXiv:nucl-th/9803035 [nucl-th].

[12] A. Andronic *et al.*, "Hadron production in central nucleus-nucleus collisions at chemical freeze-out", *Nucl. Phys.* **A772** (2006) 167–199, arXiv:nucl-th/0511071 [nucl-th].

[13] **CBM** Collaboration, T. Ablyazimov *et al.*, "Challenges in QCD matter physics – The scientific programme of the Compressed Baryonic Matter experiment at FAIR", *Eur. Phys. J.* **A53** no. 3, (2017) 60, arXiv:1607.01487 [nucl-ex].

[14] **CBM** Collaboration, P. Senger, V. Friese, *et al.*, "Nuclear matter physics at SIS-100". CBM Report 2012-01, 2011.

[15] B. Friman *et al.*, "The CBM physics book: Compressed baryonic matter in laboratory experiments", *Lect. Notes Phys.* **814** (2011) pp.1–980.

[16] H. Gutbrod *et al.*, "FAIR baseline technical report". ISBN 3-9811298-0-6 and ISBN 978-3-9811298-0-9, 2006.

[17] **NA60** Collaboration, H. J. Specht, "Thermal dileptons from hot and dense strongly interacting matter", *AIP Conf. Proc.* **1322** (2010) 1–10, `arXiv:1011.0615 [nucl-ex]`.

[18] R. Rapp and H. van Hees, "Thermal dileptons as fireball thermometer and chronometer", *Phys. Lett.* **B753** (2016) 586–590, `arXiv:1411.4612 [hep-ph]`.

[19] T. Galatyuk *et al.*, "Thermal dileptons from coarse-grained transport as fireball probes at SIS energies", *Eur. Phys. J.* **A52** no. 5, (2016) 131, `arXiv:1512.08688 [nucl-th]`.

[20] **NA60** Collaboration, R. Arnaldi *et al.*, "NA60 results on thermal dimuons", *Eur. Phys. J.* **C61** (2009) 711–720, `arXiv:0812.3053 [nucl-ex]`.

[21] **HADES** Collaboration, T. Galatyuk, "HADES overview", *Nucl. Phys.* **A931** (2014) 41–51.

[22] T. Matsui and H. Satz, "J/ψ Suppression by quark-gluon plasma formation", *Phys. Lett.* **B178** (1986) 416–422.

[23] **NA50** Collaboration, B. Alessandro *et al.*, "A new measurement of J/ψ suppression in Pb-Pb collisions at 158 GeV per nucleon", *Eur. Phys. J.* **C39** (2005) 335–345, `arXiv:hep-ex/0412036 [hep-ex]`.

[24] **PHENIX** Collaboration, A. Adare *et al.*, "J/ψ suppression at forward rapidity in Au+Au collisions at $\sqrt{s_{NN}} = 200$ GeV", *Phys. Rev.* **C84** (2011) 054912, `arXiv:1103.6269 [nucl-ex]`.

[25] **ALICE** Collaboration, B. Abelev *et al.*, "Centrality, rapidity and transverse momentum dependence of J/ψ suppression in Pb-Pb collisions at $\sqrt{s_{\rm NN}} = 2.76$ TeV", *Phys. Lett.* **B734** (2014) 314–327, `arXiv:1311.0214 [nucl-ex]`.

[26] A. Andronic *et al.*, "Production of light nuclei, hypernuclei and their antiparticles in relativistic nuclear collisions", *Phys. Lett.* **B697** (2011) 203–207, `arXiv:1010.2995 [nucl-th]`.

[27] I. Vassiliev, I. Kisel, and M. Zyzak, "Hypernuclei reconstruction at the CBM experiment", *CBM Progress Report 2016* (2017) 179–180.

[28] R. Brun and F. Rademakers, "ROOT: An object oriented data analysis framework", *Nucl. Instrum. Meth.* **A389** (1997) 81–86.

[29] R. Brun *et al.*, "GEANT3". CERN-DD-EE-84-1, 1987.

[30] **GEANT4** Collaboration, S. Agostinelli *et al.*, "GEANT4: A simulation toolkit", *Nucl. Instrum. Meth.* **A506** (2003) 250–303.

[31] G. Battistoni *et al.*, "The FLUKA code: description and benchmarking", *AIP Conf. Proc.* **896** (2007) 31–49.

[32] **CBM** Collaboration, C. Höhne *et al.*, *Technical Design Report for the CBM Ring Imaging Cherenkov Detector*. CBM Technical Design Reports. GSI, Darmstadt, 2013.

[33] I. Frohlich *et al.*, "Pluto: A Monte Carlo simulation tool for hadronic physics", *PoS* **ACAT2007** (2007) 076, arXiv:0708.2382 [nucl-ex].

[34] D. J. Lange, "The EvtGen particle decay simulation package", *Nucl. Instrum. Meth.* **A462** (2001) 152–155.

[35] B. Elisabetta and W. Zbigniew, "PHOTOS: An universal Monte Carlo for QED radiative corrections. Version 2.0", *Comput. Phys. Commun.* **79** (1994) 291–308.

[36] W. Cassing and E. L. Bratkovskaya, "Hadronic and electromagnetic probes of hot and dense nuclear matter", *Phys. Rept.* **308** (1999) 65–233.

[37] F. Seck, *Development of a realistic event generator for in-medium and QGP dileptons.* Master's thesis, Technische Universität Darmstadt, 2015.

[38] R. Rapp, J. Wambach, and H. van Hees, "The chiral restoration transition of QCD and low mass dileptons", *Landolt-Bornstein* **23** (2010) 134, arXiv:0901.3289 [hep-ph].

[39] **PHENIX** Collaboration, A. Adare *et al.*, "Detailed measurement of the e^+e^- pair continuum in $p+p$ and Au+Au collisions at $\sqrt{s_{NN}} = 200$ GeV and implications for direct photon production", *Phys. Rev.* **C81** (2010) 034911, arXiv:0912.0244 [nucl-ex].

[40] J. Book, *J/ψ production in Pb-Pb collisions with ALICE at the LHC.* PhD thesis, Goethe-Universität Frankfurt, 2014.

[41] W. Cassing, E. L. Bratkovskaya, and A. Sibirtsev, "Open charm production in relativistic nucleus-nucleus collisions", *Nucl. Phys.* **A691** (2001) 753–778, arXiv:nucl-th/0010071 [nucl-th].

[42] **CBM** Collaboration, S. Chattopadhyay *et al.*, *Technical Design Report for the CBM : Muon Chambers (MuCh).* CBM Technical Design Reports. GSI, Darmstadt, 2015.

[43] D. Pfeiffer *et al.*, "The radiation field in the Gamma Irradiation Facility GIF++ at CERN", *Nucl. Instrum. Meth.* **A866** (2017) 91–103, arXiv:1611.00299 [physics.ins-det].

[44] R. Veenhof, "GARFIELD, recent developments", *Nucl. Instrum. Meth.* **A419** (1998) 726–730.

[45] **ALICE** Collaboration, P. Cortese *et al.*, *ALICE transition-radiation detector: technical design report.* Technical Design Report ALICE. CERN, Geneva, 2001.

[46] M. Staib *et al.*, "Thermal stretching of large-area GEM foils using an infrared heating method". RD51-Note-2011-004, 2011.

[47] M. Seidl, *Studien zur Ausdehnung des Eingangsfensters des CBM-TRDs.* Bachelor's thesis, Goethe-Universität Frankfurt, 2014.

[48] T. Akesson *et al.*, "Aging studies for the ATLAS transition radiation tracker (TRT)", *Nucl. Instrum. Meth.* **A515** (2003) 166–179.

[49] **ALICE** Collaboration, S. Acharya *et al.*, "The ALICE Transition Radiation Detector: construction, operation, and performance", *Nucl. Instrum. Meth.* **A881** (2018) 88–127, arXiv:1709.02743 [physics.ins-det].

[50] **ATLAS TRT** Collaboration, E. Abat *et al.*, "The ATLAS Transition Radiation Tracker (TRT) proportional drift tube: design and performance", *JINST* **3** (2008) P02013.

[51] A. Abuhoza *et al.*, "Optimization of a setup for ageing studies of gaseous detectors", *CBM Progress Report 2011* (2012) 52.

[52] A. Andronic and J. P. Wessels, "Transition radiation detectors", *Nucl. Instrum. Meth.* **A666** (2012) 130–147, `arXiv:1111.4188 [physics.ins-det]`.

[53] M. L. Cherry *et al.*, "Transition radiation from relativistic electrons in periodic radiators", *Phys. Rev.* **D10** (1974) 3594–3607.

[54] M. J. Berger and K. Olsen, "XCOM: photon cross sections database". NIST Standard Reference Database 8, 3, 1998. `http://www.nist.gov/pml/data/xcom/index.cfm`.

[55] M. N. Mazziotta, "A Monte Carlo code for full simulation of a transition radiation detector", *Comput. Phys. Commun.* **132** (2000) 110–123, `arXiv:physics/9912042 [physics]`.

[56] C. W. Fabjan and W. Struczinski, "Coherent emission of transition radiation in periodic radiators", *Phys. Lett.* **B57** (1975) 483.

[57] G. M. Garibian, L. A. Gevorgian, and C. Yang, "The calculation of X-ray transition radiation generated in regular- and irregular-layered media", *Nucl. Instrum. Meth.* **125** no. 1, (1975) 133–137.

[58] M. W. Conroy *et al.*, "Liquid drainage from high-expansion (HiEx) aqueous foams during and after filling of a container", *Colloids and Surfaces A: Physicochemical and Engineering Aspects* **426** no. 0, (2013) 70–97.

[59] C. Bergmann, *Development, simulation and test of transition radiation detector prototypes for the Compressed Baryonic Matter experiment at the Facility for Antiproton and Ion Research.* PhD thesis, Westfälische Wilhelms-Universität Münster, 2014.

[60] T. Armbruster, *SPADIC – A self-triggered detector readout ASIC with multi-channel amplification and digitization.* PhD thesis, Ruprecht-Karls Universität Heidelberg, 2013.

[61] T. Armbruster and M. Krieger, "SPADIC project website". `http://spadic.uni-hd.de`.

[62] T. Armbruster, P. Fischer, and I. Peric, "SPADIC – A self-triggered pulse amplification and digitization ASIC", in *2010 IEEE Nuclear Science Symposium and Medical Imaging Conference (NSS/MIC)*, pp. 1358–1362. Oct, 2010.

[63] T. Armbruster *et al.*, "Multi-channel charge pulse amplification, digitization and processing ASIC for detector applications", in *2012 IEEE Nuclear Science Symposium and Medical Imaging Conference (NSS/MIC)*, pp. 697–702. Oct, 2012.

[64] F. Lemke and U. Bruening, "A hierarchical synchronized data acquisition network for CBM", *IEEE Transactions on Nuclear Science* **60** no. 5, (Oct, 2013) 3654–3660.

[65] K. Kasinski *et al.*, "STS-XYTER, a high count-rate self-triggering silicon strip detector readout IC for high resolution time and energy measurements", in *2014 IEEE Nuclear Science Symposium and Medical Imaging Conference (NSS/MIC)*, pp. 1–6. Nov, 2014.

[66] K. Kasinski *et al.*, "A protocol for hit and control synchronous transfer for the front-end electronics at the CBM experiment", *Nucl. Instrum. Meth.* **A835** (2016) 66–73.

[67] K. Kasinski, R. Szczygiel, and W. Zabolotny, "Back-end and interface implementation of the STS-XYTER2 prototype ASIC for the CBM experiment", *JINST* **11** no. 11, (2016) C11018.

[68] I. Peric *et al.*, "DCD – The multi-channel current-mode ADC chip for the readout of DEPFET pixel detectors", *IEEE Transactions on Nuclear Science* **57** no. 2, (April, 2010) 743–753.

[69] M. Krieger, *Entwurf und Simulation eines digitalen Tail-Cancellation-Filters*. Diploma thesis, Ruprecht-Karls Universität Heidelberg, 2011.

[70] E.-E. department CERN, "GBT & Versatile Link". `http://ep-ese.web.cern.ch/content/gbt-versatile-link`.

[71] **CBM** Collaboration, D. Emschermann *et al.*, *Technical design report for the CBM online systems*. CBM Technical Design Reports. GSI, Darmstadt, in preparation.

[72] J. S. Gordon and E. Mathieson, "Cathode charge distributions in multiwire chambers. 1: Measurement and theory", *Nucl. Instrum. Meth.* **A227** (1984) 267–276.

[73] E.-E. department CERN, "Development of DCDC converters @ CERN". `http://project-dcdc.web.cern.ch/project-dcdc/Default.html`.

[74] "Experimental Physics and Industrial Control System (EPICS)". `http://www.aps.anl.gov/epics/about.php`, 2017.

[75] **ALICE** Collaboration, A. Andronic *et al.*, "Energy loss of pions and electrons of 1 GeV/c to 6 GeV/c in drift chambers operated with Xe, CO(2)(15%)", *Nucl. Instrum. Meth.* **A519** (2004) 508–517, `arXiv:physics/0310122 [physics]`.

[76] W. W. M. Allison and J. H. Cobb, "Relativistic charged particle identification by energy loss", *Ann. Rev. Nucl. Part. Sci.* **30** (1980) 253–298.

[77] E. Mathieson, "Cathode charge distributions in multiwire chambers. 4: empirical formula for small anode - cathode separation", *Nucl. Instrum. Meth.* **A270** (1988) 602–603.

[78] I. Kisel, "Event reconstruction in the CBM experiment", *Nucl. Instrum. Meth.* **A566** (2006) 85–88.

[79] R. E. Kalman, "A new approach to linear filtering and prediction problems", *Transactions of the ASME–Journal of Basic Engineering* **82** no. Series D, (1960) 35–45.

[80] R. Fruhwirth, "Application of Kalman filtering to track and vertex fitting", *Nucl. Instrum. Meth.* **A262** (1987) 444–450.

[81] **Particle Data Group** Collaboration, K. A. Olive *et al.*, "Review of particle physics", *Chin. Phys.* **C38** (2014) 090001.

[82] W. Press, *Numerical Recipes: The art of scientific computing*. Cambridge University Press, 2007.

[83] R. Fruhwirth *et al.*, *Data analysis techniques for high-energy physics*. Cambridge University Press, 2000.

[84] A. Lebedev and G. Ososkov, "LIT track propagation for CBM". CBM-SOFT-note-2008-002, 2008.

[85] E. P. Akishina *et al.*, "Electron/pion identification in the CBM-TRD applying a multilayer perceptron". JINR-E–10-2007-17, 2007.

[86] E. Bechtel, *Electron identification with a likelihood method and measurements of di-electrons for the CBM-TRD.* Master's thesis, Goethe-Universität Frankfurt, 2017.

[87] B. Lasiuk and C. A. Whitten, "Use of Krypton-83 as a calibration source for the STAR TPC". STAR Note 360, 1998.

[88] **NA49** Collaboration, S. Afanasev *et al.*, "The NA49 large acceptance hadron detector", *Nucl. Instrum. Meth.* **A430** (1999) 210–244.

[89] M. Al-Helwi, *Gain calibration of the ALICE transition radiation detector with Krypton-83.* Diploma thesis, Ruprecht-Karls Universität Heidelberg, 2010.

[90] J. H. Stiller, *Gain calibration of the ALICE TRD using the decay of* ^{83}Kr *and alignment of the ALICE TRD.* Diploma thesis, Ruprecht-Karls Universität Heidelberg, 2011.

[91] V. Blobel and C. Kleinwort, "A new method for the high precision alignment of track detectors", in *Advanced statistical techniques in particle physics. Proceedings, Conference, Durham, UK, March 18-22, 2002*, pp. URL–STR(9). 2002. `arXiv:hep-ex/0208021 [hep-ex]`.